Strontium Isotopes in Jurassic and Early Cretaceous Seawater

A dissertation submitted to the

University of Oxford

for the degree of

Doctor of Philosophy

by

Charles Edward Jones

Jesus College

Department of Earth Sciences

Trinity Term, 1992

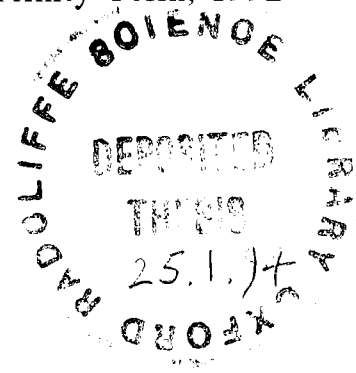

Table of Contents

List of Figures

List of Tables

Acknowledgements

The author would like to thank Hugh Jenkyns, Steve Hesselbo, and Angela Coe for their guidance in the field, for the time they devoted to collecting belemnites, and for their friendship and professional support. Brenda Rohl is especially thanked for her friendship and support and for helping to draught the diagrams of Chapters 3 and 4. Brenda and Andrew Rohl were vital to my survival and success during those bleak months when I was writing up in Oxford and my Sweetie was toiling away in the barbarian salt mines at the University of Michigan. Of course, when I came to Michigan and continued the long writing process, I relied heavily on my long-suffering wife and sweetie, Laura Kay Stepp. She was a pillar of support (as opposed to salt) and I love her for it.

Strontium Isotopes in Jurassic and Early Cretaceous Seawater

A dissertation submitted to the
University of Oxford
for the degree of
Doctor of Philosophy
by

Charles Edward Jones
Jesus College,
Department of Earth Sciences

Trinity Term, 1992

Abstract

The collection and analysis of a large number of belemnites and oysters with excellent biostratigraphic and diagenetic control has resulted in a highly detailed determination of the seawater Sr-isotope curve through the Jurassic and Early Cretaceous. The new data confirm the broad trends established by previous work, but the much sharper resolution of the new data allows the application of Sr-isotope stratigraphy with an optimal stratigraphic resolution of ± 1 to 4 ammonite subzones (± 0.5 to 2 Ma). The data show a general decline from the Hettangian (Early Jurassic) to a minimum in the Callovian and Oxfordian (Middle/Late Jurassic). This is followed by an increase through the Kimmeridgian (Late Jurassic) to a plateau reached in the Barremian (Early Cretaceous). In addition, there are major negative excursions in the Pliensbachian/Toarcian (Early Jurassic) and Aptian/Albian (Early Cretaceous).

Stable isotope data collected from belemnites and oysters have resulted in the most extensive Jurassic $\delta^{13}C$ and $\delta^{18}O$ database to date. While both the carbon and oxygen data appear to give reasonable marine signals, the scatter in the data suggests that future research must document possible biological fractionation effects and develop better indicators for the diagenetic alteration of $\delta^{13}C$ and $\delta^{18}O$.

The final chapter documents an unexpected correlation between sudden shifts in the Sr-isotope curve, the occurrence of positive $\delta^{13}C$ excursions, and the eruption of flood basalts. In the Jurassic and Cretaceous there is a correlation in time between sudden downward shifts in the Sr-isotope curve (Pliensbachian, Aptian, Cenomanian/Turonian), the occurance of positive $\delta^{13}C$ excursions, and the eruption of flood basalts. Each of these major downward shifts in the Sr-isotope curve is followed by a sudden upward shift, which although associated with a positive $\delta^{13}C$ excursion is not associated with an episode of flood basalt volcanism. In the Cenozoic the Sr-isotope curve no longer displays downward shifts, but the correlation continues between the occurrence of flood basalts and positive $\delta^{13}C$ excursions. Several lines of evidence suggest that the eruption of flood basalts is associated with pulses of hydrothermal activity, and that this hydrothermal activity brings about the conditions necessary for the genesis of carbon-burial events.

Extended Abstract

This study presents an extensive new data set yielding a detailed outline of the seawater Sr-isotope curve through the Jurassic and Early Cretaceous. Belemnites and oysters were collected from well-exposed, well-described, and well-dated stratigraphic sections exposed along the Dorset and Yorkshire coasts and in various other localities throughout Great Britain. Measurement of Mn and Fe concentrations in the fossil calcite allows diagenetically altered samples to be distinguished from more pristine samples. As a result of the excellent biostratigraphic and diagenetic control, the quality of the Jurassic and Lower Cretaceous data rivals that of the best portions of the Cenozoic Sr-isotope curve. The highest quality data are of Early Jurassic age.

Beginning in the latest Triassic, the Sr-isotope curve rises out of the Rhaetian and reaches a plateau in the Hettangian (Early Jurassic). Beginning in the earliest Sinemurian it rapidly descends until reaching a minimum in the latest Pliensbachian. After an initially slow recovery in the Toarcian, the curve suddenly jumps up across the *exaratum/falciferum* subzonal boundary. The rate of this increase is probably accentuated by a gap in the sedimentary record spanning 1 2 units of subzone time. The curve then smoothly increases through the rest of the Toarcian and Aalenian (Middle Jurassic) and reaches a peak near the Aalenian/Bajocian boundary. After an initially slow decline, the curve rapidly descends through the Late Bajocian. It is not clear whether there is a small reversal in the earliest Bathonian or if the curve simply continues its rapid descent down to the minimum located probably in the Early Callovian. The curve then rises slightly to reach a peak in the Late Callovian and then descends to a second minimum in the Early Oxfordian (Late Jurassic). From this time through the Barremian (Early Cretaceous) the curve steadily increases, with periods of apparently accelerated increase during the Early Kimmeridgian (Late Jurassic) and Ryazanian/Valanginian (Early Cretaceous). A major downward shift occurs some time during the late Barremian or early Aptian and the curve reaches another minimum during the middle-to-late Aptian. By the Albian the curve has recovered from this downward shift and is ready to begin its general increase into the Late Cretaceous. The data are of sufficient quality over many intervals that they can be used as a stratigraphic correlation tool that allows a potential correlative resolution of ± 1 to 4 ammonite subzones (± 0.5 to 2 Ma).

Stable isotopic data collected from the same belemnites and oysters have resulted in the most detailed, extensive Jurassic $\delta^{13}C$ and $\delta^{18}O$ database to date. The carbon data appear to reproduce all known positive carbon-isotope excursions in the Jurassic and Early Cretaceous and are used to confirm intervals in the Early Jurassic that are suspected to host carbon-burial events on the basis of sedimentological evidence. The $\delta^{18}O$ data seem to indicate that the Early Jurassic was warmer than the rest of the Jurassic and Early Cretaceous, but before such conclusions may be drawn with confidence, considerable work needs to be done to document possible biological fractionation effects and to develop better indicators of the diagenetic alteration of both $\delta^{13}C$ and $\delta^{18}O$.

A detailed consideration of the geochemical cycle of Sr in seawater attempts to reconcile the considerable discrepancy between the volume of the hydrothermal flux of seawater through the mid-ocean ridges as calculated by geophysical and geochemical models. Because the geophysical estimate seems more robust, the reconciliation of the two estimates requires an adjustment of the Sr cycle such that the importance of the riverine flux is reduced and additional sources of basaltic Sr are found that do not come under the constraints of the geophysically modelled axial fluid flow. The riverine component of the Sr cycle was modified through the exclusion of the anomalous Ganges and Brahmaputra rivers from the weighted global average. This results in a slightly lower average riverine Sr concentration and a significantly lower average $^{87}Sr/^{86}Sr$ ratio. Addition of the diagenetic and groundwater flux terms to the Sr cycle has little effect on the magnitude of the hydrothermal flux required to balance the Sr cycle. A detailed consideration of the hydrothermal component of the Sr cycle suggests that the axial hydrothermal fluid flux can be broken into two components, a volumetrically dominant fluid that has not undergone phase separation and that shows little net change in the average Sr concentration relative to seawater, and a brine that has undergone phase separation and shows a large enrichment in Sr relative to seawater. Although current evidence suggests that the brine flux is a minor component of the Sr cycle, the possible importance of this term provides good reason for future scrutiny. A more important hydrothermal flux is associated with the off-axis, low-temperature alteration of basalts. This term may comprise 25% of the total flux of basaltic Sr to the oceans. Despite the identification of these additional terms in the Sr cycle, the discrepancy between the geophysical and geochemical estimates can only be reduced from a

factor of 6 difference to a factor of 2 difference. The likely cause of this discrepancy is either recent glacial and tectonic erosion that has increased the flux of radiogenic riverine Sr to the oceans, or a bias in the riverine data set towards rivers draining tectonically active areas of the world that results in an inflated estimate of the global riverine $^{87}Sr/^{86}Sr$ ratio.

The final chapter documents a correlation in time between sudden shifts in the Sr-isotope curve, the occurrence of positive $\delta^{13}C$ excursions, and the eruption of flood basalts. In the Jurassic and Cretaceous there is a correlation between sudden downward shifts in the Sr-isotope curve (Pliensbachian, Aptian, Cenomanian/Turonian), positive $\delta^{13}C$ excursions, and flood basalts. Each of these major downward shifts in the Sr-isotope curve is paired with a sudden upward shift, and each upward shift is associated with a positive $\delta^{13}C$ excursion, but not with an episode of flood basalt volcanism. In the Cenozoic the Sr-isotope curve no longer displays downward shifts, but a correlation between the occurrence of flood basalts and positive $\delta^{13}C$ excursions remains. Although the Sr-isotope curve is commonly viewed as a record of continental erosion, model calculations indicate that the variations in the curve between roughly 125 and 40 Ma are faithfully reproduced when the mid-ocean ridge hydrothermal input is varied according to measured changes in the rate of oceanic crustal generation. This result, combined with the correlation between negative shifts in the Sr-isotope curve and the eruption of flood basalts, suggests that the major negative excursions in the Sr-isotope curve in the Pliensbachian/Toarcian, Aptian/Albian, and Cenomanian-Coniacian are the result of hydrothermal activity. Moreover, the occurrence of positive $\delta^{13}C$ excursions at the beginning and end of inferred hydrothermal events in the Mesozoic and at the same time as the eruption of flood basalts in the Cenozoic suggests that periods of enhanced organic carbon burial are linked to bursts of hydrothermal activity. The occurrence of $\delta^{13}C$ excursions at the beginning and end of hydrothermal events presents difficulties for current models attempting to explain the genesis of carbon-burial events.

Chapter 1: Introduction

1.1 Principles and Applications

Strontium-isotope stratigraphy is founded on three principles: 1) Sr is isotopically homogeneous in seawater at any given time; 2) The marine $^{87}Sr/^{86}Sr$ ratio has varied systematically through geological time; 3) The seawater Sr-isotope signal is accurately recorded by Ca-bearing minerals precipitated directly from normal seawater. The isotopic homogeneity of seawater Sr is a consequence of the long residence time of Sr (2 - 4 Ma; Hodell *et al.*, 1989, 1990) compared to the short mixing time of the oceans (ca. 1 - 2 ka; Broecker and Peng, 1982), which allows a given mole of Sr atoms to be dispersed and mixed several thousand times throughout the world's oceans before finally being removed as a component of biogenic carbonate. The variation in the seawater Sr-isotope curve through geological time is caused by fluctuations in the various geochemical inputs of Sr into the marine system. The modern seawater $^{87}Sr/^{86}Sr$ ratio of 0.7092 is primarily determined by the balance between radiogenic Sr delivered to the oceans by rivers weathering the continents ($^{87}Sr/^{86}Sr \approx 0.7119$; Palmer and Edmond, 1989) and nonradiogenic Sr delivered to the oceans by the mid-ocean ridge hydrothermal systems ($^{87}Sr/^{86}Sr \approx 0.7035$; Palmer and Elderfield, 1985). A minor buffering effect is provided by the re-dissolution of recently deposited marine carbonates yielding Sr of near-seawater isotopic composition ($^{87}Sr/^{86}Sr = 0.7084$; Elderfield and Gieskes, 1982).

The most obvious application of the Sr-isotope curve is as a global correlation tool. The main advantages of Sr-isotope stratigraphy are that the globally synchronous signal is not limited by faunal provincialism; the technique requires relatively small amounts of well-preserved primary marine calcite for analysis; correlation is relatively objective; and it is relatively easy for the careful novice to become involved. The main disadvantages are that the technique requires well-preserved, primary marine calcite and that at present there are few geochemical guidelines that allow one to distinguish objectively between primary and

diagenetically contaminated results. Despite these drawbacks, Sr-isotope stratigraphy is well-enough advanced to have been applied to a wide variety of stratigraphic problems (Hurst, 1986; Smalley *et al.*, 1986, 1989; Knittel and Daniels, 1987; Ludwig *et al.*, 1988; McKenzie *et al.*, 1988; Rundberg and Smalley, 1989).

In addition to simple correlation, the known history of seawater Sr isotopes allows one to constrain such processes as fluid flow and the diagenetic alteration of sediments. If the age of a given package of sediments is known, the original $^{87}Sr/^{86}Sr$ ratio of the pore waters and primary carbonate and phosphate phases may be inferred from the seawater Sr-isotope curve. Any deviation from the primary signal may be due to older porewaters advecting up towards the seafloor during compaction (Richter and DePaolo, 1987, 1988), recrystallisation of volcanic materials releasing relatively nonradiogenic Sr (Gieskes *et al.*, 1986), groundwater flow transporting relatively radiogenic Sr (Kastner *et al.*, 1990), and the breakdown of detrital minerals providing either radiogenic or nonradiogenic Sr, depending on sediment provenance (Emery *et al.*, 1987). Thus, the combination of Sr isotopes and other geochemical tracers has so far provided insight into processes of diagenesis in deep sea and shallow marine sediments (Gieskes *et al.*, 1986; Emery *et al.*, 1987), causes of certain types of dolomitisation (Saller, 1984; Aharon *et al.*, 1987; Andrews *el.*, 1987; Swart *et al.*, 1987; Vahrenkamp *et al.*, 1988), fluid flow pathways in continental margin sediments (Elderfield *et al.*, 1990; Gieskes *et al.*, 1990 Kastner *et al.*, 1990, 1991), and pathways of fluids related to mineralisation and oil migration events (Medford *et al.*, 1983; Burtner, 1987; see review by Veizer, 1989).

The evolution of the seawater Sr-isotope curve is also interesting in its own right as a biostratigraphically well-dated curve whose features reflect the balance between competing processes of tectonism, global weathering, and sea floor hydrothermal activity. As shown in Figure 1.1, the seawater Sr-isotope curve remained roughly level between 70 and 40 Ma. Then at 40 Ma this invariance was abruptly terminated and the curve began a steady if

uneven increase towards the present. This rapid rise over the past 40 Ma could have been caused by a decreasing flux of mid-ocean ridge hydrothermal fluids, an increase in the $^{87}Sr/^{86}Sr$ of river water, an increase in the mass flux of riverine Sr, or a combination of these three factors. Under the assumption that hydrothermal venting is proportional to sea-floor crustal generation rates, the limited changes in global spreading rates over the past 40 Ma appear to rule out a reduction in the hydrothermal flux as the main cause of the increase (Palmer and Elderfield, 1985). Although there are no independent constraints on the variations of either the mass flux or the $^{87}Sr/^{86}Sr$ ratio of riverine Sr over geological time, most authors interpret the last few million years of the Sr-isotope curve in terms of a higher mass flux of Sr due to increased chemical weathering of the continents in general and the Himalayas in particular (Hess *et al.*, 1986; Raymo *et al.*, 1988; Hodell *et al.*, 1989, 1990, 1991; Richter *et al.*, 1992; Krishnaswami *et al.*, 1992), and several authors have used the Sr-isotope curve as an index of continental weathering over the entire Phanerozoic (François and Walker, 1992; Richter *et al.*, 1992; François *et al.*, in press). However, despite the enthusiasm for a purely continental interpretation of the Sr-isotope curve, it is worth noting that it is difficult to eliminate the possibility that hydrothermal processes may have at times been significant in determining the evolution of the curve.

1.2 Compilation and Summary of Previous Results

Frans Wickman (1948) was the first to recognise the possibility of using the evolution of the seawater Sr-isotope curve, as recorded by limestones, to help constrain the ages of marine sediments. He reasoned that the average age, and hence the average $^{87}Sr/^{86}Sr$ ratio, of the earth's surface should increase monotonically as a function of age due to the decay of ^{87}Rb to ^{87}Sr. The world's rivers provide a link between the aging of the earth's surface and the Sr-isotopic evolution of the oceans by providing a globally averaged sample of continental Sr to the seas. Thus, in the absence of mid-ocean ridge hydrothermal springs, which were not then known to exist, the seawater $^{87}Sr/^{86}Sr$ ratio should increase

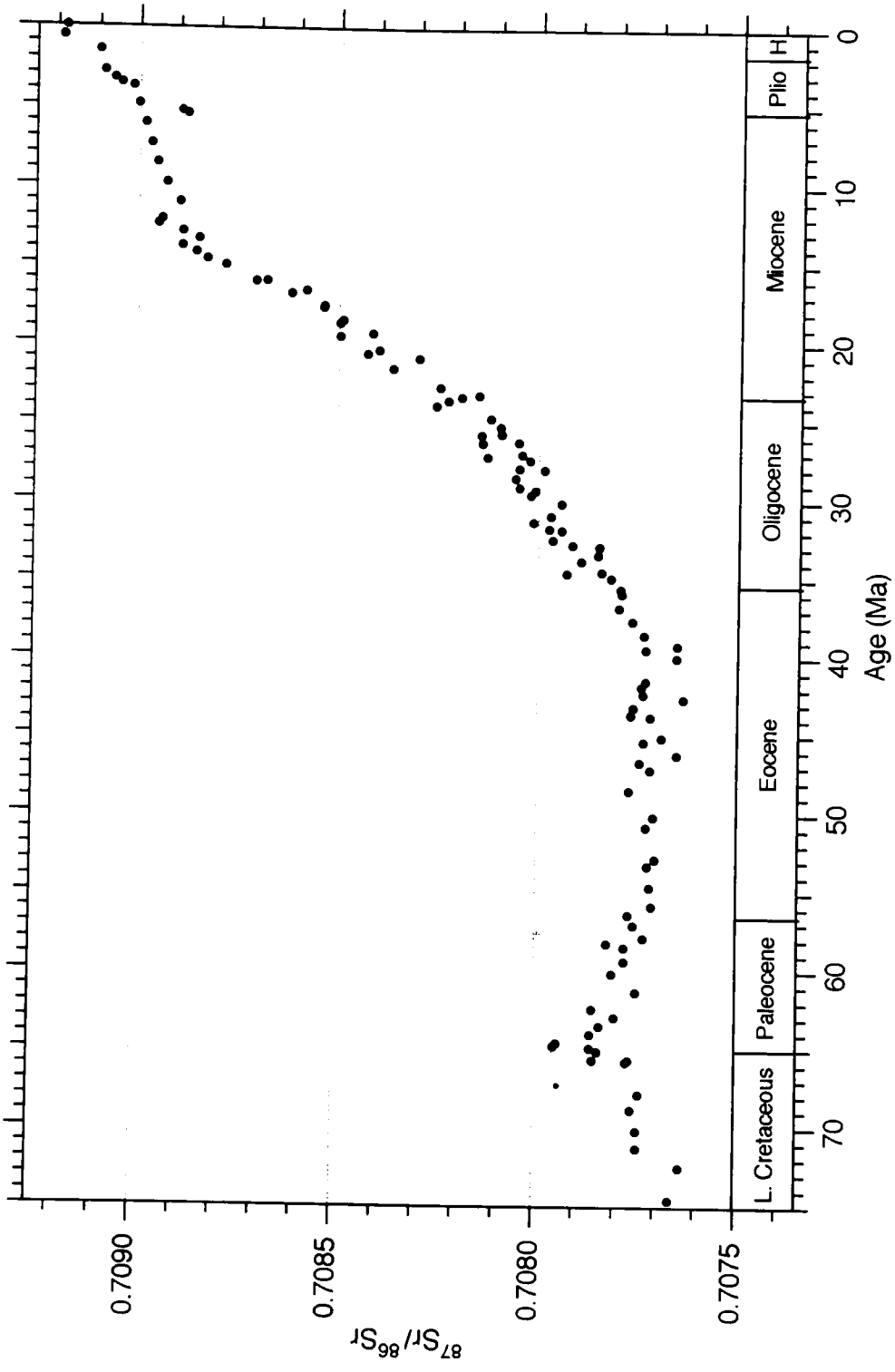

Figure 1.1: Evolution of the seawater Sr-isotope curve over the past 75 Ma. Data from Hess *et al.* (1986).

monotonically as a function of the average age of the earth's surface. A number of studies tested this idea by analysing bulk limestone samples spanning the past 2.5 Ga (Gast, 1955; Gerling and Shukolyukov, 1957; Hedge and Walthall, 1963; Hurley *et al.*, 1965). They found that the increase was much less than originally predicted and ascribed this to preferential weathering of volcanic and Rb-poor minerals and to an over-estimation of the average crustal Rb/Sr ratio. While Brookins *et al.* (1969) found that some Permian $^{87}Sr/^{86}Sr$ ratios did not in fact fit the linear trend, it was Peterman *et al.* (1970) who first proved that the seawater Sr-isotope curve has shown repeated fluctuations over Phanerozoic time. Over the next 10 years a large number of studies set out to document the details of this curve, but due to poor analytical precision and poor sample preparation, the results are now largely of historical interest (Elderfield, 1986). The results from these early studies are well-summarised by Faure (1982).

The turning point for Sr-isotope stratigraphy was the publication of a second Phanerozoic seawater curve by Burke *et al.* (1982). This study benefited from a much higher degree of analytical reproducibility, a large number of samples from DSDP cores that appear to have suffered relatively minor diagenesis, and a vast number (786) of bulk-rock samples from around the world. The DSDP material yielded a well-defined curve for the Cenozoic and much of the Late Cretaceous, but unfortunately older limestone samples from land-based outcrops gave data of much lower quality (Fig. 1.2). Thus, although Burke *et al.* (1982) conclusively demonstrated that the seawater Sr-isotope curve has undergone significant variations throughout the Phanerozoic, the scatter in data older than 70 Ma partially obscures the true path of the curve and thus impairs the application of Sr-isotope stratigraphy and limits palaeoceanographic interpretations over these intervals.

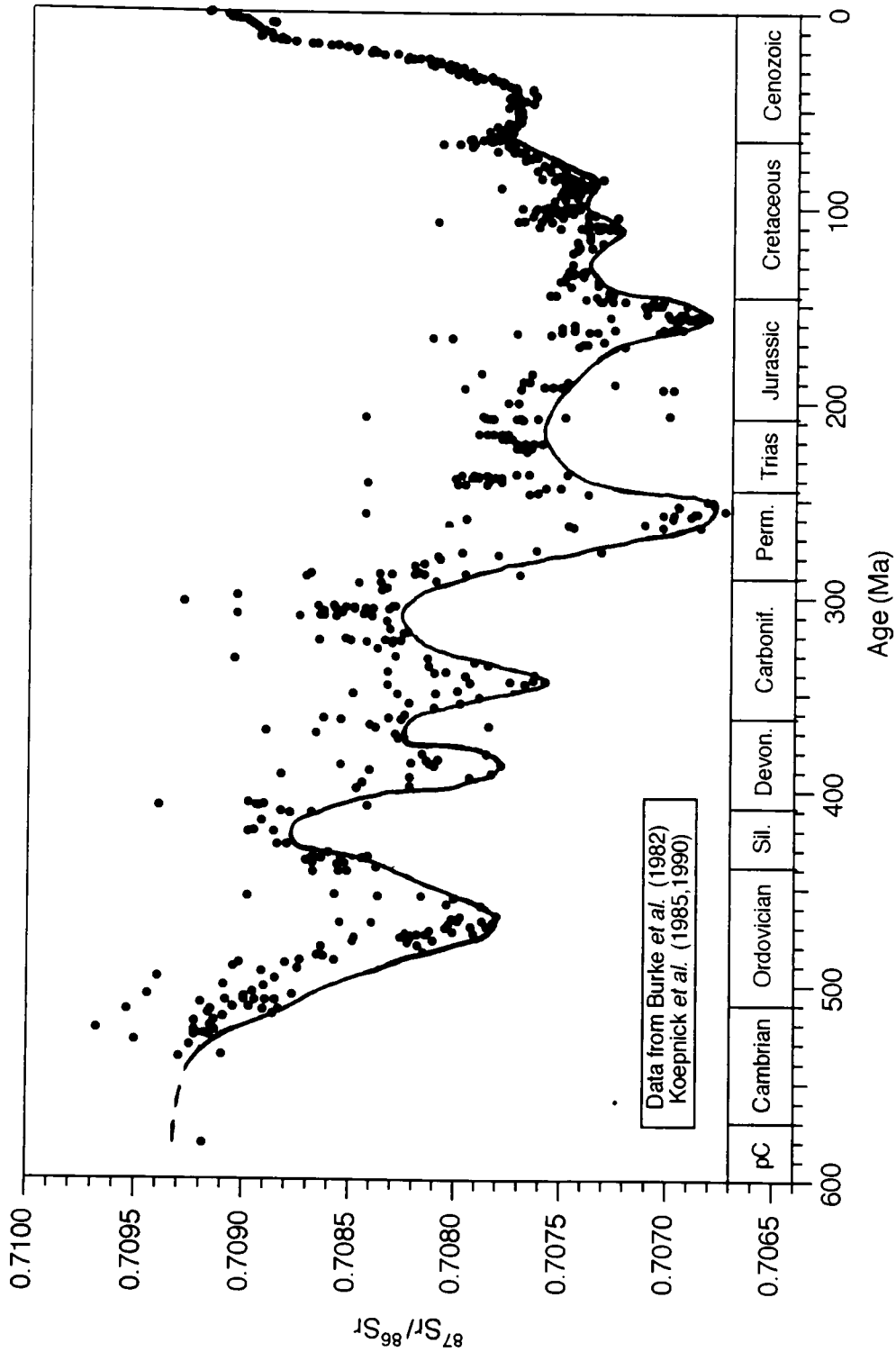

Figure 1.2: The Phanerozoic Sr-isotope curve of Burke *et al.* (1982). The line drawn along the bottom of the data scatter represents the best-estimate of the true trend of the seawater curve based on the assumption that diagenetic alteration generally raises the $^{87}Sr/^{86}Sr$ of the bulk limestone.

Since 1985 a number of studies have refined the seawater Sr-isotope curve for the Cenozoic and Late Cretaceous (DePaolo and Ingram, 1985; Palmer and Elderfield, 1985; Hess *et al.*, 1986, 1989; DePaolo, 1986; Hodell *et al.*, 1989, 1990, 1991; Miller *et al.*, 1988, 1990; Capo and DePaolo, 1990; Nelson *et al.*, 1991) and for the Precambrian and Early Palaeozoic (Veizer and Compston, 1976; Veizer *et al.*, 1983; Shaw and Wasserburg, 1985; Keto and Jacobsen, 1987; Derry and Jacobsen, 1988; Derry *et al.*, 1989). Only a smattering of data points has been published for intervening times (Jurassic: Fischer and Gygi, 1989; Smalley *et al.*, 1990; Permian: Brookins, 1988; Carboniferous: Popp *et al.*, 1986; Brand, 1991). The development of the Cenozoic and Late Cretaceous Sr-isotope curve reflects the abundance and generally good preservation of ODP material whereas the work on the Precambrian portions of the curve mainly reflects an interest in the long-term growth and evolution of the continents over the past 4.5 Ga. The intervening times have been neglected due to the difficulty of working with land-based sections, which tend to be relatively incomplete, poorly exposed, and diagenetically altered, and because most of the isotopically interesting continental growth events seem to have been completed by the beginning of the Cambrian (Condie, 1989).

The results of these studies for the Cenozoic and Mesozoic are summarised in Figures 1.3 and 1.4. Figure 1.3 shows the evolution of the Sr-isotope curve over the past 210 Ma based on data from DePaolo and Ingram (1985), Hess *et al.* (1986), DePaolo (1986), Nelson *et al.* (1991), McArthur *et al.* (1992), and this study. It illustrates at once the reproducibility and the systematic trend of the seawater curve over the past 210 Ma as well as the high quality of the Jurassic and Early Cretaceous data collected in this study. Figure 1.4 represents a comparison between previously published data for the Cretaceous, Jurassic, and Triassic (Faure, 1982; Hess *et al.*, 1986; Fischer and Gygi, 1989; Koepnick *et al.*, 1990; Smalley *et al.*, 1990; Nelson *et al.*, 1991) and the data collected in this study. The fact that the data in this study trace a line running along the bottom of the data scatter

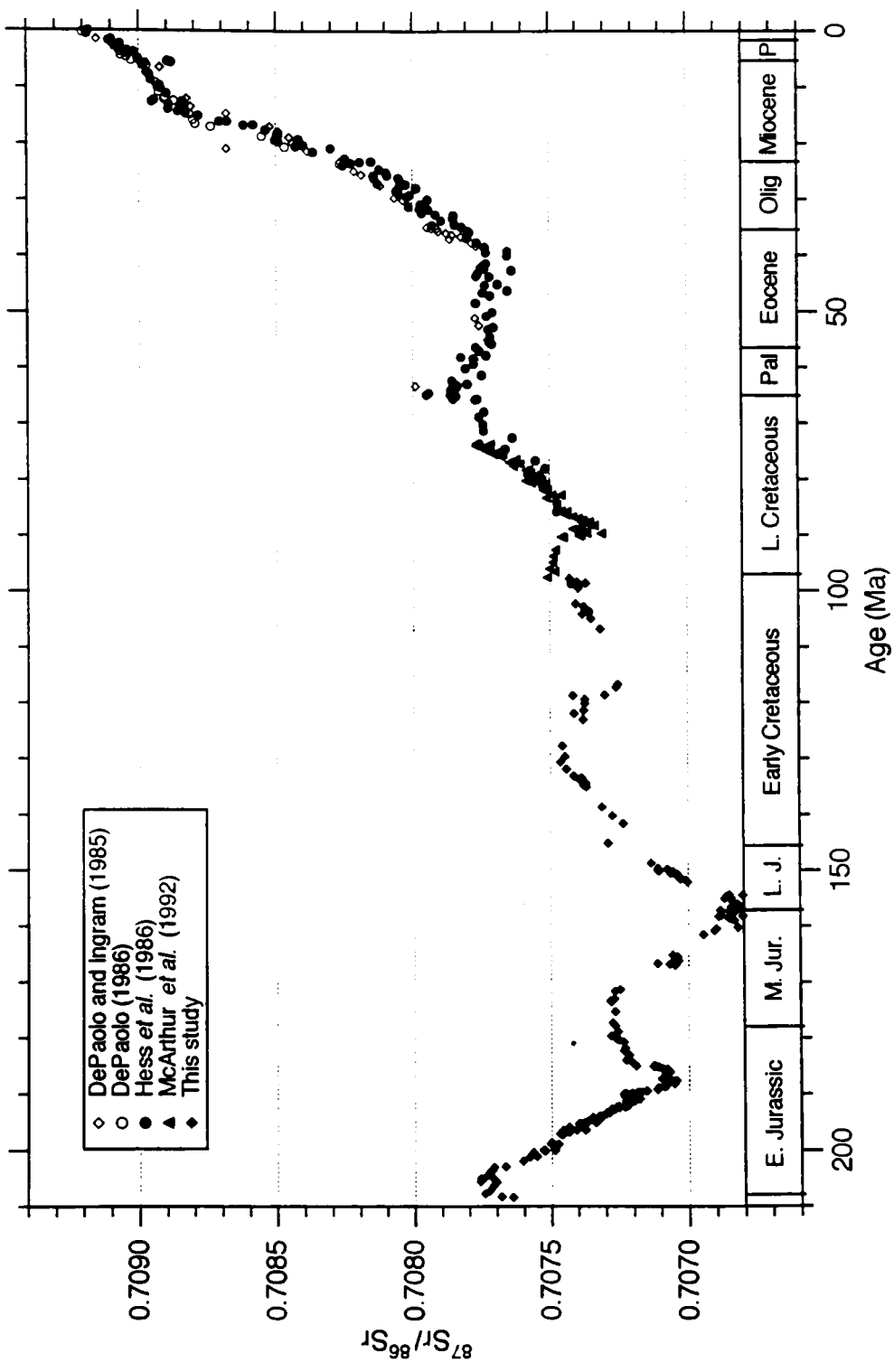

Figure 1.3: The evolution of the seawater Sr-isotope curve over the past 210 Ma. Time-scale of Harland *et al.* (1990) for the Mesozoic and Berggren *et al.* (1985) for the Cenozoic.

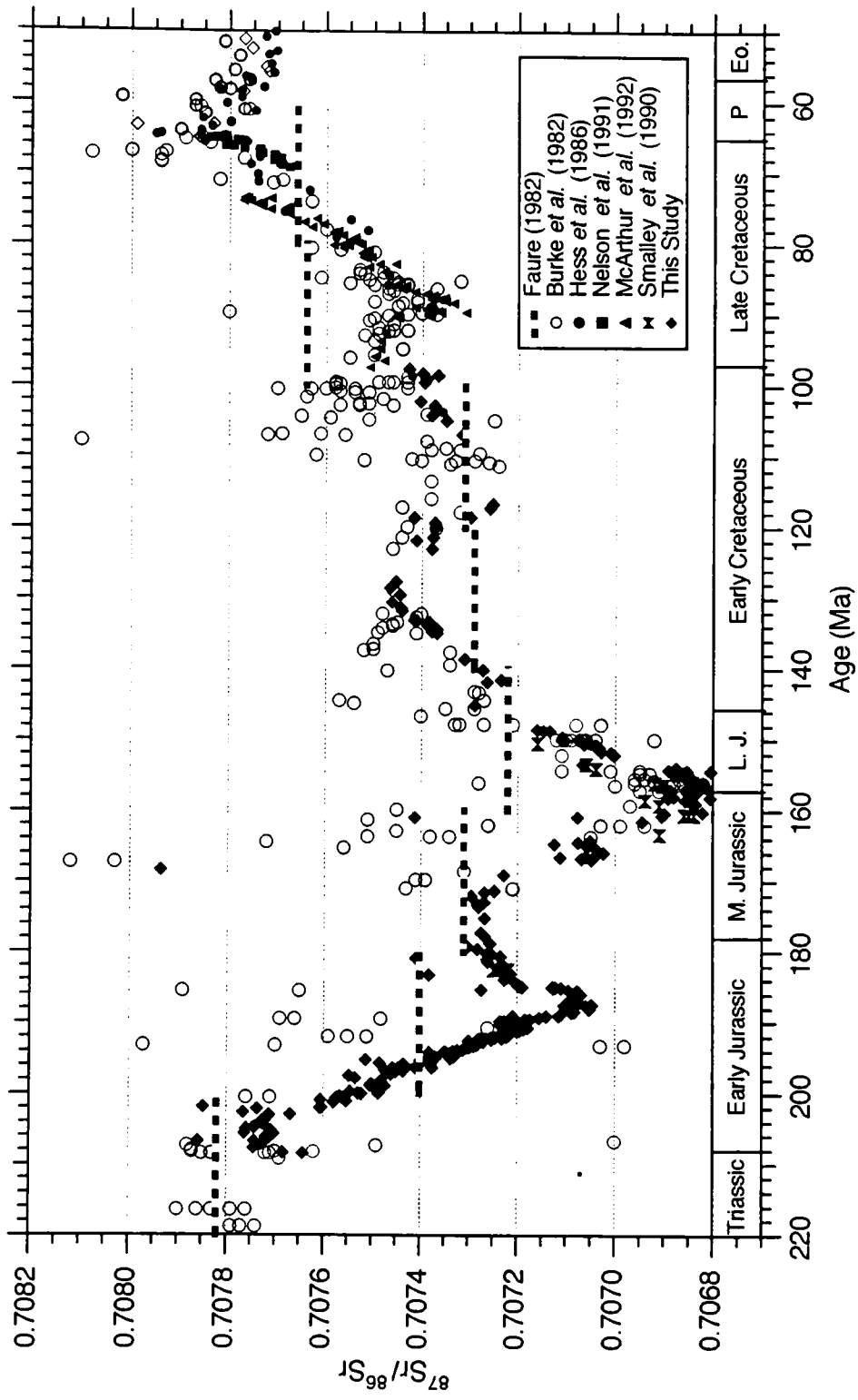

Figure 1.4: Comparison between the published Mesozoic data and the data of this study.

confirms the reasoning of Burke *et al.* (1982) in drawing their best-estimate curve at the base of the data scatter and upholds the widely-held notion that diagenetic alteration of a carbonate generally results in higher $^{87}Sr/^{86}Sr$ ratios due to the diagenetic uptake of radiogenic Sr (Veizer and Compston, 1974; Burke *et al.*, 1982).

1.3 Aims of This Study

This thesis has two main goals. The first is to define the evolution of the Sr-isotope curve over the Jurassic and Early Cretaceous. To produce the highest quality curve possible requires good analytical techniques, adequate screening for diagenetic alteration of sample material, and a detailed sampling of the bio- and litho-stratigraphically well-characterised sections. Chapter 2 discusses the analytical techniques and in particular focuses on the reproducibility of the mass spectrometry. Chapter 3 examines the utility of four diagenetic tracers--Mn, Fe, $\partial^{13}C$, and $\partial^{18}O$--to weed out samples whose $^{87}Sr/^{86}Sr$ ratios have been appreciably affected by diagenesis. Chapter 4 starts out by documenting in detail the bio- and litho-stratigraphy of the classic British Jurassic and Cretaceous stratigraphic successions sampled in this study. With this firm foundation in place, the chapter moves on to assess quantitatively the stratigraphic resolution of the best-estimate Sr-isotope curve.

The second main thrust of this thesis is to examine the causes of the fluctuations in the Sr-isotope curve. Chapter 5 takes a minor detour to examine the $\partial^{13}C$ and $\partial^{18}O$ data collected from belemnites and oysters and to document the evidence for several global carbon burial events in the Early Jurassic. Chapter 6 then extensively discusses the modern geochemical cycle of seawater Sr with the aim of better understanding the mechanisms that could produce the observed variations in the Sr-isotope curve. Finally, Chapter 7 documents an intriguing correlation between times of rapid movement in the Sr-isotope curve and the occurrence of positive $\partial^{13}C$ excursions and then moves on to constrain possible mechanisms that could link the geochemical cycles of carbon and strontium.

Chapter 2: Methods

The methodology of this project has been designed to minimise the three major sources of error encountered when constructing a seawater Sr-isotope curve: stratigraphic error due to poor biostratigraphic and/or structural control, diagenetic error due to extraneous Sr in noncarbonate or secondary calcite phases, and analytical error associated with laboratory procedures and the analytical reproducibility of the mass spectrometer. The following sections describe the methodology adopted to minimise each major source of error.

2.1 Stratigraphy of Sample Materials

The simple structure, excellent exposure, and detailed published litho- and biostratigraphic descriptions of the British Jurassic and Lower Cretaceous allow highly precise and reproducible sample collection. Most samples were collected from the extensive cliff sections exposed along the Dorset and Yorkshire coasts. These sections are characterised by finely bedded, laterally continuous strata disturbed only by minor faults and gentle folding; both structural elements serve to bring most stratigraphic horizons down to beach level where they can be readily observed. For intervals of time represented by poorer exposures, such as the slumped cliffs of the Lower Cretaceous Speeton Clay (Yorkshire), great care was taken to dig out the sections, identify all relevant beds and markers, and collect only those samples that were definitely *in situ*. Details and limitations of all exposures relevant to this study are discussed in more detail in Chapter 4.

The British Jurassic and Lower Cretaceous successions consist of a diversity of rock-types including finely bedded mudstones, impure limestones, oolites, siltstones, and fine-grained sandstones. The stratigraphy of all sections sampled in this study has been described in painstaking, bed-by-bed detail in one or more papers published over the past 150 years with the purpose of allowing future workers to recollect fossils from the same beds. These papers, noted in Tables 2.1, 2.2, and 2.3 and Chapter 4, describe the basic

lithology of each bed along with all ammonites and other fossils collected from that bed. The large number and diversity of ammonites found throughout these sections has allowed the Mesozoic sequences to be finely subdivided into a large number of zones and subzones. The Lower Jurassic, for example, contains 54 subzones, each with an estimated average duration of about 540,000 years (see below).

The data tables (2.1, 2.2, 2.3) list the exact lithostratigraphic and assigned biostratigraphic position of each sample along with its isotopic and trace element data. The sample labels in the first column are coded to indicate the initials of the formation or the main author who described the formation and the bed number in which that sample was found. The second column lists the ammonite subzone or zone to which the sample is assigned. The assignments generally follow Cope *et al.* (1980a,b) and Rawson *et al.* (1978), but with numerous minor modifications described more fully in Chapter 4. All subzones or zones that comprise each stage are listed, even if no sample was taken from a given biozone. The third column gives the position of the sample above the base of the bed relative to the total thickness of the bed, and Column 4 gives the distance above the base of the biozone relative to the total thickness of the biozone. The stratigraphic "age" of each sample (Column 5) is measured in terms of ammonite subzones to facilitate direct correlation to the British standard. By convention subzone "ages" are calculated assuming that each ammonite subzone is of equal duration and that the base of the Jurassic, which is clearly defined by the first appearance of the ammonite *P. planorbis* (Cope *et al.*, 1980a; Cope, 1991a,b), is set equal to zero. All zones that are not subdivided into subzones are assumed, following Cope *et al.* (1980a,b), to be equal to two subzone units of time. The top of the first subzone in the Jurassic, *planorbis*, marks the passage of 1 subzone unit of time, the top of the second subzone marks 2 subzone units, and so on until a total of 54 subzone units are covered by the end of the Toarcian (Early Jurassic) and 268 subzone units are covered by the end of the Albian (Early Cretaceous) (Table 2.4). The fractional

Table 2.1: Stratigraphy of samples from the Dorset Coast

Sample (Bed Number)	Zone or Subzone	Position in Bed (cm)	Position in Biozone (cm)	"Age" (In Subzones)	Error	$^{87}Sr/^{86}Sr$ 2σ‡ Individual§	$^{87}Sr/^{86}Sr$ 2σ Combined§	Fossil †	Mn (μg/g)	Fe (μg/g)	$\partial^{13}C$ (PDB)	$\partial^{18}O$ (PDB)
Ryazanian												
Cinder Bed 1	R. runctoni	--	--	178.00	1.00	0.707289 17	0.707289 17	O	215.2	241.8	1.84	-0.09
Portlandian												
--	Remaining Portlandian zones not sampled (7 zones missing)					--	--	-	–	–	–	–
U.LyditeBd 1	G. glaucolith.			162.00	1.00	0.707160 23	0.707160 23	B	105.4	492.5	2.25	-3.17
Cast Beds	P. albani	130/140	1180/1190	160.98		0.707147 16	0.707147 16	O	63.9	325.8	-1.40	-1.91
Exogyra Bed	P. albani	0-1000/1000	>1500/>1630	160.87	0.03	0.707134 52	0.707134 52	O	79.5	108.8	-2.28	-2.44
Kimmeridgian												
Blake 1c	P. rotunda	1275/1350	2050/3480	156.11		0.707097 14 0.707114 20	0.707108 15	B	11.3	50.2	0.06	0.06
Blake 2	P. rotunda	95/130	95/3480	155.03		0.707098 11 0.707118 17	0.707108 12	B	10.3	37.3	0.06	0.93
Blake 3fgh-1	P.pallasioides	1260/1320	3860/3920	154.97		0.707073 12	0.707073 12	O	234.1	137.3	2.48	-2.28
Blake 3fgh-2	P.pallasioides	810/1320	3410/3920	154.74		0.707064 16 0.707092 24	0.707076 14	B	9.3	47.6	0.33	-0.11
LwrLydite	P.pallasioides	--	--	154.00	1.00	0.707102 19	0.707102 19	B	6.8	49.5	-0.02	-0.70
Blake 3c	P.pallasioides	80/90	1840/3920	153.94		0.707110 13	0.707110 13	O	13.7	867.6	2.61	-1.74
Blake 6b/c	P.paravirgalus	260/350	1710/2320	152.74		0.707055 23	0.707055 23	O	288.6	124.5	3.03	-1.55
Blake 11	P.eastlecotten.	640/970	1990/2170	151.92		0.707052 54	0.707052 54	O	6.0	2656.4	3.37	-2.34
Blake 17	P.eastlecotten.	434/450	684/2170	151.32		0.707064 16	0.707064 16	O	22.3	507.8	2.92	-2.39
Blake 23-1	P. encombensis	270/790	270/1890	150.14		0.707040 10	0.707040 10	O	10.5	640.5	3.08	-1.57
Blake 23-2	P. encombensis	10/790	10/1890	150.01		0.707037 20	0.707037 20	O	8.5	60.6	-0.85	2.01
Blake 27	P.wheatleyensis	210/810	370/770	148.48		0.707033 9	0.707033 9	O	4.8	773.6	3.58	-2.29
Blake 28	P.smedmorensis	10 belw Clavell	2130/2140	147.99		0.707037 13	0.707037 13	O	21.5	1720.6	2.63	-1.91
Blake 35	P. scitulus	690/1530	730/1960	145.74		0.707028 42	0.707028 42	O	4.7	923.0	3.09	-1.42
Blake 38	P. elegans	40/55	1660/2100	144.58		0.707008 11	0.707008 11	O	4.7	1126.8	2.20	-2.15
Blake 41	P. elegans		150/2100	143.14		0.707003 30	0.707003 30	O	5.3	623.5	3.58	-2.26
Blake 43	A.autissiodor.	23 cm below Bed 42		142.99		0.707002 13	0.707002 13	O	8.4	270.1	3.22	-1.77
	A. eudoxus	--	--	--		--	--	-	–	–	–	–

Pearce'sPit2*	A. mutabilis	Beds M8-M17	860-1465/2160	138.08	0.14	0.707066 16	0.707066 16	A	5.8	86.5	2.89	-1.63
WykeSltStn1	R. cymodoce	2/40	2/600	135.01		0.706891 14	0.706891 14	O	34.8	338.8	3.47	-1.77
D.delta 1	P. baylei	5/100	77/331	133.47		0.706860 14	0.706860 14	O	34.0	167.0	3.64	-0.96
R.incnstns1	P. baylei	12/54	12/331	133.07		0.706864 13	0.706864 13	O	58.9	273.9	3.21	-1.28
Oxfordian												
--	R. evoluta	--	--	--		--	--	-	–	–	–	–
OsMllsFeSt1	R.pseudocord.	0/72	338/410	131.82		0.706879 12	0.706879 12	O	185.3	329.8	3.65	-0.62
Sandsfoot5	R.pseudocord.	680/780	120/220	131.55		0.706848 14	0.706848 14	O	29.8	277.3	4.28	-0.41
Sandsfoot4	R. pseudoyo	510/780	510/560	130.91		0.706871 16	0.706871 16	O	52.7	236.4	4.23	-0.57
--	R. caldonica	--	--	--		--	--	-	–	–	–	–
--	P. varicostatus	--	--	--		--	--	-	–	–	–	–
ChiefShBd2	P cautisnigrae	0/220	230/790	127.29		0.706840 13	0.706840 13	O	34.8	122.0	4.21	-1.54
--	A.nunningtonese	--	--	--		--	--	-	–	–	–	–
NodRubble 2	P. parandieri	90/295	90/295	125.31		0.706832 14	0.706832 14	O	34.7	139.4	2.30	-2.74
Shortlake1	P. antecedens	385/740	1245/1600	124.78		0.706821 17	0.706821 17	O	135.1	242.9	4.59	-1.78
PrestonGt1	C. vertebrale	160/160	160/>1575	123.10		0.706827 19	0.706827 19	O	66.8	205.8	5.48	-0.54
Nothe Grit 2	C. cordatum	100/915	100/915	122.11		0.706847 17	0.706847 17	O	51.6	164.5	5.20	-1.36
Bowleaze Cly 2a				121.81		0.706817 21	0.706817 21	O	26.9	194.6	3.27	-1.24
Bowleaze 5	C. costicardia	990/1710	740/1460	121.51		0.706903 16	0.706903 16	O	62.1	810.3	4.54	-1.13
ShellBed8a	C. costicardia		710/1460									
JordonClCly1	C. bukowskii	744/cf 1000	744/cf 1250	120.60		0.706812 11	0.706812 11	O	31.9	100.5	2.98	0.16
Mariae 1	Mariae Zone not well exposed in Dorset.			119.00	1.00	0.706842 20	0.706842 20	O	16.4	69.0	4.83	-0.30
Mariae 2				119.00	1.00	--	--	B	21.1	46.9	3.10	0.11
Bathonian												
BBr 17	Z. zigzag	(0-15)/15	(0-15)/15	85.5	1.5	0.707039 18	0.707039 18	B	13.4	88.7	0.27	0.32
Bajocian												
BBr 14-2	P. bomfordi	24/40	24/140	83.17		0.707024 18	0.707024 18	B	23.2	269.9	0.79	0.32
BBr 13	S. truellei	(28-32)/56	(28-32)/56	82.54	0.04	0.707036 14	0.707036 14	B	13.3	102.4	-0.72	-0.39
BBr 12-2	P. acris	(1-4)/7	(1-4)/7	81.36	0.21	0.707059 20	0.707059 20	B	11.3	64.2	-1.25	-0.47
SL-2ndRbbly	St.tetragona to P. acris	0.75m above Marly Bed		80.00	1.00	0.707068 20	0.707068 20	B	6.4	52.2	-0.61	-0.26
SL-SherBS1	G. garantiana	1m above Sanford Fossil Bed	100/300	79.33		0.707048 14	0.707048 14	B	7.3	50.9	0.01	-0.13
--	St. baculata	–	–	--		--	--	-	–	–	–	–

--	C. polygyralis	--	--	--		--	--	-	--	--	--	--
--	T. banksi	--	--	--		--	--	-	--	--	--	--
--	T. blagdeni	--	--	--		--	--	-	--	--	--	--
BBr 11/12	S. humphriesm to P. acris	--	--	77.50	3.50	0.707125 31 0.707107 9	0.707112 12	B	7.8 13.4	64.3 91.6	-0.05	-0.11
--	P. cycloides	--	--	--		--	--	-	--	--	--	--
SL-SndfdFB	O. sauzei	28/33 to 43/48	28/33 to 43/48	72.75	0.05	0.707230 28 0.707227 15	0.707227 14	B	23.7 25.9	155.3 173.4	1.09	-1.15
BBr 8-3	H. discites to W. laeviuscula	(3-7cm)/10cm	(3-7cm)/10cm	68.00	3.00	0.707248 20 0.707267 11	0.707267 12	B	19.5	104.1	0.42	-1.20
Aalenian												
--	G. formosum	--	-	--		--	--	-	--	--	--	--
--	G. concavum	--	--	--		--	--	-	--	--	--	--
--	B. gigantea	--	--	--		--	--	-	--	--	--	--
--	B.bradfordensis	--	--	--		--	--	-	--	--	--	--
--	L. murchisonae	--	--	--		--	--	-	--	--	--	--
--	L. obtusiformis	--	--	--		--	--	-	--	--	--	--
--	L. haugi	--	--	--		--	--	-	--	--	--	--
BBr 6-2	T. scissum	25/55	25/55	56.90		0.707284 20 0.707263 20	0.707274 14	B	12.1 14.5	120.3 107.9	0.04	-0.93
BBr 5	L. opalinum	(0-5)/5	(106-111)/111	55.96	0.02	0.707265 12 0.707272 10	0.707267 8	B	12.9 14.3	101.9 111.1	1.87	-1.52
Toarcian												
BBr 1-3	P. aalensis,	80/140	4960/5100	53.92		0.707257 23 0.707255 10	0.707255 10	B	9.5 11.2	52.4 66.4	0.49	1.73
BridportSnds6	D. moorei, and	50/130	2250/5100	52.32		0.707281 18	0.707281 18	B	18.0	123.6	0.49	-0.46
DnClCly1	D. levesquei	200/1250	200/5100	51.12		0.707261 18	0.707261 18	B	15.4	51.8	1.38	0.61
--	P. dispansum to D. tenuicostatum		--		--	--	-	--	--	--	--	
Pliensbachian												
--	P.hawskerense	--	--	--		--	--	-	--	--	--	--
--	P. apyrenum	--	--	--		--	--	-	--	--	--	--
Clay 33-1	A. gibbosus	130/229	145/264	34.55		0.707110 30	0.707110 30	B	18.0	93.7	3.44	-0.06
ThcmbsBd32	A. gibbosus	15/35	15/264	34.06		0.707114 38	0.707114 38	B	5.9	37.8	2.11	-0.13
ThncmbSnd	A. subnodosus	1100/2347	1343/2590	33.52		0.707154 20	0.707154 20	B	52.1	71.1	2.50	-0.76

MrgrCly 25	A. subnodosus	213/213	243/2590	33.09		0.707184 31	0.707184 31	B	30.0	131.0	0.76	-0.44
MrgrSt 24-5	A. subnodosus	30/30	30/2590	33.01		0.707173 17	0.707173 17	B	12.5	62.3	0.43	-1.22
DayShBd 20	A. stokesi	9/23	6338/9171	32.69		0.707206 27	0.707206 27	B	14.3	45.8	0.51	-1.21
Eype 19-4	A. stokesi	25/1509	4845/9171	32.53		0.707226 9	0.707226 9	B	28.1	91.5	0.30	-1.48
Eype 18-2	A. stokesi	61/61	4820/9171	32.53		0.707227 18	0.707234 14	B	42.5	41.1	0.07	-1.30
						0.707244 21			49.4	32.7		
3Tiers 9-2	A. stokesi	600/9171	800/9171	32.09		0.707210 9	0.707210 9	B	30.9	40.9	0.80	-0.72
GAB 127	O. figulinum	231/243	231/1250	31.18		0.707198 24	0.707198 24	B	12.2	27.1	0.88	-0.64
GAB 126c	A. capricornus	(0-15)/15	1418/1478	30.96	0.01	0.707207 18	0.707207 18	B	51.3	77.8	1.03	-1.44
GAB 122g	A. capricornus	140/640	140/1650	30.08		0.707195 14	0.707195 14	B	62.6	112.0	2.68	-2.85
GAB 122f	A. capricornus	(0-8)/8	(0-8)/1478	30.00		0.707202 20	0.707202 20	B	34.3	97.7	2.55	-2.58
GAB 122c	A. maculatum	161/183	222/282	29.79		0.707229 24	0.707229 24	B	10.2	38.9	0.07	-1.32
GAB 122b	A. maculatum	28/31	58/282	29.21		0.707223 18	0.707224 16	B	18.8	36.8	1.94	-1.11
						0.707227 31			13.4	63.4		
BM 121a	B. luridum	(0-15)/15	(0-15)/15	28.50	0.5	0.707221 16	0.707221 16	B	19.9	30.5	2.46	-1.69
BM 121b	B. luridum	0/15	0/15	28.00		0.707251 15	0.707254 13	B	28.6	79.9	1.10	-0.54
						0.707256 18			31.4	122.0		
BM 120d-1	A. valdani	3/25	205/229	27.90		0.707231 13	0.707231 13	B	44.8	86.7	1.79	-0.45
BM 120c/d-1	A. valdani	4/4	202/229	27.88		0.707295 13	0.707273 16	B	188.0	1489.6	2.14	-0.58
						0.707273 16						
BM 120b/c	A. valdani	30/30	198/229	27.86		0.707263 13	0.707263 13	B	17.9	66.4	0.37	-1.10
BM 120a3	A. valdani	24/30	192/229	27.84		0.707268 13	0.707268 13	B	62.5	275.9	-.-	-.-
BM 120a1	A. valdani	13/30	181/229	27.79		0.707263 14	0.707263 14	B	104.1	900.1	3.54	-1.93
BM 119-1	A. valdani	112/122	157/229	27.69		0.707279 21	0.707279 21	B	66.7	272.6	1.16	-1.10
BM 118d	A. valdani	23/46	23/229	27.10		0.707277 20	0.707280 8	B	12.0	41.1	-0.79	-0.91
						0.707294 6			20.4	42.9	-0.79	-0.74
BM 118c-3	T. masseanum	30/110	30/110	26.27		0.707282 17	0.707282 17	B	5.1	53.3	-0.41	-0.84
BM 118b	U. jamesoni	107/119	460/472	25.97		0.707299 14	0.707288 11	B	11.7	35.3	0.12	-0.71
						0.707284 17						
BM 118a-2a	U. jamesoni	45/119	395/472	25.84		0.707298 10	0.707298 10	B	7.3	25.1	-0.41	-0.88
BM 115-4	U. jamesoni			25.65		0.707297	0.707297	B	12.8	34.5	-0.52	-0.67
BM 115-1	U. jamesoni	183/244	183/472	25.39		0.707286 18	0.707302 10	B	54.2	104.0	-0.49	-0.58
						0.707298 15						
						0.707315 18						

BM 113d	P. brevispina	0/15	1206/1344	24.80		0.707311 20	0.707311 20	B	31.5	114.1	-0.20	-0.84
BM 112d		10/25	1098/1344	24.63		0.707323 8	0.707323 8	B	10.1	78.7	-0.21	-0.34
BM 110b		10/61	848/1344	24.26		0.707353 23	0.707348 12	B	19.4	99.1	0.26	-1.12
						0.707345 11			27.5	144.0		
BM 110a-4	and	660/838	666/1344	23.98		0.707380 23	0.707380 23	B	59.6	401.5	0.47	-0.90
						0.707345 17	0.707345 17	B	34.3	145.8		
BM 110a-2		270/838	270/1344	23.40		0.707337 17	0.707337 17	B	8.0	106.6	-1.15	-2.59
BM 110a-1	P.polymorphus	135/838	135/1344	23.20		0.707339 20	0.707339 20	B	21.3	81.1	0.16	0.00
BM 109	P. taylori	15/30	297/312	22.95		0.707319 18	0.707319 18	B	34.3	64.4	-0.55	0.20
BM 108-1	P. taylori	15/157	140/312	22.45		0.707337 17	0.707337 17	B	24.7	44.5	-0.72	0.42
BM 108-2	P. taylori	Base 108	124/312	22.40		0.707366 16	0.707367 10	B	3.9	49.5	-0.49	-0.37
						0.707368 11			9.0	34.3		
BM 106c	P. taylori	Base 106c	64/312	22.20		0.707377 11	0.707377 11	B	13.5	34.6	-0.26	0.19
BM 105	P. taylori	5/41	5/312	22.02		0.707398 18	0.707398 18	B	20.7	72.8	-0.72	0.07
Sinemurian												
--	P. aplanatum	--	--	--		--	--	-	--	--	--	--
--	L. macdonneli	--	--	--		--	--	-	--	--	--	--
BVM 104	E. raricosta.	4/10	441/447	19.99		0.707409 21	0.707409 21	B	29.5	186.7	0.02	-0.74
						0.707375 16	0.707375 16	B	19.3	82.6	--	--
BVM 103a-2	E. raricosta.	(0-3)/3	(424-427)/447	19.95		0.707406 23	0.707406 23	B	9.0	56.4	-0.35	-0.16
BVM 103a-1	E. raricosta.	Base 103a	427/447	19.95		0.707435 18	0.707435 18	B	11.6	42.5	1.49	-0.35
BVM 102	E. raricosta.	(66-71)/91	(401-406)/447	19.90	0.01	0.707441 14	0.707441 14	B	7.6	101.1	2.26	-1.03
BVM 100-2	E. raricosta.	287/295	317/447	19.71		0.707456 18	0.707456 18	B	12.2	32.5	3.27	-0.41
BVM 100-1	E. raricosta.	5/295	35/447	19.08		0.707435 11	0.707435 11	B	20.0	33.4	0.56	-0.59
BVM 97	C.densinodul.	33/168	798/947	18.84		0.707455 24	0.707455 24	B	8.3	25.3	0.54	-1.06
BVM 96	C.densinodul.	55/290	530/947	18.56		0.707457 10	0.707457 10	B	20.7	38.3	2.06	-1.16
BVM 90b	C.densinodul.	38/158	38/947	18.04		0.707460 13	0.707460 13	B	39.9	98.8	0.58	-0.70
--	O. oxynotum	--	--	--		--	--	-	--	--	--	--
--	O. simpsoni	--	--	--		--	--	-	--	--	--	--
--	E. denotatus	--	--	--		--	--	-	--	--	--	--
BVM 89-1	A. stellare	On nodule	(485-500)/500	14.99	0.01	0.707473 23	0.707473 14	B	26.4	115.2	3.22	-0.81
BVM 89-2	A. stellare	Under nodule	485/500	14.97		0.707501 31	0.707503 18	B	17.3	30.3	1.95	-0.90
						0.707511 18						
--	A. obtusum	--	--	--		--	--	-	--	--	--	--

BVM 83a	M. birchi	15/107	2354/2626	12.90		0.707528 17	0.707528 17	B	5.3	26.0	1.97	-0.85
						0.707486 20	0.707486 20	B	13.8	28.8		
--	C. brooki	--	--	--		--	--	-	–	–	–	–
SWB 70c	E. resupinatum	(0-3)/3	678/1041	10.65		0.707558 35	0.707553 17	B	13.3	27.0	2.85	-0.92
						0.707558 20						
SWB 69a	E. resupinatum	(0-5)/5	452/1041	10.43		0.707581 30	0.707578 16	B	11.2	34.8	0.88	-1.33
						0.707576 16						
BL 49/50	A.scipionian.	On top 49	0/409	9.00		0.707606 17	0.707606 17	B	62.8	378.6	-3.21	-5.49
						0.707603 13	0.707603 13	B	57.2	118.5		
--	C. lyra	--	--	--		--	--	-	–	–	–	–
BL 38	C. rotiforme	(0-33)/33	(373-406)/805	7.48	0.02	0.707762 16	0.707765 12	P	–	–	0.04	-3.29
						0.707768 18						
BL 30	C. rotiforme	48/48	48/805	7.06		0.707668 27	0.707668 27	O	13.6	36.2	1.68	-1.22
BL 28	V. conybeari	(20-25)/25	(132-137)/163	6.83	0.02	0.707711 20	0.707711 14	O	8.1	33.3	0.71	-3.74
						0.707714 18						
BL 24c	V. conybeari	(0-8)/8	(69-76)/163	6.45	0.02	0.707714 21	0.707714 21	O	31.7	99.7	0.82	-3.37
Hettangian												
BL 20	S. complanata	(0-51)/51	(417-467)/467	5.90	0.10	0.707714 21	0.707716 18	O	6.8	30.3	-0.60	-5.27
						0.707728 31						
BL 13		18/18	320/467	5.37		0.707727 18	0.707727 18	O	19.7	143.3	-1.57	-7.36
BL 6	and	(0-28)/28	(185-213)/467	4.86	0.06	0.707725 17	0.707725 12	O	40.1	62.6	-1.19	-7.46
						0.707728 16						
BL-H 91		14/20	75/467	4.32		0.707742 12	0.707740 9	O	15.3	164.8	1.85	-1.46
						0.707742 14						
BL-H 87	S. extranodosa	8/8	41/467	4.17		0.707757 18	0.707743 15	O	48.4	68.2	0.31	-4.24
						0.707732 23						
BL-H 83	A. laqueus	(0-8)/8	152-160/160	3.98	0.02	0.707781 18	0.707758 13	O	26.2	60.9	1.36	-2.47
						0.707775 17						
BL-H 75	A. laqueus	15/15	107/160	3.67		0.707710 20	0.707708 12	O	22.9	66.6	1.86	-2.68
						0.707711 14						
BL-H 71	A. laqueus	5/30	28/160	3.18		0.707762 11	0.707762 11	O	50.5	103.3	2.09	-1.52
BL-H 69	A. laqueus	10/15	10/160	3.06		0.707702 11	0.707702 11	O	44.3	163.5	0.69	-2.72
BL-H 63	W. portlocki	10/20	102/236	2.43		0.707709 15	0.707718 10	P	123.0	501.3	1.33	-1.83
						0.707729 13						

BL-H 60	W. portlocki	18/18	66/236	2.28		0.707712 25	0.707712 25	O	51.6	64.8	0.87	-2.24
BL-H 55	C. johnstoni	0/10	137/155	1.88		0.707717 33	0.707717 33	O	50.8	106.1	2.77	-1.66
BL-H 53o	C. johnstoni	(23-30)/36	(99-107)/155	1.66	0.02	0.707742 18	0.707742 18	O	29.0	199.3	-0.98	-7.55
BL-H 53s	C. johnstoni	(23-30)/36	(99-107)/155	1.66	0.02	0.707857 23	0.707857 23	E	147.5	537.3	-3.82	-11.4
BL-H 43	C. johnstoni	(0-11)/11	(0-11)/155	1.04	0.04	0.707722 17	0.707727 11	O	18.0	51.9	2.7	-1.55
						0.707732 13						
BL-H 29	P. planorbis	30/61	71/216	0.33		0.707740 18	0.707743 11	O	22.0	33.9	2.44	-1.06
						0.707748 13						
Triassic (Rhaetian)												
BL-H 12	Ostrea Beds	19/19	127/249	-0.49		0.707702 18	0.707683 16	O	10.9	33.3	3.08	-1.11
						0.707675 24						
BL-H 7-2	Ostrea Beds	(0-5)/5	81-86/249	-0.66		0.707647 21	0.707642 15	O	20.5	54.4	4.22	-0.32
						0.707644 19						

References and notes: BL = Blue Lias (Lang, 1924); SWB = Shales-with-'Beef' (Lang *et al.*, 1923); BVM = Black Ven Marls (Lang and Spath, 1926); BM = Belemnite Marls (Lang *et al.*, 1928); GAB = Green Ammonite Beds (Lang, 1936); A. stokesi through A. gibbosus (Howarth, 1957; Wilson *et al.*, 1958); D. levesquei through P. aalensis (Cope *et al.*, 1980; S.P. Hesselbo and H.C. Jenkyns, pers. comm., 1990); BBr = Inferior Oolite section at Burton Bradstock (Richardson, 1928-1930; Torrens, 1969); SL = Inferior Oolite Sanford Land section (Richardson, 1932).

‡ 2σ refers to twice the standard error on the measurement of the $^{87}Sr/^{86}Sr$ ratio.

§ "Individual" lists separate replicate analyses whereas "Combined" lists the combined analyses of a given sample.

† Fossil types: O = oyster, B = belemnite, A = ammonite, E = echinoderm spine, P = bivalve

* Hesselbo *et al.* (1990) Beds M8 - M17 exposed.

Table 2.2: Stratigraphy of samples from the Yorkshire Coast

Sample (Bed Number)	Zone or Subzone	Position in Bed (cm)	Position in Biozone (cm)	"Age" (Subzones)	Error	$^{87}Sr/^{86}Sr$ 2σ Individual	$^{87}Sr/^{86}Sr$ 2σ Combined	Fossil †	Mn (μg/g)	Fe (μg/g)	$\partial^{13}C$ (PDB)	$\partial^{18}O$ (PDB)
CRETACEOUS: Barremian												
--	P.bidentatm/scal.	--	--	--		--	--	-	--	--	--	--
--	S. stolleyi	--	--	--		--	--	-	--	--	--	--
--	A.innexum/pinque	--	--	--		--	--	-	--	--	--	--
Sp 45	P. denckmanni	20/40	100/?	220.00	1.00	0.707452 14	0.707452 14	B	8.9	28.6	1.16	-0.81
Sp 50	P. elegans	(0-50)/50	(250-300)/450	218.22	0.11	0.707464 13	0.707464 13	B	55.4	704.2	-1.17	-1.39
Sp LB2AII-2	P. fissicostatum	10/230	710/1575	215.90		0.707444 8	0.707444 8	B	6.5	28.3	0.58	-1.23
Sp LB5B	P. rarocinctum	40/100	288/801	213.72		0.707461 31	0.707461 31	B	5.9	33.4	0.45	0.09
Sp C2A	C. variabilis	15/30	121/245	211.98		0.707442 25	0.707442 25	O	85.7	691.7	3.15	0.27
Hauterivian												
Sp C2D	S. marginatus	5/10	340/345	210.98		0.707439 14	0.707439 14	B	7.4	74.2	1.51	-0.41
--	S. gottschei	--	--	--		--	--	-	--	--	--	--
Sp C6-1	S. speetonensis	140/465	140/1295	205.22		0.707414 16	0.707414 16	B	8.4	53.3	1.78	0.63
Sp C6-3	S. speetonensis	4/465	4/1295	205.01		0.707409 13	0.707409 13	B	7.6	35.8	1.76	0.50
Sp C7F	S. inversum	2/30	158/292	204.08		0.707383 13	0.707383 13	B	7.6	37.4	1.66	0.72
Sp C9D-1	E. regale	113/183	423/825	202.02		0.707387 13	0.707387 13	B	9.1	36.6	1.89	0.21
--	E. noricum	--	--	--		--	--	-	--	--	--	--
Sp D1	noricum/ambly	15/30	--	199.70	1.30	0.707363 16	0.707368 15	B	10.0	55.8	0.83	1.11
						0.707385 35						
Sp D2B	E. amblygonium	8/18	42/(62-93)	198.12	0.22	0.707379 11	0.707378 7	B	8.8	35.3	1.37	0.48
						0.707377 10						
Sp D2D	E. amblygonium	1/29	1/(62-93)	197.02		0.707367 11	0.707367 11	B	7.7	34.5	1.71	0.35
Valanginian												
--	unnamed	--	--	--		--	--	-	--	--	--	--
--	D. pitrei	--	--	--		--	--	-	--	--	--	--
--	Dichotomites sp.	--	--	--		--	--	-	--	--	--	--
Sp D2E-1	Polyptychites sp	157/215	322/380	190.69		0.707310 9	0.707310 9	B	14.1	28.1	-0.24	-0.02
Sp D4C-2	Paratollia sp.	160/350	98/215	187.91		0.707272 9	0.707272 9	B	7.9	33.5	0.42	-0.82
Ryazanian												
Sp D7A	P. albidum	5/32	76/500	185.30		0.707235 13	0.707235 13	B	11.9	65.9	0.34	0.44
Sp D7G-1	S. stenomphalus	40/45	70/83	184.69		0.707263 12	0.707263 12	B	22.0	195.6	-0.22	-0.37

--	S. icenii	--	--	--		--	--	-	--	--	--	--
--	H. kochi	--	--	--		--	--	-	--	--	--	--
--	R. runctoni	--	--	--		--	--	-	--	--	--	--
JURASSIC: Oxfordian (Kimmeridgian and Portlandian not exposed)												
YOxCl15-1	Q. mariae	65/>1000	65/>1000	118.05	0.05	0.706818 21	0.706818 21	B	5.4	45.1	2.55	-0.74
Callovian												
Hcknss 13	K. proniae to Q. lamberti	42/45	42/45	116.00	2.00	0.706851 9 0.706842 17	0.706847 8	B	57.2	182.0	3.60	0.28
KlwyR 10-2	K. curtilobus	0/56	900/1000	105.90		0.706821 18	0.706821 18	B	6.9	43.4	2.49	-0.92
KlwyR 7-2	K. curtilobus	39/191	259/1000	105.26		0.706900 12 0.706899 10	0.706899 9	B	11.1	66.6	2.44	-1.37
YCmBr a2	M. terebratus	12/13	49/50	102.98		0.707077 47	0.707077 47	O	594.7	1696.9	1.19	-5.97
YCmB a1-1	M. terebratus	35/37	35/50	102.70		0.707412 11	0.707412 11	O	74.1	427.4	3.70	0.59
Bajocian												
Scarb10-5	D. cycloides	570/800	900/908	73.99		0.707936 20	0.707936 20	B	51.5	1445.3	0.38	-14.18
MilPorOolt	Lower Bajocian	Top surface		67.00	2.0	0.707294 11	0.707294 11	B	27.9	158.3	1.10	-7.95
Toarcian												
--	P. aalensis	--	--	--		--	--	-	--	--	--	--
BWS 82	D. moorei	792/792	792/792	52.99		0.707301 16	0.707301 16	B	76.2	314.1	2.32	-3.32
--	D. levesquei	--	--	--		--	--	-	--	--	--	--
BWS 81	P. dispansum	127/175	1180/1225	50.96		0.707252 10	0.707252 10	B	12.3	45.3	2.02	-2.57
BWS 73	P. dispansum	36/46	350/1225	50.29		0.707235 23	0.707235 23	B	8.2	39.8	2.53	-5.56
StriatSh62a	P.fallaciosum	173/275	710/810	49.88		0.707414 13 0.707404 20	0.707409 12	B	515.7	1875.4	4.06	-9.09
StriatSh60	P.fallaciosum	155/160	520/810	49.64		0.707261 10	0.707261 10	B	30.2	161.0	3.07	-3.58
StriatSh56	G. striatulum	400/444	740/780	48.95		0.707272 27 0.707255 18	0.707260 15	B	62.0	166.4	2.03	-3.46
PeakSh54-2	G. striatulum	160/330	160/780	48.21		0.707231 17	0.707231 17	B	10.2	42.9	2.75	-3.06
PeakSh 44	H. variabilis	123/183	635/1125	47.13		0.707235 35	0.707235 35	B	11.4	34.4	3.09	-3.32
ASF lv	C. crassum	10/10	470/561	45.84		0.707215 5	0.707215 5	B	20.7	78.8	3.45	-3.33
ASF l	C. crassum	11/46	194/561	45.35		0.707381 11	0.707381 11	B	26.6	176.4	3.87	-1.92
ASF xliv	P. fibulatum	119/229	1173/1283	44.91		0.707221 10	0.707221 10	B	102.7	43.9	3.75	-1.67
ASF xxxiv1	P. fibulatum	96/122	629/1283	44.49		0.707221 19	0.707221 19	B	5.5	34.8	3.94	-2.89
ASF xxix	P. fibulatum	88/91	88/1283	44.07		0.707226 10	0.707226 10	B	26.9	131.2	2.20	-5.66
ASF xxii1	D. commune	47/107	1185/1910	43.62		--	--	-	--	--	3.35	-3.67

ASF xvi-1	D. commune	20/366	20/1910	43.01		0.707203 12	0.707203 12	B	10.9	46.0	4.13	-3.72
JRF xiv-1	H. falciferum	4/511	1870/2377	42.79		0.707199 16	0.707199 16	B	14.4	120.9	4.32	-3.27
JRF xii-4	H. falciferum	30/838	1013/2377	42.43		0.707195 14	0.707195 14	B	16.6	76.5	3.11	-2.84
JRF 41	H. falciferum	165/587	165/2314	42.07		0.707190 9	0.707190 9	B	157.4	109.7	1.90	-2.49
JRF 40	H. exaratum	5/30	684/709	41.96		0.707127 16	0.707127 16	B	12.2	57.3	5.89	-3.32
JRF 38-2	H. exaratum	127/152	631/709	41.89		0.707122 11	0.707122 11	B	18.9	92.9	5.13	-4.60
JRF 38-3	H. exaratum	5/152	504/709	41.71		0.707126 17	0.707126 17	B	12.3	72.6	3.03	-3.95
JRF 36	H. exaratum	90/122	456/709	41.64		0.707110 23	0.707110 23	B	13.3	45.5	2.96	-4.26
JRF 34-2	H. exaratum	139/259	155/709	41.22		0.707273 10	0.707273 10	B	48.9	250.3	2.39	-3.18
JRF 34-1	H. exaratum	10/259	26/709	41.04		0.707094 14	0.707094 14	B	9.5	30.6	1.83	-3.59
GSF 32-2	D.semicelatum	123/183	476/536	40.89		0.707077 11	0.707077 11	B	15.4	37.5	2.50	-0.60
GSF 29	D.semicelatum	24/107	47/536	40.09		0.707081 17	0.707081 17	B	7.7	25.1	2.21	-0.81
GSF 27-1	D. tenuicost.	24/61	248/272	39.91		0.707070 21	0.707070 21	B	22.3	58.0	1.97	-0.57
GSF 22	D. tenuicost.	8/8	99/272	39.36		0.707083 11	0.707083 11	B	22.2	49.8	3.27	-0.63
GSF 19b	D. cleveland.	0/5	79/165	38.48		0.707086 20	0.707083 11	B	12.7	34.8	2.20	-0.40
						0.707082 14						
GSF 12	P. paltum	(0-30)/30	(356-386)/450	37.82	0.03	0.707073 9	0.707073 9	B	18.7	48.8	1.96	-1.01
GSF 8	P. paltum	5/42	285/450	37.63		0.707099 31	0.707099 31	B	28.3	103.4	1.88	-1.08
GSF 1	P. paltum	51/51	117/450	37.26		0.707093 20	0.707093 20	B	15.2	42.9	1.55	-0.98
How 45	P. paltum	45/51	45/450	37.10		0.707047 16	0.707047 16	B	17.9	52.0	1.29	-1.09
Pliensbachian												
CIF 25	P.hawsherense	32/37	302/307	36.98		0.707104 9	0.707104 9	B	74.0	164.5	0.65	-2.79
How 41	P.hawskerense	46/46	452/549	36.82		0.707055 13	0.707059 8	B	78.8	239.8	1.55	-3.28
						0.707064 10			40.8	112.9		
How 36	P. apyrenum	15/30	643/666	35.97		0.707052 18	0.707052 18	B	19.1	51.5	0.73	-2.83
How 28	P. apyrenum	65/168	159/666	35.24		0.707082 21	0.707082 21	B	20.5	69.3	2.24	0.11
How 23	P. apyrenum	5/5	0/666	35.00		0.707089 20	0.707089 20	B	43.8	102.8	3.89	-1.18
How 20	A. gibbosus	36/36	0/592	34.00		0.707140 20	0.707140 20	B	51.4	244.7	2.59	-0.81
How 19	A. subnodosus	155/180	422/493	33.86		0.707209 17	0.707209 17	B	75.0	230.5	2.46	-3.11
How 1	A. stokesi	6/48	(5-7)/1593	32.00		0.707197 11	0.707197 11	B	26.1	77.6	2.79	-2.42
Ph 62	O. figulinum	1/30	740/880	31.84		0.707215 19	0.707215 19	B	48.1	130.9	2.61	-3.33
Ph 56	O. figulinum	85/90	550/880	31.64		0.707234 18	0.707234 18	B	53.3	128.1	2.06	-2.50
Ph 48	A.capricornus	15/80	235/320	30.72		0.707178 18	0.707178 18	B	29.1	104.6	2.85	-2.82
Ph 45-2	A.capricornus	50/55	135/320	30.42		0.707186 23	0.707186 23	B	64.3	200.3	2.91	-2.74
Ph 45-1	A.capricornus	10/55	100/320	30.28		0.707220 17	0.707220 17	B	47.0	86.4	1.81	-3.64

Ph 34-2	A. maculatum	86/135	1485/1830	29.79	0.707220 14	0.707220 14	B	70.1	133.6	2.49	-3.04
Ph 22	A. maculatum	95/155	105/1830	29.05	0.707224 18	0.707224 18	B	46.5	103.1	1.87	-0.41
Ph 16	B. luridum	75/380	1500/2120	28.71	0.707218 17	0.707218 17	B	83.1	179.6	1.53	-1.25
Ph 8	B. luridum	20/280	440/2120	28.22	0.707245 34	0.707245 34	B	112.0	294.6	1.18	-0.17
Ph 4c-3	B. luridum	154/170	110/2120	28.05	0.707253 10	0.707253 10	B	43.9	147.0	2.88	-2.29
Ph 4a	A. valdani	88/100	180/260	27.64	0.707252 14	0.707252 14	B	32.2	97.1	2.50	-0.13
Ph 2	A. valdani	35/75	45/250	27.18	0.707299 21	0.707299 21	B	53.2	150.1	2.17	-1.71
ISS 121	T. masseanum	144/145	99/100	26.99	0.707268 20	0.707268 20	B	29.8	72.5	2.93	-2.16
ISS 117	U. jamesoni zone	165/200	4180/4370	25.83	0.707297 14	0.707297 14	B	35.2	83.6	1.72	-0.80
ISS 111	U. jamesoni zone	142/165	3370/4370	25.08	0.707332 13	0.707332 13	B	85.1	231.8	1.93	-0.90
ISS 103	U. jamesoni zone	10/275	2390/4370	24.19	0.707329 18	0.707329 18	B	14.7	48.8	0.56	-0.73
PyrSh 95	U. jamesoni zone	150/250	1780/4370	23.63	0.707368 11	0.707368 11	B	31.0	61.9	0.47	-0.05
PyrSh 84	U. jamesoni zone	10/10	870/4370	22.80	0.707367 13	0.707372 10	B	45.3	91.9	-0.10	-0.43
					0.707377 14						
PyrSh 75	U. jamesoni zone	65/1400	155/4370	22.14	0.707388 17	0.707388 17	B	27.3	60.3	0.32	0.00
Sinemurian											
PyrSh 71-1	P. aplanatum	230/230	560/580	21.97	0.707511 11	0.707511 11	O	72.8	251.5	3.01	-0.99
PyrSh 69-2	P. aplanatum	230/240	310/580	21.53	0.707395 13	0.707395 13	B	75.1	89.4	1.79	-1.16
PyrSh 69-1	P. aplanatum	5/240	5/580	21.01	0.707483 11	0.707483 11	O	96.0	169.8	1.73	-1.30
SilSh 66	L. macdonneli	75/75	360/450	20.80	0.707434 16	0.707434 16	B	50.5	80.4	2.12	-1.62
SilSh 64	L. macdonneli	50/140	130/450	20.29	0.707435 11	0.707435 11	B	72.3	135.4	2.28	-1.17
SilSh 63	L. macdonneli	43/80	43/450	20.10	0.707428 13	0.707428 13	B	46.3	76.2	2.29	-1.76
SilSh 60	E. raricostatoides	40/70	480/695	19.69	0.707445 10	0.707445 10	B	56.4	101.6	2.62	-1.29
SilSh 55	E. raricostatoides	15/15	215/695	19.31	0.707472 19	0.707472 19	B	105.7	168.0	2.54	-1.44
SilSh 53-1	C. densinodulum	3/33	130/160	18.81	0.707449 14	0.707449 14	B	47.2	90.4	2.34	-1.30
SilSh 52-1	C. densinodulum	80/127	80/160	18.50	0.707468 7	0.707468 7	B	51.8	99.6	1.44	-1.76
SilSh 47	O. oxynotum	118/160	330/610	17.54	0.707547 11	0.707547 11	O	149.7	343.4	3.43	-1.83
SilSh 44-1	O. oxynotum	0/150	0/610	17.00	0.707534 17	0.707534 17	B	150.2	366.9	1.48	-1.72
SilSh 38	O. simpsoni	35/75	35/510	16.07	0.707481 10	0.707481 10	B	115.2	291.4	2.99	-1.95
SilSh 35	E. denotatus	85/100	185/440	15.42	0.707499 16	0.707499 16	B	22.7	84.8	2.59	-2.43
SilSh 31	A.stellare/A obtusum	65/90	465/640	14.45	0.707493 13	0.707493 13	B	33.1	57.1	2.53	-1.09
CalSh 26	A.stellare/A obtusum	15/15	95/640	13.30	0.707544 13	0.707544 13	O	67.4	190.9	4.38	-1.13
CalSh 22	C. turneri zone	150/180	1245/1520	12.64	0.707521 13	0.707521 13	B	38.9	107.8	2.68	-1.67
CalSh 17	C. turneri zone	80/80	885/1520	12.16	0.707589 23	0.707589 23	O	41.1	107.6	3.88	-1.71
CalSh 12	C. turneri zone	85/210	410/1520	11.54	0.707573 13	0.707573 13	B	53.8	116.6	3.25	-2.34

CalSh 8	C. turneri zone	50/50	0/1520	11.00		0.707605 9	0.707605 9	O	118.5	308.3	3.19	-2.07
CalSh 3	E. sauzeanum	195/215	--	10.50	0.50	0.707579 11	0.707579 11	B	45.3	112.1	1.50	-1.98

References and notes: Sp = Lower Cretaceous Speeton Clay: Lamplugh (1889), Neale (1960, 1962), Fletcher (1969), Rawson (1971), Rawson *et al.* (1978), Rawson and Mutterlose (1983), Doyle (1989). Callovian/Oxfordian: Wright (1968, 1977), Page (1989), Coe (1991). Bajocian: Bate (1959, Yons Nab section), Parsons (1977), Gowland (1989). Toarcian: Dean (1954), Howarth (1955, 1962, 1973, Hawsker Bottoms, Brackenberry Wyke to Port Mulgrave, Peak to Blea Wyke sections), Powell (1984), Knox (1984, Sections 1 and 2), Howard (1985). Pliensbachian and Sinemurian: Getty (1972), Phelps (1985), Hesselbo and Jenkyns (pers. comm., 1991). † Fossil types: O = oyster, B = belemnite

Table 2.3: Stratigraphy of samples from other sections

Sample (Bed Number)	Zone or Subzone	Position in Bed (cm)	Position in Biozone (cm)	"Age" (Subzones)	Error	$^{87}Sr/^{86}Sr$ 2σ Individual	$^{87}Sr/^{86}Sr$ 2σ Combined	Fossil †	Mn (μg/g)	Fe (μg/g)	$\partial^{13}C$ (PDB)	$\partial^{18}O$ (PDB)
CRETACEOUS: Albian												
---	M. periflatum	–	–	–		--	--	-	–	–	–	–
---	M. rostratum	–	–	–		--	--	-	–	–	–	–
Flk-UGault XI	C. auritus	47/1067	71/1159	266.01		0.707436 16 0.707415 14	0.707426 11	B	9.4	43.2	1.92	-0.40
MHQ-UGlt 6	H. varicosum	85/>760	95/>770	265.06	0.06	0.707398 14	0.707398 14	B	6.6	48.2	0.27	-1.12
MHQ-UGlt 4v	H. orbigyni	43/43	90/124	264.73		0.707366 11	0.707366 11	B	6.7	48.9	1.14	-1.29
FlkUGltVIIIiii	D. cristatum	0-10/10	33-43/195	263.19	0.03	0.707392 8 0.707403 13	0.707395 7	B	7.9	32.9	1.46	-0.67
MHQ-UGlt 4ii	D. cristatum	30/40	117/120	263.98		0.707390 25	0.707390 25	B	7.8	64.4	0.14	-0.97
---	A. daviesi	–	–	–		--	--	-	–	–	–	–
---	E. nitidus	–	–	–		--	--	-	–	–	–	–
---	E. meandrinus	–	–	–		--	--	-	–	–	–	–
Flk-LGlt IV-i	M. subdelaruei	0-2/2	(0-2)/13	259.08	0.08	0.707403 18	0.707403 18	B	6.7	28.2	1.98	-0.48
MHQ-LGlt3iii	D. niobe	13/33	23/81	258.28		0.707373 11	0.707373 11	B	13.0	91.1	0.61	-0.90
MHQ-LGlt2v1	A. intermedius	57/152	124/244	257.51		0.707369 18	0.707369 18	B	9.1	80.6	2.00	-0.33
CBQ-LGlt 8	H. spathi	80/>365	80/>365	256.11	0.11	0.707379 21	0.707379 21	B	14.4	111.6	0.84	-0.66
---	L. lyelli	–	–	–		--	--	-	–	–	–	–
CBQ-LGlt 7-2	P. steinmanni	15/30	15/30	254.50		0.707349 65	0.707349 65	B	20.5	30.3	1.18	-0.49
---	O. bulliensis	–	–	–		--	--	-	–	–	–	–
FolkstnBds 33	P. puzosianus	31/31	0/99	252.75		0.707315 23	0.707315 23	O	58.4	228.1	4.56	-0.24
---	O. raulinianus	–	–	–		--	--	-	–	–	–	–
---	C. floridum	–	–	–		--	--	-	–	–	–	–
---	S. kitchini	–	–	–		--	--	-	–	–	–	–
---	S. perinflata	–	–	–		--	--	-	–	–	–	–
---	L. regularis	–	–	–		--	--	-	–	–	–	–
---	L. acuticostata	–	–	–		--	--	-	–	–	–	–
---	L. schrammeni	–	–	–		--	--	-	–	–	–	–
Aptian												
---	H. anglicus	–	–	–		--	--	-	–	–	–	–
---	H. rubricosus	–	–	–		--	--	-	–	–	–	–
---	N. nolani	–	–	–		--	--	-	–	–	–	–
---	P. cunningtoni	–	–	–		--	--	-	–	–	–	–
---	T. subarcticum	–	–	–		--	--	-	–	–	–	–

---	C. buxtorfi	–	–	–		--	--	-	–	–	–	–
Fitton 36-1	C. gracile	0/600	1300/2000	237.65		0.707252 10	0.707252 10	O	128.6	203.9	5.50	-2.11
Fitton 30	C. debile	Top	1770/2000	236.89		0.707258 18	0.707258 18	O	51.8	318.8	5.27	-2.61
Fitton 24-1	C. meyendorffi	140/730	140/1750	235.08		0.707298 18	0.707298 18	O	78.5	268.6	4.19	-1.79
Fitton 23	D. transitoria	--	475/500	234.95		0.707415 41	0.707415 41	O	113.5	546.1	4.82	-1.86
Fitton 16	D. grandis	765/800	1465/1500	233.98		0.707372 27	0.707372 27	O	217.2	2070.6	5.26	-1.50
Fitton 13-3	C. parinodum	300/300	850/850	232.99		0.707371 35	0.707371 35	O	94.5	483.0	4.72	-1.84
Simpson 14	D. callidiscus	80/230	440/2040	231.22		0.707376 17	0.707376 17	O	152.3	395.8	-1.16	-4.18
Simpson 11-2	D. kiliani	220/350	460/800	230.58		0.707410 14	0.707410 14	O	664.7	3626.9	-11.36	-3.52
Simpson 4	D. fittoni	75/122	75/2200	229.03		0.707378 28	0.707378 28	O	93.8	164.6	2.21	-1.74
Simpson 1-1	P. obsoletus	65/85	65/139	228.47		--	--	O	106.0	2124.4	–	–
---	P. bodei	–	–	–		--	--	-	–	–	–	–
JURASSIC:	**Kimmeridgian**											
Flodigry 45-3	R. cymodoce	270/>900	735/>1365	135.90	0.20	0.706875 11	0.706875 11	B	36.8	225.7	2.56	-1.06
Flodigry 41	P. baylei	5/150	655/840	134.56		0.706853 11	0.706853 11	B	5.7	36.4	1.07	0.29
Flodigry 38	P. baylei	50/65	520/840	134.24		0.706805 8	0.706805 8	B	10.0	46.9	0.62	0.12
Callovian												
LambertiLs 3	Q. lamberti	13/30	13/30	117.43		0.706853 14	0.706853 14	O	25.1	150.5	1.54	-0.22
U.SpinCly 5	Q. henrici	84/91	84/91	116.92		0.706833 16	0.706833 16	B	12.6	88.8	2.05	-0.02
DunansClay4	Q. henrici	0/70	Poorly dated	116.50	0.50	0.706838 18	0.706838 18	B	6.9	40.6	3.82	0.16
---	K. spinosum	–	–	–		--	--	-	–	–	–	–
MOC 13b	K. proniae	Limited exposure		114.50	0.50	0.706880 11	0.706880 11	O	21.0	206.9	3.82	-0.32
DunansClay2	K. pron/phae	145/190	Poorly dated	114.00	1.00	0.706806 14	0.706806 14	B	5.7	30.2	4.05	0.09
LOC 11j	K. phaeinum	200/290	740/1240	113.60		0.706892 20	0.706892 20	O	19.9	209.0	3.33	-0.31
LOC 8e	K. grossouvrei	79/185	203/410	112.50		0.706856 15	0.706856 15	B	10.6	115.0	2.65	-0.14
LOC 4	K. obductum	225/335	225/375	111.60		0.706846 10	0.706846 10	B	10.9	35.9	2.18	-0.15
LOC 3a	K. jason	295/365	305/560	110.54		0.706835 6	0.706835 6	B	11.4	106.5	3.46	0.01
---	K. medea	–	–	–		--	--	-	–	–	–	–
---	S. enodatum	–	–	–		--	--	-	–	–	–	–
---	S. calloviense	–	–	–		--	--	-	–	–	–	–
---	K. galilaei	–	–	–		--	--	-	–	–	–	–
---	K. curtilobus	–	–	–		--	--	-	–	–	–	–
---	K. gowerianus	–	–	–		--	--	-	–	–	–	–
BelSands 9-1	M. kamptus	Base	Poorly dated	104.00	3.00	0.706905 11	0.706905 11	B	20.8	130.4	2.73	-2.09
---	M. terebratus	–	–	–		--	--	-	–	–	–	–
---	K. keppleri	–	–	–		--	--	-	–	–	–	–
Bathonian												
Sh-ChCrnBr5	C. discus	75/100	245/270	100.91		0.706945 16	0.706945 16	O	49.0	188.2	3.14	-1.43

---	C. hollani	–	–	–		--	--	-	–	–	–	–
---	O. aspidodies	–	–	–		--	--	-	–	–	–	–
---	P. hodsoni	–	–	–		--	--	-	–	–	–	–
---	M. morrisi	–	–	–		--	--	-	–	–	–	–
---	T. subcontractus	–	–	–		--	--	-	–	–	–	–
TayntonStn	P. progracilis	Lower 3 m		90.00	1.00	0.707051 16	0.707051 16	O	27.4	359.1	2.61	-0.93
CoralBed4e	A. tenuiplicatus	25/30	No zonal index	89.00	1.00	0.707075 13	0.707075 13	O	73.2	320.0	3.67	0.85
LNerineaBd4b	A. tenuiplicatus	20/20	No zonal index	88.00	1.00	0.707124 11	0.707124 11	O	150.7	929.5	2.89	-0.31
ChppngNortLs	O. yeovilensis	115/150	115/150	86.77	0.50	0.707057 13	0.707057 11	O	21.6	162.7	3.76	1.86
---	M. macrescens	–	–	–		--	--	-	–	–	–	–
---	P. convergens	–	–	–		--	--	-	–	–	–	–
Bajocian												
---	6 Zones Missing	–	–	–		--	--	-	–	–	–	–
BBSp 8-1	S. ovalis	22/30	22/30	68.46		0.707248 8	0.707248 8	B	11.0	103.4	1.29	-0.10
BBSp 6	H. discites	8/30	8/55	65.29		0.707269 10	0.707269 10	B	11.4	108.7	-0.41	0.25
Aalenian												
BBSp 5-2	G. formosum	8/20	8/20 - 48/60	64.60	0.20	0.707282 14	0.707282 14	B	16.9	148.5	0.62	-0.34
BBSp 4-1	G. formosum	3/40	3/40 - 3/60	64.06	0.01	0.707279 13	0.707279 13	B	8.4	51.6	0.23	-0.18
---	G. concavum	–	–	–		--	--	-	–	–	–	–
---	B. gigantea	–	–	–		--	--	-	–	–	–	–
---	B. bradfordensis	–	–	–		--	--	-	–	–	–	–
BBSp 3a	L. murchisonae	44/54	44/50	60.88		0.707267 13	0.707267 13	B	7.8	49.9	0.71	0.53
---	L. obtusiformis	–	–	–		--	--	-	–	–	–	–
---	L. haugi	–	–	–		--	--	-	–	–	–	–
---	T. scissum	–	–	–		--	--	-	–	–	–	–
---	L. opalinum	–	–	–		--	--	-	–	–	–	–
Simemurian												
DonBay 246-2	C.scipionianum	165/198	568/~5500	9.10	0.20	0.707847 14	0.707847 14	A	15.0	106.2	-0.78	-2.25
DonBay 228-2	C. lyra	30/30	1530/3330	8.46	0.10	0.707736 21	0.707736 21	O	38.5	230.5	2.34	-0.98

References and notes: Albian samples from near Folkstone (Casey, 1961, p. 528; Owen, 1975). Callovian samples from Calvert (Callomon, 1968) and Scotland (Sykes, 1975). Bathonian samples from Shipton-upon-Cherwell Cement Works (Page, 1989), Snowshill Hill Quarry (Channon, 1950; Torrens, 1968, 1969). Aalenian/Bajocian samples from Barns Batch Spinney near Bristol (Parsons, 1979; Callomon and Chandler, 1990). Sinemurian samples from Somerset (Ivimey-Cook and Donovan, 1983). † Fossil types: O = oyster, B = belemnite, A = ammonite

"age" of a sample is calculated using the relative position of the sample in that biozone as tabulated in Column 4 and assuming a constant sedimentation rate within a biozone. Thus, for example, sample BL-H75 was collected from the top of Lang's (1924) Bed H75 in the Blue Lias. Cope *et al.* (1980a) assign this bed to the *laqueus* subzone, which extends from Bed H69 at the base to H83 at the top. Sample BL-H75 was therefore found 107 cm above the base of the 160 cm-thick *laqueus* subzone, the base of which marks the passage of 3 subzone units of time, and the assigned subzone "age" therefore becomes 3.67. Stated errors on the subzonal "ages" (Column 6) are due to uncertainties in the exact stratigraphic horizon sampled or to a lack of zonally significant ammonites clearly defining the base or top of the biozone. Errors due to variations in sedimentation rates within a biozone cannot be quantitatively estimated. In some cases zonal boundaries are published as uncertain, but with no located ammonite data to allow quantification of their uncertainties. Although these uncertainties are generally insignificant compared to errors on the $^{87}Sr/^{86}Sr$ axis, the interested reader may wish to consult the primary sources cited in Tables 2.1, 2.2, and 2.3.

Measuring geological time using ammonite subzone units is useful when attempting to correlate other lithological successions to the well-characterised zones, subzones, and lithological successions of the Jurassic and Cretaceous of Great Britain. However, in other situations it is more useful to convert "ages" measured in ammonite subzone units to ages measured in millions of years. (Throughout this study "age" refers to time measured in subzone units whereas age written without quotes refers to time measured in millions of years (Ma)). This conversion requires that certain biostratigraphic horizons be radiometrically dated and that there exists biostratigraphic units of time that can be used as equal-duration time units in a linear interpolation between these radiometrically determined tie-points. The time scales of Kent and Gradstein (1985) and Harland *et al.* (1990) use ammonite zones as equal-duration units, but for this study it is much more convenient to use subzones as the basic unit of time. In fact, because zones are defined on the basis of

their constituent subzones (Dean *et al.*, 1961; Callomon, 1985), the subzone is arguably a better choice for an equal-duration unit. Either way, however, yields nearly the same ages for the stage boundaries of the Jurassic and Early Cretaceous (Table 2.4).

Table 2.4: Zones, Subzones, and the Radiometric Time Scale.

Stage boundary ages are calculated using radiometrically calibrated tie-points and zones or subzones as equal-duration time units. The final column (GTS 89) presents the time scale used in this study. It is based on subzones and additional palaeomagnetically calibrated tie-points from Harland *et al.* (1990). Zones and subzones are numbered consecutively up from the base of the Jurassic.

Stage Boundary	Zone	Ma	Subzone	Ma	GTS89†
Cenomanian/Albian*	115	97.0 *	268	97.0 *	97.0 *
Albian/Aptian*	108	112.0 *	244	112.0 *	112.0 *
Aptian/Barremian	101	119.5	227	120.5	124.5 *
Barremian/Hauterivian	93	128.0	211	128.5	131.8 *
Hauterivian/Valanginian*	86	135.5 *	197	135.5 *	135.0 *
Valanginian/Ryazanian	81	138.7	187	138.7	140.7 *
Ryazanian/Portlandian	76	141.9	177	141.9	145.6 *
Portlandian/Kimmeridgian	67	147.7	159	147.7	149.0
Tithonian/Kimmeridgian	59	152.8	143	152.8	152.1 *
Kimmeridgian/Oxfordian*	54	156.0 *	133	156.0 *	154.7 *
Oxfordian/Callovian	48	158.9	118	159.1	157.1 *
Callovian/Bathonian	41	162.3	101	162.7	161.4
Bathonian/L.Bajocian	33	166.2	84	166.2	165.8
Late/Early Bajocian +	29	168.2 +	74.5	168.2 +	168.2 +
E.Bajocian/Aalenian	25	173.6	65	173.1	173.1
Aalenian/Toarcian	20	180.4	54	178.8	178.8
Toarcian/Pliensbachian	14	188.6	37	187.5	187.5
Pliensbachian/Sinemurian	9	195.4	22	195.3	195.3
Sinemurian/Hettangian*	3	203.5 *	6	203.5 *	203.5 *
Hettangian/Rhaetian	0	208.0	0	208.0	208.0
Rhaetian/Norian*	-1	209.5 *	-2	209.5 *	209.5 *

† refers to reliance on **A Geologic Time Scale 1989** by Harland *et al.* (1990).
* indicates stage boundary used as a tie-point.
+ indicates a pseudo-tie-point placed in the mid-Humphriesianum subzone.

The final time scale used in this study is presented in the last column of Table 2.4. The stage boundary ages are calculated using ammonite subzones as equal-duration time units and using both the radiometrically and palaeomagnetically derived tie-points of Harland *et al.* (1990). The equations used to convert subzone units to ages measured in

millions of years are listed in Table 2.5. Table 2.6 presents a comparison of the average lengths of zones and subzones between the various tie-points used in the time scale. Zones average between 0.38 and 2.14 Ma long and subzones range between 0.16 and 0.75 Ma long. Although the errors on the stage boundary ages are far too large to make accurate estimates of the duration of zones or subzones, these calculations at least serve to emphasise that despite the assumption of uniform-duration subzone units, ammonite subzones are in fact likely to be a highly nonuniform measure of time.

Table 2.5: Equations used to convert subzone "ages" to ages measured in millions of years.

Stratigraphic Interval	Equation	Range of Subzone Units
Albian	15/24*(244 - X) + 112.0	(244 < X < 268)
Aptian	12.5/17*(227 X) + 124.5	(227 < X < 244)
Barremian	7.3/16*(211 X) + 131.8	(211 < X < 227)
Hauterivian	3.2/14*(197 X) + 135.0	(197 < X < 211)
Valanginian	5.7/10*(187 X) + 140.7	(187 < X < 197)
Ryazanian	4.9/10*(177 X) + 145.6	(177 < X < 187)
Tithonian†	6.5/34*(143 X) + 152.1	(143 < X < 177)
Kimmeridgian†	2.6/10*(133 X) + 154.7	(133 < X < 143)
Oxfordian	2.4/15*(118 - X) + 157.1	(118 < X < 133)
Mid-Bajocian to basal Oxfordian	11.1/43.5*(74.5 - X) + 168.2	(74.5 < X < 118)
Basal Sinemurian to Mid-Bajocian	35.3/68.5*(6 - X) + 203.5	(6 < X < 74.5)
Basal Rhaetian to basal Sinemurian	6/8*(-2 X) + 209.5	(-2 < X < 6)

†The Tithonian stage is equivalent to the Portlandian and Late Kimmeridgian of Great Britain; the Kimmeridgian is equal to the British Early Kimmeridgian.

In summary, the clearly defined lithostratigraphy has allowed careful sample collection that ensures that all samples from a set of related exposures are in the correct relative order. The abundance and thorough collection of ammonites in these sections over the course of several decades tightly constrains the positions of the subzonal boundaries and makes it unlikely that the assigned "ages" are far from their correct position in (local) ammonite subzone time. When data from separate time-equivalent successions are

collated, the samples may be slightly out of sequence due to diachroneity in the first appearances of ammonite species or to variations in the sedimentation rates within a given biozone at separate localities. It is thus concluded that scatter due to stratigraphic error is minimal and insignificant. The Sr-isotope curve resulting from this study should allow other stratigraphic sections from around the world to be directly correlated to the standard ammonite biozonation schemes of the British Jurassic and Early Cretaceous as well as to the associated classic English lithologic successions. It is worth emphasising that throughout this study great care was taken to collect samples from the solid outcrop with close reference to the published stratigraphic descriptions. This allows future workers to reproduce this data set, for verification or standardisation purposes, simply by consulting the papers and stratigraphic details cited in Tables 2.1, 2.2, and 2.3.

Table 2.6: Comparison of the average duration of the zones and subzones for each interval of time between the tie-points of Harland *et al.* (1990).

Interval	Ma/zone	Ma/Subzone	Subzones/Zone
Albian	2.14	0.65	2.78
Aptian	1.79	0.74	2.43
Barremian	0.91	0.46	2.00 +
Hauterivian	0.46	0.23	2.00 +
Valanginian	1.14	0.57	2.00 +
Ryazanian	0.98	0.49	2.00 +
Tithonian*	0.38	0.19	2.00 +
Kimmeridgian	0.52	0.26	2.00 +
Oxfordian	0.40	0.16	2.50
Mid-Bajocian Callovian	0.58	0.26	2.29
Sinemurian - Mid. Bajocian	1.36	0.52	2.63
Rhaetian Sinemurian	1.50	0.75	2.00
Average for Jurassic and Early Cretaceous:	0.97	0.42	2.32

*The Tithonian stage is equivalent to the Portlandian and Late Kimmeridgian of Great Britain; the Kimmeridgian is equal to the British Early Kimmeridgian.
+The zones in these stages are generally not subdivided into subzones.

2.2 Diagenetic Error

Diagenetic error presents the most serious limitations for Sr-isotope stratigraphy. Many land-based limestones and dolomites have had a complex diagenetic history and most contain a significant proportion of clay minerals. While the primary marine signal may be retained somewhere within a bulk limestone, this signal is frequently obscured by the leaching of extraneous Sr from diagenetic cements or silicate minerals during sample dissolution (see for example Banner *et al.*, 1988). Sr-isotope curves derived from bulk limestones are thus apt to show considerable scatter (e.g., Brookins *et al.*, 1969; Burke *et al.*, 1982; Koepnick *et al.*, 1985, 1990). A second approach is to analyse only so-called "well-preserved" fossil aragonite, calcite, or phosphate. The difficulty here is determining exactly what the phrase "well-preserved" actually means with regards to the preservation of a primary marine Sr-isotope signal. Careful efforts directed towards selecting only well-preserved material have still yielded a considerable degree of data scatter (e.g., Popp *et al.*, 1986; Brand, 1991). Given these difficulties, the methodology developed in this study was designed first to remove as much secondary material as possible from apparently well-preserved low-Mg calcite macrofossils and then to develop geochemical tracers that would allow diagenetically altered material to be distinguished *a priori* from unaltered material.

Thus all samples used in this study were rigorously cleaned before Sr-isotopic analysis. The matrix was first removed from the fossil (almost exclusively belemnites or oysters) using a grinding stone or dentist's drill followed by a distilled water ultrasonic bath. From this point onwards, only distilled, deionized water and ultrapure HCl came into contact with the fossil material and all samples were cleaned, dissolved, and stored exclusively in Teflon or quartz glass beakers that were acid-washed in 50% concentrated HNO_3 or HCl for at least 24 hours. After the initial ultrasonic bath to remove any remaining mud, the samples were placed for 15 minutes in a 0.6 M HCl ultrasonic bath to remove any extraneous adsorbed Sr, dissolve away an external layer of calcite, and

highlight any remaining matrix, borings, or other imperfections in the calcite. Small samples received a shorter acid bath to prevent total dissolution. Cathodoluminescence studies (Sælen, 1989; this study) indicated that the secondary (Mn-rich) calcite in belemnites is located along the central axis and along two or three very thin, radially propagating cracks. The 0.6 M HCl treatment described above deeply etched the calcite in these cracks, apparently because the high organic content of the belemnite calcite strongly inhibits dissolution relative to the inorganically precipitated diagenetic calcites. The samples were then crushed to < 30 mg pieces to expose as much crack-filling calcite as possible and then were placed in a 0.3 M HCl ultrasonic bath. Additional drops of 6 M HCl were added to larger samples to maintain a vigorous dissolution for at least 10 minutes. This treatment should have preferentially removed as much of the inorganically precipitated, crack-filling secondary calcite as possible and left behind pure belemnite calcite. In oysters the secondary calcite is most likely to be concentrated between the parallel laminae of the shell structure and in any cracks formed during compaction of the sediments. This two-step acid-dissolution treatment is probably less effective for oysters because oyster calcite dissolves approximately as rapidly as does any diagenetic calcite. However, the crushing and acid treatment should still have removed a significant proportion of any secondary calcite present.

60 mg of sample were then accurately weighed out and dissolved in 4 ml of 2.5 M HCl. 1 ml was loaded onto standard ion exchange columns for the Sr separation while the remaining 3 ml were analysed for Fe and Mn using atomic adsorption spectrophotometry in flame mode. The Sr was loaded in water and 0.25 M H_3PO_4 onto a single Ta filament and analysed on a VG Isomass 54E single collector thermal ionisation mass spectrometer. Blanks for the whole procedure were less than 1 ng Sr (compared to ~15,000 ng loaded on the columns) and all results were normalised to an $^{86}Sr/^{88}Sr$ ratio of 0.1194. The very low Rb/Sr ratios found in belemnites (Fischer and Gygi, 1989) and other low-Mg calcite

material (DePaolo and Ingram, 1985; Hess *et al.*, 1986; DePaolo, 1986; Capo and DePaolo, 1990) result in negligible corrections to the measured $^{87}Sr/^{86}Sr$ ratio due to the decay of ^{87}Rb to ^{87}Sr over the past 200 Ma.

The stable isotopes of carbon and oxygen were measured on samples prepared as above and then crushed, treated with 5% H_2O_2 and acetone to remove organic matter, and oven-dried at 60°C for 30 minutes. Turrets of 36 samples and 8 standards were analysed under computer control on a VG Isogas Prism using a common acid bath of anhydrous orthophosphoric acid held at 90°C. The results were calibrated to the PDB standard and expressed in the conventional $\partial^{13}C$ and $\partial^{18}O$ notation using internal laboratory standards and the Carrara Marble standard. Analytical precision for the Prism was always better than 0.1 ‰ (1 standard deviation) for $\partial^{13}C$ and $\partial^{18}O$ based on 8 daily analyses of the Carrara Marble. The use of a common acid bath always carries the risk of a "memory effect". However, because most samples yielded fairly similar $\partial^{13}C$ and $\partial^{18}O$ values, this would not generally present a significant source of error. Replicate analyses of samples yielding extreme values along with the following two or three samples generally confirmed the original analysis, suggesting that the memory effect was minimal in all cases. The application of Fe, Mn, $\partial^{13}C$, and $\partial^{18}O$ as tracers of diagenesis is discussed in Chapter 3.

2.3 Analytical Error

The analytical reproducibility of the Oxford VG Isomass 54E has recently been significantly improved due to the installation of a Schlumberger Solartron 7150+ digital multimeter and a Keithley 642 remote head electrometer. This new hardware has greatly reduced the electronic corrections ('tau corrections') associated with the decay of the electronic signal in the remote head resistor, improved the analytical reproducibility by housing the remote electrometer in a stable microenvironment, and improved the linearity of the electronic response such that a $1 \cdot 10^{-11}$ A and an $8 \cdot 10^{-11}$ A beam give analytically identical ratios on a standard. Nearly all analyses were performed after the new hardware

was installed in June 1990.

Machine performance was routinely monitored by running 2 standards in every turret load of 14 samples. The Oxford Age and Isotope Research Laboratory has traditionally run only the Eimer and Amend $SrCO_3$ standard. However, this standard is no longer commercially available and more recently established labs run only the NBS SRM 987 standard. To facilitate comparison between older and newer data sets I have consistently analysed both the Eimer and Amend and NBS 987 standards in the same turrets. The weighted average (weighted by analytical errors using the IBM-compatible program **Isoplot 2.11** written by Ludwig (1990)) of 34 analyses of the E & A standard is 0.708028 with a 95% confidence interval of ± 5 in the 6th decimal place (Figure 2.1a). The weighted average of 26 analyses of NBS 987 is 0.710254 ± 6 (Figure 2.1b). Eight samples of modern marine shell material from Britain and the Queen Charlotte Islands (W. Canada) were also analysed, but unfortunately the samples did not run well and gave relatively scattered results (Fig. 2.2). The weighted average for modern seawater is 0.709189 ± 22. These figures represent the best-estimates of the true values of each standard as measured in the Oxford Age and Isotope Research Laboratory.

An estimate of the analytical reproducibility of the VG 54E over the course of this study is provided by the variation of the repeated measurements of the E & A and NBS 987 standards. Excluding two results that lie well outside of a 95% confidence interval (Isoplot 2.11), the analytical reproducibility (= 'external population errors' of Fig. 2.1) is better than ± 25 in the 6th decimal place for the E & A and NBS 987 standards. This compares favourably with other recent studies (Hodell *et al.*, 1989, 1990, 1991; Miller *et al.*, 1988, 1990).

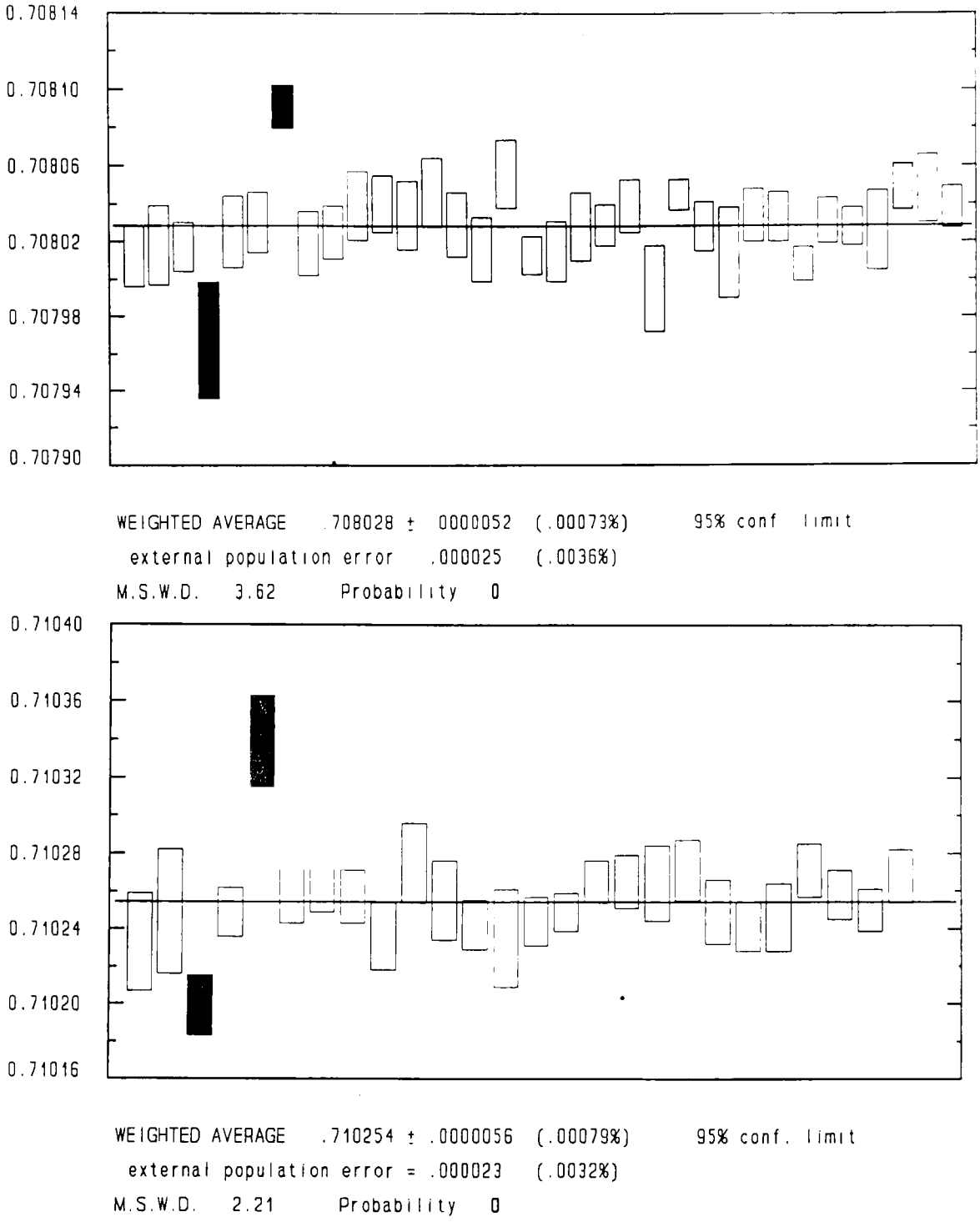

Figure 2.1 Weighted average (according to errors) of 34 analyses of the Eimer and Amend standard (top) and 26 analyses of the NBS 987 standard (bottom) calculated using Ludwig (1990). Shaded boxes represent outliers rejected as being beyond the 95% confidence interval.

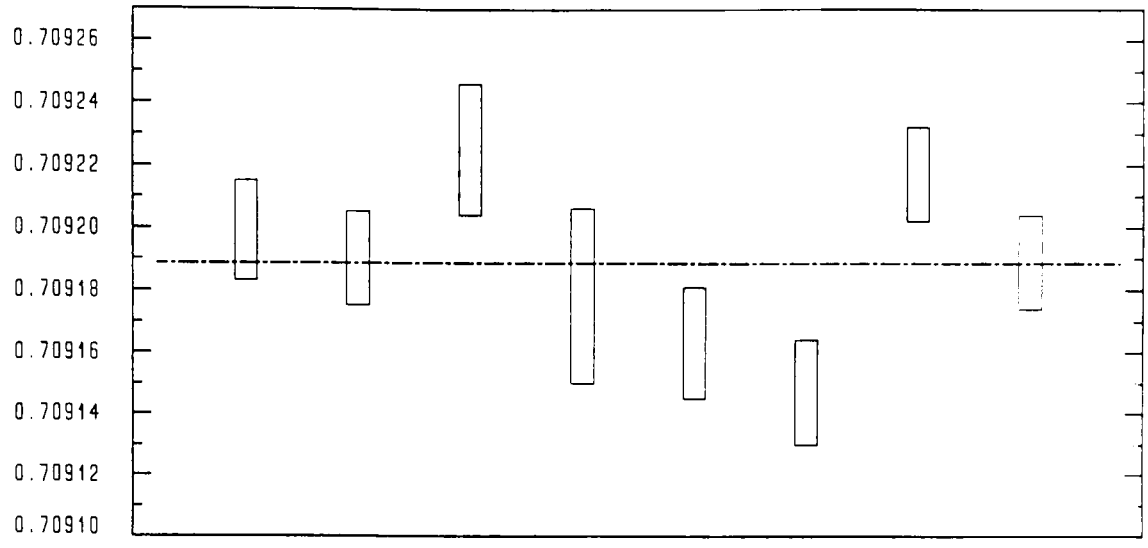

WEIGHTED AVERAGE - .709189 ± .000022 (.0031%) 95% conf limit
external population error .000051 (.0072%)
M.S.W.D. 8.67 Probability 0
Robust (Biweight/9) 'Average' .709189 ± .000022 (Gaussian)

Figure 2.2 Weighted average of 8 samples of modern marine shell material collected from Britain and the Queen Charlotte Islands (western Canada).

Possible systematic offsets of data restricted to a given turret load were monitored by measuring the E & A standard at the beginning and end of each turret run (using the same filament) and the NBS 987 standard at the middle of each run, and by loading samples of a variety of different ages into each turret. The E & A standard was analysed twice to minimise the possibility of one analysis being unrepresentative of the whole turret. The advantage of loading samples of a variety of ages together in the same turret is that when the results from all turrets are plotted together on the Sr-isotope curve, each sample from a given turret is surrounded by samples from a variety of other turrets. Thus, if most turrets give reproducible results while only a few show systematic offsets, these offset data should plot systematically above or below the main trend of the Sr-isotope curve.

As indicated in Figure 2.1, most turrets give results for the standards that are

analytically indistinguishable from one another. Accordingly, most of the data forming the Sr-isotope curve show no systematic, turret-by-turret offsets relative to the main trend of the data. However, it turns out that the data from a number of turrets are systematically offset (usually higher) than the rest of the data, and that this offset is accurately recorded by measurement of the E & A standard. As a result, it is possible to correct for these offsets by normalising the data in each turret according to the value of the E & A standard measured in that turret. Although one could apply a normalisation only to those data that show an obvious offset or to those turrets whose standards are offset by a certain amount relative to the mean value, it turns out that any line drawn to distinguish between those turrets that should or should not be normalised would be quite arbitrary and thus that it is most consistent to normalise the data of every turret according to the value of E & A measured in that turret. The effect of this normalisation on each turret relative to the whole data set was systematically monitored with the following results: 1) In no case does the normalisation result in a new, unwanted offset. 2) As expected, the relative positioning of the data from most turrets is little changed by the normalisation. 3) All obvious systematic offsets were corrected by the normalisation. A comparison of the unnormalised and normalised Lower Jurassic data (Fig. 2.3) shows that the overall effect of the normalisation is relatively small. It is only in the finest structure of the curve that the normalisation increases the resolution of the curve. The causes behind the offsets of a few turrets are not known, but they may involve the considerable temperature and humidity variations encountered in the lab during the course of this study or the problems encountered with maintaining a good vacuum pressure in the mass spectrometer.

Figures 2.4 and 2.5 compare the reproducibility of 46 replicate analyses before and after the turret-by-turret normalisation. In the unnormalised data set one turret was normalised from an extreme E & A of 0.708091 to an E & A of 0.708028 to avoid making

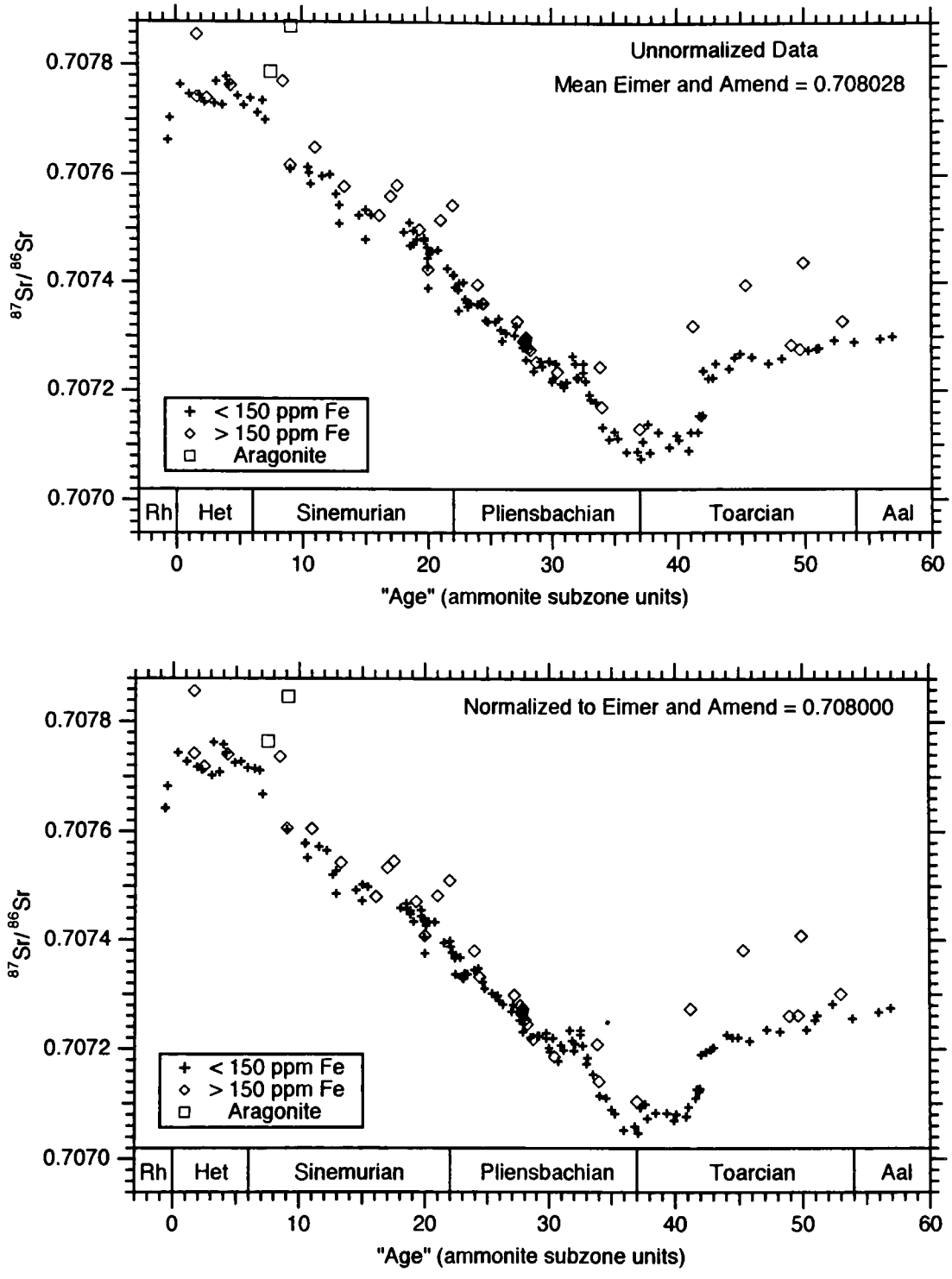

Figure 2.3 Comparison between unnormalised (top) and normalised (bottom) data from the Lower Jurassic of Great Britain. Time axis is in ammonite subzone units counting up from the basal Jurassic. Crosses represent samples with no evidence of diagenesis and diamonds represent samples suspected of diagenetic alteration based on their iron content (see Chapter 3).

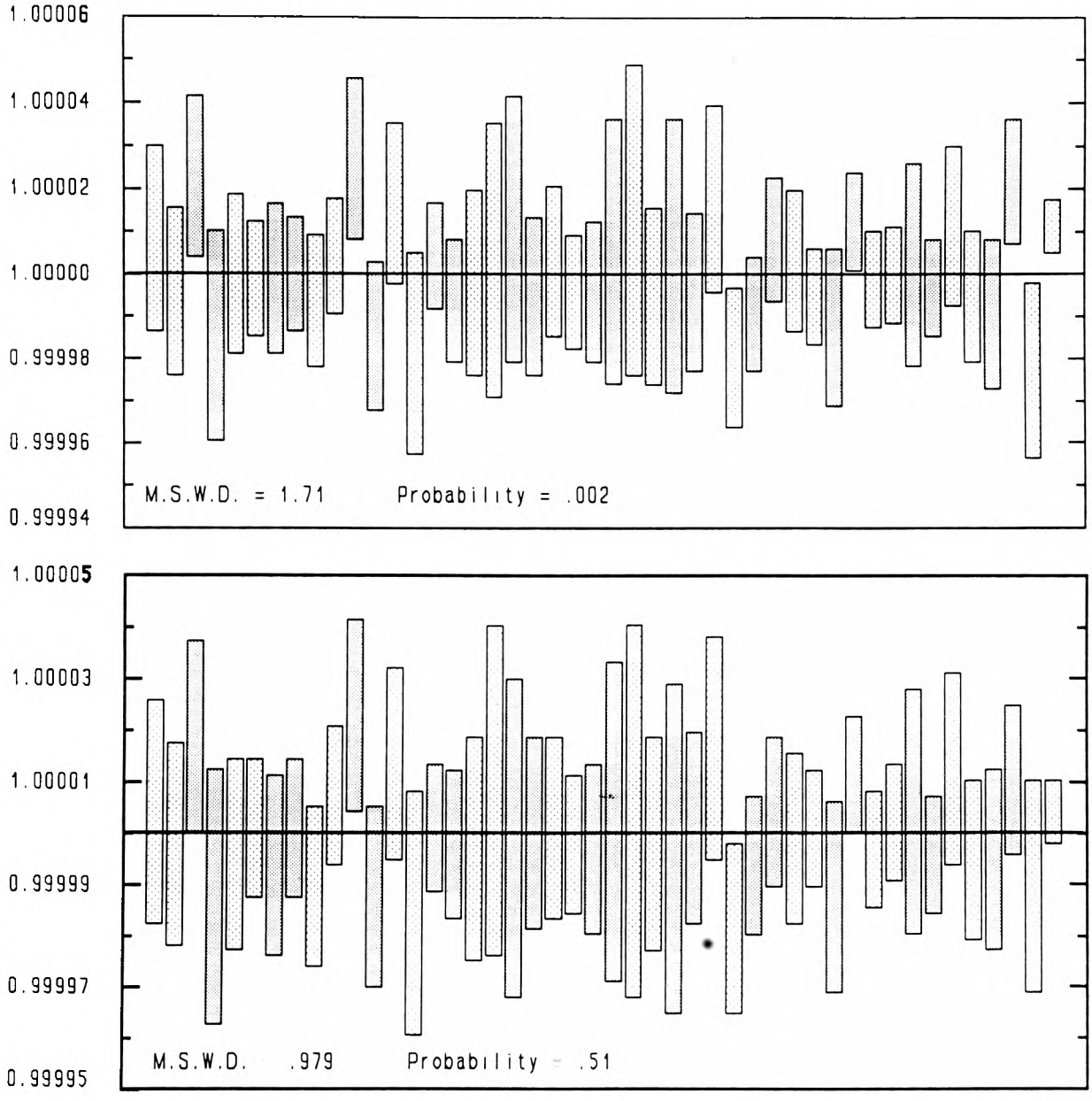

Figure 2.4 Comparison of 23 replicate analyses plotted relative to their weighted means and normalised to unity (= horizontal line). Shading differentiates adjacent sample pairs. Upper diagram shows unnormalised data; lower diagram shows the turret-by-turret normalised data.

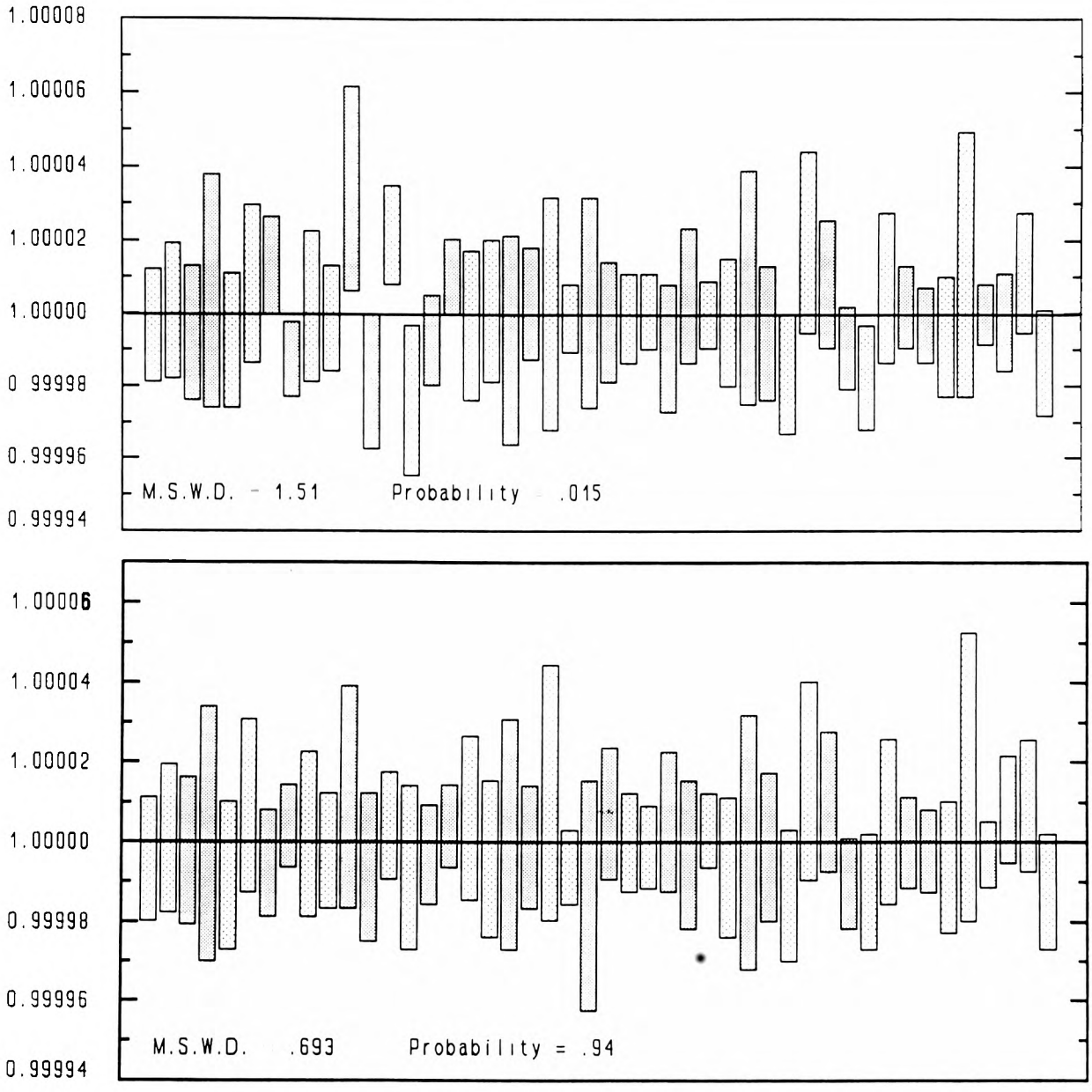

Figure 2.5 Comparison of 23 replicate analyses plotted relative to their weighted means and normalised to unity (= horizontal line). Shading differentiates adjacent sample pairs. Upper diagram shows unnormalised data; lower diagram shows the turret-by-turret normalised data.

the unnormalised data look unnecessarily bad. Among the normalised data there are three turrets with failed or poorly run E & A standards; in these cases normalisations compatible with measurements from the previous turret were applied. In Figures 2.4 and 2.5 each pair of replicate analyses is plotted relative to the weighted average (weighted according to the number of individual ratios measured for each analysis) and arithmetically normalised to unity. This allows all replicates to be displayed on the same ordinate while still preserving their original variability. The unnormalised data (Fig. 2.4a and 2.5a) include 5 replicates with non-overlapping error bars and 11 whose error bars do not include the weighted average (the horizonal line at unity). By contrast, all error bars of the normalised replicates overlap (Fig. 2.4b and 2.5b), and only 2 do not overlap with their weighted averages. The overall improved reproducibility of the normalised replicates is reflected in better values for the M.S.W.D. (mean square of the weighted deviates) and for the probability of the data scatter being due to analytical error alone. The M.S.W.D. and probability, as calculated by Isoplot (Ludwig, 1990), are measures of the ability of the analytically determined error bars to explain the observed scatter in the data. An M.S.W.D. of unity indicates a perfect match between the observed scatter and the size of the error bars. If the M.S.W.D. is greater than unity, then some of the scatter is not accounted for by the error bars; an M.S.W.D. of less than unity indicates that the error bars are too generous relative to the observed scatter. The probability is a measure of the likelihood that the analytical error alone explains the observed scatter. A probability of zero indicates that such an explanation is very unlikely. In both Figures 2.4 and 2.5 the M.S.W.D. and probability values indicate better results for the turret-by-turret normalised data.

A similar conclusion is reached when comparing the data obtained from replicate analyses of a suite of 12 different belemnites collected from a single bedding plane (Fig. 2.6; discussed in more detail in Chapter 4). Again, comparison of replicate analyses shows a higher degree of consistency in the normalised data set. Moreover, while the

unnormalised replicate data appear more or less to scatter randomly about the mean, the normalised data seem to indicate that there is a consistent variability between samples.

In total there are 58 replicate analyses. Of these, 100% of the normalised replicates plot within their 2σ error bars (~95% confidence interval) and 97% (56 out of 58) plot in range of their weighted averages. Of the unnormalised data, 88% (51/58) plot within their error bars and 76% (44/58) plot with range of their weighted average. Thus, in conclusion, the consistently applied turret-by-turret normalisation has both qualitatively (Fig. 2.3) and quantitatively improved the quality of this data set without introducing any unwanted artifacts. In future studies it may also be useful to adopt such a normalisation procedure, but in each case the efficacy of the normalisation must be carefully evaluated. All data presented in this thesis are normalised to E & A = 0.708000.

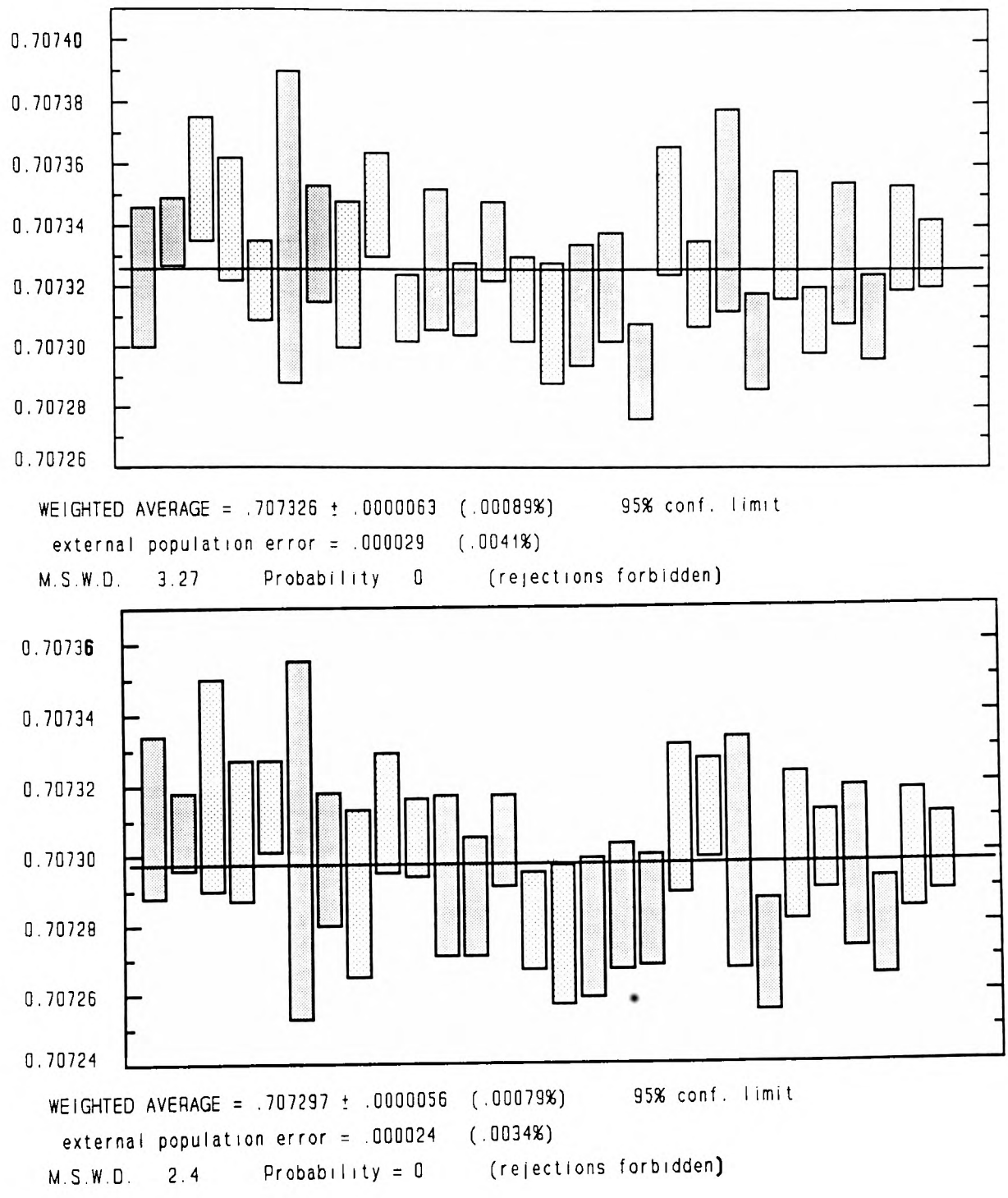

Figure 2.6 Comparison between unnormalised (top) and normalised (bottom) replicate analyses of 12 belemnites from a single bedding plane within Lang's Bed 115. Shading differentiates adjacent samples.

Chapter 3: Diagenesis

3.1 Introduction

Any attempt to reconstruct the history of a geochemical tracer in seawater is bedeviled by the possibility of contamination from diagenetic and non-carbonate phases. In this study such contamination is minimised by using only well-preserved belemnites and oysters that have been physically separated from their matrix and put through the double partial dissolution technique described earlier. However, despite careful sample preparation and all visual appearances of good preservation, it is still possible for samples to contain significant amounts of diagenetic calcite (e.g., Stevens and Clayton, 1971). It is therefore useful to develop a set of geochemical tracers that monitors the diagenesis of the Sr-isotopic signal in calcitic macrofossils.

Attempts to reconstruct the history of seawater Sr isotopes using land-based outcrops commonly use, implicitly or explicitly, the Sr isotopes themselves as the primary indicator of diagenesis (e.g., Veizer and Compston, 1974; Burke *et al.*, 1982; Derry and Jacobsen, 1988; Derry *et al.*, 1989). Because of the long residence time of Sr in seawater, the seawater Sr-isotope curve is expected to be relatively smooth, with no sudden spikes. Therefore, any points that deviate significantly from the main trend of the data set are taken as diagenetically altered. In the case of material from land-based outcrops, it is generally expected that diagenetic carbonates yield higher $^{87}Sr/^{86}Sr$ ratios than their precursor phases due to the incorporation of radiogenic ^{87}Sr from the breakdown of high Rb/Sr detrital silicate minerals (Moore, 1989).

Both meteoric fluids and *in situ* alteration of detrital minerals tend to contribute radiogenic Sr to a diagenetic system. The predominance of radiogenic ^{87}Sr in meteoric fluids is perhaps best illustrated by the fact that 93% of the measured global river runoff, along with many subsurface waters, have higher $^{87}Sr/^{86}Sr$ ratios than modern or palaeo-seawaters (Palmer and Edmond, 1989; Doe *et al.*, 1966; Burtner, 1987; Emery *et al.*, 1987;

Moore, 1989; Veizer, 1989). Because of their high Rb/Sr ratios, the breakdown and recrystallisation of small amounts of clay minerals and other detrital silicate phases can release large amounts of ^{87}Sr into a diagenetic system. For example, Banner *et al.* (1988) calculate that homogenisation of 4% glauconite (present-day 230 ppm Rb, 5.5 ppm Sr, $^{87}Sr/^{86}Sr$ = 1.3329) with 96% dolomite (1 ppm Rb, 110 ppm Sr, $^{87}Sr/^{86}Sr$ = 0.7080) results in a whole-rock $^{87}Sr/^{86}Sr$ of 0.7092. It is thus not surprising that Burke *et al.* (1982) find that eliminating data from bulk-rock samples containing more than 10% insoluble residue significantly reduces the scatter in their seawater Sr-isotope curve. The exceptions to the general rule are those sedimentary sequences that either contain volcanogenic sediments or were recrystallised by meteoric fluids weathering a volcanic terrane. Diagenetic alteration of carbonates in these situations should lower the final Sr-isotope ratio.

The predominance of situations in which diagenesis increases a carbonate $^{87}Sr/^{86}Sr$ ratio is best illustrated by the superposition of the data of the present study over the large, globally extensive data set of Koepnick *et al.* (1985, 1990) (Fig. 3.1). In their original work, Burke *et al.* (1982) note that their data tend to cluster at the lower range of the scatter and to "smear" up towards more radiogenic values due to variable diagenetic alteration of the samples. They use this observation to justify drawing their "best-estimate" curve along the lower limits of their data set. The data from the present study confirm this interpretation by tightly defining a curve that closely follows the minimum ranges of the Koepnick *et al.* data. The only exceptions plotting significantly below this curve are a few in the Early Jurassic, which come from a volcanic terrane characterised by nonradiogenic (low $^{87}Sr/^{86}Sr$ ratios) surface waters, and a few in the Late Jurassic, which, like most of the Jurassic samples of Koepnick *et al.* (1990), are dated only to the stage and therefore may be somewhat misplotted on the time axis.

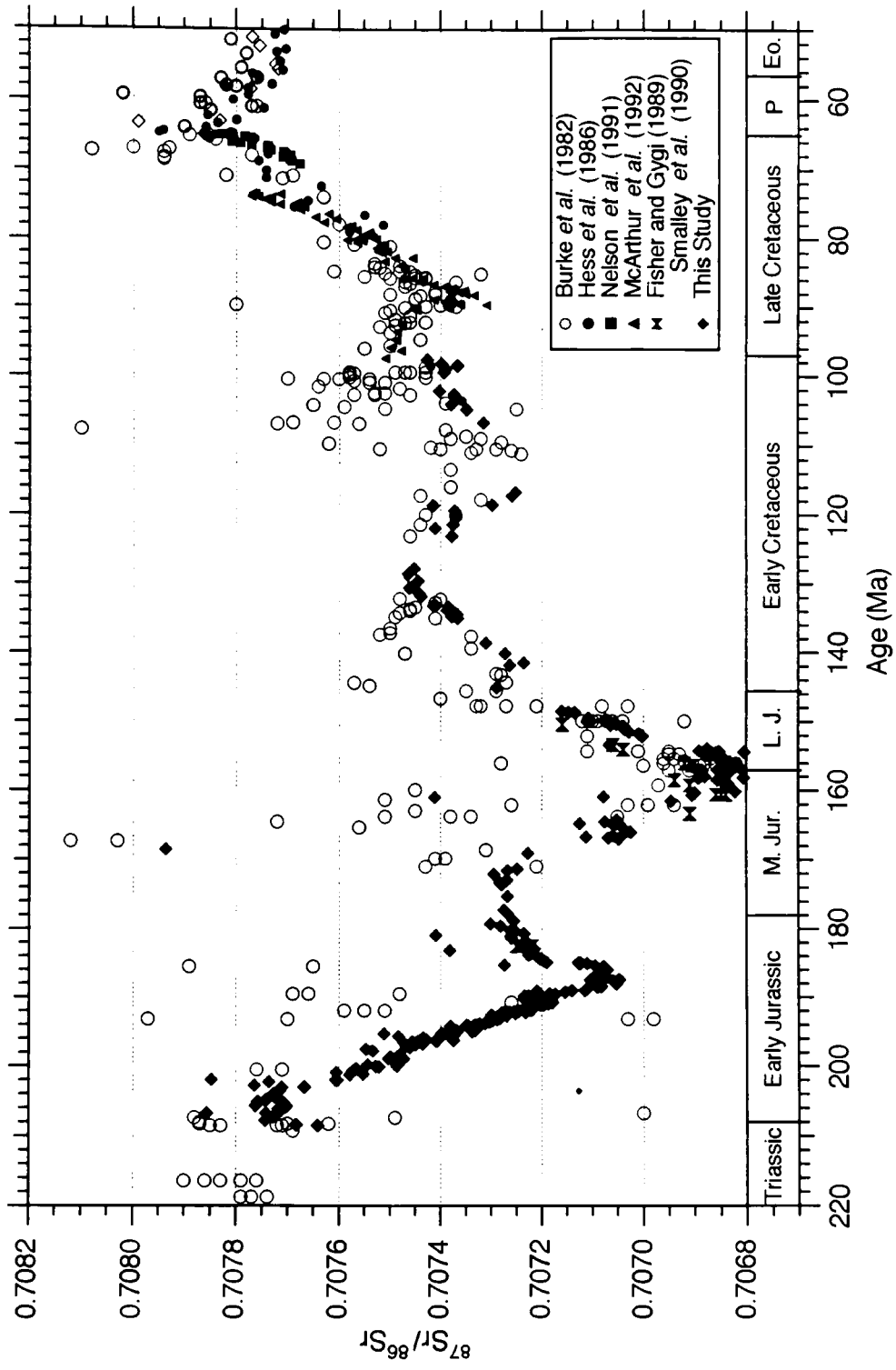

Figure 3.1 Comparison between the bulk-rock carbonate data of Koepnick *et al.* (1985, 1990) and the calcitic macrofossil data collected in this study. All data converted to the time scale of Harland *et al.* (1990) and normalised to NBS 987 = 0.710230.

Thus, given a sufficiently dense data set, it is probably a valid, albeit intellectually unsatisfying exercise to form a best-estimate curve based on the trend of the main body of the data and ignoring the "fliers". Sufficient knowledge of the geological setting of the samples should further allow one to predict over which intervals diagenesis should result in higher or lower isotopic ratios. However, in a general application of Sr-isotope stratigraphy one may wish to date, for example, a suite of 10 samples from well cuttings or a borehole. Given the lack of stratigraphic context and low sample density, it is impossible to assess realistically the quality of the Sr-isotope results based on the Sr-isotope data alone. It is thus essential to develop independent criteria to evaluate the diagenetic alteration of Sr isotopes in carbonates.

3.2 Tracers of Diagenesis

The choice of tracers selected for this study (Fe, Mn, $\partial^{13}C$, $\partial^{18}O$) is heavily influenced by the discussion of Veizer (1983) so we begin with a summary of his reasoning. Marine organisms precipitate $CaCO_3$ as either high-Mg calcite (HMC), aragonite, or low-Mg calcite (LMC). HMC and aragonite are thermodynamically stable in seawater while LMC tends to be stable in most terrestrial weathering environments. In this study we are primarily concerned with LMC because it is the primary mineralogy of oysters and belemnite rostra (Milliman, 1974; Veizer, 1974; Sælen, 1989).

In simple terms the trace element composition of a given calcite is governed by the composition of the primary fluid and the magnitude of the distribution coefficient D_x for each element X. D_x is defined by

$$(m_x/m_{Ca})_{LMC} = D_x(m_x/m_{Ca})_{fluid},$$

where m_x and m_{Ca} are the molar concentrations of element X and Ca in the solid (LMC) and fluid phases. While this equation is strictly valid only for ideal solutions in complete equilibrium and with no concentration gradients in either the solid or fluid phases, it illustrates that as a first approximation the trace element composition of a calcite is

determined by the molar abundance of element X relative to Ca in the fluid, and not, for example, by the salinity of the fluid. The magnitude of D_x, ideally determined under a wide variety of experimental conditions, allows us to predict whether a given element is likely to be relatively enriched or depleted in the solid phase. If $D_x < 1$ then element X is selectively excluded from the calcite structure while if $D_x > 1$ then element X is selectively incorporated into the calcite structure. Table 3.1 summarises the distribution coefficients of a number of elements:

Table 3.1: Distribution Coefficients for Selected Elements (Veizer, 1983)

Element	D < 1	Element	D > 1
Sr	0.13 D.P.	Mn	6 D.P.
	0.05 A →dLMC,		15 A →dLMC,
	HMC →dLMC		HMC →dLMC
	0.03 LMC →dLMC		30 LMC →dLMC
Na	$2\text{-}3 * 10^{-5}$	Fe	1 < X < 20
Mg	0.006 - 0.013	Cu	25
Ba	0.1 0.4	Co	2 - 5
$(UO_2)^{2+}$	< 0.02	Zn	5 - 20
		Cd	8 - 30

D.P. = direct precipitation; A = aragonite; HMC = high magnesium calcite; LMC = low magnesium calcite; dLMC = diagenetic LMC

The trace element composition of a primary marine calcite is hence determined by the composition of seawater, the magnitude of D_x for each element, and any biological fractionation imposed during precipitation. Biogenic calcites are thus generally characterised by low (<<1000 ppm) concentrations of Fe, Mn, Zn, Co, Cd, Cu, Ba, and UO_2 and high (>>1000 ppm) concentrations of Mg, Sr, and Na (Milliman, 1974; Veizer, 1983). The choice of elements used to monitor diagenesis depends on the relative difference in the molar ratios between seawater and the probable diagenetic fluids, the magnitude of D_x, and the absolute concentration of the elements of interest relative to available analytical capabilities. In this study Mn and Fe were selected due to the probable

large differences between the molar metal/Ca ratios of oxygenated seawater and the reducing diagenetic fluids expected in organic-rich sedimentary sequences, the large observed difference in Mn and Fe concentrations between primary belemnite and bulk-rock LMC (Veizer, 1974), the relatively large distribution coefficients of Mn ($D_{Mn} \approx 3$ to 22) and Fe ($D_{Fe} \approx 1.5$ to 7.7) (Dromgoole and Walter, 1990), and the ease and accuracy of analysis using atomic absorption spectrophotometry. In the following sections the expected prevalence of Mn^{2+} and Fe^{2+} in diagenetic fluids is demonstrated for a variety of burial and meteoric diagenetic environments. The discussion is focused on diagenesis in mudrocks because diagenesis in this setting appears to be well-understood and because mudrocks are the dominant lithology of many sections sampled in this study.

3.2.1 Behaviour of Mn and Fe during Diagenesis

During burial of fine-grained, relatively organic-rich sediments, a series of geochemical reactions governs the breakdown of organic matter and modifies the chemistry of the porewaters and sediments. Early diagenesis is catalyzed by the bacterial degradation (oxidation) of organic matter, which proceeds by a series of reactions acting sequentially according to a decreasing yield of free energy (Irwin *et al.*, 1977; Froelich *et al.*, 1979; Berner, 1981a):

1. $CH_2O + O_2 \rightarrow CO_2 + H_2O$ (Oxic diagenesis)
2. $5CH_2O + 4NO_3^- \rightarrow 2N + 4HCO_2 + CO_2 + 3H_2O$ (Nitrate reduction)
3. $CH_2O + 3CO_2 + H_2O + 2MnO_2 \rightarrow 2Mn^{2+} + 4HCO_3^-$ (Mn^{4+} reduction)
4. $CH_2O + 7CO_2 + 4Fe(OH)_3 \rightarrow 4Fe^{2+} + 8HCO_3^- + 3H_2O$ (Fe^{3+} reduction)
5. $2CH_2O + SO_4^{2-} \rightarrow H_2S + 2HCO_3^-$ (Sulphate reduction)
6. $2CH_2O \rightarrow CH_4 + CO_2$ (Fermentation or methanogenesis)
7. $RCO_2H \rightarrow RH + CO_2$ (Abiotic decarboxylation)

Consideration of these reactions is particularly appropriate in this study because not only are many of the sequences sampled in this study made up of relatively organic-rich,

fine-grained sediments (i.e. much of the British Lower Jurassic, Callovian, Kimmeridgian, and Lower Cretaceous), but there is also evidence for many of these processes found fossilised within these sequences (Irwin *et al.*, 1977; Irwin, 1980; Raiswell, 1976, 1988; Fischer, 1986; Bottrell and Raiswell, 1989; Scotchman, 1991).

While the first four reactions occur only within the first few tens to hundreds of centimetres below the sediment/water interface (Froelich *et al.*, 1979; Sørensen and Jørgensen, 1987), sulphate reduction occurs down to a depth of about 10 - 20 m (Coleman and Raiswell, 1981; Claypool and Threlkeld, 1983), fermentation occurs down to a depth of 0.5 - 1 km, and decarboxylation occurs down to perhaps 2.5 km (Curtis, 1977). The positioning of the actual boundaries between diagenetic zones depends on such factors as sedimentation rates, organic matter content, and geothermal gradients. While very small amounts of carbonate can precipitate during the reduction of Mn and Fe oxides (Froelich *et al.*, 1979), it is sulphate reduction and methanogenesis (fermentation) that allow significant volumes of carbonate to precipitate (Curtis, 1977; Claypool and Threlkeld, 1983; Curtis and Coleman, 1985; Raiswell, 1988; Irwin *et al.*, 1977; Irwin, 1980; Matsumoto, 1983).

Diagenetic carbonate precipitated during the zone of sulphate reduction is expected to be low in Mn and Fe because the production of H_2S results in the rapid precipitation of pyrite and presumably alabandite (Berner, 1981b; Berner, 1984; Scotchman, 1991). In their examination of sulphate reduction in sediments Leslie *et al.* (1990) find that below an initial maximum, the down-core Fe^{2+} concentrations asymptotically approach the lower detection limit of 1 μM. Even this value represents significantly more Fe^{2+} than is found in seawater (Holland, 1978) and, assuming a seawater concentration of 10.2 mM Ca and the range of D_{Fe} reported by Dromgoole and Walter (1990), can result in a diagenetic calcite containing at most 80 - 200 ppm Fe. After sulphate reduction ends and methanogenesis begins, Fe^{2+} begins to accumulate in the pore waters and eventually reaches concentrations sufficient to precipitate ferroan calcite, ankerite, and even siderite (Curtis, 1977;

Matsumoto, 1983; Irwin *et al.*, 1977; Irwin, 1980). Limited data also suggest elevated Mn^{2+} levels during methanogenesis (Matsumoto, 1983; Scotchman, 1991). At greater depths, where diagenetic zones ranging from decarboxylation to low-grade metamorphism occur, pore waters should continue to be reducing and relatively rich in Mn^{2+} and Fe^{2+}. For example, Moore (1989) reports Mn and Fe concentrations in the subsurface brines of the Jurassic Smackover Formation of the U.S. Gulf Coast as 550 μM and 700 μM, respectively. Calcite cements apparently precipitating from these fluids contain approximately 500 ppm Mn and 2000 ppm Fe.

Diagenesis involving meteoric fluids can include a diverse array of geochemical situations. Of particular relevance to this study is whether or not the fluids are reducing, and hence can support dissolved Mn^{2+} and Fe^{2+}, or oxidising and hence unable to mobilise Mn and Fe. The oxygen content of meteoric fluids depends on the composition of the host rocks and the amount of time spent isolated from the atmosphere below the water table. In soils penetrated by roots, soil gases tend to be quite enriched in CO_2 but depleted in O_2 (Holland, 1978; Eriksson, 1985). Within the root zone a given packet of water can equilibrate with soil gases, but once this water has seeped below the water table, it is effectively in a closed system with respect to CO_2 and O_2 (Eriksson, 1985). The combination of the oxidation of pyrite and organic matter in the British Mesozoic mudrocks plus the long residence time in these relatively impermeable formations makes reducing conditions quite likely. In the oolitic and sandy units, however, meteoric fluids are more likely to remain oxidising due to the lack of readily oxidisable material and the higher fluid flow rates through these more permeable units. Thus it is likely that any diagenesis that occurs between the root zone and the water table in a typical Cotswold quarry occurs under relatively oxidising conditions. Only if diagenesis occurs within a system of regionally extensive groundwaters (on the scale of a few kilometres) will these fluids tend to be reducing enough to support dissolved Mn^{2+} and Fe^{2+} (Eriksson, 1985; Moore, 1989).

Surface weathering at the outcrop is a special case of meteoric diagenesis. Weathering crusts are ubiquitous features at all but the most freshly exposed mudrock outcrops and, upon visual examination, appear to range in thickness from a few centimetres on the vertical, fresh exposures of Dorset's Belemnite Marls to a few tens of centimetres on the slumped mudstones of the Gault near Folkstone in Kent. Rainwater soaking into a mudrock by capillary action is corrosive because it is oxidising and undersaturated with respect to $CaCO_3$. As it soaks in, dissolution of $CaCO_3$ brings the solution to saturation with calcite and the oxygen begins to react with the pyrite to form sulphuric acid, which in turn attacks carbonates and silicates (Berner and Berner, 1987). Because large quantities of oxygen are required to complete pyrite oxidation,

$$19/4\ O_{2\,(aq)} + FeS_2 \rightarrow 1/2\ Fe_2O_3 + 2\ SO_{4\,(aq)},$$

it is likely that beyond some depth in the outcrop the shortage of O_2 allows dissolved Fe^{2+} to persist. During drier weather the water evaporates and gypsum and carbonate precipitate. Frequent repetition of this cycle results in a surface crust leached of all rainwater-soluble minerals overlying a deeper volume of rock that has undergone a variable degree of alteration. Visual examination of pyrite-rich horizons in the field provides ample evidence for these weathering reactions in the form of abundant Fe oxyhydroxides ('rust'), elemental sulphur ('yellow bands'), and gypsum (selenite). Calcite precipitated under these conditions is expected to be Fe-rich, due the proximity of dissolving pyrite, and variably Mn-rich, depending on the amount of Mn locally available.

In summary, it appears that in many diagenetic environments, especially those dominated by mudrocks, Mn^{2+} and Fe^{2+} should commonly occur in sufficient quantities relative to Ca to enable high levels of Mn^{2+} and Fe^{2+} in calcite to be used as a fingerprint for diagenesis. In oolites and sandstones, however, elevated levels of Mn^{2+} and Fe^{2+} are not guaranteed, and it remains to be determined whether or not the conclusions based on the mudrock samples apply to other geological circumstances as well. Because further

information regarding the specific environment of diagenesis may be obtainable through the analysis of calcite $\partial^{13}C$ and $\partial^{18}O$ values, a discussion of carbon and oxygen isotope systematics during diagenesis follows.

3.2.2 Behaviour of $\partial^{13}C$ and $\partial^{18}O$ during Diagenesis

In contrast to the relatively consistent response of Sr isotopes and Mn and Fe concentrations to diagenesis, the stable isotopes of carbon and oxygen display variable and distinctive behaviour depending on the specific environment of alteration. An important parameter in stable isotope diagenesis is the ratio of carbon or oxygen initially contained in the fluid to that obtained from rock dissolution (Veizer, 1983; Lohmann, 1988). Carbon, in the form of bicarbonate, tends to be quite dilute in natural waters compared to the amounts of HCO_3^- derived from carbonate dissolution or the breakdown of organic matter. Thus the response of $\partial^{13}C$ to diagenesis is highly dependent on the nature of the host rocks and the organic matter degradation. Oxygen, by contrast, is obviously highly concentrated in water and, because water oxygen exchanges rapidly with HCO_3 oxygen (Hendy, 1971), the isotopic composition of the fluid tends to determine the $\partial^{18}O$ of the diagenetic calcite.

During burial diagenesis of mudrocks, the $\partial^{13}C$ of pore waters, and hence of diagenetic calcites, is highly dependent on the breakdown of organic matter. During sulphate reduction the oxidation of organic matter and upwards-diffusing methane yields carbonate $\partial^{13}C$ values as low as -20 to -35 ‰ (Irwin *et al.*, 1977; Curtis and Coleman, 1986; Raiswell, 1988). Methanogenesis (fermentation) converts organic matter into methane and carbon dioxide. Because the methane is isotopically very light (-60 to -75 ‰), the residual CO_2 is relatively heavy and yields calcite $\partial^{13}C$ values of +10 to +15 ‰ (Irwin *et al.*, 1977; Claypool and Threlkeld, 1983). Once decarboxylation begins to take over, porewater $\partial^{13}C$ begins to decrease (Irwin *et al.*, 1977) and eventually reaches approximately -20 ‰ (Curtis and Coleman, 1986). During sulphate reduction oxygen become increasingly isotopically lighter, apparently due to the input of oxygen derived

from the reduction of SO_4^{--} (Coleman and Raiswell, 1981; Sass *et al.*, 1991). During methanogenesis and decarboxylation the $\partial^{18}O$ values continue to decrease due to the increased temperatures associated with deeper burial. After some point the residual ^{18}O begins to buffer and even reverse the trend towards lower $\delta^{18}O$ values (Moore, 1989).

Under meteoric conditions water entering the recharge area will have a $\partial^{13}C$ of approximately -16 ‰ due to equilibration with soil gas (Lohmann, 1988). Because of the low initial concentration of carbon, the meteoric $\partial^{13}C$ rapidly rises until it equilibrates with the host carbonates. Meanwhile the oxygen isotopes, dominated by the initial $\partial^{18}O$ of the meteoric fluid (~ -6 to -8 ‰ PDB in Britain; Anderson and Arthur, 1983), tend to remain invariant until the system becomes highly rock-dominated (Lohmann, 1988). Thus the bulk of meteorically precipitated carbonates are likely to have $\partial^{13}C$ values only slightly lighter than the primary host rock carbonates but $\partial^{18}O$ values that are quite negative. The response of the stable isotopes to surface weathering of an outcrop is expected to be similar. Thus, in summary, $\partial^{18}O$ is generally a much more sensitive indicator of meteoric diagenesis than is $\partial^{13}C$ whereas $\partial^{13}C$ is a much more sensitive indicator of burial diagenesis in mudrocks that is $\partial^{18}O$.

With this background discussion in place we can move on to consider the observed geochemistry of belemnites and oysters in an attempt to address the problem of calcite diagenesis as it affects Sr isotopes. The first step is to define the initial, primary composition of the belemnites and oysters used in this study. Then we can examine the ability of the four tracers to predict which samples are most likely to be significantly altered with respect to the Sr isotope system.

3.3 Results for Mn and Fe

The Mn and Fe data for all belemnites are displayed in the histograms of Figure 3.2. The Mn data show a strong peak for samples containing between 5 and 15 ppm Mn followed by a rapid decrease in the number of individuals with higher levels of Mn. The

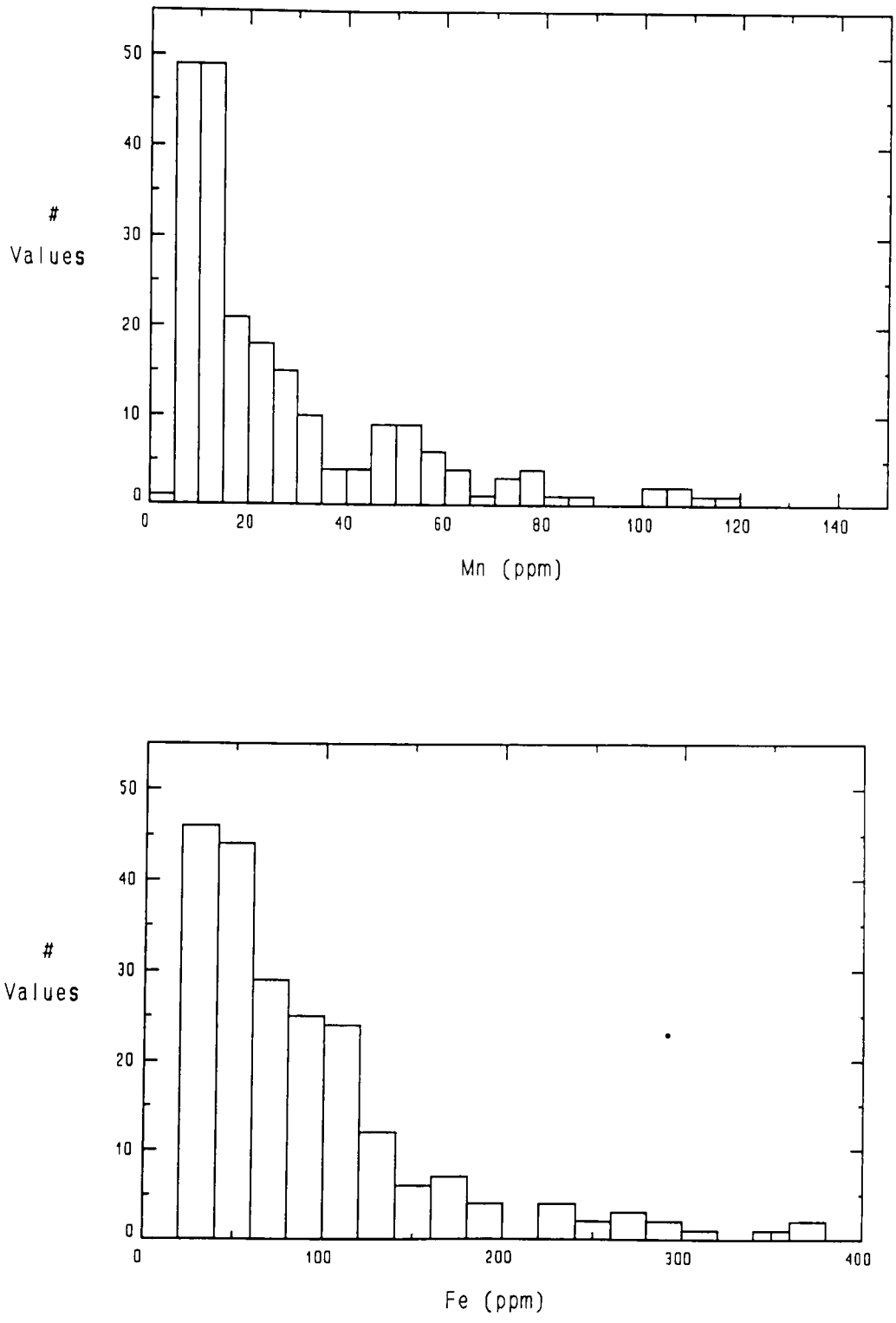

Figure 3.2 Histograms showing the Mn (top) and Fe (bottom) data for all belemnites collected in this study.

asymptotic tail is reached by 35 - 60 ppm. To get an impression of the generality of these results, Figure 3.3 compares Mn data for belemnites collected from the Dorset and Yorkshire sections. The Dorset data again show the large peak at 5 - 15 ppm Mn followed by a dramatic drop in the number of specimens with higher Mn levels. A reasonable cutoff between the main body of data and the asymptotic tail is 35 ppm. The Yorkshire data also show the significant 5 - 15 ppm peak, but the succeeding decline is more irregular as compared to the Dorset data. There is a secondary maximum at 45 - 60 ppm and possibly a third between 70 and 80 ppm. These maxima are largely due to Sinemurian/Pliensbachian samples from Robin Hood's Bay in Yorkshire. In the whole data set there are 3 samples with more than 150 ppm Mn (up to 516 ppm).

The Fe data for all belemnites (Fig. 3.2b) show a peak in the number of individuals containing between 25 and 60 ppm Fe followed by a step down to a secondary plateau for specimens containing 60 to 120 ppm Fe. The transition to the asymptotic tail occurs between 120 and 140 ppm. In Figure 3.4 the data from the Dorset and Yorkshire coasts are again compared. The Dorset data show the three divisions of the whole data set (25 - 60 ppm; 60 - 120 ppm; > 120 ppm Fe) while the Yorkshire data show a smoother decline from a maximum at 25 - 40 ppm to a reasonable cutoff at 140 - 180 ppm. Four samples from the Dorset coast and three from the Yorkshire coast contain more than 400 ppm Fe (up to 1490 and 1875 ppm, respectively).

The oysters as a group tend to show significantly higher levels of both Mn and Fe (Figure 3.5). The Mn data show a well-defined maximum in specimens containing 5 - 30 ppm Mn followed by an irregular decline to an asymptotic cutoff at about 80 ppm. Two samples have more than 300 ppm Mn (up to 665 ppm). The Fe data show a broad maximum between 50 and 250 ppm followed by an irregular decline to an asymptotic cutoff of 350 ppm. Of the 7 samples that have more than 1000 ppm Fe (up to 3630 ppm), a large proportion are from the silty/sandy sediments of the Aptian of the Isle of Wight.

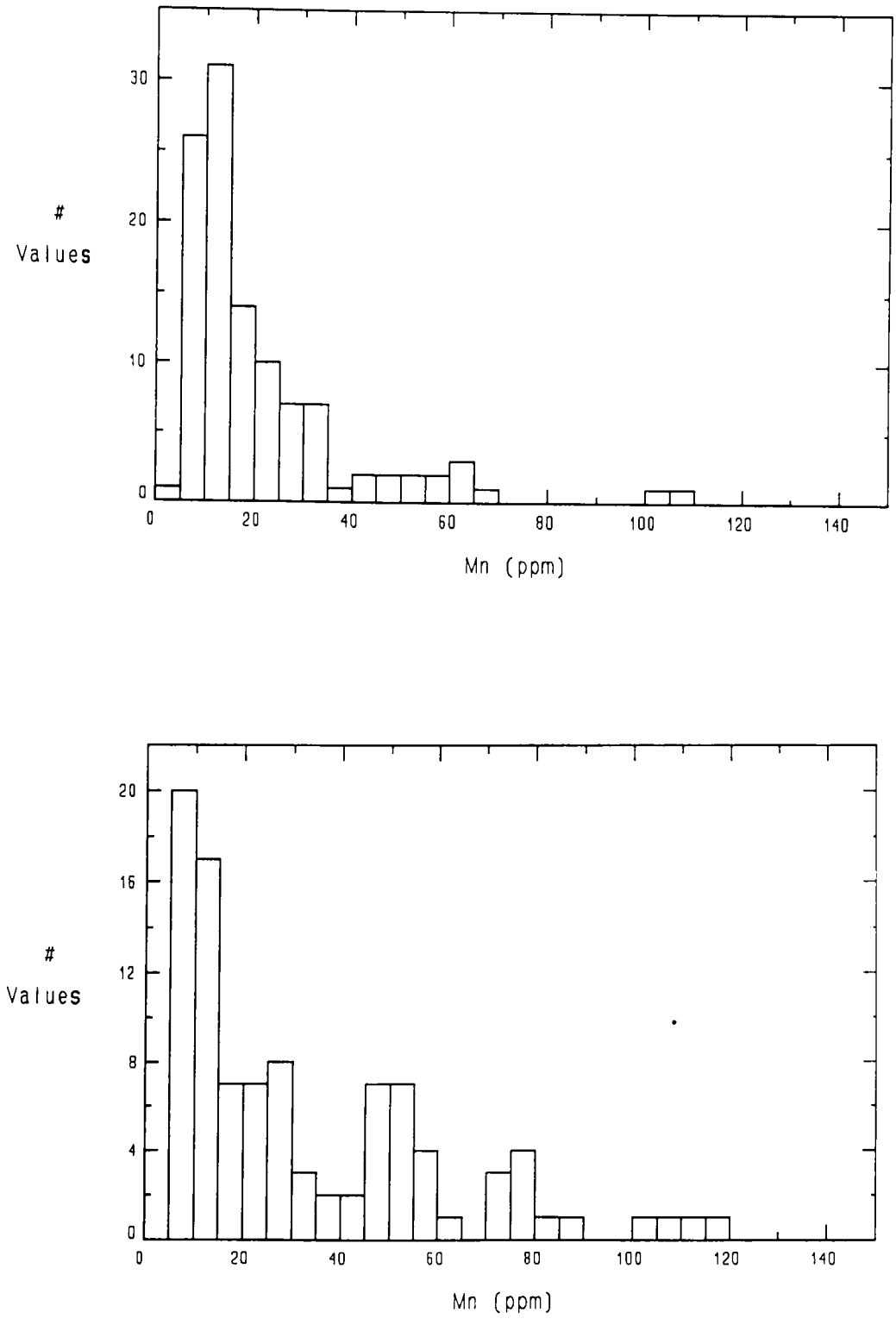

Figure 3.3 Comparison between Mn data for Dorset (top) and Yorkshire (bottom) belemnites.

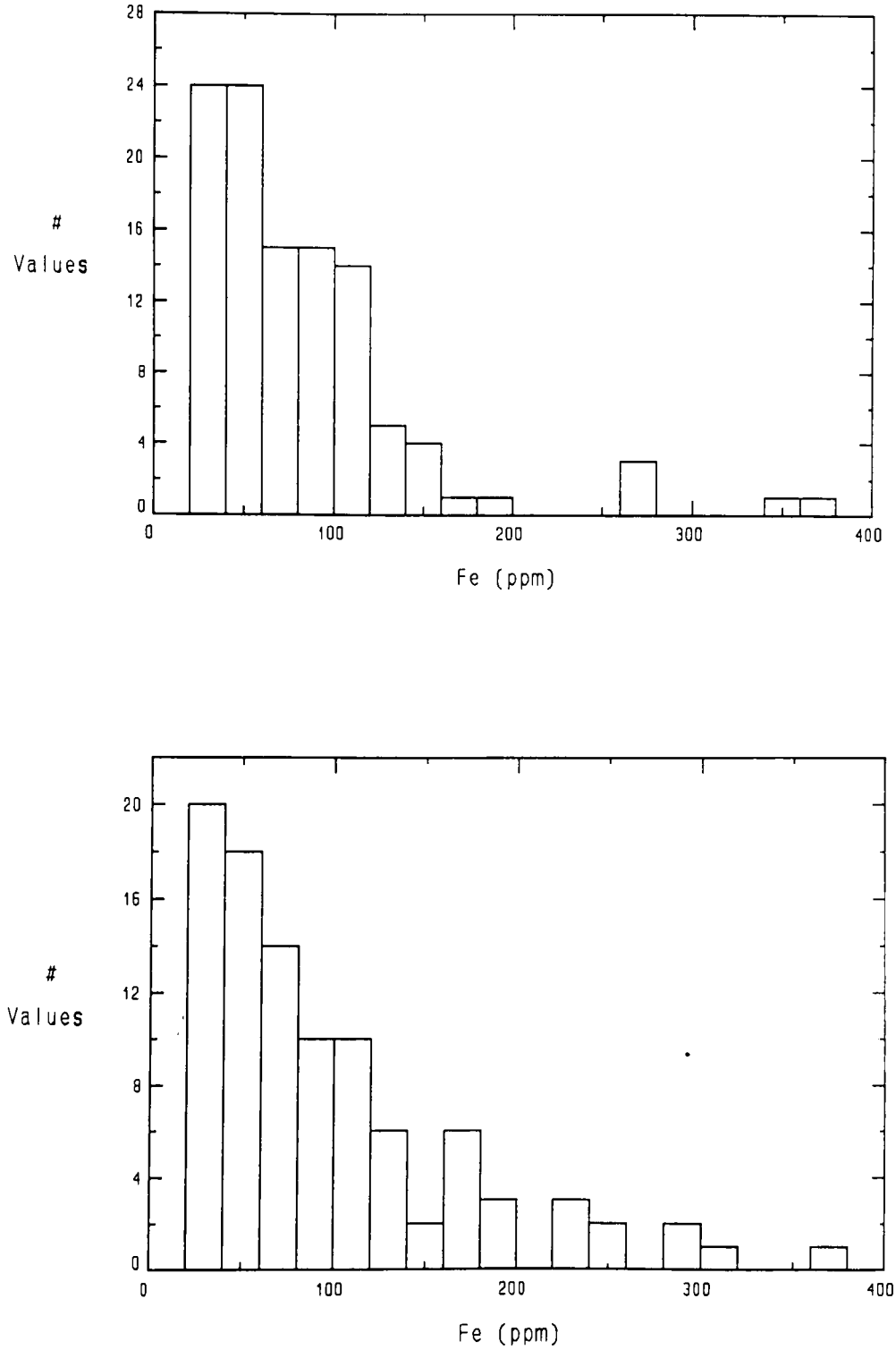

Figure 3.4 Comparison between Fe data for Dorset (top) and Yorkshire (bottom) belemnites.

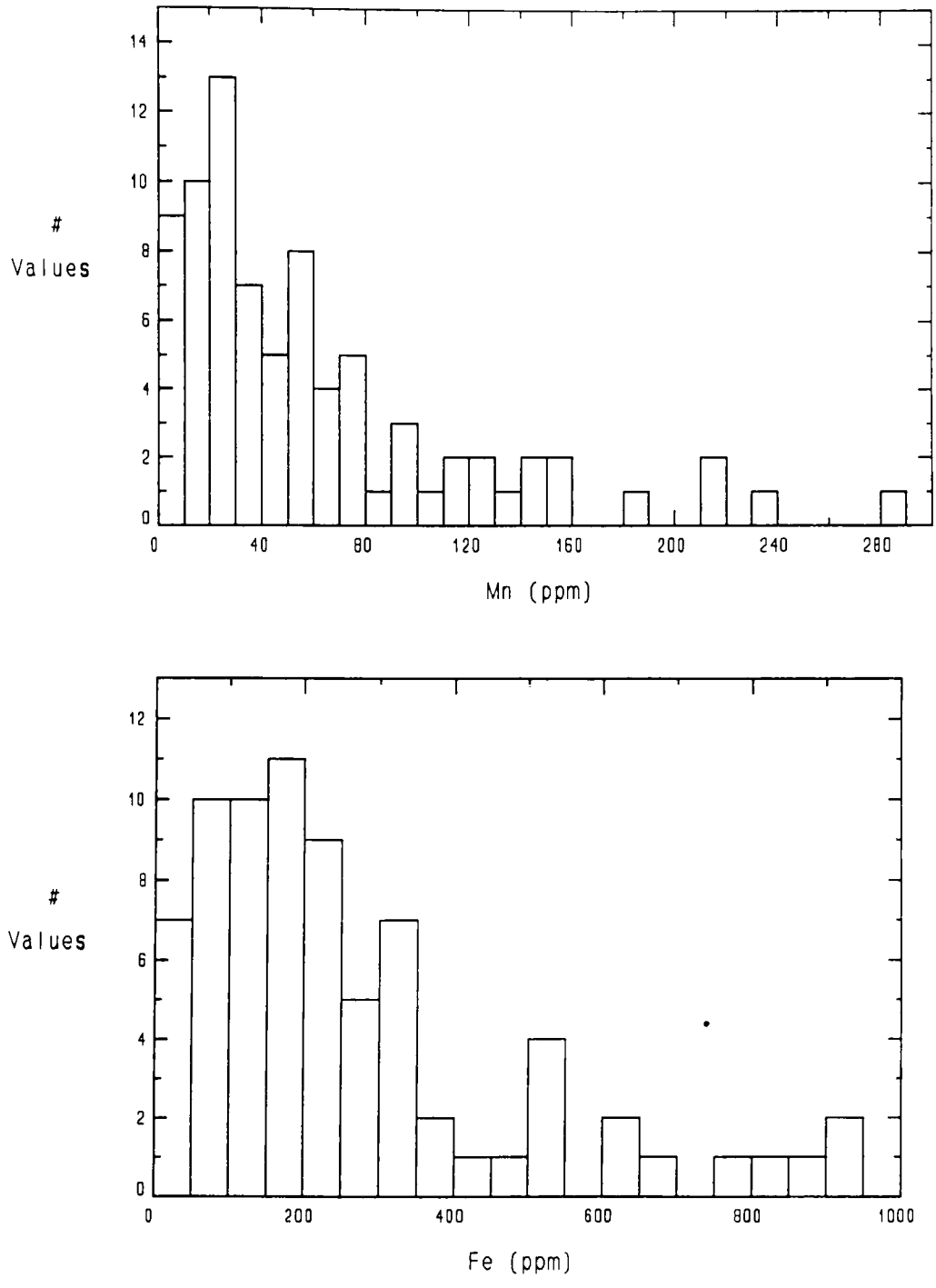

Figure 3.5 Mn (top) and Fe (bottom) data for all oysters.

Cross-plots of the Mn and Fe data (Fig. 3.6) show a general broad linear relationship for the bulk of the belemnite and oyster data. However, a significant number of particularly oyster samples show elevated Fe concentrations without correspondingly higher Mn concentrations. In part this is an artefact of the dissolution of the heavily pyritised oysters from the Upper Kimmeridgian of Dorset. These samples generally show quite low levels of Mn, but, because it was impossible to separate pyrite from the oyster calcite, significant quantities of partially decomposed pyrite undoubtedly dissolved during storage of the Mn and Fe sample aliquots. The elimination of these clear exceptions still leaves a number of samples with somewhat elevated Mn concentrations (> 40 ppm) that plots well to the right of the broadly linear relationship defined by the bulk of the data.

The prominent peak in the numbers of belemnites containing 5 - 15 ppm Mn (Figs. 3.2 3.3) indicates that this range of values characterises relatively unaltered low-Mg belemnite calcite. The Fe histograms suggest a "best-estimate" range of 25 - 60 ppm for primary belemnite calcite, although concentrations up to 120 ppm are allowed by the data. Similarly, the oyster data suggest primary Mn levels between 5 and 30 ppm while Fe may range from 25 up to as high as 250 ppm. This range of values is compatible with the data of Milliman (1974), who reports on the order of 9 - 13 ppm Mn and 140 - 200 ppm Fe for LMC planktonic foraminifera and 11 78 ppm Mn and 12 170 ppm Fe for a variety of benthonic LMC macrofauna, and with the conclusions of Veizer (1974) regarding the primary composition of German belemnites.

Maxima at low Mn and Fe concentrations followed by a rapidly decreasing number of samples with higher levels of Mn and Fe is consistent with the bulk of individuals retaining largely primary calcite while a minority contains variable but significant amounts of Mn- and Fe-rich diagenetic calcite. As discussed above, the precipitation of such calcite is expected from most major diagenetic environments associated with mudrocks. It is, however, also possible to interpret the elevated concentrations of these redox-sensitive

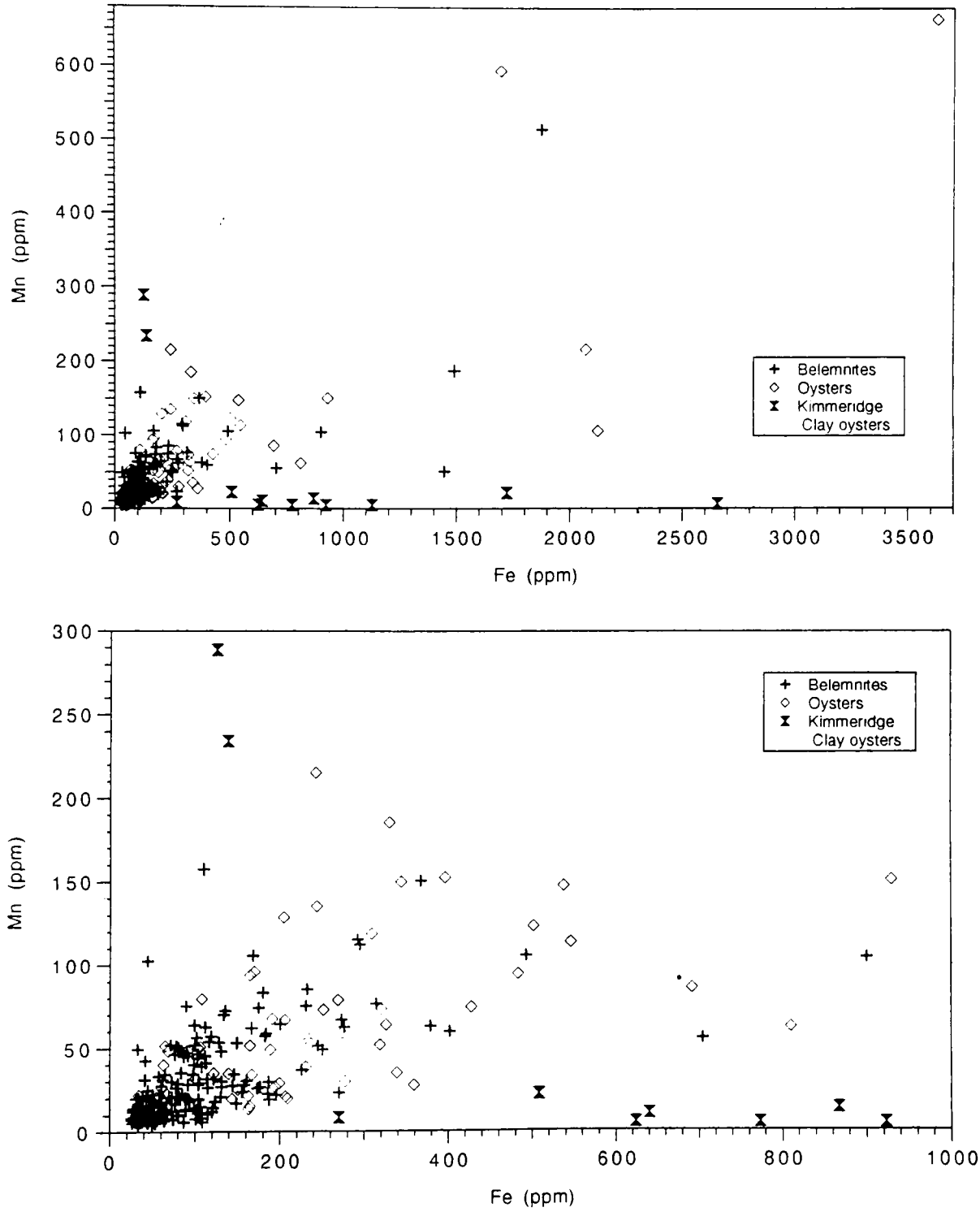

Figure 3.6 Cross-plots showing the relationship between Mn and Fe concentrations in all samples (top) and in the samples containing less than 300 ppm Mn and 1000 ppm Fe (bottom).

elements as a primary signal indicative of low-oxygen palaeo-seawaters (e.g., Morrison and Brand, 1988; Morrison and Veizer, 1990). In order to distinguish between these two interpretations it is necessary to highlight any temporal and regional patterns that might characterise a palaeo-seawater signal by plotting the whole Mn and Fe data set as a function of time and place. Because elevated Mn and Fe concentrations are expected from both diagenesis and low-oxygen seawaters, the apparent Mn maxima in the Sinemurian-Pliensbachian and Oxfordian cannot be uniquely interpreted. Because the minimum Mn and Fe concentrations at any given time and place probably represent the best-preserved material available, it is these minimum Mn and Fe levels that would be best interpreted in terms of a regional palaeoceanographic signal.

From Figure 3.7 it is clear that throughout the time interval studied there are fairly constant minimum baselines for Mn at about 5 - 10 ppm and Fe at about 25 ppm. The Oxfordian, Aptian, and Yorkshire Pliensbachian contain significant numbers of fossils containing elevated metal concentrations and might therefore be interpreted as times characterised by low palaeo-oxygen levels. However, a consideration of the data of Figure 3.7 in their sedimentological and palaeotological context leads to a firm rejection of such a hypothesis. For example, a text-book example of sediments deposited under low-oxygen conditions is provided by the organic-rich clays and markedly reduced benthonic macrofaunal diversity of the Kimmeridge Clay Formation (Oschmann, 1988; Wignall, 1990). Even if the oysters of the Kimmeridge Clay had lived during a moment in which the bottom waters were temporarily relatively oxidising, it is likely that the porewaters escaping from the compacting sediments would have been relatively Mn-rich and therefore would have kept the oysters bathed in Mn-rich waters. However, despite this strong evidence for low-oxygen conditions, the Kimmeridge Clay oysters show Mn levels that are as low or lower than the minimum levels found in belemnites (Fig. 3.7).

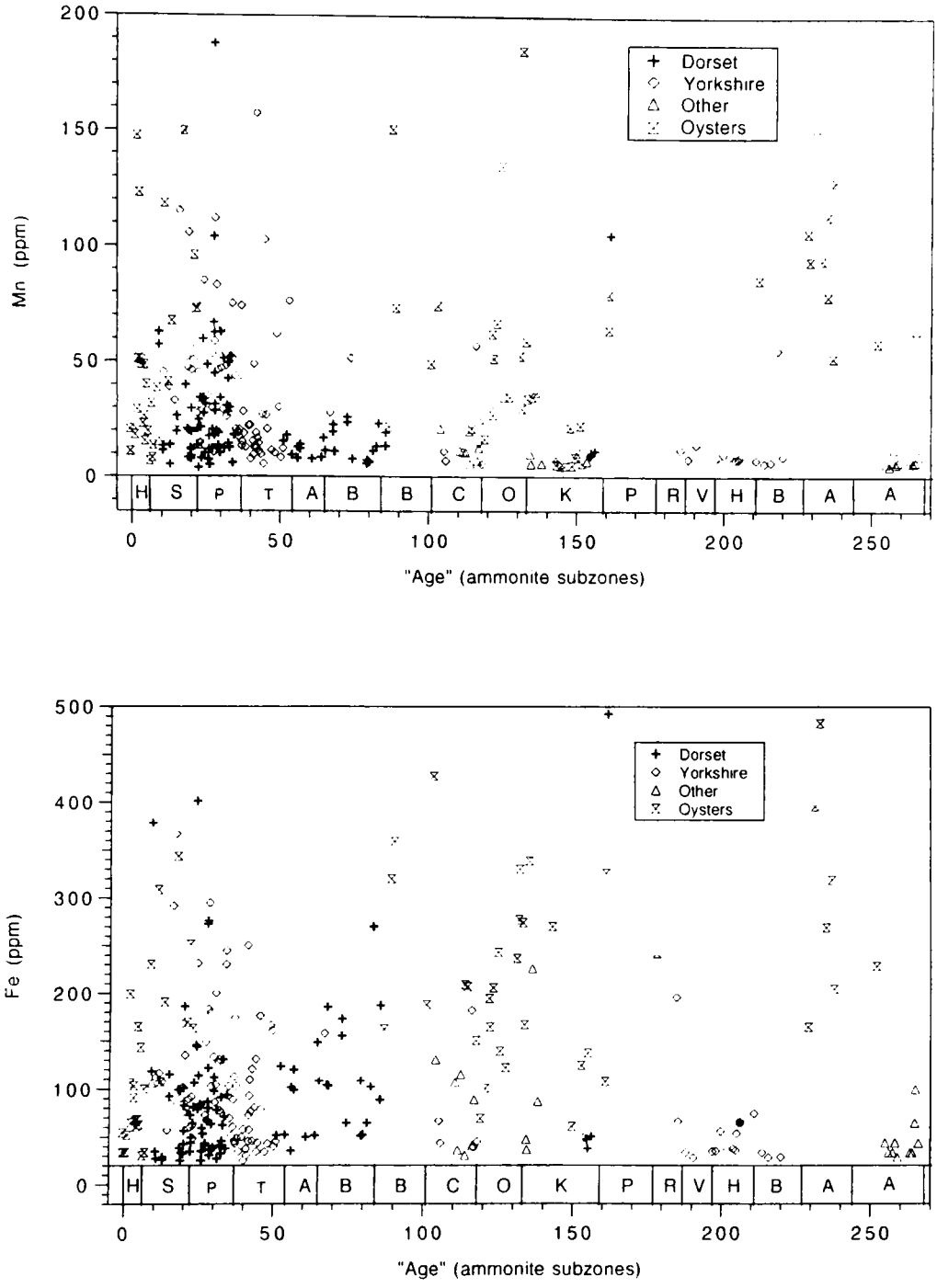

Figure 3.7 Mn (top) and Fe (bottom) data plotted as a function of "age" measured in subzone units. Belemnites from different localities (Dorset, Yorkshire, Other) and oysters are differentiated. Letters refer to stages of the Jurassic (Hettangian, Sinemurian, Pliensbachian, Toarcian, Aalenian, Bajocian, Bathonian, Callovian, Oxfordian, Kimmeridgian, Portlandian) and Lower Cretaceous (Ryazanian, Valanginian, Hauterivian, Barremian, Aptian, Albian).

By contrast, the majority of Oxfordian and Aptian oysters collected in this study lived on silty sands and oolites deposited in relatively shallow waters that probably were well-oxygenated. The concentration of dissolved Mn and Fe in and around these sediments as they were deposited should therefore have been greatly reduced as compared to the Kimmeridge Clay. Nevertheless, the Oxfordian and Aptian oysters show highly elevated minimum Mn and Fe concentrations. Because the minimum Mn and Fe levels do not correspond to their expected trends based on sedimentological and palaeontological indicators of palaeo-seawater oxygen levels, it is concluded that elevated Mn and Fe concentrations are a result of diagenesis. Thus it appears that the oysters of the oolitic/sandy sediments of the Oxfordian and Aptian are generally more altered than those oysters collected from the organic-rich mudstones of the Kimmeridge Clay. This is consistent with the higher expected permeabilities of the coarser shallow-water sediments.

An expanded view of the Lower Jurassic (Fig. 3.8) shows that whereas most Mn and Fe data define generally low baselines consistent with the rest of the data set, the Yorkshire Sinemurian and Pliensbachian data show consistently higher minimum values. It is not until the Toarcian that these baselines drop down to the normal levels. The remarkable similarity and consistency of the Mn and Fe signals seem to suggest some sort of primary variation. Again, these data provide no support for an interpretation involving palaeo-oxygen levels. During the lower Toarcian, globally extensive anoxic waters allowed the deposition of black shales in Yorkshire and around the world (Jenkyns, 1988). Elevated Mn concentrations in the water column are attested to by the synchronous deposition of regionally extensive, economically viable Mn-carbonates in Central Europe (Jenkyns *et al.*, 1991). Although the present writer considers it highly unlikely that the free-swimming, predatory belemnites would venture into low-oxygen waters, it is the contention of Morrison and Veizer (1990) that they did in fact inhabit low-oxygen

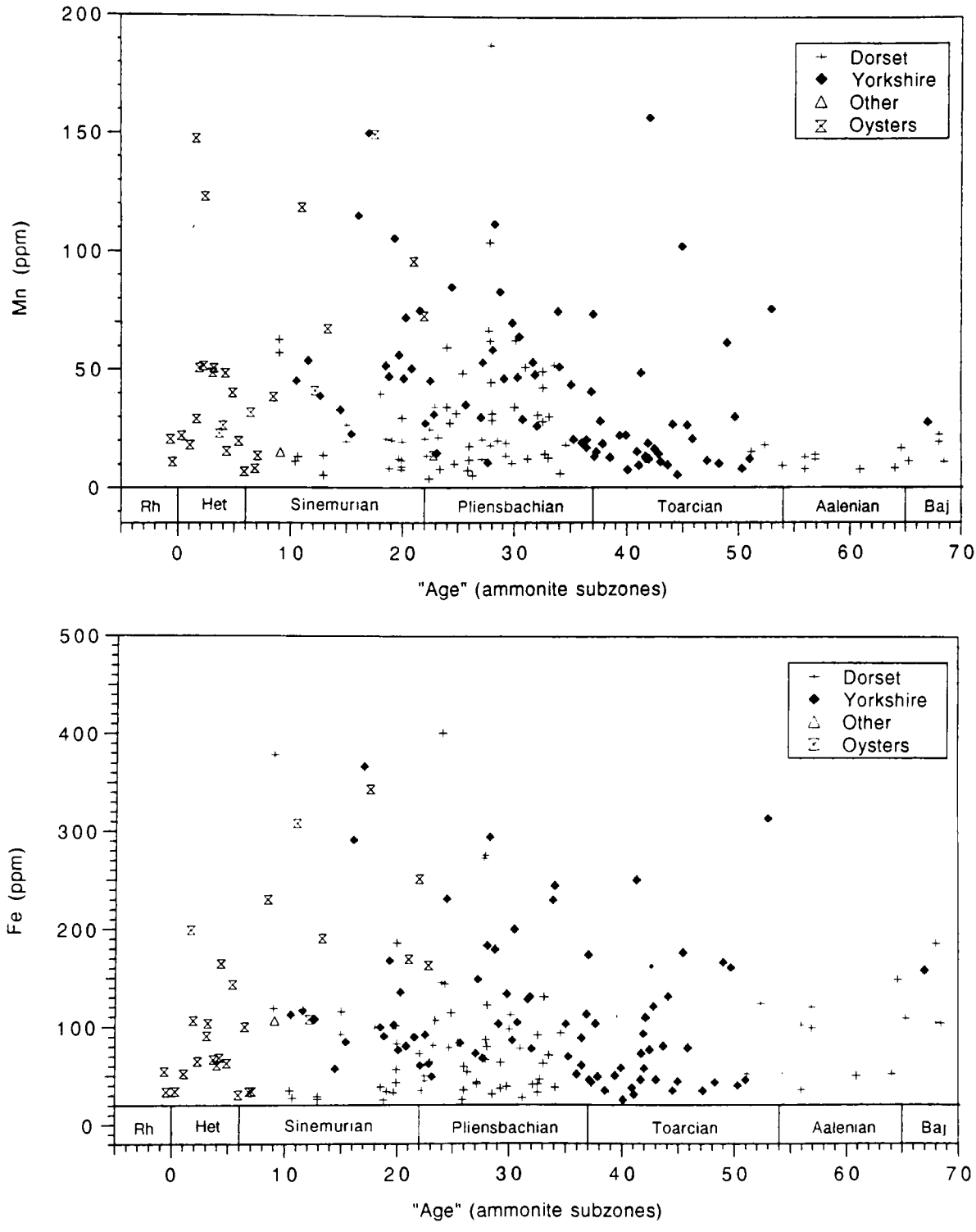

Figure 3.8 Mn (top) and Fe (bottom) data plotted as a function of "age" through the Lower Jurassic. Belemnites from different localities and oysters are differentiated.

(Mn-rich), even brackish waters. If belemnites had been living in the low-oxygen, Mn-rich waters of the Yorkshire lower Toarcian, it is possible that they would have recorded these elevated Mn levels. Instead, the data of the Yorkshire Toarcian mark this time as the return to *low* Mn concentrations in belemnites. Thus it appears that neither belemnites nor oysters record the oxygen levels of palaeoseawater and diagenesis therefore remains the simplest interpretation of elevated Mn and Fe concentrations in calcitic macrofossils.

The explanation of the consistently higher *minimum* Mn and Fe concentrations in the Yorkshire Sinemurian and Pliensbachian is not clear. It may have to do with these sediments having been deposited nearer to the North Sea deltaic systems (Pienkowski, 1991; Richards, 1991) as compared to Dorset. The rivers feeding these deltas with their loads of freshly weathered sediments could act as a source of Mn and Fe oxyhydroxides to local seawater (Carroll, 1958; Porrenga, 1967). Higher levels of Mn and Fe could be incorporated into a belemnite rostrum either because belemnites living near such a source could consume these oxyhydroxides simply by living in these waters, or because higher levels of Mn and Fe oxyhydroxides in sediments could yield consistently higher levels of pore water Mn^{2+} and Fe^{2+} that could then find their way into the rostrum during the earliest stages of fossilisation. A third possibility is that the whole population of fossil material incorporated a remarkably consistent proportion of diagenetic calcite during the relatively intense diagenetic/low-grade hydrothermal event centred in the Sinemurian/Pliensbachian strata of Robin Hood's Bay (Hemingway and Riddler, 1982).

3.4 Results for $\partial^{13}C$ and $\partial^{18}O$

The belemnite carbon isotope data (Fig. 3.9 a) show a bimodal distribution due to the superpositioning of the Dorset data, which show a main peak at about +0.5‰ and a secondary peak at about +2‰, over the Yorkshire data, which show a single, well-developed peak at +2‰. The oyster $\partial^{13}C$ data (Fig. 3.9 b) are on average shifted about 1‰ heavier than the belemnite data, with a peak at about 3‰. The Aptian oysters

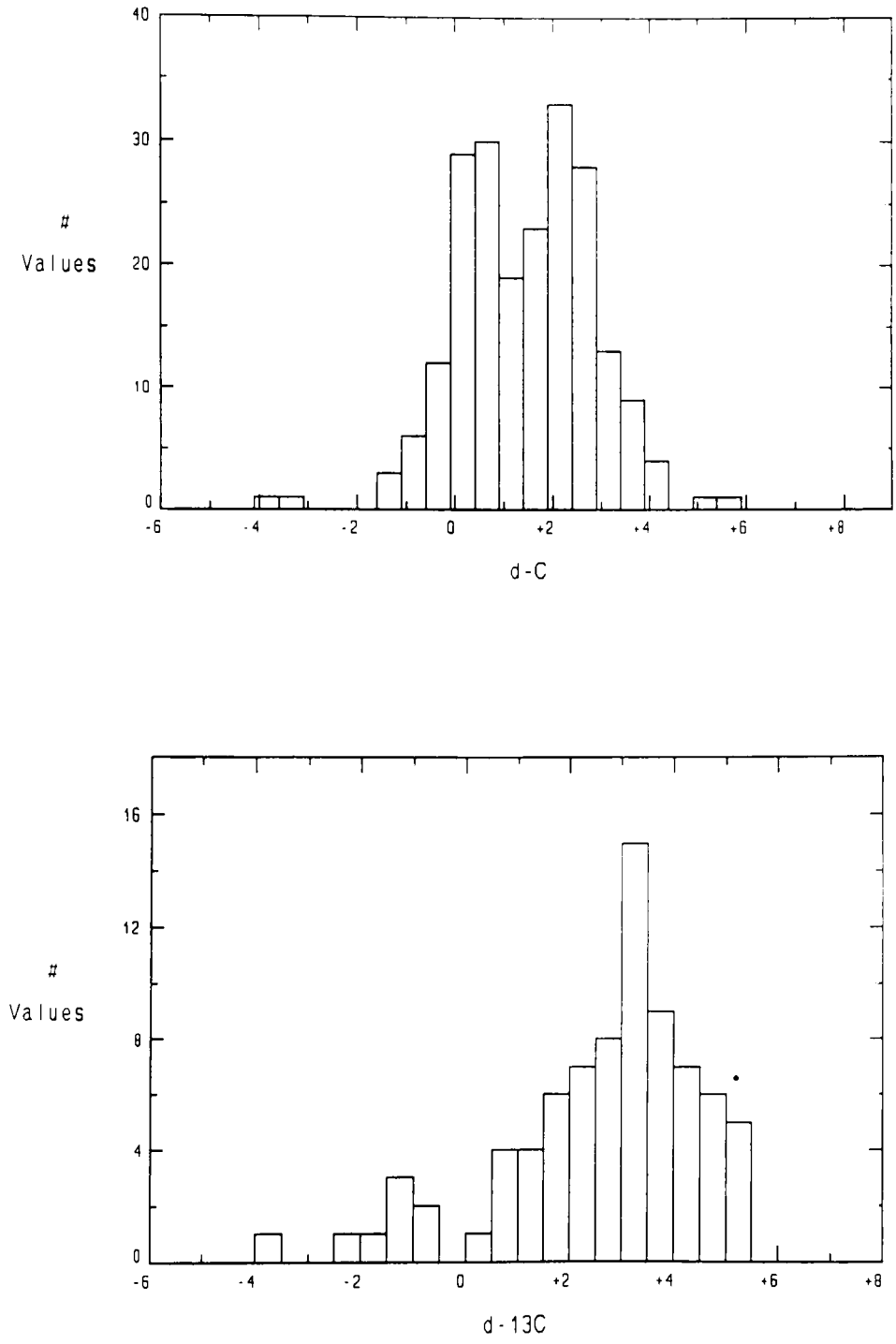

Figure 3.9 Histograms of $\partial^{13}C$ data for belemnites (top) and oysters (bottom).

from the Isle of Wight contribute significantly to the > 3.5‰ data. In both data sets the distributions centre around plausible marine values with few specimens yielding extreme values. One data point (-11‰) is omitted from the oyster diagram.

The belemnite oxygen isotope data are again bimodal (Fig. 3.10 a), but in this case it is the Yorkshire data set that has yielded the secondary hump at -3.5‰. Otherwise the data sets form a strong maximum centred at about -1‰. The oyster data are again offset relative to the belemnite data (Fig. 3.10 b), but this time the oyster data are about 1‰ *lighter* than the belemnite data. The maximum is centred near -2‰. Again, both data sets are dominated by plausible marine values with few points deviating towards extreme values.

Because the bulk of the stable isotope data are closely clustered near normal marine values, it turns out that $\partial^{13}C$ and $\partial^{18}O$ are not very useful for highlighting samples that have suffered alteration of their primary Sr-isotope ratios. Thus a full discussion of the stable isotope data, along with a more detailed consideration of belemnite and oyster diagenesis, will be left until Chapter 5.

3.5 Aragonite Samples

Three samples whose original primary mineralogy was aragonite were sampled to determine whether or not aragonite is likely to be useful in Sr-isotope stratigraphy. In principle, the very high concentrations of Sr found in aragonite should effectively dilute any Sr-isotope signal inherited during diagenesis. During small scale dissolution/reprecipitation, for example, the diagenetic pore waters should be swamped with primary marine Sr as the fossil is converted from aragonite containing some 1000 to 5000 ppm Sr (Milliman, 1974) to an inorganically precipitated LMC containing a few hundred ppm Sr (Veizer, 1983). Of the three samples studied, one, BL38, is a bivalve that undoubtedly had transformed to diagenetic LMC. Unfortunately the sample was too small to obtain Mn and Fe data. The carbon and oxygen isotope data are consistent with minor

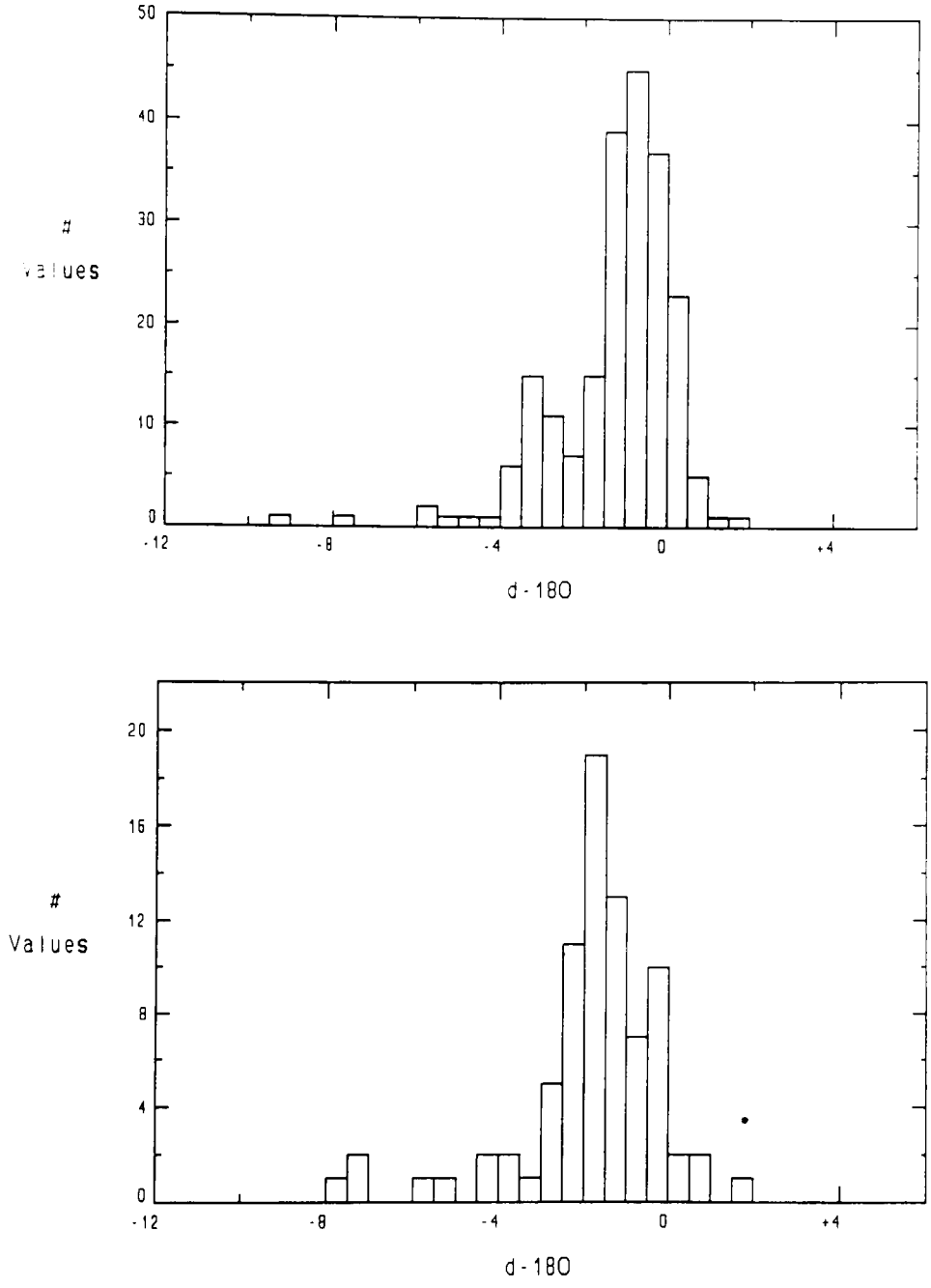

Figure 3.10 Histograms of $\partial^{18}O$ data for belemnites (top) and oysters (bottom).

diagenesis (Table 2.1), but are not remarkably extreme. The other two samples are what appear to be very well-preserved ammonite aragonite collected from organic-rich shales. These samples have retained their nacreous lustre and under the SEM show the tabular structure that characterises unaltered aragonite (e.g., Brand, 1991). Moreover, there is no trace element or stable isotope evidence to suggest diagenetic alteration of either sample. Sample "DonBay 246" appears to be generally better preserved under the SEM, although the sample is cut by diagenetic crack-filling calcites that formed when the ammonite was compacted. Every effort was made to avoid this diagenetic calcite during sample preparation, and the Mn and Fe data indicate no great contribution from such calcite (Table 2.3). An X-ray diffraction (XRD) trace, however, proves that secondary calcite can make up a significant proportion of the sample (Fig. 3.11). Sample "Pearce's Pit 2" appears to be better preserved under a hand lens, although under the SEM the tabular structure is less clearly defined. An XRD trace shows no evidence of calcite (Fig. 3.11). In summary, the samples range between "altered" (BL38), "partially altered" (DonBay 246), and, at least by Brand's (1991) criteria, "unaltered" (Pearce's Pit 2). As will be shown below, all three aragonite samples plot well above their expected values on the Sr-isotope curve and thus appear to be altered.

3.6 Using Trace Elements to Detect Diagenesis of Sr Isotopes

Having established that high calcite Fe and Mn concentrations are most probably good indicators of the presence of diagenetic calcite, the approach adopted here is to empirically determine what levels of Fe and Mn usefully discriminate between the diagenetic outliers and the main body of the Sr-isotope data. This approach is clearly only semi-quantitative. Although we can measure the present-day composition of the fossil material, the composition of the diagenetic fluids is unknown, and it is easy to imagine situations in which diagenetic calcites precipitate from either a low-Fe fluid containing quite radiogenic Sr or an Fe-rich fluid containing nearly marine Sr. Because the Rhaetian to

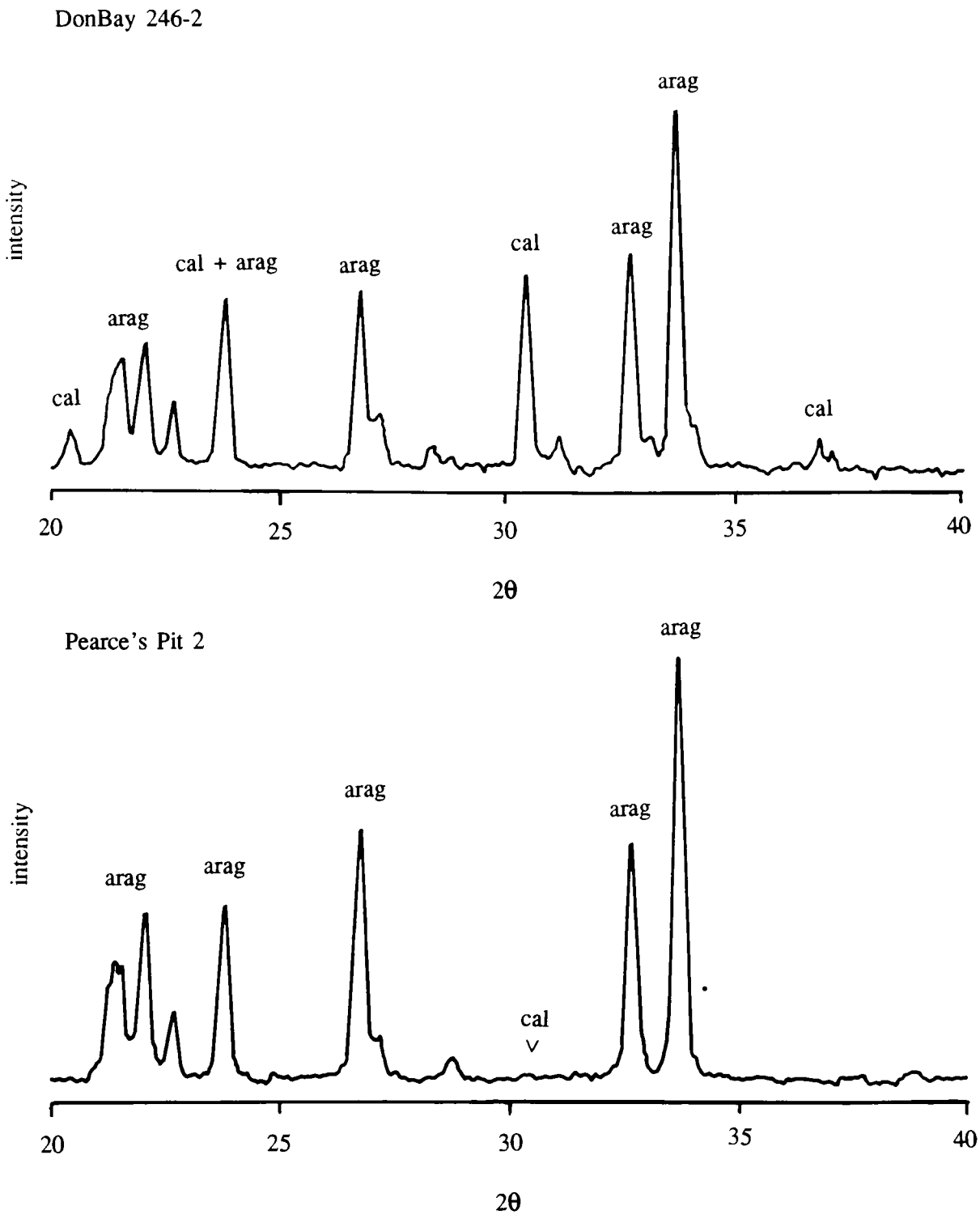

Figure 3.11 Two XRD traces showing a significant fraction of calcite contaminating the aragonite of sample "DonBay 246" (top) and showing no trace of calcite in the aragonite of sample "Pearce's Pit 2" (bottom).

Bajocian interval has exceptionally dense data cover, this interval is considered first before moving on to the sparser data of the rest of the Jurassic and Lower Cretaceous. Although much of the Lower Jurassic comprises a relatively homogeneous collection of mudstones, marls, and impure limestones, some lithological diversity is introduced by the silty sandstones of the upper Pliensbachian and upper Toarcian and the silty oolites of the Aalenian and Bajocian.

In Figure 3.12a the Sr-isotope data are divided into eight categories: belemnites containing less than 150 ppm Fe, between 150 and 200 ppm Fe, and more than 200 ppm Fe; oysters containing less than 150 ppm Fe, between 150 and 200 ppm Fe, between 200 and 300 ppm Fe, and more than 300 ppm Fe; and samples whose primary mineralogy is aragonite. Both aragonite samples (BL38 = "altered" and DonBay 246 = "partially altered") and most samples containing more than 200 ppm Fe plot significantly above the main trend of the data. Taking the limit down to 150 ppm Fe includes all points conspicuously above the curve. Closer inspection of the data reveals a number of minor deviations that are not accounted for by the greater than 150 ppm limit. These may reflect real variations in the Sr-isotope curve or may be due to analytical error, alteration by Fe-poor fluids, or, particularly in the case of the Sinemurian data that scatter below the curve, mixing of samples of different ages on hiatus surfaces (see Chapter 4). Whereas there appears to be more scatter than can be accounted for by Fe-indicated diagenesis in the oyster-dominated Hettangian, it generally appears that oysters have the same useful Fe cut-off as belemnites. In general, therefore, Fe seems to be a useful indicator of diagenesis as it affects Sr isotopes in calcite. Of the two aragonite samples, it is curious that the clearly altered bivalve has plotted quite close to the rest of the data while the better-preserved ammonite sample, which is still largely aragonite, plots well off of the curve.

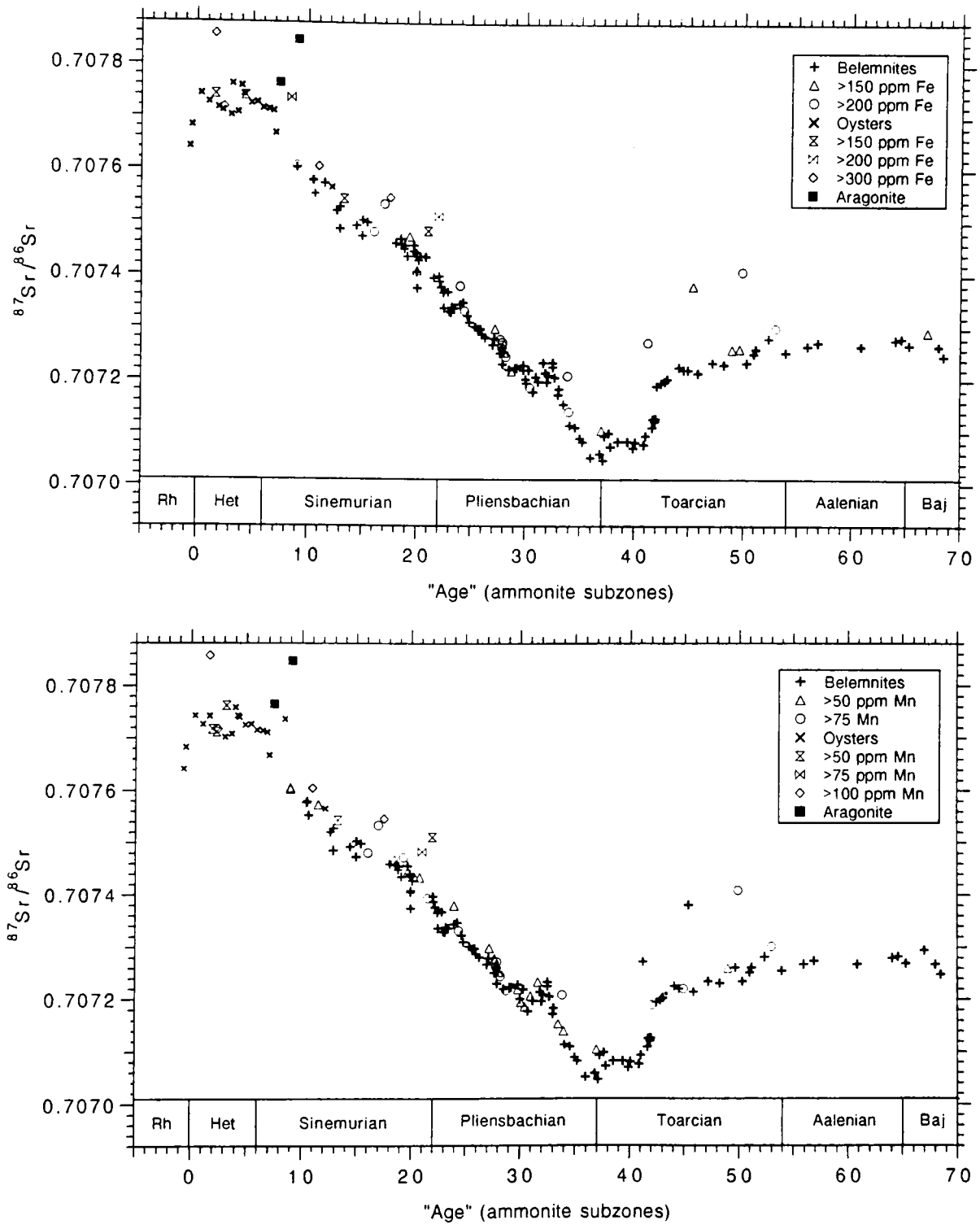

Figure 3.12 The Lower Jurassic Sr-isotope curve (as a function of subzone "age") with data points differentiated according to their fossil type and their Fe (top) or Mn (bottom) concentrations. All data in this and future graphs are normalised to Eimer and Amend = 0.708000.

For a sample of unknown age, it is helpful to have some indication of the probability of it preserving the primary $^{87}Sr/^{86}Sr$ ratio necessary to assign a correct stratigraphic age. Of the samples containing more than 200 ppm Fe, 12/21 (56%) significantly deviate from the curve. Of the 9 that do not deviate, a large proportion (5/9) come from a narrow interval near the highly condensed, pyritiferous Belemnite Bed (Lang's Bed 120c). Eliminating these samples as anomalous yields a perhaps more representative discrimination efficiency of 12/16 (75%). Of the samples containing between 150 and 200 ppm Fe, a similar percentage (10/14 = 71%) plot significantly above the curve. Thus, the results of this study suggest that if a belemnite or oyster of unknown age has less than 150 ppm Fe, it almost certainly retains a Sr-isotope signal not resolvably different from the primary value. If the Fe levels exceed 150 ppm, however, diagenetic alteration of the Sr-isotope signal is quite likely and great care must be taken when attempting to constrain the age of a sample.

In a similar fashion, the Sr-isotope data of Figure 3.12b are divided into eight categories based on their Mn contents: belemnites containing less than 50 ppm Mn, between 50 and 75 ppm Mn, and more than 75 ppm Mn; oysters containing less than 50 ppm Mn, between 50 and 75 ppm Mn, between 75 and 100 ppm Mn, and more than 100 ppm Mn; and samples made up of aragonite. In general Mn is not as efficient as Fe at highlighting diagenetically altered samples. Of the samples containing more than 75 ppm Mn, 10/19 (53%) deviate significantly from the main Sr-isotope curve. Lowering the maximum allowable Mn content to 50 ppm highlights a few more deviations, but not all, and results in the highlighting of a large number of samples that do not deviate from the curve (8 altered out of 25 highlighted = 32%). Lowering the Mn limit further makes identification of diagenesis still less efficient. There are 3 "fliers" that do not contain more than 50 ppm Mn; these do nevertheless show somewhat elevated Mn levels of 27, 38, and 49 ppm. In conclusion, Mn is not as effective as Fe at predicting which samples are likely

to have resolvably altered $^{87}Sr/^{86}Sr$ ratios. However, Mn may still be useful in some cases in that low Mn concentrations (<< 50 ppm) indicate a strong probability of a sample retaining its primary Sr-isotope signal.

It is worth noting that the good preservation of the material collected from the upper Toarcian sands and Aalenian-Bajocian oolites provides little opportunity to test the effectiveness of Fe and Mn in these sediments. In the upper Toarcian sands there is one sample (BWS 82) with elevated Fe concentrations, and it plots above the main trend of the data. The three preceding samples (BridportSnds6, DnClCly1 and BWS 81) also plot somewhat above the flat Toarcian-Aalenian portion of the curve, and it is unclear whether they define a small feature in the late Toarcian Sr-isotope curve or have suffered a mild dose of oxic diagenesis.

In contrast to the relatively homogeneous Lower Jurassic, the rest of the Jurassic system and the overlying Lower Cretaceous is lithologically quite diverse, consisting of oolites, siltstones, sandstones, condensed phosphatic mudstones, organic-rich mudstones, and rather weathered mudstones. In addition, oysters are important over many intervals. From Figures 3.13a,b it is immediately apparent that several intervals are characterised by more scatter than can easily be accounted for by Fe- or Mn-indicated diagenesis. Although the scatter in the belemnite data of the Albian seems a bit excessive, the worst belemnite scatter is through the Callovian, Oxfordian, and lower Kimmeridgian. These data, compiled from localities in Dorset, Oxfordshire, Yorkshire, and Scotland, show no Fe or Mn evidence for diagenesis and yet show such a high degree of scatter as to make their interpretation as a primary seawater signal extremely unlikely. The reasons for this scatter are not clear. The three oldest Callovian belemnite samples come from sandstones and thus may have suffered diagenesis under oxidising conditions that prohibited mobilisation of dissolved Fe^{2+}. The two belemnite samples with the lowest $^{87}Sr/^{86}Sr$ ratios in the upper Callovian and lowest Kimmeridgian come from the Isle of Skye and thus may have

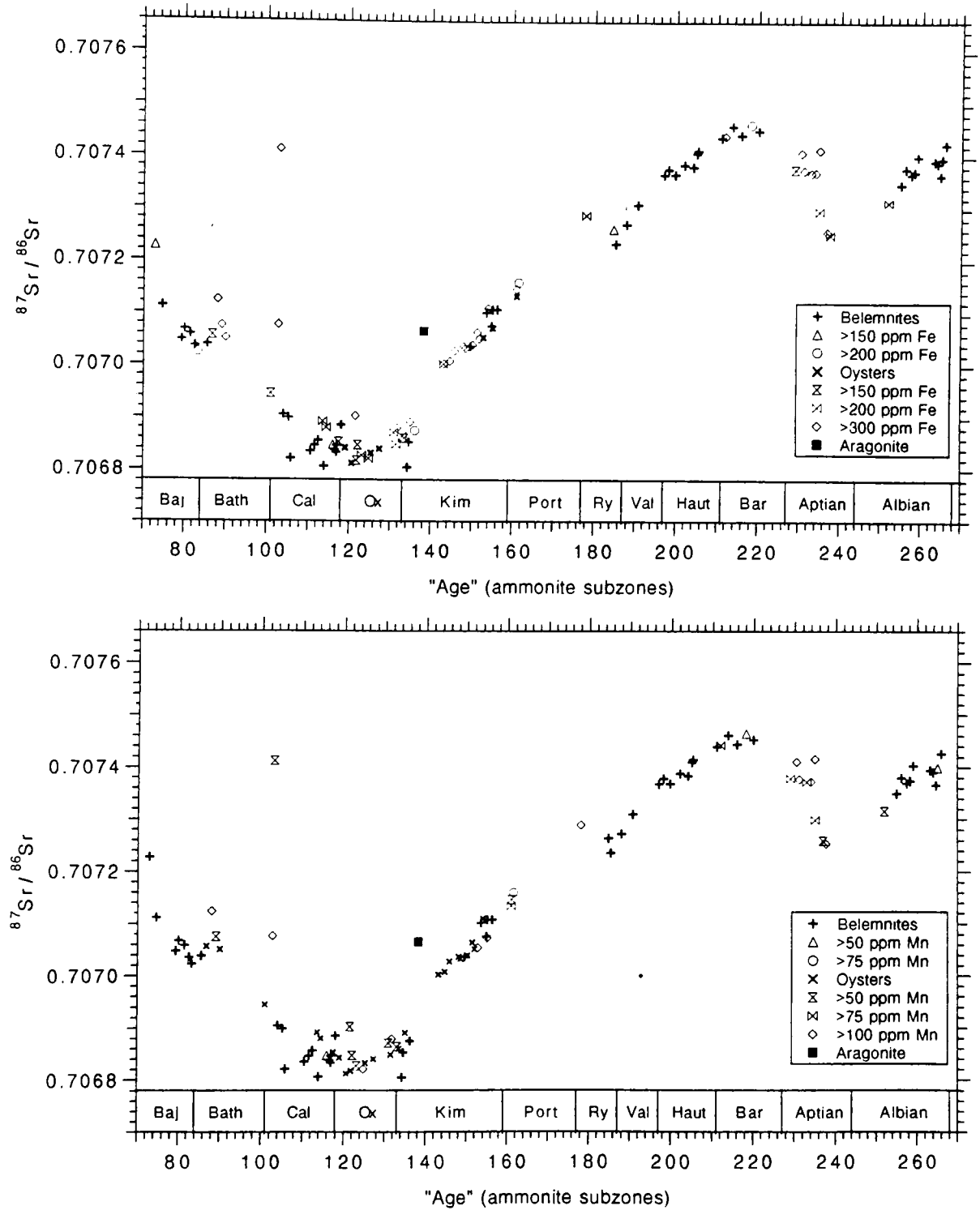

Figure 3.13 The Middle Jurassic to Lower Cretaceous Sr-isotope curve (as a function of subzone "age") with data points differentiated according to their fossil type and their Fe (top) or Mn (bottom) concentrations.

suffered unusual diagenesis associated with the emplacement of the Tertiary flood basalts. The Bathonian to Callovian interval clearly requires more work and will be discussed in more detail in Chapter 4. The belemnite data of the Bajocian, lowest Bathonian, upper Kimmeridgian, and Ryazanian through Barremian behave much more consistently but because most samples appear to be well-preserved, they provide little opportunity to test further the applicability of Fe and Mn as tracers of Sr-isotope diagenesis in belemnites.

Much of the data of the Bathonian, Callovian, Oxfordian, Kimmeridgian, Portlandian, and Aptian come from oysters. While the few oysters containing less than 150 ppm Fe do show Sr-isotope data consistent with adjacent trends, oysters with 150 - 200 ppm Fe and 200 - 300 ppm Fe show no systematic deviations from the main trend of the data. Clear deviations from the Sr-isotope curve (Bathonian, Oxfordian) occur only when oyster Fe concentrations exceed 300 ppm, although it must be noted that similarly Fe-rich oysters from near the Oxfordian/Kimmeridgian boundary and in the Portlandian, Barremian, and Aptian still manage to plot along with the rest of the data. As mentioned earlier, the elevated Fe concentrations of the oysters of the Upper Kimmeridgian are attributable to pyrite dissolution during sample storage.

The low Mn concentrations (< 50 ppm) found in many of the oysters is more consistent with the generally good preservation indicated by the self-consistent Sr-isotope data (Fig. 3.13b). For example, the Mn concentrations in oysters from the Bathonian, Oxfordian, and lower Kimmeridgian are frequently less than 50 ppm (generally ranging between 20 and 40 ppm Mn) and the Sr-isotope data seem to define a fairly regular trend, particularly in the Oxfordian. In the Upper Kimmeridgian the very low Mn concentrations suggest a high degree of preservation consistent with the fine Sr-isotope data. The greatest anomaly with respect to using Fe and Mn as indicators of diagenesis is in the Aptian. The Aptian oysters show very high concentrations of both Fe and Mn and thus indicate relatively intense diagenesis in the permeable silty sands found on the Isle of Wight.

However, these samples nevertheless define a Sr-isotope curve that is both self-consistent and consistent with the minimum limits set by the larger data set of Koepnick *et al.* (1985, 1990; see Fig. 3.1).

Fe appears to be less effective in detecting diagenesis in oysters. Many of the Oxfordian and Aptian oysters come from sediments dominated by terrigenous siliciclastics such that diagenesis should clearly raise the Sr-isotope ratios. To combine high Fe concentrations with relatively unaltered Sr-isotope ratios requires either alteration by exceptionally Fe-rich but Sr-poor, nonradiogenic diagenetic fluids or the incorporation of Fe-rich minerals (oxides, carbonates) on the surfaces of primary calcite crystals in oysters. (The possibility of a contribution from detrital silicates incorporated into the oyster shells during growth is eliminated because if a dissolved sample showed any non-pyritic insoluble residue, it was discarded and another portion of the fossil was selected for dissolution.) Because most of the oysters sampled in the Bathonian, Callovian, Oxfordian, Portlandian, Barremian, Aptian, and Albian show foliated calcite shell structures, it is possible that Fe-bearing fluids have migrated between these different shell layers by capillary action. An increase in alkalinity caused by the dissolution of minute quantities of oyster calcite may have facilitated the precipitation of Fe-bearing minerals on the surfaces of the oyster calcite. In this way the presence or absence of Fe-bearing diagenetic calcites could be masked by the dissolution of surfacial Fe-rich minerals released during sample dissolution. Because the *Gryphaea* oysters commonly found in the Lower Jurassic have more massive shell structures, such surface adsorption is less likely and this could explain why Fe remains an effective indicator of diagenesis in Lower Jurassic oysters. Future work will have to develop more careful sample preparation techniques or different tracers of diagenetic calcites so as to avoid the possibility of surfacial Fe contamination in oysters.

3.7 Summary

Primary belemnite and oyster calcite is characterised by relatively low

concentrations of Mn and Fe. Secondary calcites from many but not all diagenetic settings should generally contain significantly higher levels of Mn and Fe. Thus, monitoring Fe and Mn concentrations in belemnites and oysters potentially provides independent criteria for determining which samples are likely to yield diagenetically altered $^{87}Sr/^{86}Sr$ ratios. It turns out that belemnite Fe concentrations greater than 150 ppm indicate a high probability that the primary $^{87}Sr/^{86}Sr$ ratio has been measurably altered. This gauge works particularly well for mudrocks, but there is some indication that it is not as effective in oolites and sandier sediments that may support diagenesis under oxic conditions. The worst interval is in the Callovian sands, where it is possible that oxic diagenesis has prevented the mobilisation and hence incorporation of excess Fe. Fe concentrations are only moderately useful for detecting oyster diagenesis. While samples containing less than 150 ppm are very likely to preserve their primary Sr isotope signal, samples with 150 to 300 ppm Fe show variably altered Sr-isotope ratios and even concentrations in excess of 300 ppm do not guarantee markedly altered ratios. This may in part be due to Fe oxyhydroxides adhering to the surfaces of the foliated oyster calcites. While elevated Mn concentrations are less useful for highlighting samples with altered Sr-isotope ratios, low Mn concentrations (< 20 ppm) seem to be useful for indicating a high probability of good sample preservation in both belemnites and oysters. In oysters it is desirable to look at both Fe and Mn concentrations to obtain a 'feel' for any diagenetic alteration, but at present the best way to gauge the Sr-isotopic alteration of an oyster is to place it within the context of a whole suite of oysters collected with tight stratigraphic control. Future studies should independently document the utility of Mn and Fe as tracers of Sr-isotope diagenesis in each geological setting. The stable isotope data for carbon and oxygen do not show enough of a deviation from plausible marine values to allow their useful application in the detection of Sr-isotope diagenesis.

Chapter 4: Sr-Isotope Stratigraphy

4.1 Introduction

For the purposes of Sr-isotope stratigraphy it is vital that the data points of the reference curve are solidly tied to a clearly defined litho- and bio-stratigraphic framework. In this chapter the classic English lithologic successions and ammonite biostratigraphy are discussed in the context of assigning relative ages to the sample material, examining the reproducibility of the curve based on contemporaneous samples collected from separate localities, and highlighting problematic intervals and small-scale features in the curve that may serve as highly precise time markers. The stratigraphy of the samples collected for this study is conveniently divided into the exposures of the Lower Jurassic, the rest of the Jurassic, and the Lower Cretaceous. The Lower Jurassic is characterised by excellent coastal exposures, minor structural disturbances, relatively homogenous lithologies, generally abundant fossil material, and detailed published lithologic and biostratigraphic descriptions. The rest of the Jurassic and Lower Cretaceous is quite variable with respect to lithology, abundance of appropriate fossil material, provinciality of biostratigraphic markers, the quality and type of outcrop exposure, and the quality of the literature coverage. As a result, the Lower Jurassic data allow the fullest exploration of the potential of Sr-isotope stratigraphy whereas the data from rest of the Jurassic and Lower Cretaceous illustrate some of its limitations.

Figure 4.1 provides an overview of the Jurassic and Lower Cretaceous Sr-isotope curve plotted as a function of equal-duration ammonite subzone units. In this chapter the Sr-isotope data are differentiated according to whether they are belemnites, oysters, or aragonite samples. The belemnites are further subdivided according to whether they came from Dorset, Yorkshire, or one of the other localities, and whether they contain more than 150 ppm Fe and thus are likely to be diagenetically altered. Oysters are subdivided according to their Fe content only (< 150 ppm; 150 to 300 ppm; > 300 ppm Fe).

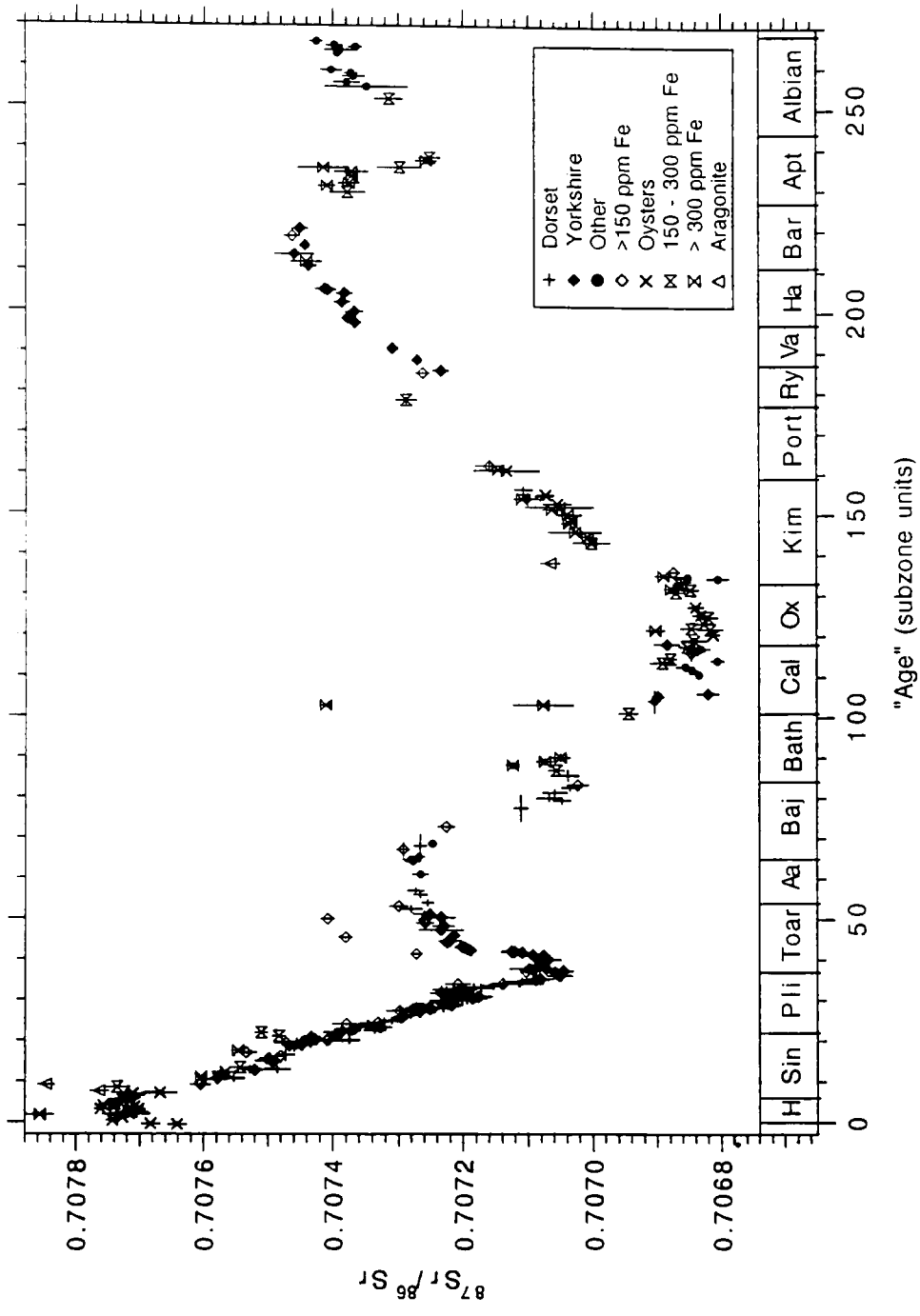

Figure 4.1 Sr-isotope curve for the Jurassic and Lower Cretaceous of Britain. "Age" is measured in ammonite subzone units and all data are normalised to Eimer and Amend = 0.708000. Data are differentiated according to sample type (belemnites, oysters, aragonite), sample locality (for belemnites only: Dorset, Yorkshire, Other), and Fe content (> 150 ppm for belemnites; between 150 and 300 ppm and > 300 ppm for oysters).

4.2 The Lower Jurassic

The ammonite zonal and subzonal scheme for the British Lower Jurassic is relatively stable and has remained largely unchanged from the synthesis of Dean, Donovan, and Howarth in 1961 to the correlation charts of Cope *et al.* (1980a). The subzonal scheme used in this work follows Cope *et al.* (1980a) with the following modifications (Ivimey-Cook and Donovan, 1983): the *reynesi* and *sauzeanum* subzones have for taxonomic reasons been renamed after the subzonal indices *C. lyra* and *E. resupinatum*, and the *bucklandi* subzone has been deleted because it is not easily recognised; its strata have been reassigned to the *rotiforme* subzone. The correlation of the Dorset and Yorkshire strata to the ammonite subzone scheme follows Cope *et al.* (1980a) with the exceptions of the bulk of the Yorkshire Pliensbachian, which follows Phelps (1985), and the Yorkshire Sinemurian and lower Pliensbachian, which follows Getty (1972) and unpublished data collected in conjunction with the work of Hesselbo and Jenkyns (pers. comm., 1991).

The Lower Jurassic Dorset and Yorkshire sections (Fig. 4.2) form a remarkably complete succession of mudstones, siltstones, impure limestones, and, in the upper Pliensbachian and upper Toarcian, fine-grained sands (Plates 1 and 2). The Yorkshire succession differs in that it is generally thicker, more expanded and complete, and time-equivalent sediments are generally slightly coarser and contain less carbonate. Thus the Yorkshire strata consist predominantly of silty mudstones (van Buchem and McCave, 1989), display an extra interval of sandy beds in the middle to upper Sinemurian (equivalent in time to an erosive episode in Dorset), and show a thick succession of mudstones in the Toarcian (compared to the 0.5 - 2.6 m-thick Junction Bed in Dorset). On both coasts the mudstones, siltstones, and sandstones are so weakly lithified that it generally requires little effort to convert the rock back into disaggregated sediment. However, the Yorkshire rocks are somewhat more lithified as compared to Dorset.

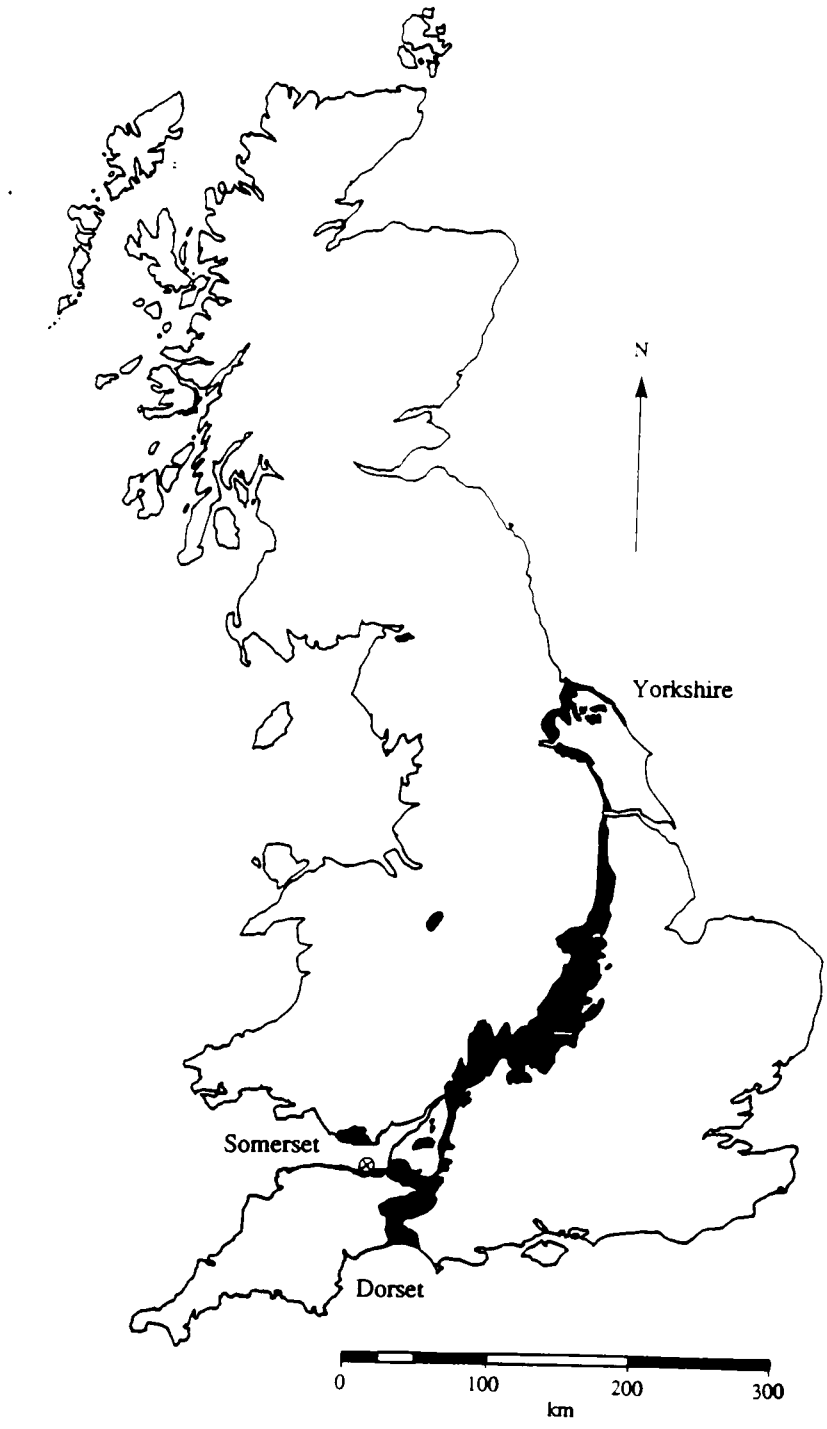

Figure 4.2 Map showing the disposition of Lower Jurassic strata in Great Britain and the outcrop localities sampled in this study.

4.2.1 Rhaetian and Hettangian

In overview (Fig. 4.3), the latest Rhaetian and Hettangian portions of the Sr-isotope curve are relatively well-constrained. The Sinemurian data show a fair amount of scatter due to a paucity of samples from Dorset plus a number of altered samples from Yorkshire, and the Pliensbachian and Toarcian data yield a tightly constrained Sr-isotope curve. Close comparison of the data from Dorset and Yorkshire (Fig. 4.3) reveals a high degree of reproducibility between the two independently biostratigraphically calibrated data sets. Such reproducibility is reassuring both for the application of Sr-isotope stratigraphy and for the generally assumed synchroneity in the first appearances of new ammonite species in Dorset and Yorkshire (Cope *et al.*, 1980a).

The Rhaetian, Hettangian, and lowest Sinemurian sections of the curve (Fig. 4.3) rest exclusively on oyster samples collected from the Ostrea Beds and Blue Lias of Dorset. These strata consist of rhythmically bedded (decimetre-scale) mudstones and impure limestones (Lang, 1924) that appear to reflect a forcing mechanism operating on a Milankovitch time scale (Weedon, 1985). As in nearly all of the Dorset Lias, the ammonites have been extensively collected and there is very little room for "slop" in the placement of subzonal boundaries. These sections are complete in the sense that all ammonite subzones are present, but there is some evidence for missing strata in the *angulata* zone (Smith, 1989) and at the top of the *lyra* subzone (e.g., concentrations of fish teeth and belemnites on top of Lang's Bed 49). During the Rhaetian, the Sr-isotope curve rises from what appears to be a minor dip in the Late Triassic (Koepnick *et al.*, 1985, 1990; Fig. 3.1) to reach a plateau at approximately 0.70772 throughout the Hettangian and earliest Sinemurian. On a fine scale this plateau appears to be broken into two segments recording a decline from 0.70775 to 0.70771; one segment runs from the basal Jurassic to the *laqueus* subzone and the other from the *laqueus* to the *rotiforme* subzone. The

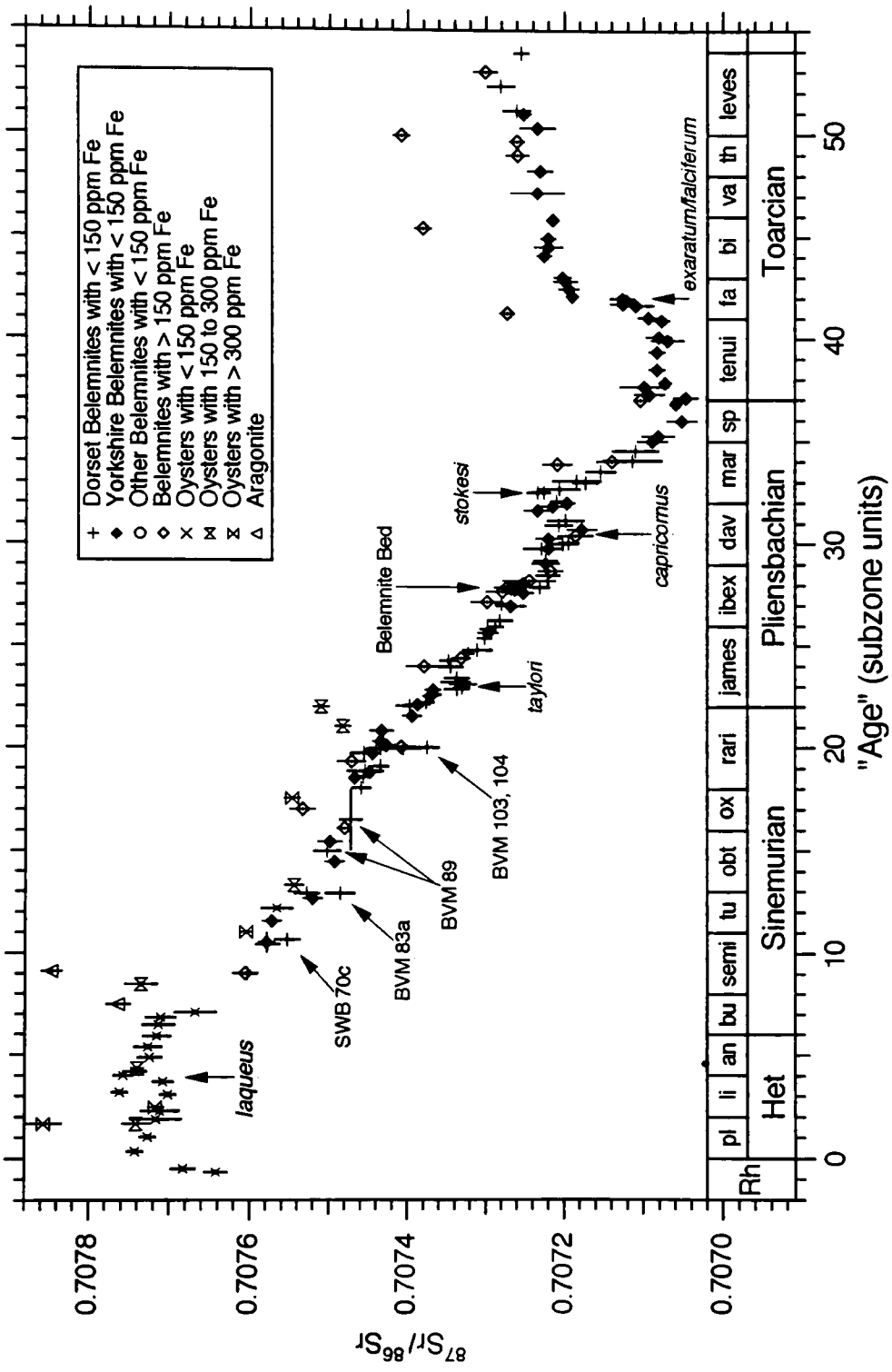

Figure 4.3 Sr-isotope curve for the Lower Jurassic. Stages and zones are labelled on the ammonite subzone time axis counting up from the base of the Jurassic.

discontinuity in the *laqueus* subzone, which could be taken as evidence for some sort of stratigraphic break, occurs before the gap found by Smith (1989) in the mid-*angulata* zone. Because there is no evidence for a significant gap in the *laqueus* subzone (Smith, 1989), and because such a sudden discontinuity in the Sr-isotope curve is unlikely to be a primary feature due to the long residence time of Sr in seawater, it seems best to regard this feature as a diagenetic or analytical artefact. It is probable that the curve should display at most only a small wiggle through the *laqueus* subzone.

4.2.2 Sinemurian

In Dorset the Blue Lias is followed by the black organic-rich mudstones of the Shales-with-Beef and the Black Ven Marls (Lang *et al.*, 1923; Lang and Spath, 1926). While there are belemnite concentrations suggestive of minor hiatuses at Lang's Beds 49, 69a, 71c, and the base of 83a, the major gaps in the Dorset Sinemurian occur at the Coinstone (Lang's Bed 89) where 3 full subzones are missing and at the base of the Belemnite Marls (Lang *et al.*, 1928) where 2 subzones are cut out (Fold-Out 1).

In Yorkshire (Robin Hood's Bay) the oldest sampled Jurassic rocks are the Upper Sinemurian Calcareous Shales. Mr. L. Bairstow extensively documented the litho- and bio-stratigraphy of the mid-Sinemurian through mid-Pliensbachian of Robin Hood's Bay but unfortunately, after decades of research, never published his efforts. Following his death the location of his manuscripts seems to be unknown and his fossils have been sold to private collectors. It was therefore necessary for Drs S.P. Hesselbo and H.C. Jenkyns to re-compile a detailed lithologic log of the Yorkshire sections while A.L. Coe and I re-collected the ammonites. These have been provisionally identified by Drs D.J. Donovan and K.N. Page and allow the placement of tentative subzonal boundaries in the Calcareous Shales, Siliceous Shales, and the lower Pyritous Shales (Fold-Out 2). The base of the *resupinatum* subzone of the lowest Calcareous Shales is undefined and the *brooki/birchi* and *obtusum/stellare* subzonal boundaries are as yet poorly constrained. The subzonal

boundaries of the rest of the Upper Sinemurian (*denotatus* - *aplanatum*) are well-defined by the unpublished work of Getty (1972) and confirmed by our efforts. Although over this interval the relative order of samples will not change, the assigned numerical subzonal "ages" (Table 2.2) may change slightly as more ammonites are collected.

The Sinemurian succession (Calcareous Shales, Siliceous Shales, and the lower Pyritous Shales) consists predominantly of silty mudstones with many beds and nodular horizons of impure and sideritic limestones. Minor sandy limestone beds appear near the top of the Calcareous Shales (*turneri/obtusum* zonal boundary) and throughout the upper half of the Siliceous Shales (*oxynotum* to *raricostatum* zones). The latter episode of sandy beds coincides with the erosive episodes of the Coinstone and uppermost Sinemurian horizons in Dorset. Sphalerite and galena, although disseminated throughout the succession, are commonly found in the chambers and phragmacones of ammonites and belemnites located on top of the prominent carbonate horizons. These minerals in combination with regional patterns of heavy mineral corrosion and authigenic mineral formation suggest localised low-grade metamorphism due to one or more episodes of post-depositional hydrothermal fluid flow along the Cleveland structural axis (Hemingway and Riddler, 1982). The area of most intense diagenesis intersects the coast precisely in the Sinemurian and lowest Pliensbachian of Robin Hood's Bay (Hemingway and Riddler's figures 5, 6, and 8).

The trend of the Sinemurian portion of the Sr-isotope curve is the most poorly constrained of the Lower Jurassic. While the Dorset Sinemurian yields abundant material only in the *densinodulum* and *raricostatoides* subzones (Upper Sinemurian), the abundant Yorkshire material appears to have suffered during the regional diagenetic/hydrothermal event noted above. The curve begins its descent in the *bucklandi* zone of the lowest Sinemurian. Throughout the *bucklandi*, *semicostatum*, *turneri*, and *obtusum* zones (which include parts of the Blue Lias, Shales-with-Beef, and the Black Ven Marls), belemnites are

so rare that, despite careful and thorough collection by Lang and Spath (1926) and the present writer, they have only been collected from a number of discrete belemnite-rich horizons that apparently represent pauses in sedimentation or mild erosive events. Of these horizons (Lang's Beds BL 49/50, SWB 69a, SWB 70c, BVM 83, BVM 89, BVM 103, and BVM 104), SWB 70c, BVM 83, BVM 89, and BVM 103/104 have each yielded one apparently well-preserved sample that plots significantly below the main trend of the data (Fig. 4.3). When examined in their stratigraphic context (Plate 1), samples from beds 89, 103, and 104 are understood as a mixture of material dating from above and below a gap of 2 or 3 subzones. The large "age" error bars placed on one of the BVM 89 samples illustrates the reasonable positioning of that sample in the stratigraphic gap (Fig. 4.3). Unfortunately this simple explanation does not seem to apply to the samples from beds SWB 70c (*sauzeanum*) and BVM 83 (*birchi*). There is no evidence at either level for a subzonal break or for a small-scale downwards shift in the curve that could accommodate mixing of belemnites across a short gap in time. It is possible that there may be a local diagenetic source of nonradiogenic Sr, such as a volcanic ash, but at present it is simpler to attribute these results to analytical error.

4.2.3 The Bedding Plane Test

Samples from the upper Sinemurian and Pliensbachian of Dorset have yielded the highest quality data of this study. To test the maximum resolution attainable through this interval a set of 12 belemnites was collected from a single bedding plane within Lang's Bed 115 in the Belemnite Marls. This horizon shows gradational, bioturbated contacts with adjacent strata and thus represents as close to a single instant in time as is possible in the geological record. (As indicated above, it is important to avoid belemnite-rich horizons that represent a hiatus or erosive gap because individuals of different ages could be mixed together.) The mean of the 28 analyses of the 12 individuals is 0.707297 ± 20 (Fig. 4.4). Of the 28 results, the measured error bars of 23 analyses (82%) overlap the mean of the

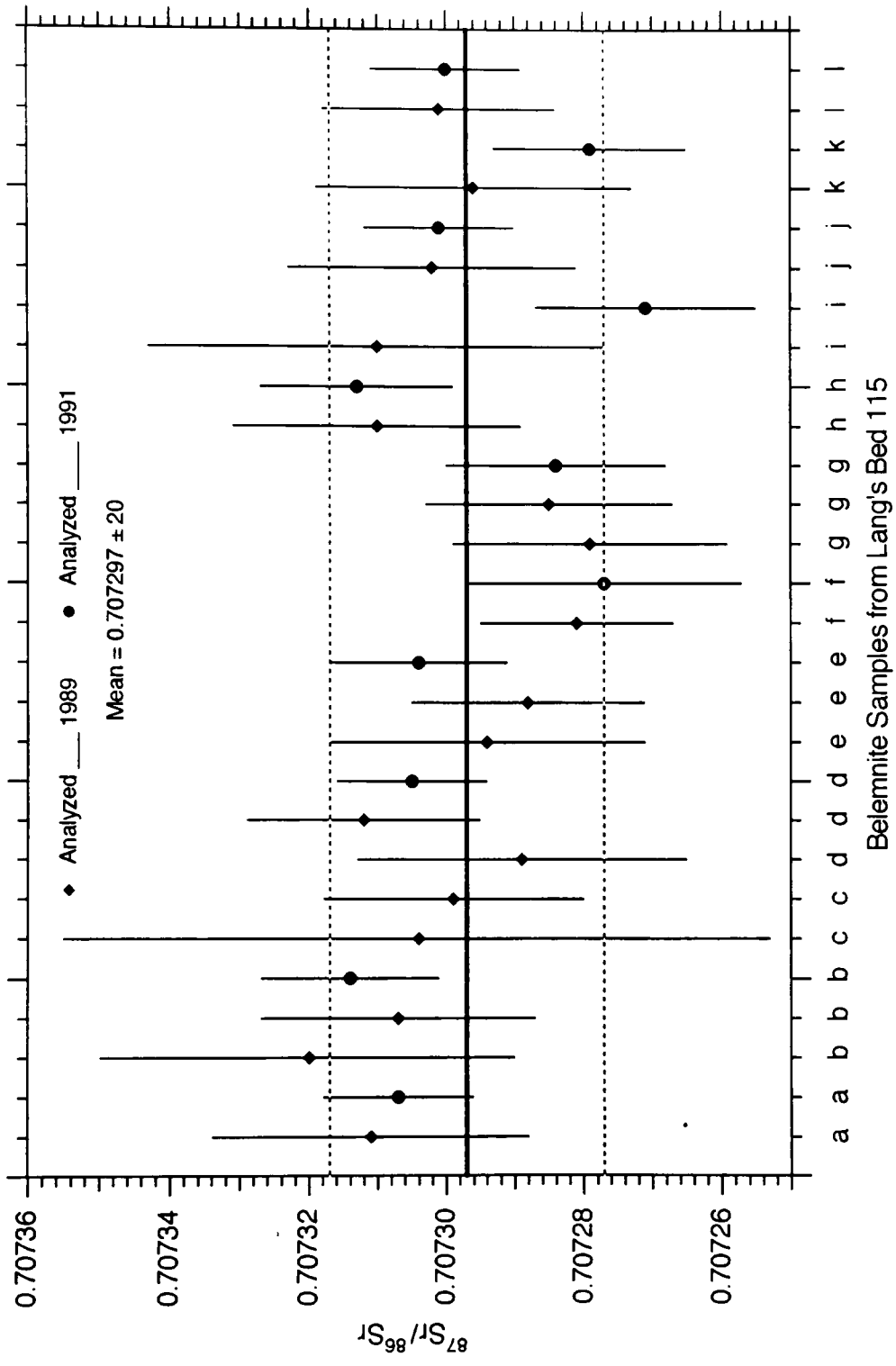

Figure 4.4 The bedding-plane test. 12 different belemnites from the same stratigraphic horizon yield average $^{87}Sr/^{86}Sr$ ratios that are not more than $\pm 20 \cdot 10^{-6}$ away from the mean of whole data set. The letters along the X-axis refer to individual belemnite samples.

whole data set. If error bars of $\pm 20 \bullet 10^{-6}$ are uniformly applied to each data point, these error bars overlap the grand mean in 26 out of the 28 analyses (93%). When all replicate analyses are combined, no sample plots outside these error limits and all samples are thus analytically indistinguishable from the data set mean of 0.707297. It should be pointed out that this conclusion is specific only to the Belemnite Marls because belemnites from units with different lithological characteristics may have encountered different diagenetic conditions.

Looking at the data set more closely reveals that replicate analyses of these samples tend to be highly reproducible such that multiple analyses of samples a, b, and h all plot above the data set mean at around 0.707310 whereas samples f and g plot below the mean at around 0.707280. This may indicate that the samples preserve a slightly heterogeneous $^{87}Sr/^{86}Sr$ signal, but a difference of only $30 \bullet 10^{-6}$ is too near the limits of the analytical resolution to be certain. If this heterogeneity is real, it may be because either the samples lived at slightly different times (lateral variations in bed thicknesses make it impossible to be certain that all samples come from exactly the same time-plane) or their are slight differences in the diagenetic alteration of the samples.

4.2.4 Pliensbachian

The positioning of the gap at or near Lang's Beds BVM 103 and 104 determines the positioning of the Sinemurian-Pliensbachian stage boundary and thus merits further discussion (Fig. 4.5). Lithologically, one would place the gap between Lang's Bed 102, a 90 cm-thick, easily weathered black mudstone typical of the Black Ven Marls, and Lang's Bed 103, a 13 cm-thick impure resistant limestone that marks the transition to the paler, more carbonate-rich Belemnite Marls above. The highest lithologically deduced boundary would be at a concentration of belemnites and pyrite that marks the contact between the limestone beds 103a (3 cm) and 103b (10 cm). However, the discovery of fragments of a coarse ('raricostate') *Echioceras* in Bed 104 (Spath, 1956) implies that the 2-subzone gap

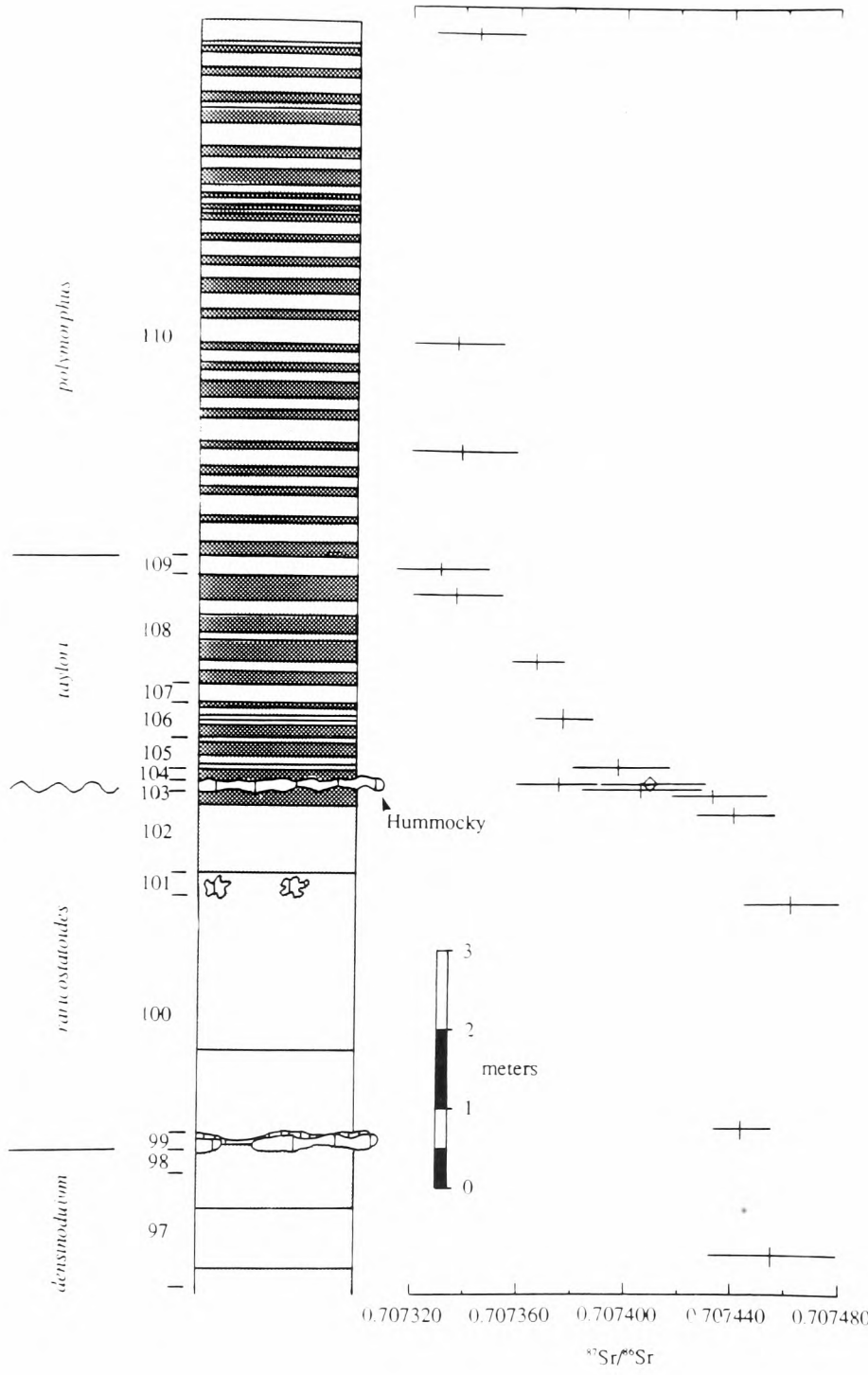

Figure 4.5 A close-up of the Sinemurian/Pliensbachian boundary in Dorset showing the behaviour of the Sr-isotope curve as it passes into the Pliensbachian. Shading refers to light, medium, or dark grey mudstones and vertical hatching refers to carbonate beds or concretionary horizons. Bed numbers are from Lang and Spath (1926) and Lang *et al.* (1928) and the stratigraphic log from S.P. Hesselbo (pers. comm.,1991).

in fact lies in the finely gradational contact between Beds 104 (10 cm-thick) and 105 (41 cm-thick).

The Dorset and Yorkshire Sr-isotope data indicate that the curve declines from 0.70746 in the *densinodulum* subzone to 0.70744 in the *raricostatoides* subzone, and the Yorkshire data further indicate that the curve goes no lower than 0.70743 in the succeeding *macdonneli* subzone and does not reach 0.70740 until the middle-to-end of the succeeding *aplanatum* subzone marking the end of the Sinemurian (Tables 2.1, 2.2). Figure 4.5 shows that the Dorset data remain steady at *raricostatoides* levels of about 0.70744 up through a sample taken from the base of 103a. If beds 103 and 104 are truly of *raricostatoides* age (Spath, 1956; Cope *et al.*, 1980a), then their samples should give $^{87}Sr/^{86}Sr$ ratios at or above 0.70743. Instead, the next sample, also from 103a, shows a $^{87}Sr/^{86}Sr$ ratio more compatible with an *aplanatum* subzone age (0.707406), and the 104 sample containing less than 150 ppm Fe seems to be clearly set in the lowest Pliensbachian ($^{87}Sr/^{86}Sr = 0.70738$). Although teetering on the edges of analytical reproducibility, these data are compatible with the placement of the gap at the prominent lithological break between beds 102 and 103.

In some sense a difference of 23 cm in the placement of a stage boundary seems trivial. However, if one is trying to understand the nature of the sedimentary processes that form erosive or non-depositional gaps in mudrocks, or to distinguish between erosive gaps and condensed intervals, it is essential to know exactly where the gap is located. For example, if in this case the gap is located between Beds 104 and 105 (Cope *et al.*, 1980a), then a significant hiatus of 2 subzones can, in mudrocks, be cleverly hidden across what appears to be a finely gradational contact. On the other hand, if the gap is between Beds 102 and 103, or if some part of it is concentrated in 103a, then it appears either that the *Echioceras* fragments of 104 have been mixed with younger belemnites by the erosive processes that formed the gap, or that a raricostate *Echioceras* managed to survive into the

Pliensbachian, or that the *Echioceras* in question was misidentified. The Sr-isotope data are as yet too few in number and too near the limits of analytical resolution to be taken as entirely conclusive, but they do suggest a useful application of seawater Sr isotopes to the stratigraphic record.

Apart from this gap at or below the base of the stage, the Dorset Pliensbachian is complete as regards the ammonites. The Belemnite Marls (Lang *et al.*, 1928) mark a return to Milankovitch-scale alternations between relatively carbonate-rich (pale) and carbonate-poor (dark) banded mudstones (Weedon and Jenkyns, 1990). The tightening of cycles up-section suggests an increasing degree of condensation that culminates in a pyritiferous belemnite horizon in the *valdani* subzone known as the Belemnite Bed (Lang's Bed 120c) and the compression of the whole of the *luridum* subzone into 24 cm of sediment capped by the Belemnite Stone (Bed 121; Phelps, 1985). The succeeding Green Ammonite Beds (Lang, 1936) represent a period of increased accumulation rates that characterise the rest of the Pliensbachian sequence up to the *spinatum* zone (Howarth, 1957). This episode of high accumulation rates, which includes several intervals of fine sand, is punctuated by a condensed limestone bed, the Marlstone Rock, at the top of the Pliensbachian (*spinatum* zone).

In Yorkshire the basal Pliensbachian (*jamesoni* zone) is characterised by the dark, organic-rich mudstones of the Pyritous Shales. The placement of the subzonal boundaries within the *jamesoni* zone (Plate 2, S.P. Hesselbo, pers. comm., 1991) follows Bairstow's thicknesses for each subzone as recorded in Cope *et al.* (1980a). Bairstow's measurements indicate that the *taylori* subzone is much thicker (by a factor of 4 or 5) than adjacent subzones. By contrast, the *taylori* subzone of Dorset is of unremarkable thickness, suggesting that if the parallelism that exists between the Dorset and Yorkshire sequences extends to the *jamesoni* zone, then the *taylori* subzone in Dorset either is missing potential strata at its erosive base or is relatively condensed. In Yorkshire the Milankovitch-scale

banding that characterises the Dorset Belemnite Marls begins around *polymorphus* time in the Pyritous Shales (van Buchem and McCave, 1989) and continues up through the paler Ironstone Shales (Phelps, 1985). As in Dorset this banding becomes tighter towards the top of the section, suggesting a progressively condensed sequence, and culminates in a series of minor belemnite horizons and lag concentrations in the *valdani* subzone. The *luridum* and succeeding subzones are characterised by increased sedimentation rates, including the deposition of silty, fine-grained sands (Staithes Sandstone, Howarth, 1955; Phelps, 1985), and the *margaritatus* and *spinatum* zones see a return to the finer-grained sediments of the Cleveland Ironstone Formation (Howarth, 1955). There appears to be a short (< 1 subzone) gap at the top of the *margaritatus* zone (Howarth, 1955; Cope *et al.*, 1980a; Howard, 1985).

The Pliensbachian is ideal for examining the fine structure of the Sr-isotope curve and for comparing the reproducibility of the Dorset and Yorkshire data sets because of good sample preservation and the relatively detailed sampling of both coastal sections. Immediately across the Sinemurian/Pliensbachian boundary the curve appears to drop suddenly in the mid-*taylori* subzone (basal *jamesoni* zone) and then level off for a short time before resuming its otherwise steady downwards trend (Fig. 4.3). In Dorset this sudden drop is clearly defined by 10 data points (Plate 1, Fig. 4.5). At first glance the Yorkshire data appear less striking (Plate 2), but when plotted as a function of subzone units (Fig. 4.3), they do confirm the feature. At present it is not possible to determine whether this feature is a real palaeo-seawater excursion or whether it is an artifact of the non-uniform duration of ammonite subzones. The feature could be a result of an anomalously long *taylori* subzone, which would produce an apparently rapid rate of change when normalised to uniform subzone units, plus an unusually short *polymorphus* subzone, which would flatten the curve when expressed in subzone units. In fact, the *polymorphus* and succeeding *brevispina* subzones are not distinguishable even in Dorset (Cope *et al.*,

1980a), and it may be that the two should be merged. If this were so, the slight plateau and the gap in the data following the *taylori* subzone (Fig. 4.3) would be compressed along the time-axis and the curve would resume its steady descent that much sooner after the *taylori* subzone. It may be worth undertaking future work to determine whether this feature is the result of a real seawater Sr-isotope excursion, which could offer a highly precise albeit small "event" offering global correlation at the basal Pliensbachian, or the result of a somewhat lengthy *taylori* subzone, which is of interest for understanding the detailed depositional history of the British sediments.

After the *taylori* dip the curve descends smoothly until the *ibex* zone, when there appears to be a slight divergence between the Yorkshire and Dorset data (Fig. 4.3). The Yorkshire data show the curve simply continuing its steady descent through the *ibex* and *davoei* zones. Meanwhile, the Dorset data seem to level off for a moment in the lower *ibex* zone before suddenly dropping in the middle *ibex* zone. This is unlikely to be a primary palaeoceanographic signal and is instead best viewed as an artefact of the sedimentary record in Dorset. A plot of the Sr-isotope data against the stratigraphic section (Fig. 4.6) shows that the sudden step in the Dorset data occurs entirely across the Belemnite Bed. This bed, a 1 to 2 cm-thick layer packed with belemnites and pyrite, was suspected on the basis of sedimentological evidence to host a stratigraphic gap of short but unknown duration. The length of time represented by the Belemnite Bed may be calculated by assuming that the seawater curve was moving at the average rate measured between the Sinemurian *raricostatoides* and the Pliensbachian *luridum* subzones (0.000025/subzone $\approx$ 0.000050/Ma). Thus, for the Sr-isotope curve to evolve from 0.707260 before the Belemnite Bed to 0.707230 after the Belemnite Bed requires slightly more than 1 subzone unit of time. Thus, although a jump of 0.000030 is near the limits of analytical resolution, the data seem to confirm sedimentological observations suggesting that the Belemnite Bed represents a significant proportion of the time inhabited by *valdani* subzone ammonites.

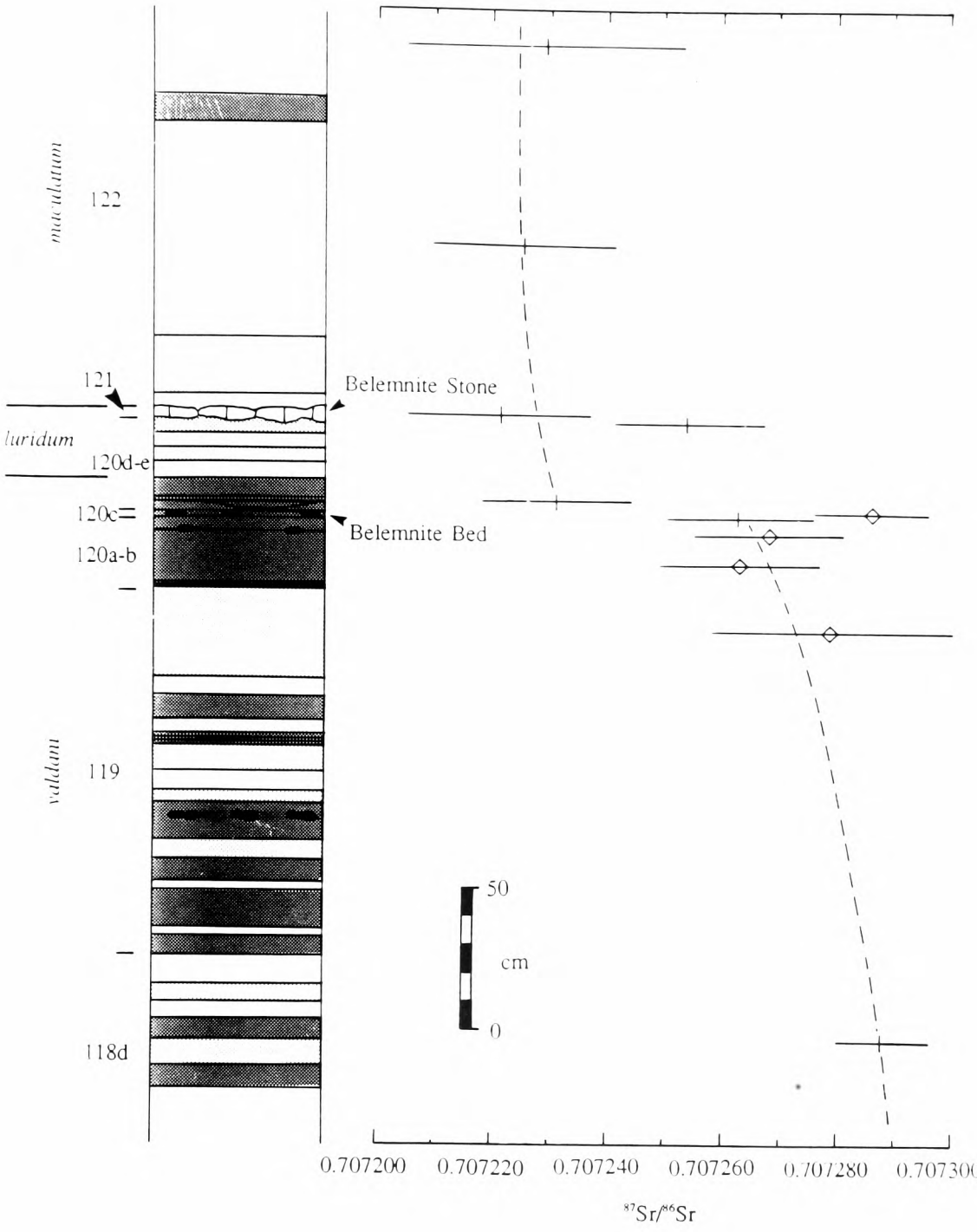

Figure 4.6 A close-up of the Belemnite Bed and the Belemnite Stone at the top of the Belemnite Marls in Dorset showing the behaviour of the Sr-isotope curve as it passes through the upper *valdani* subzone. Lithological shading as in Figure 4.6; black blobs indicate exceptional pyrite concretions. Bed numbers are from Lang *et al.* (1928) and the section is from S.P. Hesselbo (pers. comm., 1991).

The curve also appears to level off for a moment during the *luridum* and *maculatum* subzones before beginning a poorly defined but significant "wiggle" that reaches a minimum in the *capricornus* subzone and a maximum probably in the *stokesi* subzone. Unfortunately, the scatter in the data prevents a closer resolution of this reversal of the overall downward trend of the curve. After the *stokesi* subzone the curve descends smoothly to the Lower Jurassic minimum of about 0.707050 at the Pliensbachian/Toarcian boundary.

4.2.5 Toarcian

Most of the Toarcian of Dorset (14 subzone units) is represented by the Junction Bed, which, despite being only 0.5 - 2.6 m thick, is nearly complete with respect to the ammonites (Cope *et al.*, 1980a). No samples were collected from the Junction Bed due to the difficulty of accurately dating the samples. The 3 remaining subzones of the Toarcian, by contrast, show 51 m of the Downcliff Clay and Bridport Sands. The 3 samples collected over this interval are located against the detailed lithologic logs constructed by Drs. S.P. Hesselbo and H.C. Jenkyns (unpublished data, 1991). While subzonal ammonites have been recorded from these units, they are not properly located and the positions of the subzonal boundaries are uncertain. It makes little practical difference whether the "ages" of the samples are calculated using the estimated subzonal boundaries of Hesselbo and Jenkyns or assuming a constant sedimentation rate throughout the interval. To be consistent with the "ages" of other data calculated without firm ammonite evidence, these "ages" were calculated assuming a constant sedimentation rate.

In Yorkshire the lower Toarcian consists of a variety of mudstones including the Grey Shales, Jet Rock, Alum Shales, Peak Shales, and the Striatulus Shales (Howarth, 1962, 1973; Dean, 1954; Knox, 1984). The upper Toarcian (*levesquei* zone) sees a return to sandy sediments (Blea Wyke Sands, Dean, 1954; Knox, 1984) and is finally terminated by an erosive break that puts the *moorei* subzone in contact with the lower Aalenian (Cope

et al., 1980b). These Toarcian sections show all ammonite subzones except for the *aalensis*, although it should be noted that the *levesquei* subzone is not proved (Dean, 1954).

The Toarcian Sr-isotope curve gently rises from the Pliensbachian minimum before beginning an accelerated increase in the *exaratum* subzone. Despite the lack of evidence for diagenesis, it is doubtful whether the two higher points in the lowest Toarcian record an unaltered seawater signal (Fig. 4.3). Upon reaching the end of the *exaratum* subzone, the curve suddenly skips from 0.707127 to 0.707190 as it crosses the *exaratum/falciferum* subzonal boundary (Fig. 4.7), and then it continues its gentle increase through the rest of the Toarcian.

This "skip" at the *exaratum/falciferum* boundary is significant in that it implies a certain amount of "time" missing at this horizon. The amount of time may be estimated using different plausible rates of change for seawater Sr isotopes. The most rapid sustained rate of change in the Lower Jurassic curve occurs during the Pliensbachian, when the curve shifts from 0.707230 in the mid-*stokesi* to 0.707050 in the upper-*apyrenum* . Taking this rate (0.000050/subzone) as the maximum likely rate of change across the *exaratum/falciferum* boundary implies that at least 1.3 subzone units of time are required for the seawater curve to evolve naturally from 0.707127 to 0.707190. Using the average rate of change observed from the upper Sinemurian through the lower Pliensbachian (0.000025/subzone) increases the estimated gap to 2.4 subzone units.

The presence of a significant stratigraphic gap at this time is completely unexpected. While the gap does mark a subzonal boundary, the index ammonites are of the same genus on either side of the gap (*Harpoceras exaratum* and *H. falciferum*) and are found in direct succession all over Europe (e.g., Jenkyns, 1988). Whereas in Dorset the 3-subzone gap above the *stellare* subzone is marked by the distinctive bored and encrusted Coinstone horizon (Lang, 1945; Hallam, 1969; Hesselbo and Palmer, submitted, 1991), and the

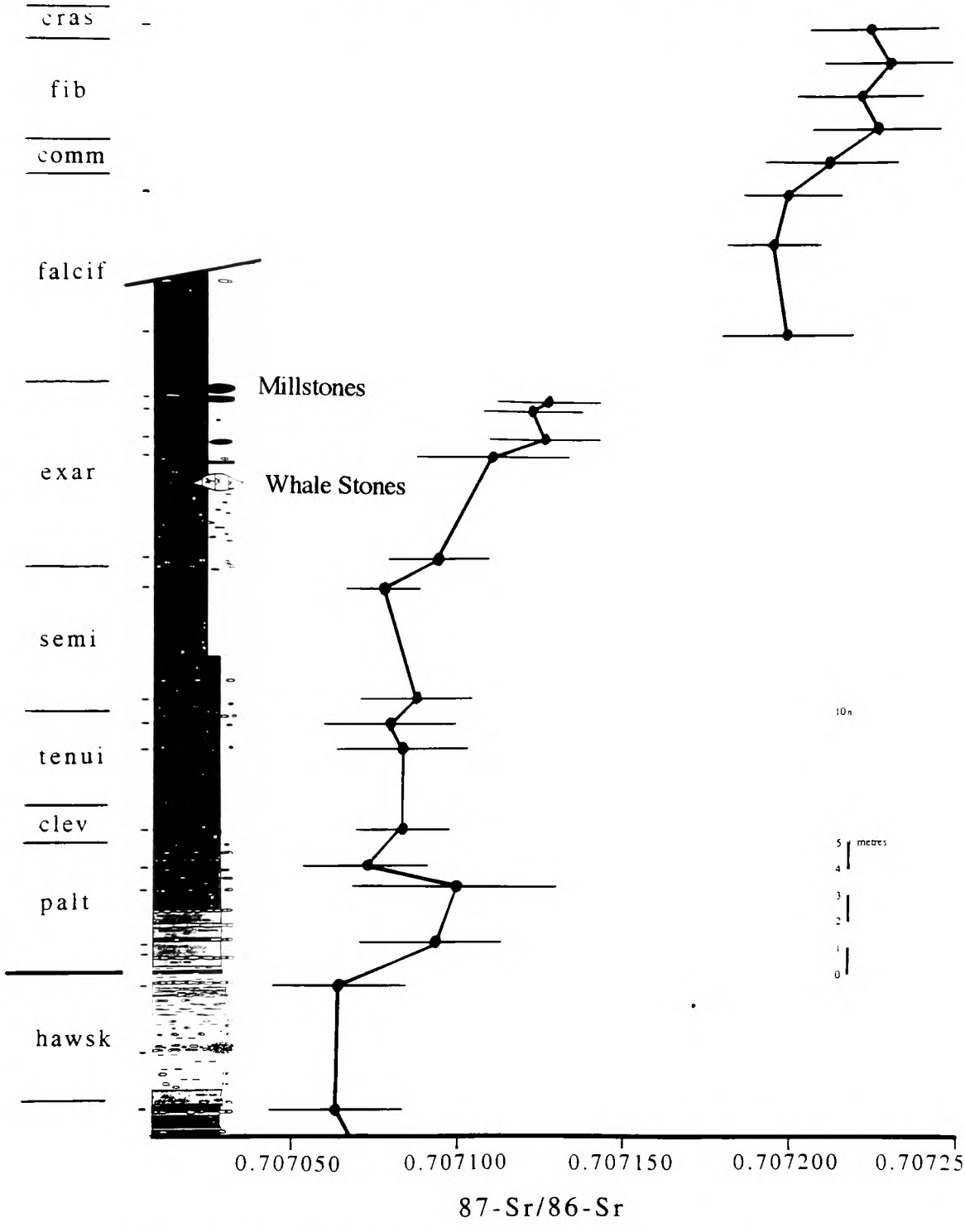

Figure 4.7 Sr-isotope stratigraphy of the lower Toarcian of Yorkshire showing the "skip" across the *exaratum/falciferum* boundary (Howarth, 1962; section from S.P. Hesselbo, pers. comm., 1991). Lithological shading as in Figure 4.5. Samples collected above the mid-*falciferum* subzone come from a separate section.

2-subzone gap at the top of the Sinemurian is marked by the problematic but lithologically distinctive Hummocky Limestone, in Yorkshire the *exaratum/falciferum* boundary is marked only by the ordinary-looking Millstone nodules and a number of unremarkable minor shell beds (Morris, 1980). The single outstanding feature of this section, and the one that may offer additional support for the existence of a 1- or 2-subzone gap, is the Whale Stone concretionary horizon (see Fig. 4.6).

The Whale Stones occur some 3 m below the Millstones and consist, as the name implies, of enormous oblong concretions up to several metres long and a metre or more thick and wide (Hallam, 1962; Howarth, 1962; Morris, 1980). At their cores and along the same horizon occur the 'extraordinary' Lower Pseudovertebrae concretions (Hallam, 1962; Howarth, 1962). According to Morris (1980), the Millstones and Whale Stones are distinguished from the many other concretionary horizons in the section by not having the pyritic margins that indicate formation in the zone of sulphate reduction (e.g., Coleman and Raiswell, 1981). Moreover, while the pyrite-coated nodules have $\partial^{13}C$ values of -12 to -15‰ that are typical of formation under sulphate reduction, the Whale Stones show values of more than +7 to +8 ‰. Such heavy carbon is strongly suggestive of formation during methanogenesis (Campos and Hallam, 1979). One analysis of a Millstone gives $\partial^{13}C$ = +4.3 ‰, which, although quite heavy, is less positive than contemporary belemnites measured from this section (see Chapter 5; Table 2.2) and thus may have precipitated directly from seawater.

The growth of early (burial) diagenetic concretions requires pore fluids to supply diffusional Ca^{2+} and HCO_3^- for $CaCO_3$ precipitation, pore space to allow room for the $CaCO_3$ to precipitate, and time for these processes to become focused at one horizon and produce sizeable concretions. In a marine setting the simplest way to obtain these conditions is to slow or stop sedimentation. This halts the compaction of the sediments and keeps a zone of sulphate reduction or methanogenesis at one level long enough to supply

plenty of HCO_3^- from the degradation of organic matter (Coleman and Raiswell, 1981; Raiswell, 1988). While precipitation of diagenetic carbonates can continue to several hundred meters depth (Irwin, 1980; Matsumoto, 1983), the growth of diagenetic concretions slows exponentially with depth as compaction of the sediments makes diffusion less efficient and removes the pore spaces required for carbonate precipitation (Irwin, 1980). Thus the bulk of an early diagenetic concretion forms relatively near the surface, in relatively uncompacted sediment, and all other things being equal, the relative sizes of concretions should be proportional to the amount of time they were left to grow near the surface.

The Whale Stones began life as the Lower Pseudovertebrae concretions, which show $\partial^{13}C$ values and pyrite coatings consistent with formation in the sulphate reduction zone (Campos and Hallam, 1979). After sulphate reduction ended, probably when the horizon was buried to a depth where pore fluids lost diffusional contact with seawater SO_4^- (on the order of 15 m; Claypool and Threlkeld, 1983), methanogenesis was able to take over as the main producer of HCO_3^-. A shallow depth of burial during formation is in fact suggested by a primary porosity of some 80% preserved in the Whale Stones (Campos and Hallam, 1979). For the Whale Stones to have grown to such an enormous size during methanogenesis implies that sedimentation must have slowed or ceased for some time. Although a suitable hiatus or condensed interval is not immediately apparent in the first few metres above the Whale Stones, the "skip" in the Sr-isotope curve puts the gap near the Millstone concretions. Upon closer examination the Millstones seem to be a reasonable horizon on which to focus this hiatus in sedimentation, not only because of the "skip" in the Sr-isotope curve over this interval, but also because this horizon shows occasional scours and an increased abundance of shell-beds (Morris, 1980), it is the only other concretionary horizon in these sediments without pyritic skins, and it is the only concretionary horizon with plausible marine stable isotope ratios (Campos and Hallam,

1979). Thus it may be that the Millstones are analogous to the problematic Hummocky Limestone (Fig. 4.5), which is similar in that it is known to cap a 2-subzone gap, it also gives plausible marine stable isotope ratios (Reynolds, 1991), and there are no features that immediately indicate a stratigraphic gap at that level.

It may be rewarding to carry out more work over this interval. Detailed Sr- isotope data would be useful to pinpoint the gap and determine whether it represents a sharp discontinuity or a markedly condensed interval. A more systematic collection of stable isotope data from the concretions in the section would yield clues as to how they formed and help constrain the sedimentary history of the section. It would also be useful to examine other sections in Europe for gaps at this time and to integrate this knowledge with carbon-isotope and other data to shed more light on the nature of the early Toarcian anoxic event that occurred at exactly this time (Jenkyns, 1988).

4.3 The Middle and Upper Jurassic

The rocks of the Middle and Upper Jurassic are lithologically diverse and variably exposed, described, and biostratigraphically dated. This has made it more difficult to collect well-dated samples and results in a sparser data set. In addition, the samples have been exposed to a much wider range of diagenetic environments that might collectively be expected to have degraded the original seawater Sr-isotope signal. The principal sample localities are shown in Figure 4.8.

The correlation charts of Cope *et al.* (1980b) are somewhat out-of-date for much of the Middle and Upper Jurassic. The Aalenian and Bajocian have been revised in a key paper by Callomon and Chandler (1990). The Lower Callovian ammonite biostratigraphy has been expanded by Callomon *et al.* (1988) and Page (1989). The correlation of the Dorset Oxfordian sediments to the ammonite standard has been revised by Wright (1986a,b), and the Kimmeridgian (*sensu anglico*) has been described in detail by Cox and Gallois (1981). The Portlandian follows Cope *et al.* (1980b) and Wimbledon (1986).

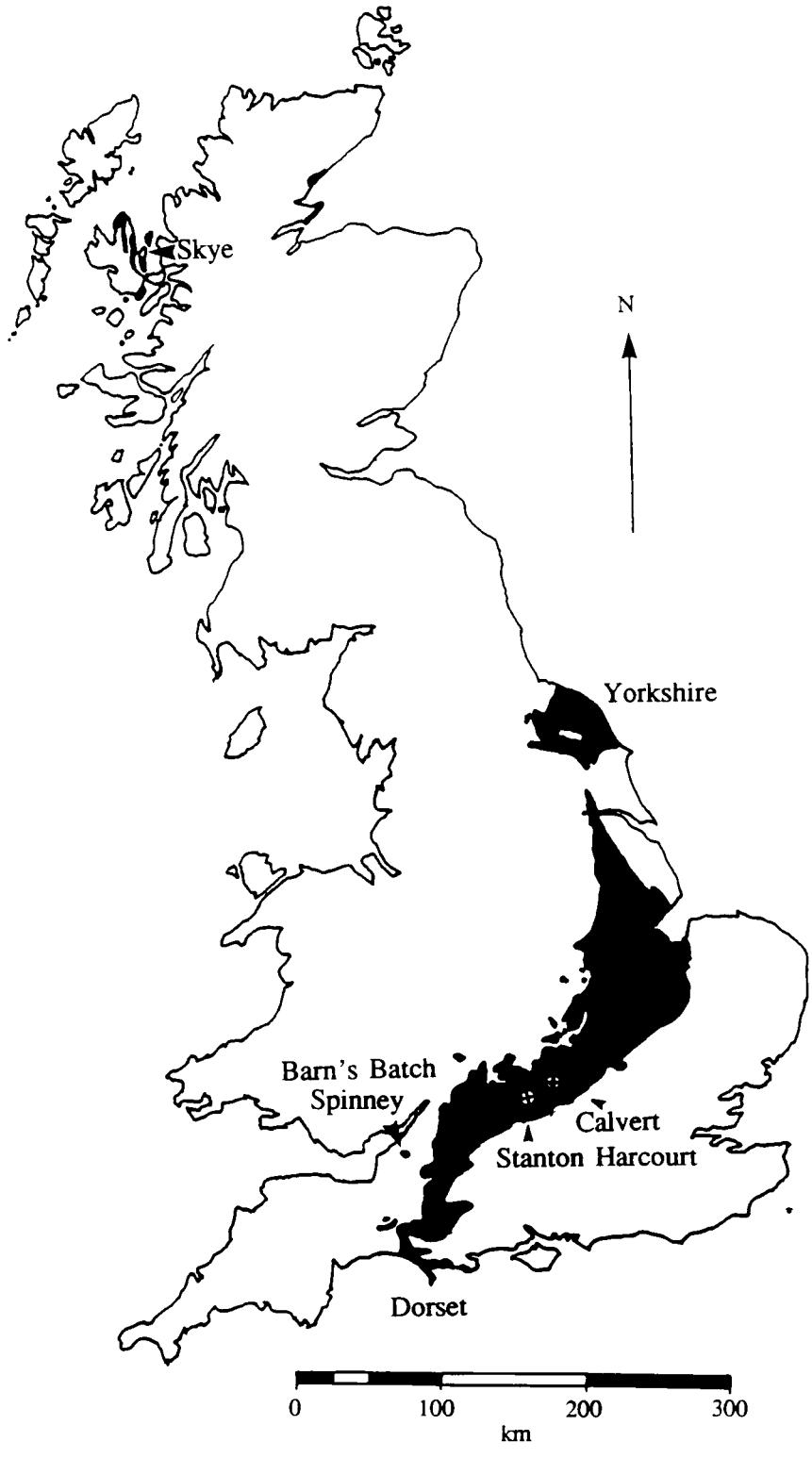

Figure 4.8 Map showing the Middle and Upper Jurassic rocks in Britain and the principal sample localities used in this study.

4.3.1 Aalenian and Bajocian

The continuous successions of muds and siltstones of the Lower Jurassic are in marked contrast to the highly incomplete, thin, discontinuous sections of the Inferior Oolite of southern Britain (Aalenian - Bajocian). Any one section is likely to contain several significant biostratigraphic gaps and this makes the piecing together of a continuous Sr-isotope curve subject to the time-axis errors associated with correlation between distant exposures. Fortunately the thorough work of Callomon and Chandler (1990) has defined a large number of ammonite horizons, usually several per subzone, that allows highly precise correlation between sections. Thus, time-axis errors due to combining several sections are probably minimal and insignificant. The sections sampled in this study (Burton Bradstock, Sandford Lane Quarry, Barn's Batch Spinney) consist of blocky to rubbly beds of oolitic limestone with occasional marly partings; these are well-described by Buckman (1893), Buckman and Wilson (1896), Richardson (1928, 1932), Parsons (1974, 1979), Torrens (1969b), and Callomon and Chandler (1990). The Aalenian/Bajocian portion of the Sr-isotope curve (Fig. 4.9) is characterised by a smooth, concave-down feature continuing from the middle Toarcian through the *discites/ovalis* zones. From this point the curve begins a poorly documented descent on its way to the Bathonian. The belemnites collected from the Yorkshire Scarborough Formation, a thin marine horizon in a predominantly nonmarine sequence dating from the *humphriesianum* zone (Parsons, 1977), show highly elevated Fe concentrations. Sample Scarb 10-5, for example, contains 1445 ppm Fe and gives the most radiogenic $^{87}Sr/^{86}Sr$ ratio of the entire study (0.707936).

4.3.2 Bathonian

The British Bathonian is poorly exposed and poorly dated compared to the rest of the Jurassic. Instead of yielding a relatively continuous supply of ammonites that allows strata to be accurately assigned to one subzone or another, the English Bathonian frequently offers only a few ammonites from a few beds widely spaced in time. Thus a sample from

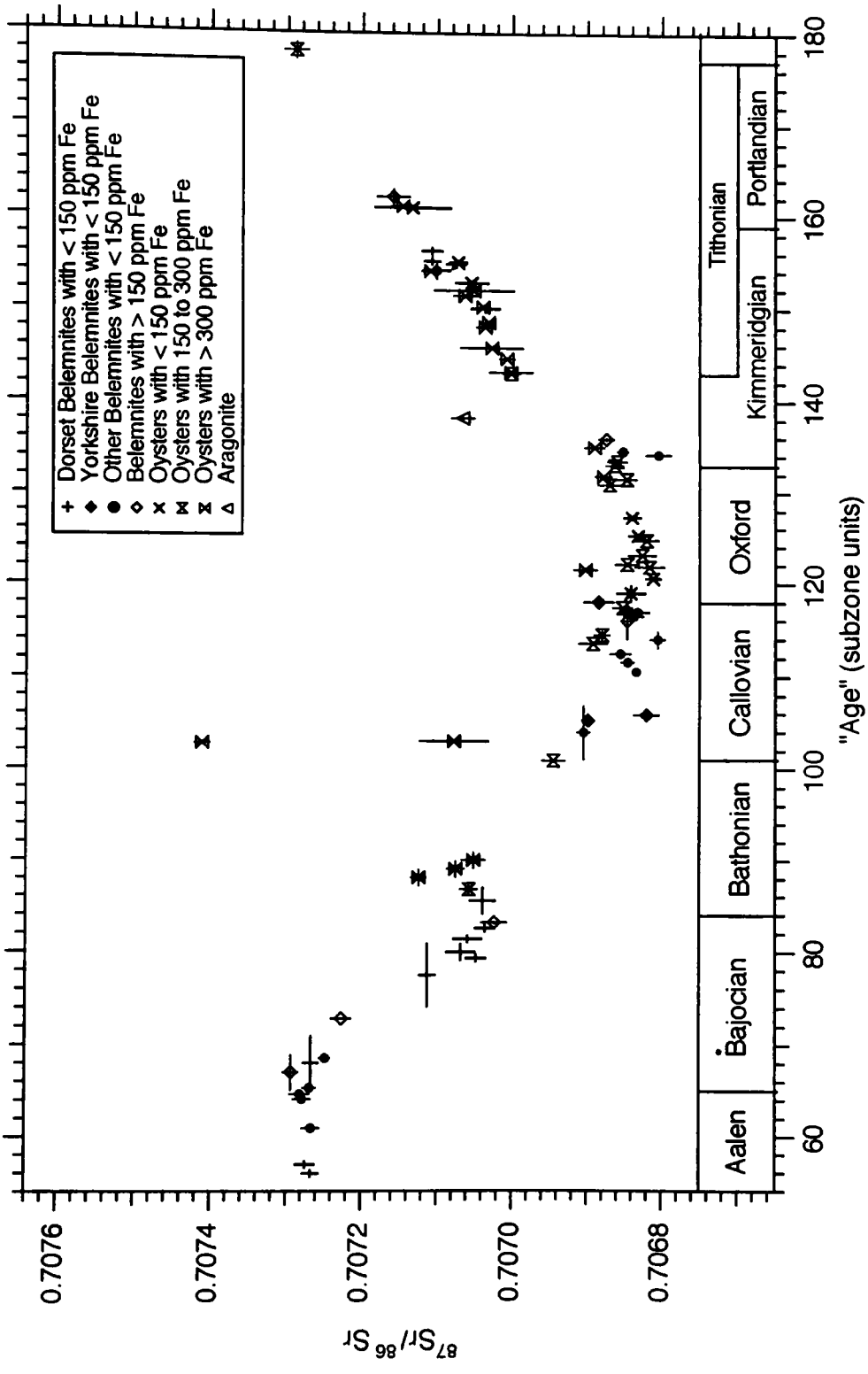

Figure 4.9 Sr-isotope curve for the Middle and Upper Jurassic. Symbols and time units as in Figure 4.1.

above an ammonite-bearing horizon may belong either to the same zone or to one or more above it. A great deal of effort has been expended searching the literature for well-dated, presently exposed Bathonian quarries containing oysters or belemnites, but with little success. Samples have been collected from Burton Bradstock (Inferior Oolite, Richardson, 1928), Snowshill Hill Quarry (Great Oolite carbonates and silty beds, Torrens, 1968, 1969a), and the Shipton-on-Cherwell Cement Works (Lower Cornbrash, Page, 1989). The Burton Bradstock belemnite (BBr 17) and the Snowshill Hill oysters (Table 2.3) appear to signal a small reversal in the downwards plunge from the Upper Bajocian to the Lower Callovian. Unfortunately the highly elevated Fe concentrations in the oysters indicate an unknown and possibly significant diagenetic overprint on the primary Sr-isotope ratios.

4.3.3 Callovian

In southern England the Callovian is variably exposed in quarries, brick pits, sewage pipe trenches, and the drainage pits of gravel quarries. Most Callovian exposures are thus continuously changing, but have fortunately proved consistent enough to allow confident collection of a number of samples with a bio- and litho-stratigraphic resolution similar to that of the Lower Jurassic. The Upper Cornbrash (*macrocephalus* zone) has been sampled in the Home Farm Quarry (Cox *et al.*, 1991), and the Shipton-on-Cherwell Cement Works Quarry (Page, 1989). The overlying Kellaways Clay and Kellaways Rock is only rarely exposed (Callomon, 1955) and remains unsampled. The best exposures of the Callovian are the freshly exposed organic-rich clays of the Oxford Clay at the London Brick Company clay pits near Calvert (Callomon, 1968). In fresh exposures, the high organic content of the clays tends to favour good fossil preservation, including the preservation of primary ammonite aragonite, but where these clays have been exposed to long-term surface weathering, such as is the case for the *athleta* zone samples, the formation of sulphuric acid from the decomposition of pyrite results in poorly preserved

fossil material. The Callovian/Oxfordian boundary is exposed in the drainage trenches of a gravel quarry near Stanton Harcourt (Arc Southern, National Grid Reference SP 4105). This section has never been described in detail, but the lithologic succession closely matches the description of the Woodham Brick Pit (Arkell, 1939; Callomon, 1968), which is now unfortunately covered up. It is assumed that, as at Woodham (Cope *et al.*, 1980b), the Lamberti Limestone belongs entirely to the *lamberti* subzone while the Upper Spinosum Clays belong to the *henrici* subzone. There is a chance that this assumption is invalid (compare the definition of the *lamberti* and *henrici* subzones by Callomon and Sykes in Cope *et al.* (1980b) with the correlation column C7 which indicates that the Lamberti Limestone can extend into the *henrici* subzone), but either way the effect is small when plotting the data.

In Yorkshire the best exposure of the Callovian is the coastal section near Scarborough (Cayton Bay, Redcliff section). There the Upper Cornbrash is followed by the clays and sands of the Shales-of-the-Cornbrash, Kellaways Rock, Langdale Beds, Hackness Rock, and finally the Oxford Clay (Oxfordian) (Wright, 1968, 1977). While most beds are well-dated by ammonites, a significant proportion yields none (Page, 1989). I have followed Page (1989) in taking the subzone boundaries at the bases of the beds yielding ammonites, but obviously the thicknesses of the subzones could be considerably different depending on the subzone to which the non-ammonite bearing beds actually belong. Thus while the samples are in the correct relative order and are assigned to the correct subzones, they may not be positioned correctly within a given subzone "age" unit. The dating of the samples from the Hackness Rock is somewhat problematic because half of the Hackness Rock (Bed 12) bears no ammonites while Bed 13 contains ammonites representing the *proniae* and *lamberti* subzones (Cope *et al.*, 1980b). I have assumed error bars on the samples collected from these beds spanning the *proniae* to *lamberti* subzones. In addition to the English material I have analysed 3 belemnites from the Callovian exposed

on the Isle of Skye (Sykes, 1975) and collected by A.L. Coe.

It is difficult to determine the precise trend of the Sr-isotope curve during the Callovian (Fig. 4.9). The Lower Cornbrash oyster of the latest Bathonian and the following two belemnites (Scottish BelSands 9-1 and Yorkshire KlwyR 7-2) seem to bring the curve quite high relative to the succeeding data points. While the Lower Cornbrash oyster (and certainly the very radiogenic Upper Cornbrash oysters from Yorkshire) may be regarded as altered (containing > 150 ppm Fe), there is no evidence to support alteration of the two belemnite samples. However, as noted in Chapter 3, diagenetic alteration may not have imparted elevated Fe concentrations to the belemnites if it took place in well-oxygenated fluids percolating through the sandstone matrix. The succeeding Yorkshire sample (KlwyR10-2) plots much lower, but is consistent with the upward trend of the next 3 samples from Calvert. Because the two Yorkshire Kellaways Rock samples are from the same subzone (*curtilobus*), it seems very unlikely that the data are recording a real "jump" in the Sr-isotope curve. The 2 oyster samples of the *athleta* zone (upper Callovian) appear to be altered and plot somewhat higher than one might expect, but an apparently unaltered Scottish belemnite from this zone plots much lower than expected. It is not clear why this sample would plot so low, although one possibility is that this belemnite (DunansClay2) was altered by oxygenated waters that had associated with the Tertiary flood basalts of Skye. By the *lamberti* zone a large number of samples from a variety of localities confirm that by the uppermost Callovian the Sr-isotope curve rests at about 0.706850.

The Middle and Upper Jurassic data of this study can be compared with a few data points recently published by Fischer and Gygi (1989) and Smalley *et al.* (1990). Because the Smalley *et al.* (1990) data are biostratigraphically dated only to the stage, the "age" and associated error bars had to be estimated based on the position of the assigned numerical age (in Ma) within the stage. The assigned age of the Bathonian sample, for example, is midway between the ages of the upper and lower stage boundaries and suggests that

perhaps the error bars should cover the whole stage. Smalley *et al.* (1990) attempt to control for diagenesis by measuring the stable isotopic composition of their samples. However, as noted earlier the stable isotopes of oxygen and carbon are unfortunately relatively insensitive indicators of Sr-isotope diagenesis. Thus it is not possible to judge independently the state of preservation of the samples analysed in either study.

Figure 4.10 shows the data of Fischer and Gygi (1989) and Smalley *et al.* (1990) superimposed over the data of this study. The Bathonian sample does not greatly constrain the trend of the curve, but along with the 3 lower Callovian samples plotting near KlwyR10-2, it does suggest that the Bathonian curve comes in relatively low to reach its minimum some time in the lower Callovian. The remaining 2 Callovian samples are much higher than anything else in the Callovian and Oxfordian, which suggests that they are diagenetically altered. A best-guess for the Bathonian and Callovian is that the curve comes down rapidly from the Inferior Oolite data near the Bajocian/Bathonian boundary to reach a minimum in the Lower Callovian. The curve then recovers somewhat to reach a maximum in the *athleta* zone (Upper Callovian) before finally beginning its descent into the Oxfordian.

4.3.4 Oxfordian

The Oxfordian ammonite biostratigraphy, although worked out in detail, is complicated by extreme ammonite provincialism that forces the use of three separate European biostratigraphic schemes (Cope *et al.*, 1980b). The Northwest European scheme is used here because it most directly applies to the sampled Dorset coast sections (Wright, 1986a,b) and because its intermediate position between the Boreal and Submediterranean provinces allows better correlation throughout Europe. The Oxfordian samples come from a number of separate, relatively poor exposures along the Dorset Coast (Wright, 1986a,b; Coe, 1992). The subzonal boundaries are not precisely constrained in certain sections due to a relative paucity of ammonites. Therefore, although the "age" assignments in this study

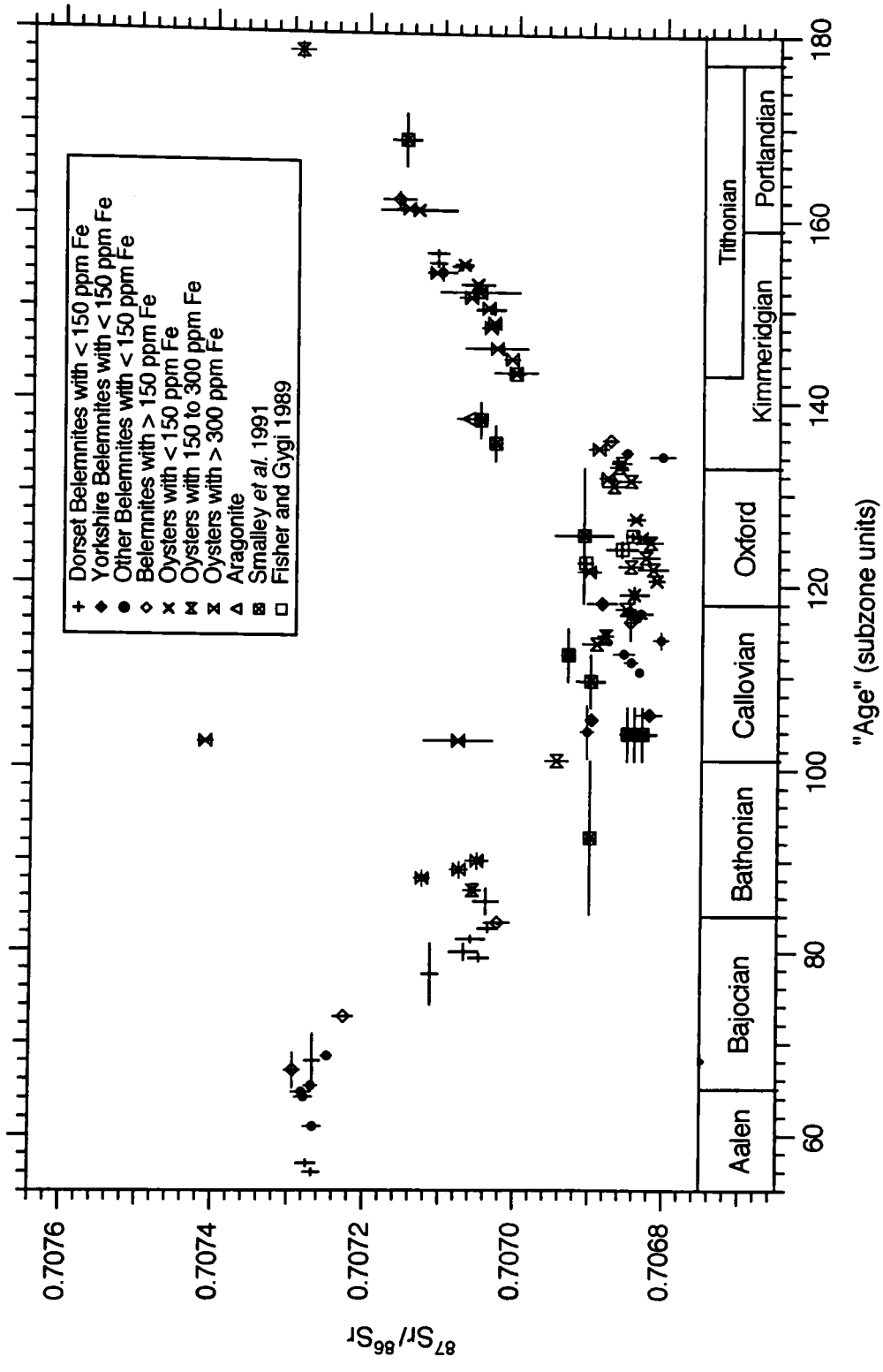

Figure 4.10 Sr-isotope curve for the Middle and Upper Jurassic including the data from Fischer and Gygi (1989) and Smalley *et al.* (1990).

are internally consistent, they may in places be in error by a maximum of one subzone with respect to real ammonite subzone time. In all cases the lithostratigraphy and thickness of the subzones are taken from Coe (1992) because her sections are the most detailed and precise available.

The Dorset Oxfordian is lithologically quite diverse--ranging from clays and sands to oolites and carbonates--and contains several biostratigraphic gaps (see Wright, 1986a,b). In addition, the lack of belemnites through the Oxfordian has forced the collection of a number of different oyster genera, ranging from large, massive *Gryphaea* in the Jordan Cliff Clays to flaky, foliated *Liostrea* in the Nothe Grit to small foliated and partially silicified *Nanogyra* in the Shortlake Member. The best exposure of the Oxfordian-Kimmeridgian boundary is a section of organic-rich, pyritic mudstones that are unfortunately highly disturbed by the action of a nearby fault (Brookfield, 1978; Cox and Gallois, 1981; Coe, 1992). Despite the weathered, distorted nature of the exposure, the section is well-dated, fossiliferous, and stratigraphically well-characterised. Three additional samples from the lowest Kimmeridgian were analysed from the Flodigry Shales from the Isle of Skye (Wright, 1989; collected by A.L. Coe).

The Oxfordian Sr-isotope curve is quite well-constrained compared to the scatter of the Callovian (Fig. 4.9). Despite generally elevated Fe concentrations, the oysters containing less than <300 ppm Fe define a clear minimum (~ 0.706810) in the *bukowski* subzone followed by a steady increase to about 0.706860 in the lowest Kimmeridgian (*baylei* zone). The 3 Scottish belemnite samples (Flodigry 38, 41, 45-3) again yield one point that plots quite low (38) while the other two support the main data trend in the *baylei/cymodoce* zones. The Oxfordian data from both Fischer and Gygi (1989) and Smalley *et al.* (1990) generally plot higher than the data of this study, again indicating the probable impact of diagenesis on their samples.

4.3.5 Kimmeridgian

The English Kimmeridgian, although generally broken down only into zones, is well-constrained by ammonite biostratigraphy. For historical reasons the English Kimmeridgian is considered to cover the entire interval represented by the Kimmeridge Clay in its type exposure on the Dorset Coast whereas in France the Kimmeridgian is restricted to what is the Lower Kimmeridgian in Britain (Cope *et al.*, 1980b). The succeeding Portlandian therefore covers a much shorter interval in Britain as compared to France. In the time scale of Harland *et al.* (1990) the Tethyan Tithonian stage is directly equated with the European Boreal Portlandian (i.e. both begin in the *elegans* zone at the base of the English Upper Kimmeridgian). In this work the British usage of the stage boundaries is retained.

The Kimmeridgian samples were collected from the type locality of the stage near Kimmeridge, Dorset (Cox and Gallois, 1981; Coe, 1992). The lithological sections of Cox and Gallois (1981) and Coe (1992) closely match except in the uppermost *pallasioides* zone, where due to difficult exposures, about 2 meters of strata are missing in the section of Cox and Gallois. The sample labels follow the bed numbering scheme of Blake (1875) as partially modified by Cope (1967, 1978). This scheme is quite simple to use provided that it is remembered that Blake's bed numbers count beds from the top down, whereas Cope's lettered subdivisions go from the bottom up. The uppermost Kimmeridge Clay (*rotunda* and *fittoni* zones) is not well exposed and there is some doubt as to the exact placement of zonal boundaries (Cope, 1978). The Portlandian samples were collected by A.L. Coe according to the sections described in Arkell (1933) and Wimbledon (1986).

The Kimmeridgian and Portlandian data define a consistently rising curve from 0.707000 to about 0.707140. There is a small amount of scatter in the *rotunda* zone involving both belemnites and oysters that is not readily explainable in terms of either Fe-indicated diagenesis or a sudden shift in the curve. The lower Kimmeridgian aragonite

sample (Pearce's Pit 2, *cymodoce* zone) plots well above what is expected by a simple interpolation between the Lower and Upper Kimmeridgian data. It thus appears to have shared a similar degree of diagenesis as the Sinemurian aragonite sample (DonBay246- 2), and again without any trace element or stable isotopic evidence suggesting diagenesis. The data of Smalley *et al.* (1990) include two samples dated as Kimmeridgian and one as Tithonian (Fig. 4.10). The two Kimmeridgian points plot much higher than expected, again probably due to diagenesis. The Tithonian sample is quite consistent with the data trend and may thus be well-preserved.

4.4 The Lower Cretaceous

The English Lower Cretaceous provides exposures of mudstones, siltstones, and sandstones that are relatively patchy, poorly exposed, variably fossiliferous, and biostratigraphically incomplete. The ammonite provincialism near the Jurassic/Cretaceous boundary is again extreme, making correlation between the Boreal and Tethyan realms difficult. The boundary in Britain is conveniently but arbitrarily taken at the Cinder Bed; there are no ammonites to prove or define this boundary (Cope *et al.*, 1980b). The complete lack of overlap between the Boreal and Tethyan ammonites during the lowest Cretaceous means that it is not known whether the base of the Boreal Ryazanian stage occurs before, during, or after the base of the supposedly equivalent Berriasian stage of the Tethyan realm (Hancock, 1988). By the end of the Ryazanian/Berriasian, however, a number of incursions of Tethyan "marker" ammonites into the Boreal realm allow the determination that the bases of the Boreal and Tethyan Valanginian, Hauterivian, and Barremian stages are synchronous to within an ammonite zone (Kemper *et al.*, 1981). The basal zone of the boreal Valanginian correlates with a level high in the basal zone of the Tethyan Valanginian. The base of the Hauterivian stage in the Boreal and Tethyan provinces is synchronous to within a narrow margin of error (Rawson, 1983), and the English *variabilis* zone at the base of the Barremian shares elements with the basal zone of

the Tethyan Barremian. By the Aptian many of the characteristic ammonites have essentially world-wide distributions (Hancock, 1988) and the base of the stage is confidently defined across Europe (Birkelund *et al.*, 1984). The base of the Albian, although somewhat difficult to define (Birkelund *et al.*, 1984), is also widely recognisable (Owen, 1984).

The Ryazanian to Barremian stages are best represented in England by the Speeton Clay of Yorkshire (Fig. 4.11). Correlation of the Speeton Clay to the English ammonite standard follows Rawson *et al.* (1978) for the Ryazanian, Valanginian, and Hauterivian, and Rawson and Mutterlose (1983) for the Barremian. The strata are comprehensively described by Lamplugh (1889), Neale (1960, 1962), Rawson (1971), Doyle (1989), Fletcher (1969), and Rawson and Mutterlose (1983). A map of the cliff (Neale, 1974) showing the location of the marker beds is very helpful, particularly for working out the stratigraphy of the large slumped blocks. Although these detailed descriptions approach the detail of Lang's papers on the Lower Jurassic of Dorset, the "generally obscure and difficult state of the cliffs" (Lamplugh, 1889) makes accurate sample collection difficult, particularly in the middle to upper C beds and the B beds. However, with persistent digging, much patience, and an insistence on exactly matching sections to the published descriptions, it is possible to collect samples firmly tied to the lithostratigraphy.

The best Aptian sections in England are exposed on the Isle of Wight off the Hampshire Coast (Fig. 4.11). The ammonite zones and subzones of the Aptian follow Casey (1961) and the lithostratigraphy of the predominantly silty sandstone units is described by Fitton (1847), Casey (1961), and Simpson (1985). The sections are fairly straightforward and yield relatively abundant if not-so-well-preserved oysters. The phosphatic mudstones of the Gault (Albian) have been sampled at Folkstone in Kent and Leighton Buzzard in Bedfordshire. The Albian ammonite subzonation follows Owen (1984, 1985, 1988) while the stratigraphy of the Folkstone sections is covered by Casey

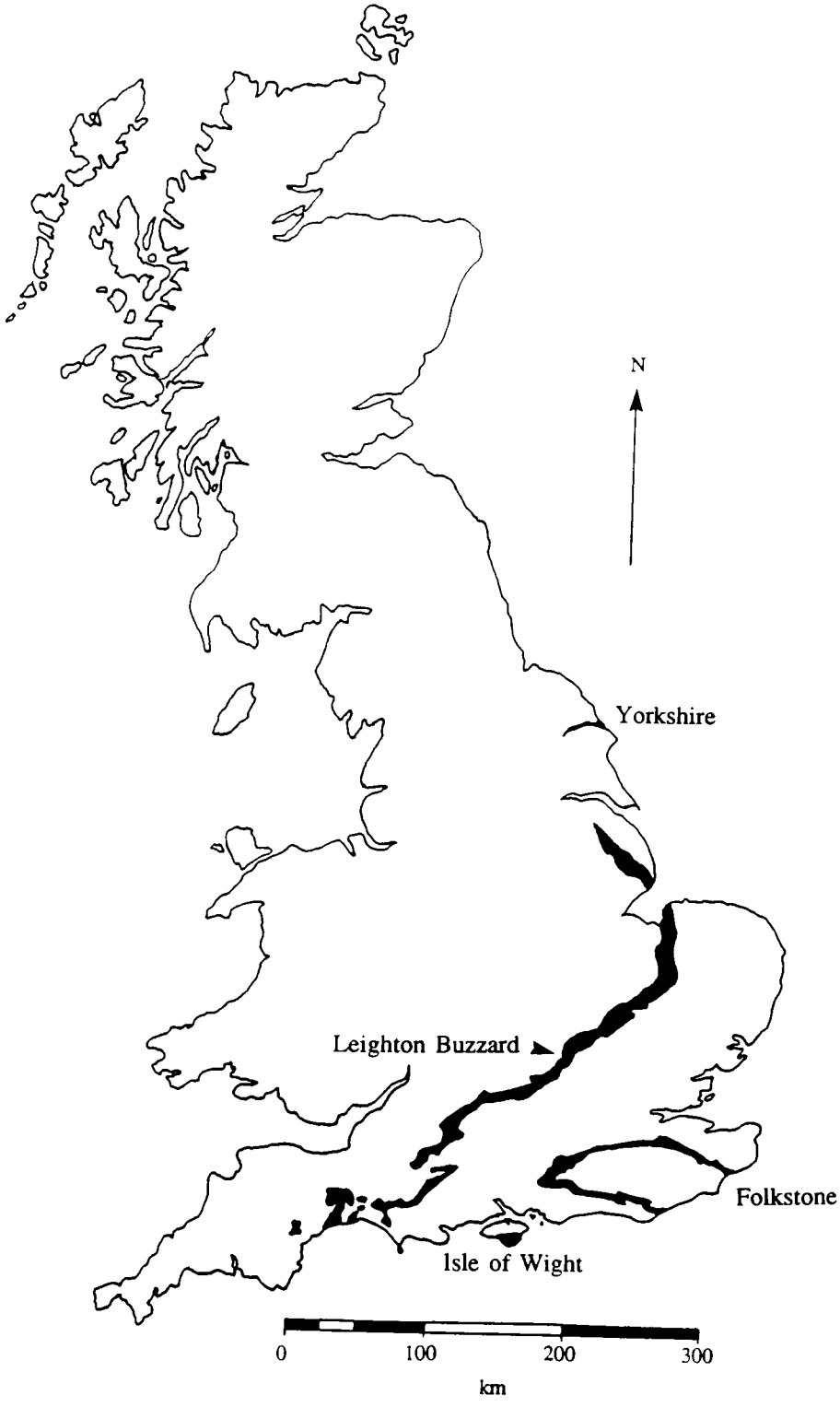

Figure 4.11 Map showing the outcrops of the Lower Cretaceous of Britain and the principal sample localities.

(1961) and Owen (1975) and the Leighton Buzzard sections by Owen (1972). With some digging the Gault sections are easy to follow and generally yield abundant belemnites.

The Lower Cretaceous Sr-isotope curve continues the smooth increase established in the Kimmeridgian, rising from about 0.707230 in the upper Ryazanian to a plateau of about 0.707450 in the Barremian (Fig. 4.12). The Ryazanian-through-Hauterivian curve does not follow the linear trend projected from the Kimmeridgian/Portlandian data, which suggests that the curve must level off somewhat during the Portlandian or lower Ryazanian. The one Tithonian data point of Smalley *et al.* (1990) appears to support this inference (Fig. 4.11). The accuracy of the Aptian data is difficult to establish due to the elevated Fe concentrations indicating diagenetic alteration of the oysters. However, the data are internally quite consistent and moreover plot along the lower limits of the data scatter of Koepnick *et al.* (1985) (Fig. 3.1). This suggests that the Aptian data are at least broadly accurate in recording a significant downwards shift from the Barremian plateau (0.707450) to an Aptian minimum near 0.707250. In the Albian an Fe-rich oyster from the *mammillatum* superzone (FlkstnBds 33) appears to record the recovery to what appears to be a slowly increasing curve through the rest of the Albian. This is also consistent with the data of Koepnick *et al.* (1985) (Fig. 3.1).

4.5 Summary

In summary (Fig. 4.13), the Jurassic and Lower Cretaceous Sr-isotope curve rises out of the latest Triassic and reaches a plateau in the Hettangian. It rapidly descends from the lowest Sinemurian to a minimum reached in the uppermost Pliensbachian. After an initially slow recovery in the Toarcian, it suddenly jumps up across the *exaratum/falciferum* subzonal boundary. The rate of this increase is probably accentuated by a gap in the sedimentary record spanning 1 2 units of subzone time. The curve then smoothly increases through the rest of the Toarcian and Aalenian and reaches a peak near the Aalenian/Bajocian boundary. After an initially slow start, the curve rapidly descends

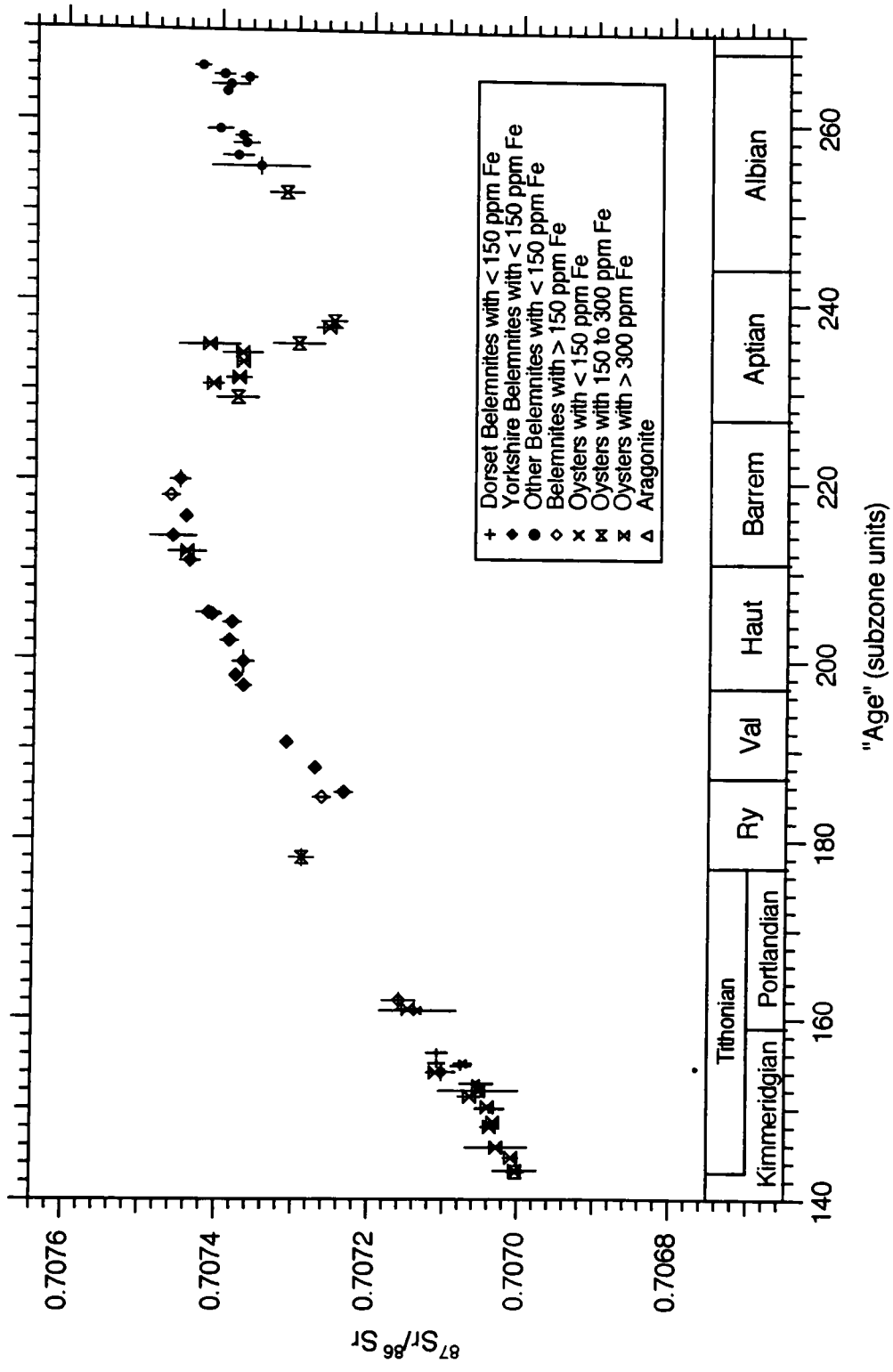

Figure 4.12 Sr-isotope curve for the Lower Cretaceous. Symbols as in Figure 4.1.

through the Upper Bajocian. It is not clear whether there is a small reversal in the lowest Bathonian or if the curve simply continues its rapid descent down to the minimum located probably the Lower Callovian. The curve then rises slightly to reach a peak in the Upper Callovian before descending to a second minimum in the Lower Oxfordian. From this point through the Barremian the curve steadily increases, with periods of apparently accelerated increase during the Lower Kimmeridgian and Ryazanian/Valanginian. A major reversal of this general increase occurs sometime during the upper Barremian or lower Aptian and the curve reaches another minimum during the middle-to-upper Aptian. By the Albian the curve has recovered from this downwards shift and is ready to begin a general increase into the Upper Cretaceous.

4.6 Stratigraphic Resolution of the Seawater Sr-Isotope Curve

The most straightforward application of the seawater Sr-isotope curve is for the global correlation of marine sediments. In principle this is done by measuring the $^{87}Sr/^{86}Sr$ ratio of a sample of unknown age, tracing this value across the graph of the Sr-isotope curve, and noting the age where the sample isotope ratio intersects the curve. The errors on the age determination should take into account the 2σ errors of the $^{87}Sr/^{86}Sr$ ratio of the unknown, the data scatter in the relevant portions of the reference curve, and any uncertainty associated with the diagenetic alteration of the sample materials. In the case of a belemnite collected from the freshly exposed Lower Jurassic mudstones of the Belemnite Marls, for example, it appears that the measured $^{87}Sr/^{86}Sr$ ratio is likely to be within $\pm 25 \cdot 10^{-6}$ of the primary seawater value provided that the belemnite Fe content is below 150 ppm. By contrast, the oysters of the Oxfordian show a fair amount of scatter and, until better methods are developed for distinguishing between altered and unaltered samples, this scatter has to be taken into account when assigning an age.

There are several techniques for obtaining an age from a Sr-isotope curve. The simplest way is to use a pencil and ruler to read off directly the age of a sample. However,

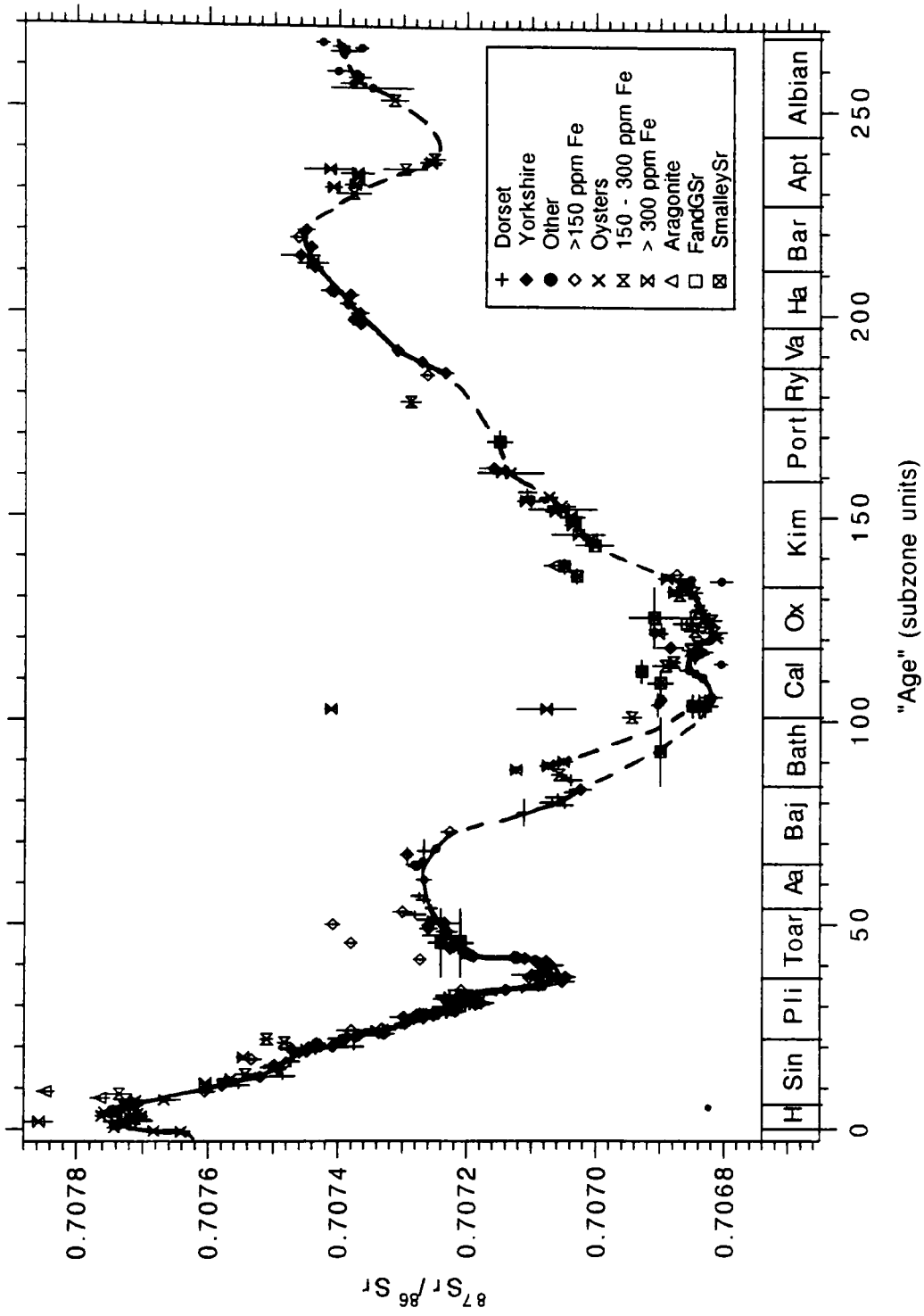

Figure 4.13 "Best-estimate" Sr-isotope curve for the Jurassic and Lower Cretaceous. Dashed lines express uncertainty as to the actual trend of the curve.

for the present purpose of estimating the stratigraphic resolution of the Jurassic and Lower Cretaceous Sr-isotope curve, it is certainly better to have a slightly more rigorous and objective procedure. A more mathematical approach is to use a series of line segments as approximations to the observed Sr-isotope curve (Elderfield, 1986; McKenzie *et al.*, 1988; Hodell *et al.*, 1989). This method has the advantage of allowing a statistical treatment of the errors associated with the linear regression and the measurement of the sample $^{87}Sr/^{86}Sr$ ratios. However, while it is possible to fit line segments through certain portions of the Jurassic and Lower Cretaceous data, over many intervals lines are relatively poor approximations to the curves defined by the data (see Fig. 4.13).

A third approach is adopted by Ludwig *et al.* (1988). They approximate the seawater Sr-isotope curve using spline curves and then use these splines to assign numerical ages to samples collected from the Enewetak borehole. Spline curves have the advantage of being flexible enough to follow the curvature of the data and to approximate small-scale features in the data. Their main disadvantage is that the curve is not represented by a single mathematical expression but instead by a whole collection of cubic polynomials designed to fit or approximate the trend of a data set. As such, there is no rigorous way to derive the statistical errors of the age assignments (Ludwig, 1990).

The application of splines to Sr-isotope stratigraphy is greatly facilitated by a spline-fitting utility included with the IBM-compatible software program **Isoplot 2.11** (Ludwig, 1990). Although this program includes Akima, Normal, and Smoothed Spline options, in this study only the Smoothed Spline option is used because it creates a best-fit average of a dense data set using a least-squares method. This spline curve should give the best approximation of the "real" seawater curve.

The first step in Sr-isotope stratigraphy is to select the data that will form the reference curve. While it may be considered valid to eliminate diagenetically altered samples simply by removing those that do not look good, a more objective result is

obtained if diagenetically altered samples are eliminated using an independent criterion such as trace element concentrations. Thus, for this exercise all belemnites and Lower Jurassic oysters containing more than 150 ppm Fe, all Bathonian through Lower Kimmeridgian oysters containing more than 300 ppm Fe, and all aragonite samples are deleted from the reference curve. In addition, samples BVM 89-1, BVM 103a-2, and BVM 104 are excluded because their "scatter" is attributable to mixing of samples of different ages at stratigraphic gaps, and the Cinder Bed oyster sample (242 ppm Fe) is deleted simply because it looks bad.

When executing the Smoothed Spline option it is necessary to specify the minimum time interval over which the cubic polynomials attempt to follow the data and the minimum number of data points used to construct each segment. Values of 1 and 9, respectively, result in a spline that most sensibly follows the Lower Jurassic data while values of 10 and 9 yield a sensible spline for the Upper Jurassic and Lower Cretaceous data (Figs. 4.14 and 4.15). Selecting other values for the minimum x-interval and the number of points used to fit each spline results either in overly broad approximations to the data or in unwanted overshoots and other oscillatory artefacts.

The current versions of Isoplot do not handle inflections in the reference curve very well. Ideally, when one isotopic ratio intersects the curve at 2 or more points, the program would calculate an age and associated errors at each point of intersection. Instead, Isoplot calculates an intermediate age located between the two points of intersection and gives very large error bars on this age. To overcome this problem the reference curve has to be broken into segments such that only unique age assignments are possible. Thus, the Rhaetian through Hettangian portion of the curve, which shows a rise to a plateau, is separated from the Sinemurian to uppermost Pliensbachian portion of the curve, and this is separated from the curve running from the basal Toarcian through the maximum in the Bajocian. The Bajocian to Callovian interval forms a fourth segment, the basal Oxfordian

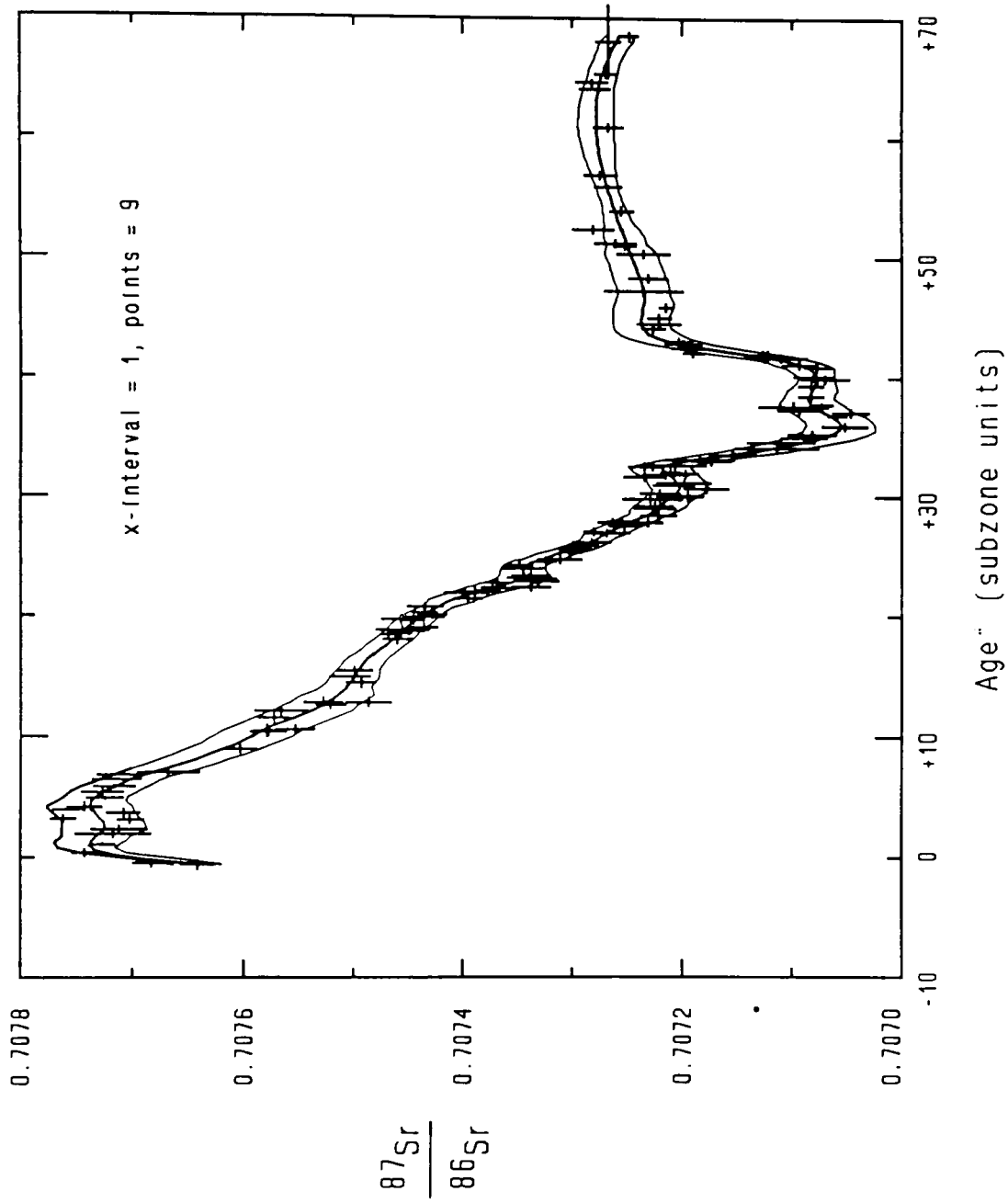

Figure 4.14 Isoplot spline curve for the Lower Jurassic with an x-interval of 1 and 9 data points used for curve fitting (see text and Ludwig, 1990, for explanation.)

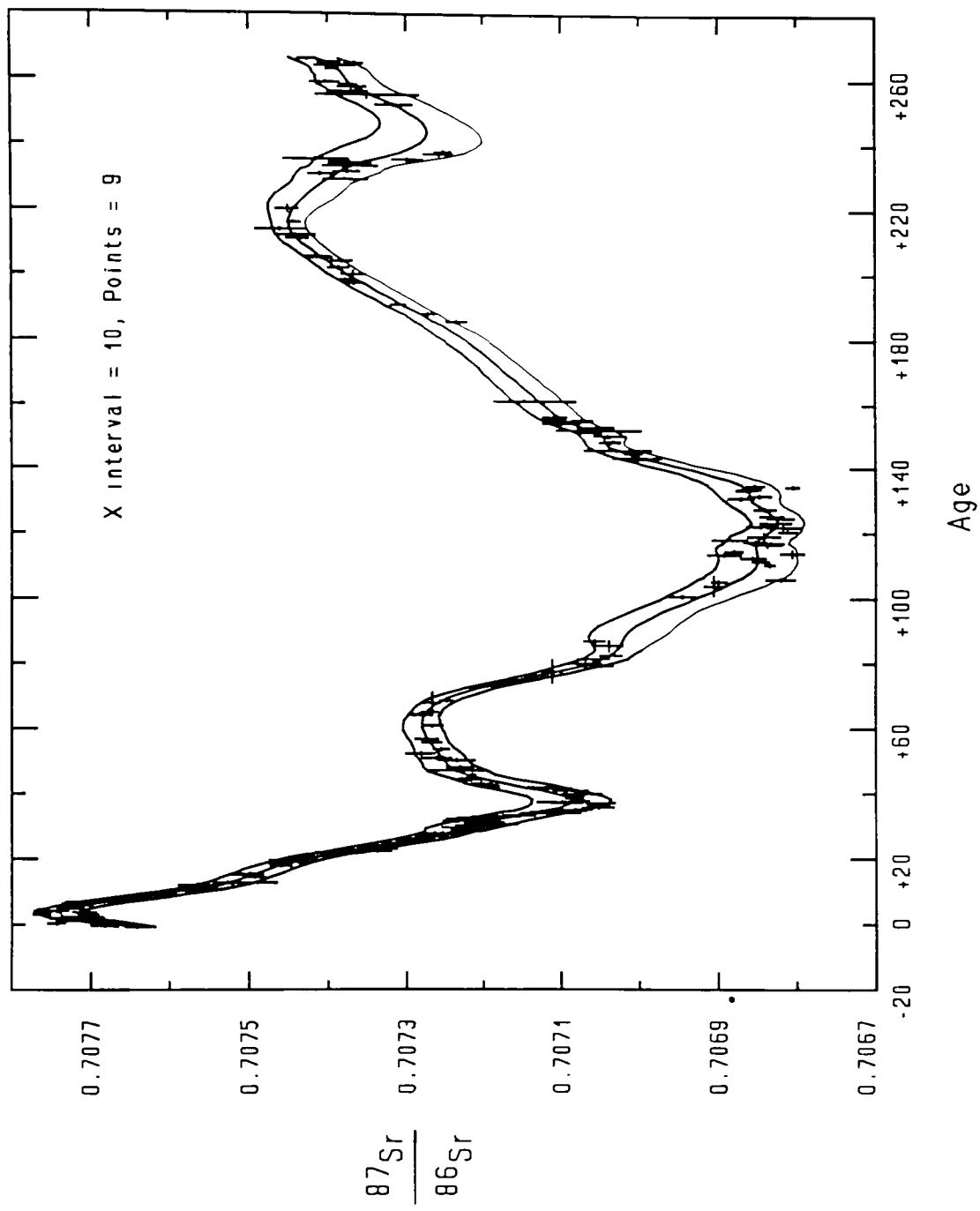

Figure 4.15 Isoplot spline curve for the Jurassic and Lower Cretaceous with an x-interval of 10 and 9 data points used for curve fitting (see text and Ludwig, 1990, for explanation.)

through Barremian a fifth, and the Aptian/Albian interval is divided into two further curves. Clearly, at least until the software improves, it may be simpler over some intervals not to use Isoplot.

Isoplot's spline curves (Fig. 4.15) consist of a central spline representing the best-estimate of the true seawater signal and upper and lower "error envelope" splines intended to enclose most of the data points. These error splines have no rigorous statistical significance and serve only as a visual guide to the degree of data scatter. Note that the curve shows little detail where the data are sparse, such as in the Lower Sinemurian (6 to 13 subzone units; see Tables 2.1, 2.2, and 2.3 for conversion of subzone "ages" to subzone names), whereas where the data are dense, such as in the Pliensbachian (22 to 37 subzone units), the spline curve closely follows the details of the data set.

Isoplot presents the results of its spline calculations both graphically (Fig. 4.16) and on an information screen (Fig. 4.17). The calculated best-estimate ages are based on the intersection of the sample $^{87}Sr/^{86}Sr$ ratio with the central spline curve. Error estimates around this age are calculated in three different ways. The smallest error estimates are based on the interception of the sample 2σ error bars with the central spline curve (listed as "ages for plus- and minus- limit on ratio" in Fig. 4.17). Somewhat larger error bars are based on the interception of the 2σ errors with the error envelopes (listed as "ages from curve upper- and lower- limit" in Fig. 4.17), and the largest error limits are calculated according to a relatively rigorous statistical formulation. The best-estimate age and the statistically derived error limits are presented as the final result at the bottom of the screen (Fig. 4.17).

One obvious test of the stratigraphic resolution of the Lower Jurassic Sr-isotope curve is to run each of the Bedding-Plane Test analyses (Fig. 4.4) as an unknown. The results, presented in Figure 4.18, demonstrate that all but one of the calculated "ages" fall within ± 1 subzone unit of the true age, and that 20 out of 28 plot within ± 0.5 subzone units

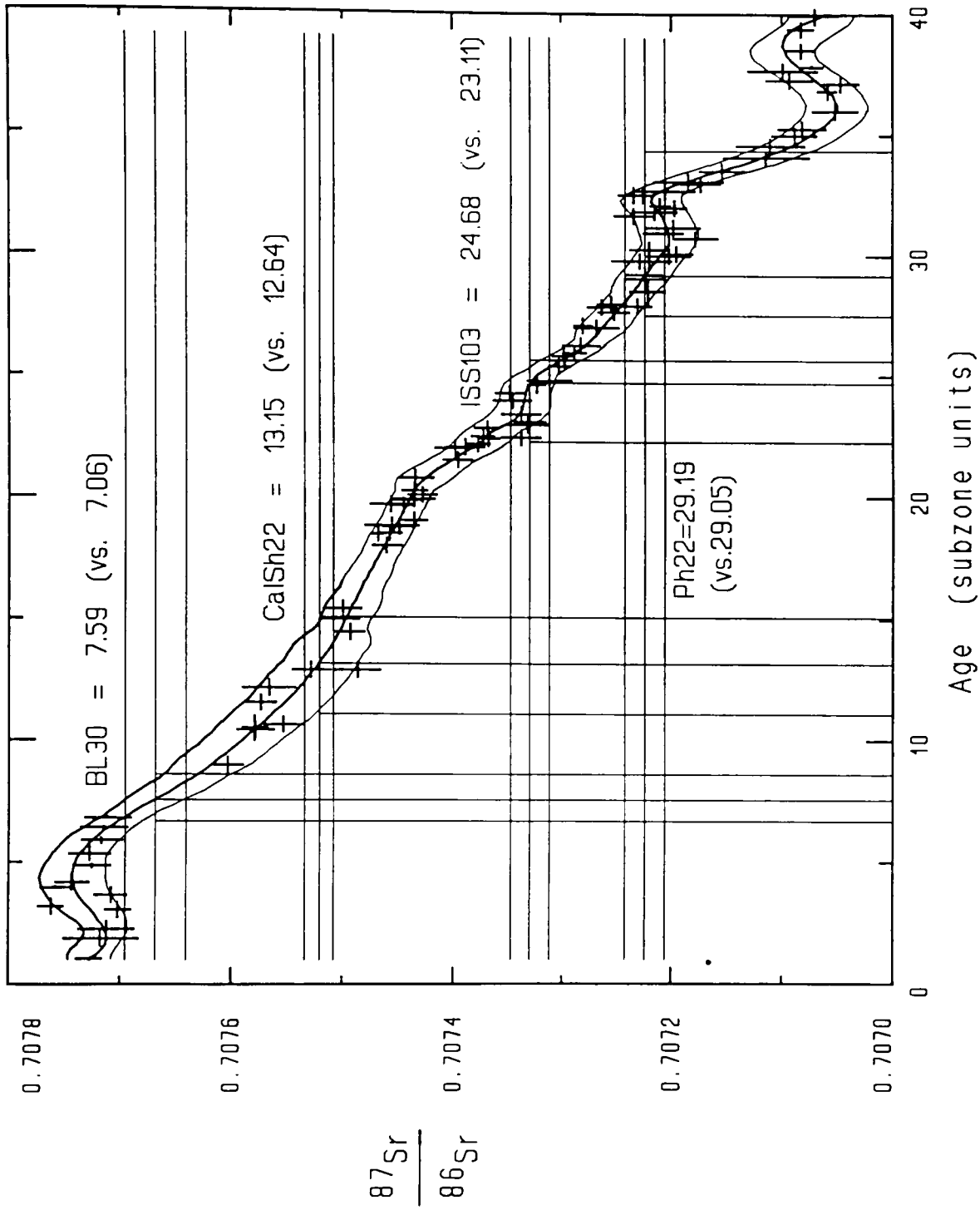

Figure 4.16 Spline curve for the Lower Jurassic showing the results from 4 samples run as unknowns. The calculated results may be compared with the actual "ages" listed in the parentheses.

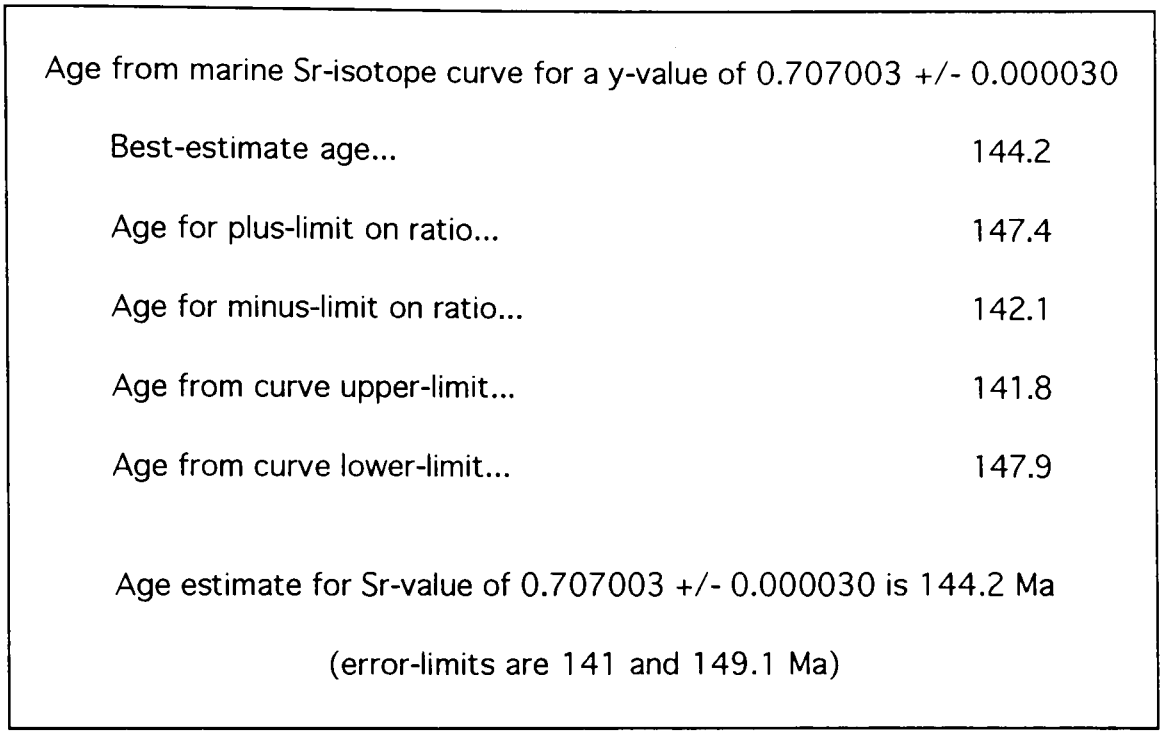

Figure 4.17 Isoplot screen showing typical output from calculated "age" for a sample run as an unknown. Note that the time units are subzone units and not millions of years.

of the true age. It turns out that the statistically derived error estimates presented by Isoplot are nearly always much too generous. Therefore, to give a better feel for the potential accuracy of Sr-isotope stratigraphy and for the age errors associated simply with sample analytical errors, only the uncertainty associated with the interception of the $\pm 2\sigma$ analytical errors with the central spline curve is shown in this and all subsequent diagrams. In the case of the Bedding Plane Test analyses, these error limits, the smallest presented by Isoplot (see Fig. 4.17), intersect the actual age the samples in 23 out of 28 analyses (82%).

Although the Bedding Plane Test is an interesting exercise, it is limited in that the stratigraphic resolution of the Sr-isotope curve varies through time due to variations in the slope of the curve, variability in the sampling density, and the degree of data scatter. Therefore, a useful first step in any study involving Sr-isotope stratigraphy is to test the ability of the relevant sections of the Sr-isotope curve to reproduce the actual ages of

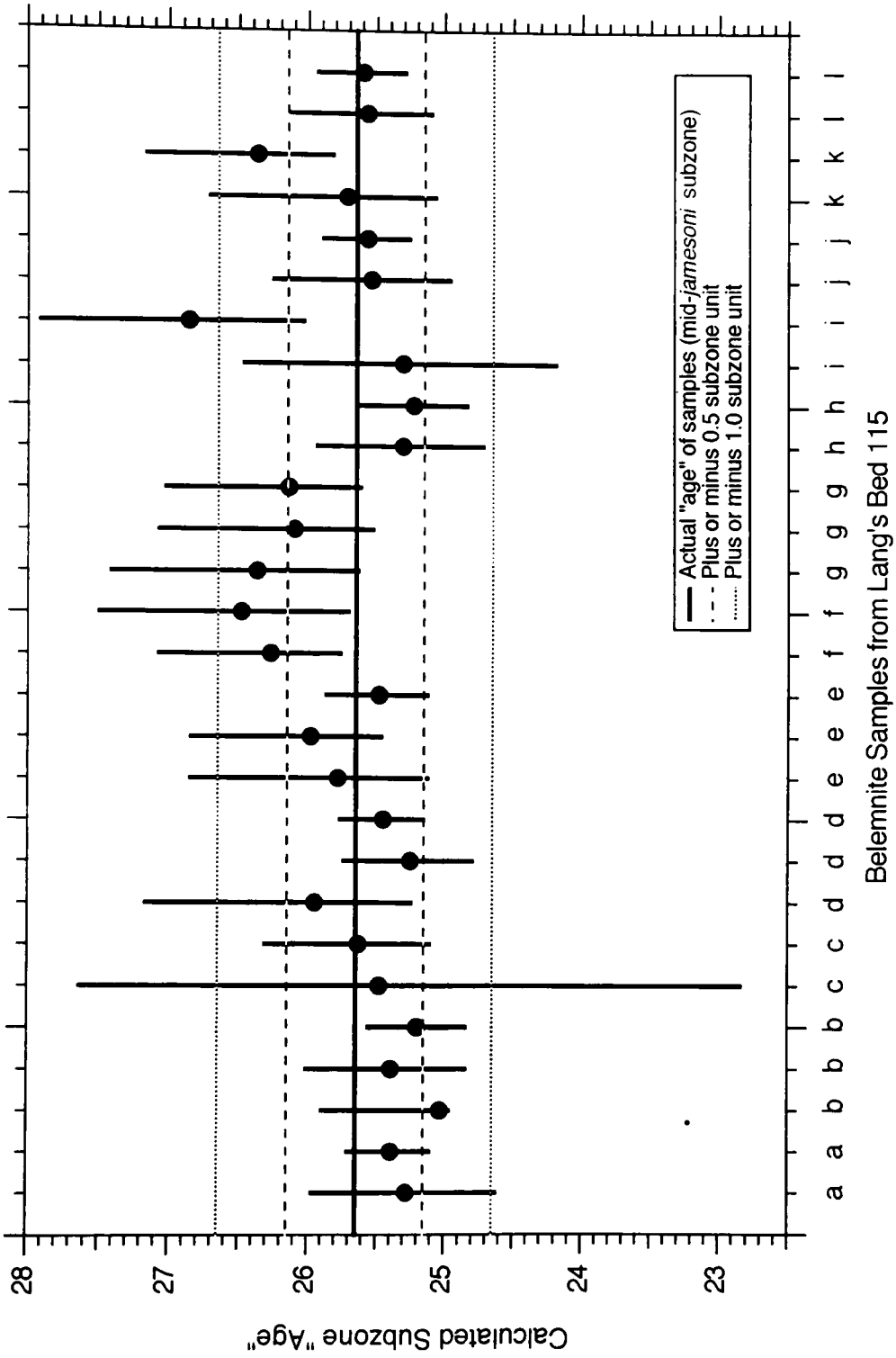

Figure 4.18 Subzone "ages" calculated by Isoplot for the 28 analyses of the 12 belemnites from the bedding plane test (see Fig. 4.4). All but one of the analyses plot within 1 subzone of the true "age" of the samples.

selected samples throughout the data set. This is done by removing a given point from the data set, calculating the spline curve over that interval, and using the spline to calculate the age of the deleted sample. Comparison of the actual and calculated ages yields the highest degree of accuracy possible. It does not take into account diagenetic noise that will vary from locality to locality or the problem regarding the interlaboratory comparison of analytical results. In this study only the Sinemurian-to-Pliensbachian, Toarcian-to-Bajocian, and Oxfordian-to-Barremian intervals are examined because the other intervals do not have a sufficiently dense data set that allows the removal of one point without significantly altering the calculated spline curve. All dates are given in ammonite subzone units (= "ages") because the radiometric time scale is poorly calibrated for the Jurassic and Early Cretaceous and because correlation to the original bio- and litho-stratigraphy of the British sections is a more meaningful exercise.

Figure 4.19 presents the results for the Sinemurian to Pliensbachian segment of the curve. Of the 25 calculated ages, 20 are within one subzone unit of the correct age. Of the 5 that are not, 3 have very large error limits associated with the inflection in the late Pliensbachian Sr-isotope curve (Fig. 4.16). In all cases the calculated "ages" match the actual "ages" within the wide statistically derived error limits (not shown). When just the errors associated with the 2σ analytical errors are considered, 20 out of 25 (80%) include the correct age of the sample. These results suggest that the Sinemurian and Pliensbachian portions of the Sr-isotope curve yield a stratigraphic resolution that is to within at least plus or minus 2 subzone units of time, and that may over some intervals be as good as plus or minus one subzone unit of time. This is roughly equivalent to a resolution of plus or minus 0.5 to 1 Ma using the time scale of Harland *et al.* (1990). Although the late Pliensbachian inflection decreases the resolution possible if just one unknown sample is analyzed, measurement of a whole suite of samples across this interval should reproduce the inflection and thus allow highly precise correlation.

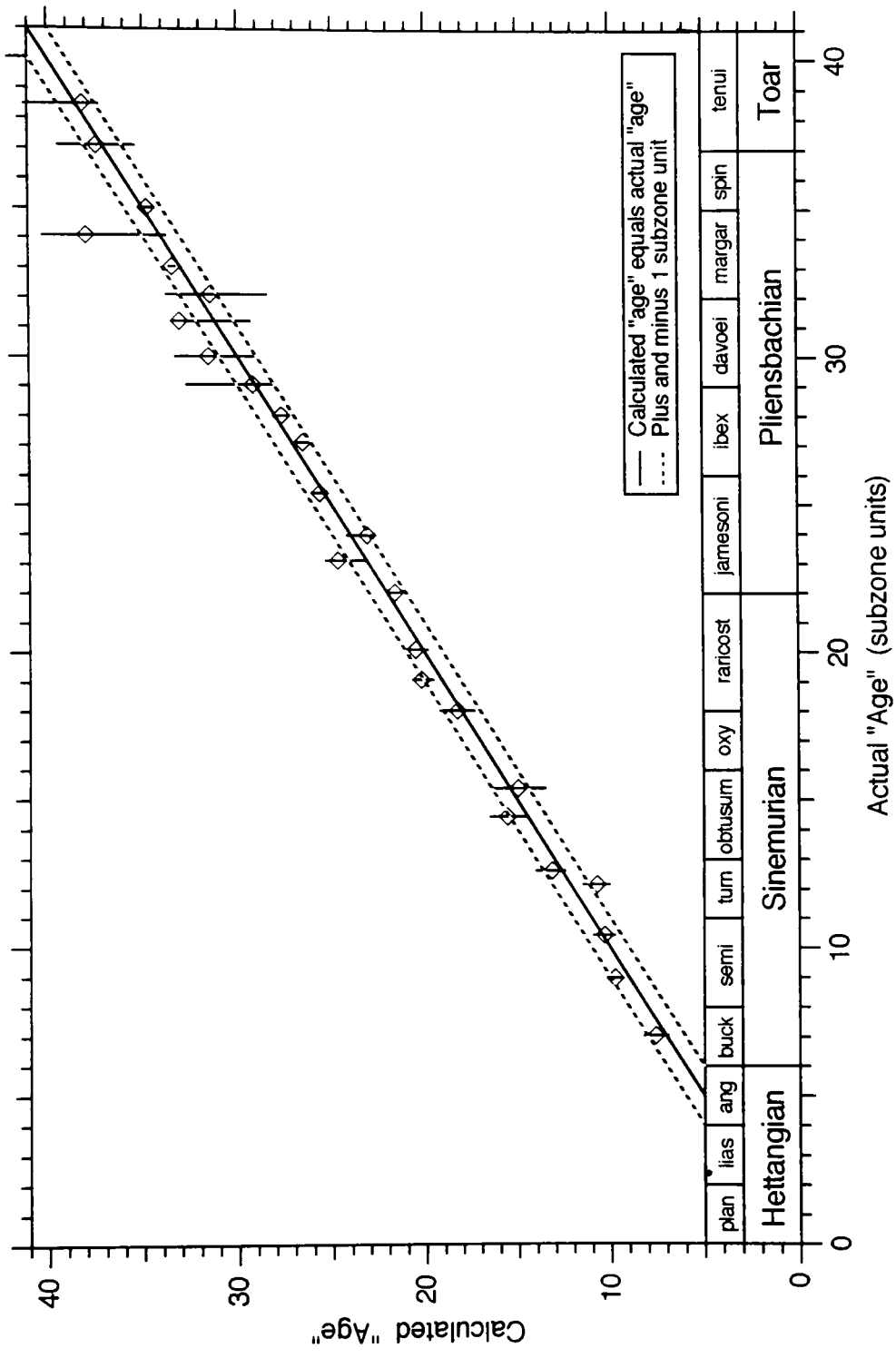

Figure 4.19 Comparison between the actual and the calculated "ages" of Sinemurian and Pliensbachian samples as calculated by Isoplot 2.11. The error bars are based on the intercept of the 2σ analytical errors with the central spline curve. The solid line indicates a perfect match between the calculated and actual "ages". Dotted lines show errors of ±1 subzone.

The loss of stratigraphic resolution that occurs as one approaches a flatter portion of the curve is demonstrated in Figure 4.20. The calculated "ages" are relatively imprecise during the *tenuicostatum* zone, when the curve is fairly flat, and become highly precise and accurate during the steep feature in the *falciferum* zone. The errors and scatter increase dramatically when the curve flattens out into the upper Toarcian and Aalenian (see Fig. 4.13). Even with this loss of resolution, however, all but 2 of the calculated ages plot within two subzone units of the actual age, and the error bars of only 1 sample do not intersect the actual age. (This sample is 1 of 2 in the *tenuicostatum* zone that seem to plot too high compared to neighbouring data but which cannot be eliminated on the basis of high diagenetic Fe concentrations; see Figure 4.3.)

The Upper Jurassic and Lower Cretaceous portions of the Sr-isotope curve are characterised by more data scatter, particularly in the Oxfordian, and sparser data coverage, particularly through the Lower Cretaceous. The effect of the increased scatter in the Oxfordian is seen in larger error bars and calculated "ages" that are more than 2 subzone units away from the correct "ages" (Fig. 4.21). The main effect of a sparse data set is that removing one sample has a relatively large impact on the shape of the calculated spline curve. This results in a higher probability of Isoplot miscalculating the correct "age" of a given sample that has been removed from the data set. As a result, whereas the stratigraphic resolution offered by the Sr-isotope curve is no more than plus or minus roughly 4 subzone units in the Oxfordian, the resolution increases to within 2 subzone units in the Upper Kimmeridgean, and degrades again to roughly 4 subzone units in the Lower Cretaceous. These correspond to a resolution of ±2 Ma, ±1 Ma, and ±4 Ma, respectively, using the time scale of Harland *et al.* (1990).

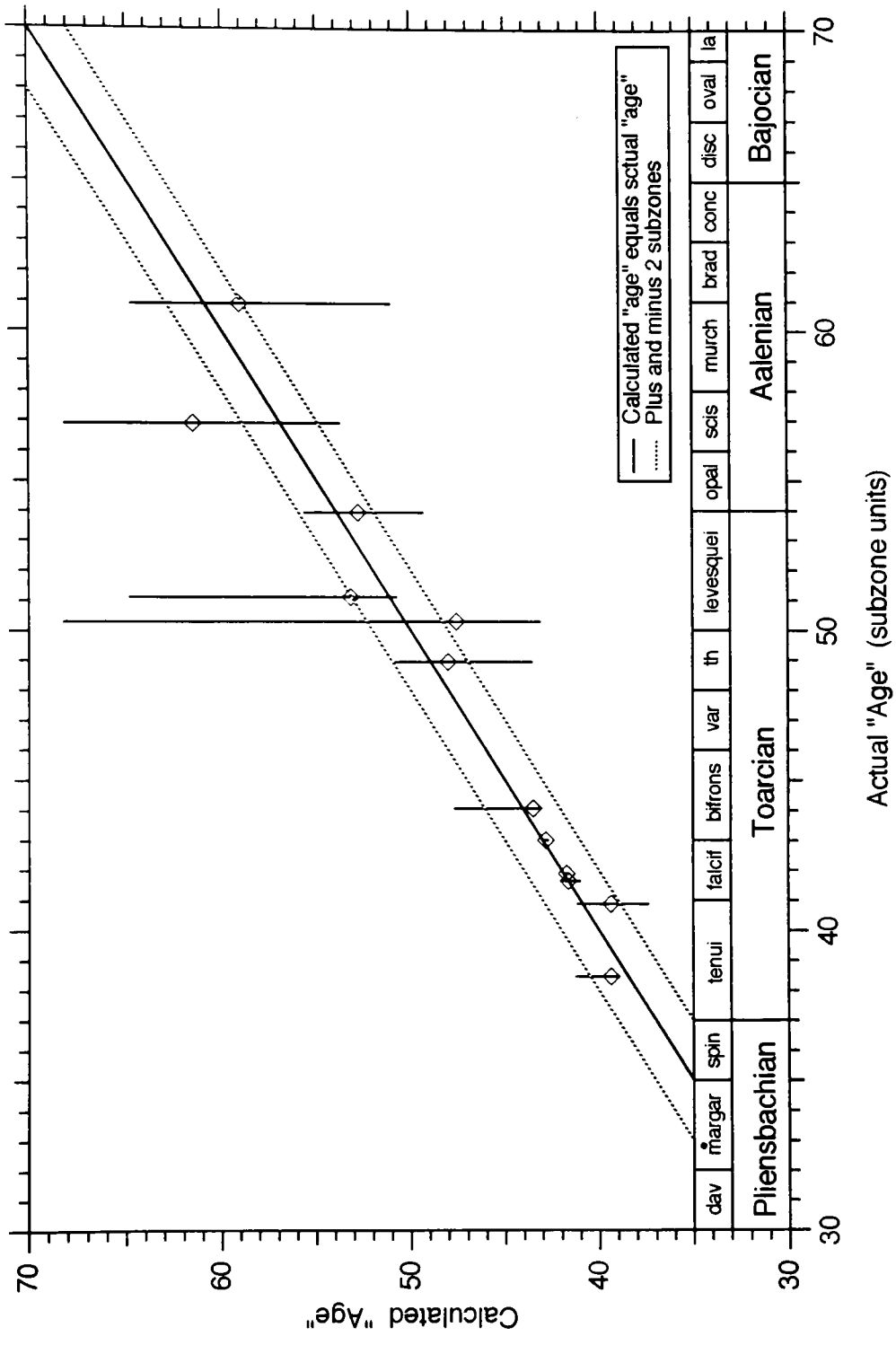

Figure 4.20 Comparison between the actual and the calculated "ages" of Toarcian and Aalenian samples as calculated by Isoplot 2.11. Error bars reflect the intercept of the 2σ analytical errors with the central spline curve. The solid line represents a perfect match between calculated and actual "ages". Dotted lines show errors of ± 2 subzones.

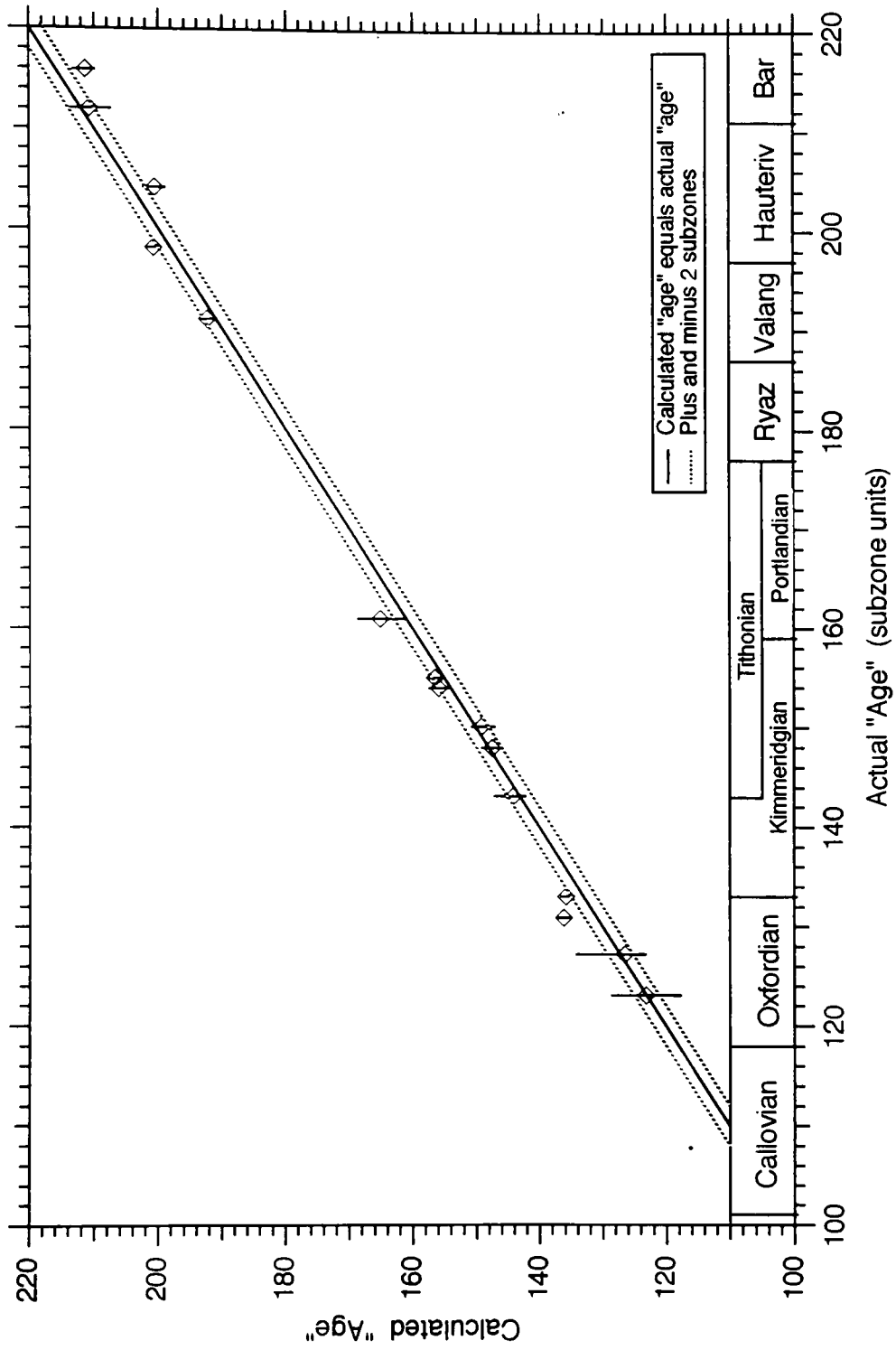

Figure 4.21 Comparison between the actual and the calculated "ages" of Oxfordian-to-Barremian samples as calculated by Isoplot 2.11. Error bars reflect the intercept of the 2σ analytical errors with the central spline curve. The solid line represents a perfect match between calculated and actual "ages". Dotted lines show errors of ± 2 subzones.

4.7 Conclusion: Sr-Isotope Stratigraphy

The combination of well-preserved sample material and a high-resolution lithostratigraphic and biostratigraphic framework makes the seawater Sr-isotope curve derived in this study ideal for the application of Sr-isotope stratigraphy. Although there are several important intervals that require more work, these data offer a highly precise correlation tool that compares favourably with the best of the Cenozoic data (e.g., Hess *et al.*, 1986, 1989; Miller *et al.*, 1988, 1991; Hodell *et al.*, 1989, 1990, 1991). The importance of being able to correlate other sections of the world to the classic Jurassic and Lower Cretaceous sections of Great Britain lies not only in their significance as an international reference standard, but also in that they form one of the key successions used by Haq *et al.* (1987) for the calibration of the sea level curve covering this period. Thus, Sr-isotope stratigraphy may help to provide important constraints as to the relative timing of sequence stratigraphic surfaces and other apparently global events recorded in stratigraphic sections around the world.

Chapter 5: $\partial^{13}C$ and $\partial^{18}O$ in Jurassic and Lower Cretaceous Belemnites and Oysters

5.1 Introduction

The stable isotopes of carbon and oxygen were originally measured in this study as possible indicators of diagenesis. However, because most samples yielded $\partial^{13}C$ and $\partial^{18}O$ values that are indistinguishable from normal marine values, it is possible that belemnites and oysters retain an interpretable palaeoceanographic signal. Ideally, a study focused on stable isotopes in belemnites and oysters would include identification of all fossil material to the finest taxonomic level. Such a study would pay close attention to the isotopic variability within individual specimens and to possible interspecific vital effects in order to define an error envelope around the seawater curve and highlight any systematic patterns that may relate to the life habits of individual taxonomic groups. However, because this study was designed to collect high-quality Sr-isotope data, which are not subject to interspecific vital effects, the data of this study are of use largely as an assessment of the potential ability of belemnites and oysters to record and preserve a stable isotope palaeoseawater signal.

Measurement of the stable isotopes of carbon and especially oxygen in belemnites goes back to the early days of stable isotopic palaeotemperature determinations (Urey *et al.*, 1951; Lowenstam and Epstein, 1954). Palaeotemperature work focusing especially on the Cretaceous flourished during the 50's and the 60's (see references in Naydin *et al.*, 1966; Stevens and Clayton, 1971), but seems to have come to a halt by the early 70's. This was due in part to the fact that the various regional palaeotemperature curves could not be combined to yield a simple global curve and in part to the increasing suspicion that belemnites may not be as well-preserved as originally thought. In this regard, Spaeth *et al.* (1971) seem to have had the final word regarding belemnite preservation. They proposed that living belemnite rostra consisted of alternating concentric layers of solid, clear calcite,

which could remain well-preserved to the present day, and a spongy organic matrix containing spicular calcite needles, which would rot away after death and leave a considerable volume to be replaced by diagenetic calcite. In their model a large but variable proportion of any given belemnite consists of diagenetic calcite and thus renders any palaeotemperature work highly suspect.

Since that time only a few studies have aimed at an improved understanding of the primary structures and diagenesis of belemnites. Veizer (1974) measured the Mn, Fe, Mg, and Sr contents of 40 belemnites and their matrices. Assuming appropriate metal concentrations in seawater and appropriate distribution coefficients for calcite precipitating from seawater, Veizer was able to calculate that most belemnites contain a maximum of about 10 - 20% diagenetic calcite. More recently Sælen (1989) and Sælen and Karstang (1989) used a variety of optical and trace element techniques to learn more about the primary structure and diagenetic history of belemnites. They concluded that belemnites are most likely to be significantly altered along the apical line and alveolus, that different species preserve what appears to be primary differences in trace element and stable isotopic compositions (differences that are unrelated to the lithology of the matrix), and that the very tight spacing of the radial and concentric calcite crystals indicates a very low primary porosity that makes belemnite rostra "rather impervious" to diagenesis. In sum, the available geochemical and micromorphological data suggest that at least some 80 - 90% of a belemnite is primary calcite.

As a final introductory note, it is worth mentioning that all belemnites sampled in this study are visually well-preserved. They are translucent honey-brown to opaque dark brown in colour (depending on whether they come from southern England or Yorkshire, respectively) and all retain the primary concentric banding and radial calcite structure that characterise belemnite rostra. By contrast, a number of belemnites figured by Sælen (1989) and undoubtedly analysed by other authors show irregular whitish areas around the

outside of the fossil. Such belemnites must be diagenetically altered and should be avoided.

5.2 Diagenetic alteration of $\partial^{13}C$ and $\partial^{18}O$

In most studies aimed at discriminating between primary and diagenetic calcite, the diagenetic fluid is assumed to have been meteoric (Stevens and Clayton, 1971; Veizer, 1974; Veizer, 1983; Brand, 1987, 1989; Morrison and Brand, 1988). Meteoric diagenesis is relatively easy to detect using a combination of Sr isotopes, Mn and Fe concentrations, and $\partial^{13}C$ and $\partial^{18}O$ values. The predominance of detrital silicate minerals in most sedimentary sequences means that the diagenetic alteration of a marine carbonate is most likely to raise its $^{87}Sr/^{86}Sr$ ratio and increase its Mn and Fe concentrations. The predominance of isotopically light oxygen in meteoric fluids tends to shift altered bulk carbonate $\partial^{18}O$ towards more negative values. The low abundance of isotopically light dissolved carbon in such waters tends to have little effect on the primary $\partial^{13}C$ signal.

In this study it was shown that belemnites and oysters particularly from mudrocks yield reproducible $^{87}Sr/^{86}Sr$ ratios, have generally low Mn and Fe concentrations, and show $\partial^{13}C$ and $\partial^{18}O$ results that are indistinguishable from plausible marine values (Chapter 3). While these data indicate that meteoric diagenesis has not generally added a significant component to the fossil calcites, they do not eliminate the possibility that the primary stable isotopic ratios were reset during sulphate reduction or one of the other phases of marine burial diagenesis. Therefore, a prerequisite to any interpretation of the $\partial^{13}C$ and $\partial^{18}O$ data obtained in this study is an examination of the sensitivity of the primary isotope ratios to the various stages of diagenesis to which the samples may have been exposed and of the ability of the tracers employed in this study to detect the addition of diagenetic calcites.

This sensitivity analysis is broken into two parts. In the first part the ability of five geochemical tracers to detect the addition of diagenetic calcite is examined using simple mixing diagrams. A variety of diagenetic calcites are added to an unaltered belemnite of assumed composition until the bulk sample would be analytically recognisable as

diagenetically altered. The results of these calculations are then applied in the second part in an effort to reject those samples that are likely to have been altered under one or more diagenetic environments. The remaining samples should either produce a more internally consistent curve in a manner analogous to the Sr-isotope data or show no improvement, depending on the nature and variability of sample diagenesis. Throughout this essay meteoric and burial diagenesis are considered within the context of the mudrocks that dominate the sediments of the Lower Jurassic. Burial diagenesis in carbonates (oolites, iron stones) and sandstones is not directly addressed.

5.2.1 Diagenetic Mixing Lines

Figure 5.1 shows the mixing lines between a belemnite with a primary Sr concentration of 1300 ppm (Veizer, 1974; Sælen and Karstang, 1989) and a $^{87}Sr/^{86}Sr$ ratio of 0.7075, and three end-member diagenetic calcites. Over densely sampled intervals where well-preserved fossil material yields consistent Sr-isotope data tightly defining a curve, diagenetically altered material may be detected if its $^{87}Sr/^{86}Sr$ ratio is more than 0.000050 above the main trend of the data. If the deviation from the primary Sr-isotopic composition cannot be so precisely determined, Sr isotopes become markedly less effective at constraining the maximum amount of diagenetic calcite due to the 1/x form of the mixing lines. The range of possible Sr contents and isotopic ratios is large for diagenetic calcites, depending on the relative contributions from the break-down of silicate rocks and the recrystallisation of aragonite and other Sr-rich minerals. Curve 1 (Fig. 5.1) shows a mixing line with what is probably an extreme end-member of meteoric diagenesis; most diagenetic calcites in marine rocks are likely to have $^{87}Sr/^{86}Sr$ ratios below 0.7105 and Sr concentrations in excess of 100 ppm. In this example if the proportion of diagenetic calcite exceeds 20%, the sample $^{87}Sr/^{86}Sr$ ratio is raised above the diagenetic detection limit of 0.000050 above the primary ratio of 0.707500. Increasing the Sr concentration in this meteoric calcite from 100 ppm to 1000 ppm causes the curve to move towards a straight

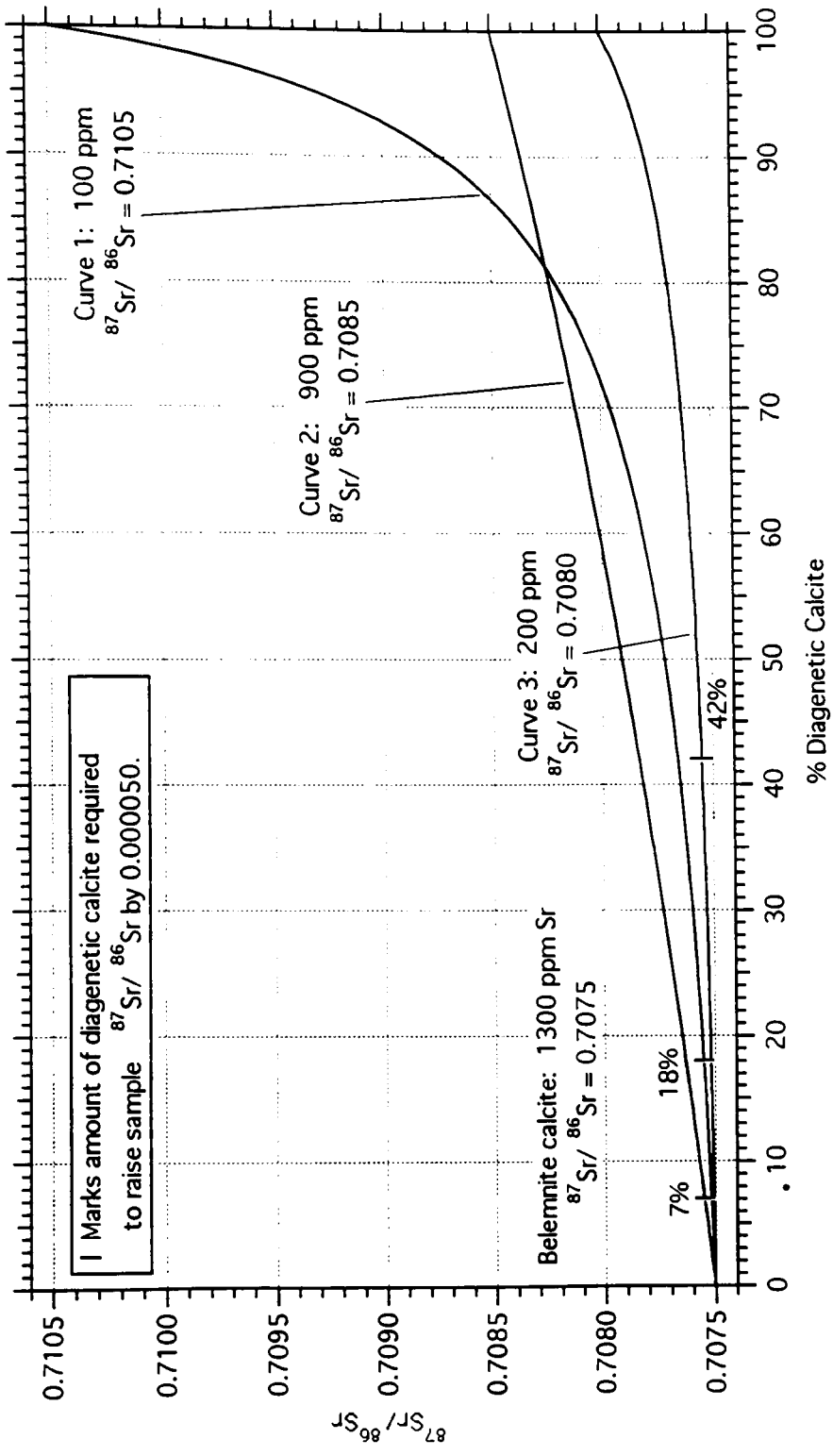

Figure 5.1: Mixing curves between primary belemnite calcite and three end-member diagenetic calcites showing the maximum amounts of diagenetic calcite that can be incorporated before being detected as an offset of the primary $^{87}Sr/^{86}Sr$ ratio.

line connecting the primary $^{87}Sr/^{86}Sr$ of 0.7075 with the diagenetic end-member at 0.7105, with the result that the Sr isotopes become increasingly sensitive to addition of diagenetic calcite.

The other two end-members in Figure 5.1 are more typical examples of what might be expected for diagenetically altered Jurassic carbonate (Emery *et al.*, 1987; Sellwood *et al.*, 1989). The diagenetic Sr-isotope ratios are only moderately above the primary ratio of 0.7075 and Sr concentrations range between 100 and 900 ppm (Veizer, 1974; Al-Aasm and Veizer, 1982). The Curve 2 diagenetic calcite (900 ppm Sr, 0.7085) is detectable once it exceeds about 10% of the bulk sample whereas the Curve 3 example (100 ppm, 0.7080) allows up to 40% secondary calcite before it raises the primary $^{87}Sr/^{86}Sr$ ratio by more than 0.000050.

These results suggest that Sr isotopes should be effective at detecting meteoric diagenesis, which typically involves relatively radiogenic Sr, while remaining insensitive to marine diagenesis. During early burial diagenesis the stability of the detrital silicate minerals plus the dissolution/recrystallisation of aragonite and other carbonate phases should lead to a diagenetic solution with $^{87}Sr/^{86}Sr$ ratios near primary marine values. While advection of pore waters from deeper compacting sediments does bring up older marine Sr, the isotopic composition of these fluids will not be much different from the primary marine values. Thus Sr-isotopes remain insensitive to burial diagenesis until burial has reached the point at which detrital silicate minerals begin to recrystallise and inject isotopically distinctive Sr. Sr isotopes are not directly used in this study to highlight diagenetically altered samples because of the relatively limited conditions under which alteration of the primary signal occurs and because Fe concentrations tend to highlight the same samples as do the Sr isotopes (Chapter 3).

Mixing diagrams for Mn and Fe (Fig. 5.2) yield similar but slightly tighter constraints on fossil diagenesis. Calcites precipitating under reducing conditions in

sediments containing detrital minerals are likely to show high concentrations of Mn and Fe. For example, diagenetic calcite apparently precipitating from the oil field brines of the Jurassic Smackover Formation of the U.S. Gulf Coast contains some 500 ppm Mn and 2000 ppm Fe (Moore, 1989). A mixture of such calcite with primary belemnite calcite (minima of 5 ppm Mn and 25 ppm Fe) requires only 9% and 6% diagenetic calcite, respectively, to move the bulk sample beyond the 50ppm Mn and 150 ppm Fe limits established by the Lower Jurassic Sr-isotope data as indicating significant diagenetic alteration. Even more restrictive constraints are imposed if the primary belemnite concentrations are set at the maximum primary limits of 15 ppm Mn and 60 ppm Fe (Chapter 3; Fig. 3.2). If a calcite contains only 100 ppm Mn and 300 ppm Fe (twice the Sr-isotope diagenetic limits), nearly 50% of a sample can be diagenetic calcite before exceeding the 50 ppm Mn and 150 ppm Fe limits. Thus, like Sr isotopes, Mn and Fe can effectively detect meteoric diagenesis, but only in the case when such diagenesis takes place under reducing conditions.

Mn and Fe are probably ineffective at detecting calcite precipitated during sulphate reduction. This is because the precipitation of Mn and Fe sulphides keeps pore-water concentrations of these elements low. However, whereas the stability of detrital silicate minerals and the instability of aragonite render Sr isotopes insensitive to calcite precipitated during the more advanced burial diagenetic stages of methanogenesis and perhaps decarboxylation, the lack of reduced sulphur species in these pore waters allows Mn and Fe concentrations to reach levels comparable to and in excess of the Smackover Formation cements (Astin and Scotchman, 1988). In fact, ferroan carbonates and siderites are frequently associated with methanogenesis (Irwin *et al.*, 1977; Matsumoto, 1983; Scotchman, 1991). As a result, in contrast to Sr, Mn and Fe should be very effective at detecting calcite precipitated during the burial diagenetic zones of methanogenesis and decarboxylation.

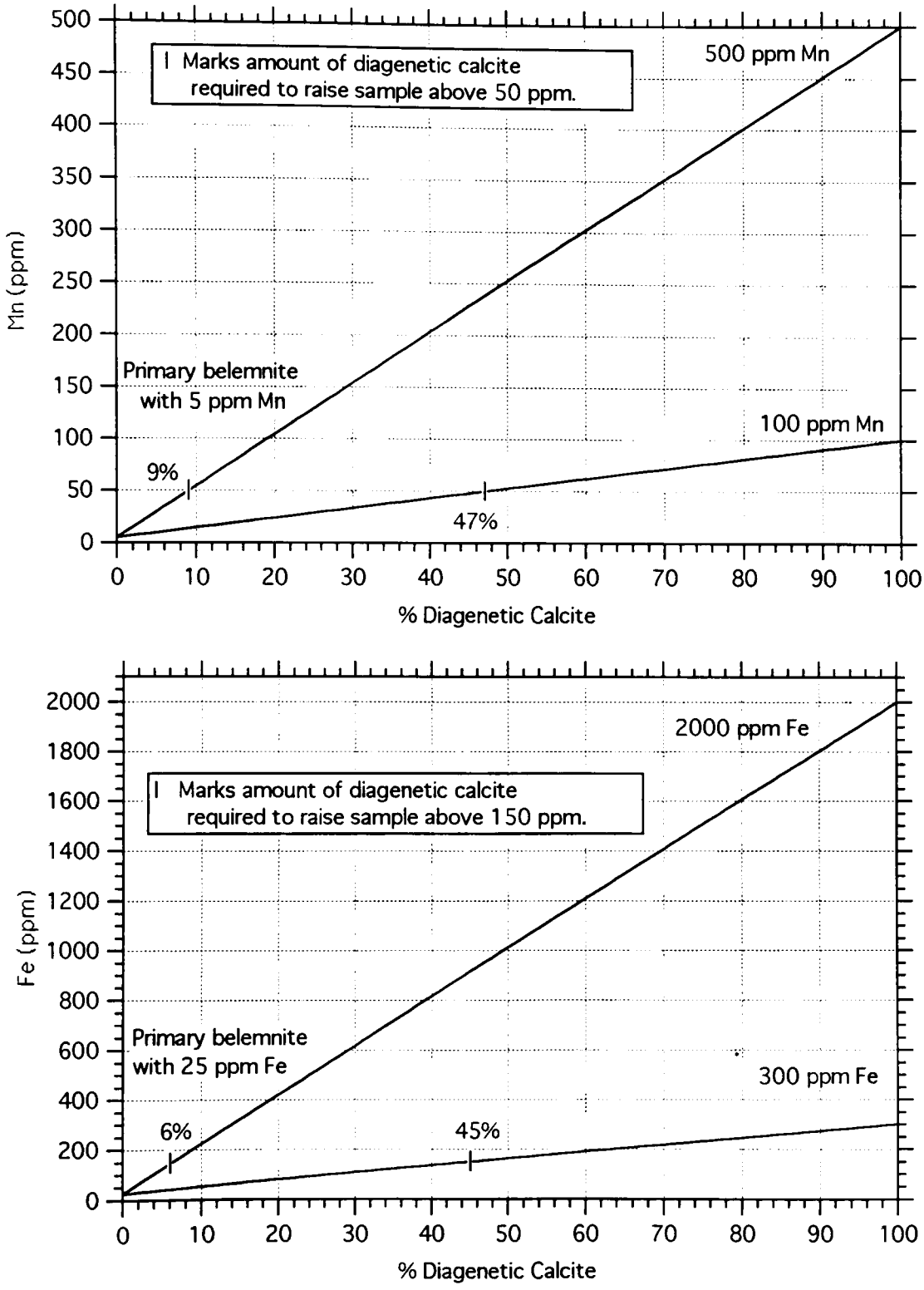

Figure 5.2: Mixing curves between a primary belemnite and two end-member diagenetic calcites showing the maximum amounts of diagenetic calcite that can be incorporated before being detected as elevated Mn (top) or Fe (bottom) concentrations.

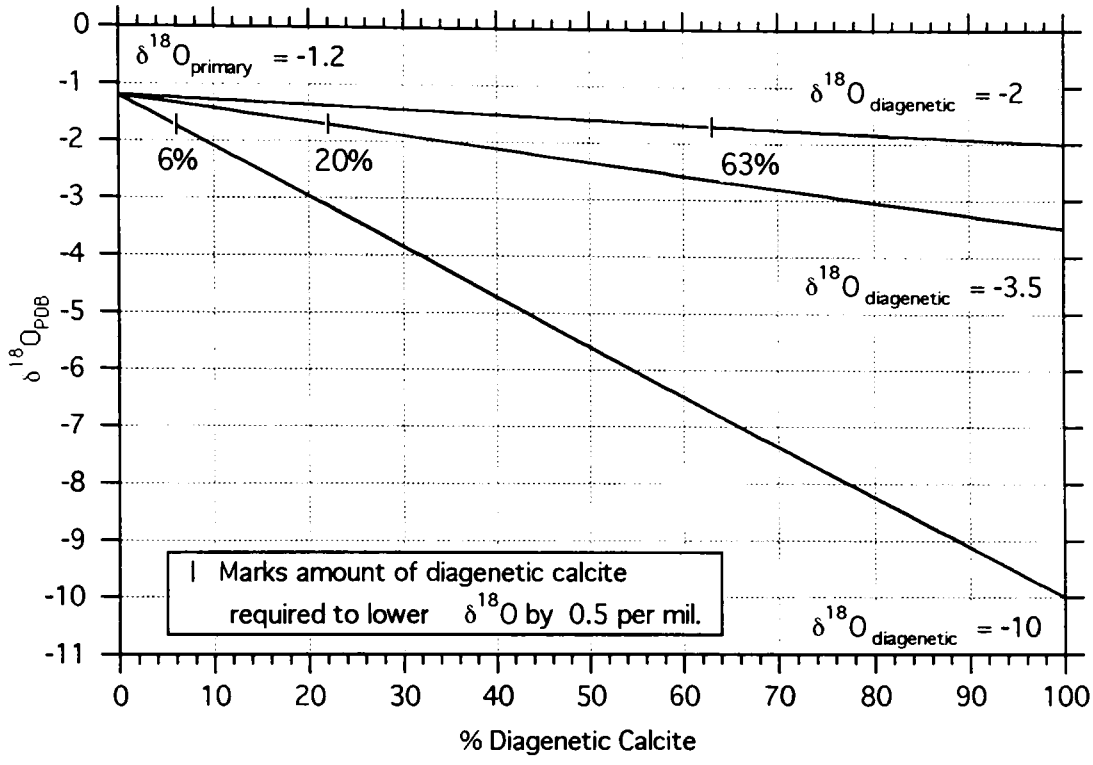

Figure 5.3: Mixing curves between a primary belemnite and three end-member diagenetic calcites showing the sensitivity of primary belemnite $\partial^{18}O$ to the incorporation of various diagenetic calcites.

Figure 5.3 shows the mixing lines for a belemnite with a primary $\partial^{18}O$ of -1.2‰, appropriate for a pre-glacial, ice-free world (Shackleton and Kennett, 1975), and 2 diagenetic calcites with $\partial^{18}O$ values typical of nodules thought to have formed by sulphate reduction (Irwin *et al.*, 1977; Coleman and Raiswell, 1981; Astin and Scotchman, 1988; Scotchman, 1991; Sass *et al.*, 1991). Most examples attributed to sulphate reduction fall within the range $\partial^{18}O$ = -3.5 to -2‰. While more negative values have been observed in sulphate reduction nodules (down to -10‰), $\partial^{18}O$ values lower than -4‰ are generally associated with carbonate precipitated under the higher temperatures associated with the deeper burial depths of methanogenesis and decarboxylation and with meteorically

precipitated carbonates (Lohmann, 1988). A diagenetically induced offset of 0.5‰ is taken as the maximum acceptable limit to the distortion of the primary marine $\partial^{18}O$ signal.

Incorporation of more than 6 to 20% meteoric or deep-burial carbonate with a $\partial^{18}O$ of less than -3.5‰ causes a significant alteration of the primary belemnite signal (Fig. 5.3). However, belemnites altered in the zone of sulphate reduction can incorporate between 20 and 63% secondary calcite at -2 to -3.5‰ before the $\partial^{18}O$ composition is lowered by more than 0.5‰. Thus, while primary $\partial^{18}O$ values are likely to be retained during sulphate reduction, $\partial^{18}O$, Mn, and Fe should all be strongly affected by other types of diagenesis.

Figure 5.4 shows the mixing lines between a belemnite with $\partial^{13}C = +2‰$ and three diagenetic calcite end-members. Meteoric diagenetic carbonates can have $\partial^{13}C$ values ranging between the host-rock average (little or no offset from the primary marine values) and less than -10‰ if precipitation occurs near a soil containing root-derived CO_2 (Lohmann, 1988). Carbonates formed during early marine burial diagenesis show markedly different $\partial^{13}C$ values, depending on the zone in which they precipitate. Sulphate reduction tends to produce strongly negative $\partial^{13}C$ values typically in the range of -10 to -16‰ (Irwin *et al.*, 1977; Coleman and Raiswell, 1981). Mixture of bicarbonate produced during sulphate reduction with bicarbonate derived either from normal marine carbonates or methanogenic carbonates produces intermediate $\partial^{13}C$ values ranging between -2 to -6‰ (Astin and Scotchman, 1988; Scotchman, 1991). During methanogenesis the production of isotopically very light methane ($\partial^{13}C = -65$ to -75‰; Irwin *et al.*, 1977; Claypool and Threlkeld, 1983) leaves behind a residual reservoir of isotopically heavy bicarbonate. As a result, methanogenic carbonates tend to show positive $\partial^{13}C$ values of up to +8‰ (Irwin *et al.*, 1977; Campos and Hallam, 1979). Decarboxylation tends to produce $\partial^{13}C$ values similar to those of sulphate reduction.

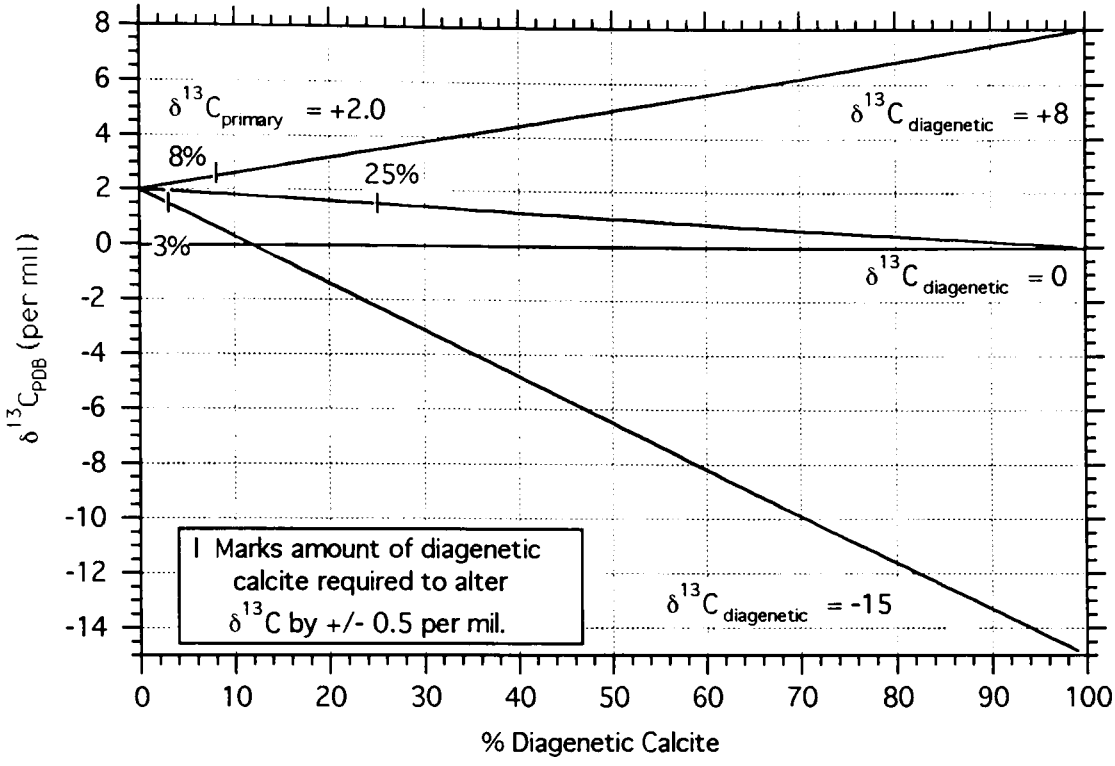

Figure 5.4: Mixing curves between a primary belemnite and three end-member diagenetic calcites showing the sensitivity of primary belemnite $\partial^{13}C$ to the incorporation of various diagenetic calcites.

Although meteoric diagenesis can produce carbonates with quite negative $\partial^{13}C$ values, the overwhelming mass of host rock carbon relative to the fluid carbon means that meteorically derived secondary carbonate generally has only a slight effect on the bulk $\partial^{13}C$ values. By contrast, incorporation of only 3% diagenetic carbonate precipitated during sulphate reduction ($\partial^{13}C_{diag} \approx$ -15‰) produces a 0.5‰ deviation from the primary value (Fig. 5.4). Fossil $\partial^{13}C$ is therefore very sensitive to the incorporation of carbonate during sulphate reduction or methanogenesis. During methanogenesis the porewater $\partial^{13}C$ values tend towards +8‰ and the primary belemnite $\partial^{13}C$ signal is again highly sensitive to alteration. Incorporation of some 10% diagenetic calcite, depending on the $\partial^{13}C$ actually attained by the methanogenic carbonate, is sufficient to significantly alter the primary bulk fossil $\partial^{13}C$ composition.

In summary, if the belemnites and oysters analysed in this study were largely altered under meteoric conditions, removal of samples with altered Sr, Mn, and Fe values should

reduce the scatter in the $\partial^{18}O$ data while having little impact on the quality of the $\partial^{13}C$ data. By contrast, if most diagenesis occurred during methanogenesis or deeper burial, removal of high Mn and Fe samples should variably improve the scatter in both data sets, depending on the temperatures of alteration and the extent of methanogenic production of isotopically heavy carbon. If most diagenesis occurred during sulphate reduction, however, Mn, Fe, $\partial^{18}O$, and $^{87}Sr/^{86}Sr$ should remain largely unaffected whereas the $\partial^{13}C$ should show significant scatter towards negative values.

5.2.2 Results for $\partial^{18}O$ and $\partial^{13}C$

The most consistent pattern between $\partial^{18}O$ values and Mn and Fe concentrations is that the more metal-rich samples tend to plot nearer the bottom of the envelope of data scatter (Figs. 5.5, 5.6). The most altered samples with respect to oxygen ($\partial^{18}O$ « -3.5‰) show no consistent pattern with respect to metal enrichments, indicating that these samples were probably altered under a variety of conditions. A similar pattern is observed in the carbon isotope data, except that in this case the more metal-enriched samples tend to plot along the *top* of the envelope of data scatter (Fig. 5.7, 5.8). The most altered samples with respect to $\partial^{13}C$ (« -1.5‰) tend to have high Mn and Fe concentrations, but the number of such altered samples is small. Another general pattern is that higher Mn and Fe concentrations tend to be associated with the Lower Jurassic Yorkshire samples as compared to those from Dorset (see Chapter 3). Accordingly, the Yorkshire $\partial^{18}O$ data tend to plot lower and the $\partial^{13}C$ data tend to plot higher than the respective Dorset data (Figs. 5.9, 5.10).

Taken alone, the stable isotope data could be interpreted in terms of slightly warmer (lower $\partial^{18}O$) and more productive (higher $\partial^{13}C$) waters in Yorkshire as compared to Dorset. However, in combination with the Mn and Fe data, it seems more logical to conclude that the Yorkshire samples tended to incorporate more methanogenic calcite than did the Dorset samples. Complete fossilisation of the Dorset belemnites during sulphate reduction is consistent with their generally low Mn and Fe concentrations and implies that the $\partial^{18}O$ values

should be indistinguishable from the primary belemnite values whereas the $\partial^{13}C$ values may be lowered somewhat by the incorporation of unknown (but small) quantities of -15‰ diagenetic calcite. The fossilisation of the Yorkshire belemnites during methanogenesis is consistent with their generally higher Mn and Fe concentrations, lower $\partial^{18}O$ values associated with the higher temperatures found at deeper burial depths, and with the more positive $\partial^{13}C$ values that could either be associated with a more primary signal or with variable incorporation of isotopically heavy methanogenic calcites. Because methanogenesis takes place once pore waters are placed out of reach of the diffusion of SO_4^{2-} from overlying seawater (beginning about 10 m below the sediment-water interface; Claypool and Threlkeld, 1983), the fossilisation of the Yorkshire belemnites during the zone of methanogenesis is consistent with the generally higher sedimentation rates in Yorkshire as compared to Dorset.

In conclusion, Mn and Fe are not useful in this study for distinguishing altered stable isotopic values from unaltered values. However, systematic patterns between the Mn and Fe data and the $\partial^{18}O$ and $\partial^{13}C$ data indicate that the belemnite and oyster data set has been at least slightly affected by diagenesis. The Dorset data may be affected by the incorporation of sulphate reduction calcite. This implies that whereas the $\partial^{18}O$ values may be taken as representative of the original biogenic calcites, the $\partial^{13}C$ values are likely to be displaced towards more negative values. The Yorkshire data are more consistent with the inclusion of methanogenic calcite in the fossil samples. This implies that whereas the measured belemnite $\partial^{18}O$ values may be too low, the $\partial^{13}C$ values may be too high. However, the Yorkshire $\partial^{13}C$ values are more likely to be more accurate than the corresponding Dorset data because the methanogenic calcites are less positive (up to +8‰) than the sulphate reduction calcites are negative (typically -15‰). At present it is not possible to go beyond this largely qualitative assessment of the extent of diagenetic alteration of the primary marine signal in the sampled belemnites and oysters.

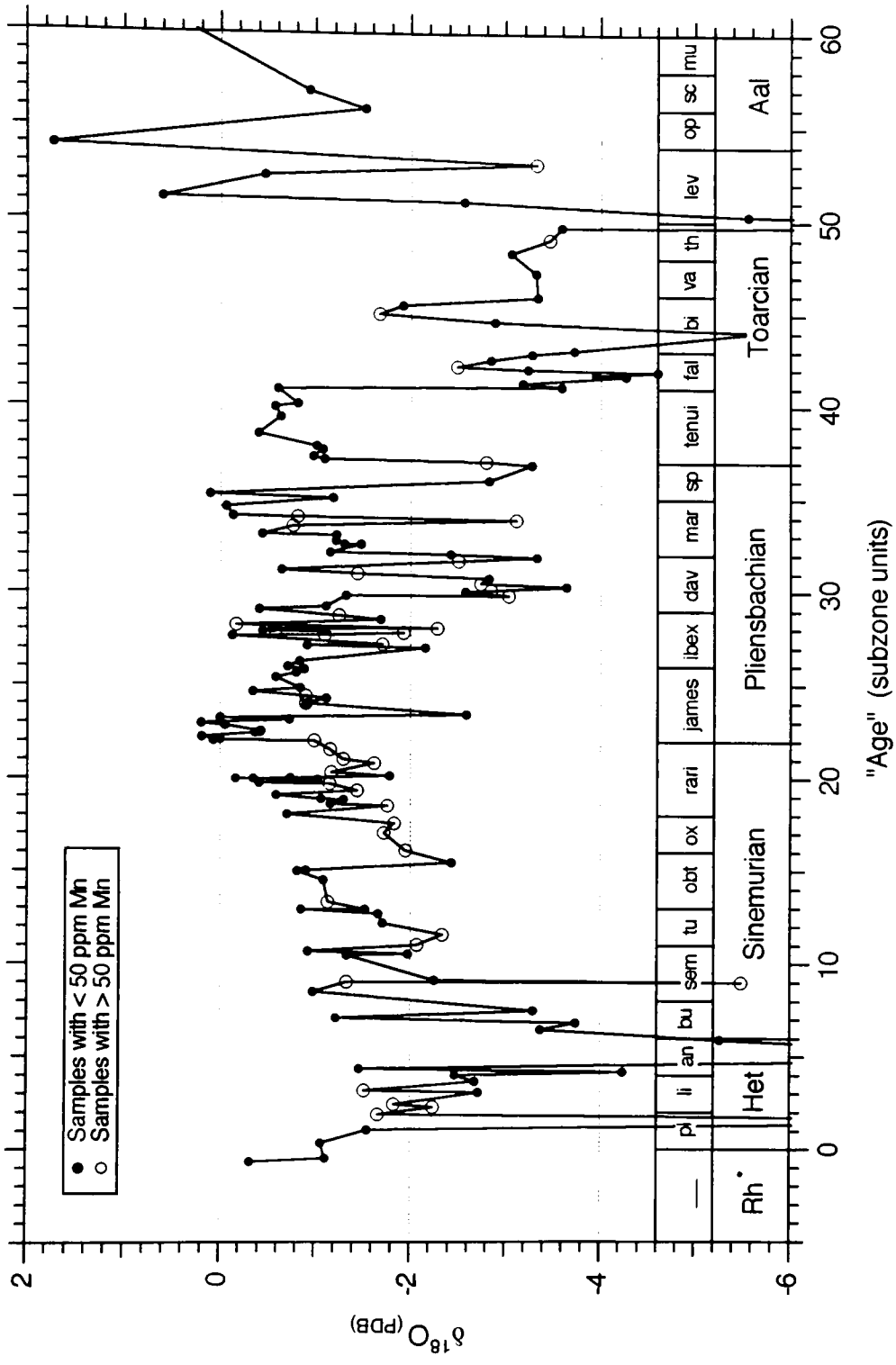

Figure 5.5: Comparison between $\partial^{18}O$ values of belemnite and oyster samples containing more and less than 50 ppm Mn. Samples with less than 50 ppm Mn tend to be well-preserved with respect to their Sr-isotopic compositions; selection of a different Mn cut-off does not significantly affect the ability of Mn to resolve between apparently altered and unaltered material.

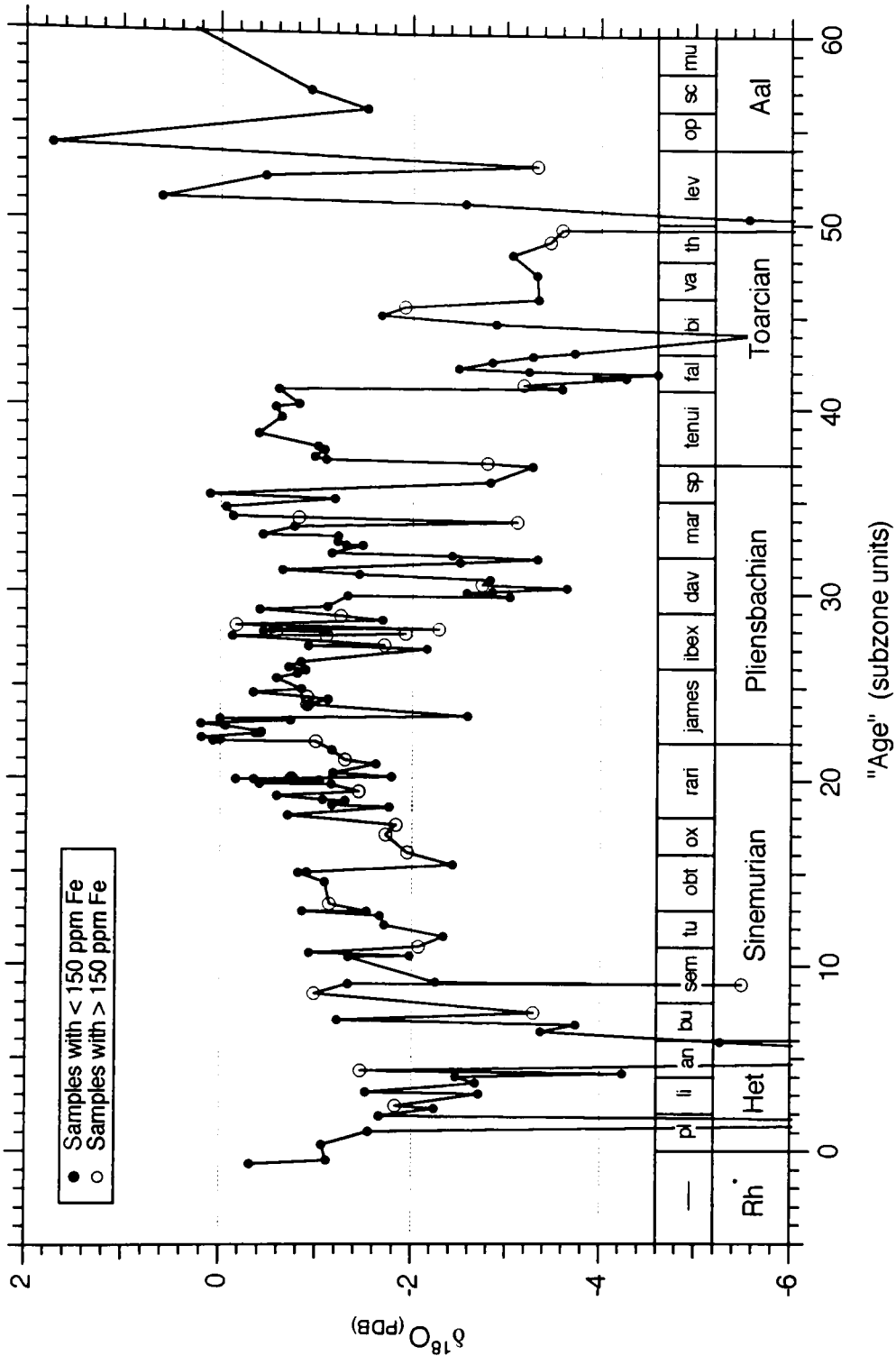

Figure 5.6: Comparison between $\partial^{18}O$ values of belemnite and oyster samples containing more and less than 150 ppm Fe. Samples with less than 150 ppm Fe tend to be well-preserved with respect to their Sr-isotopic compositions; selection of a different Fe cut-off does not significantly affect the ability of Fe to resolve between apparently altered and unaltered material.

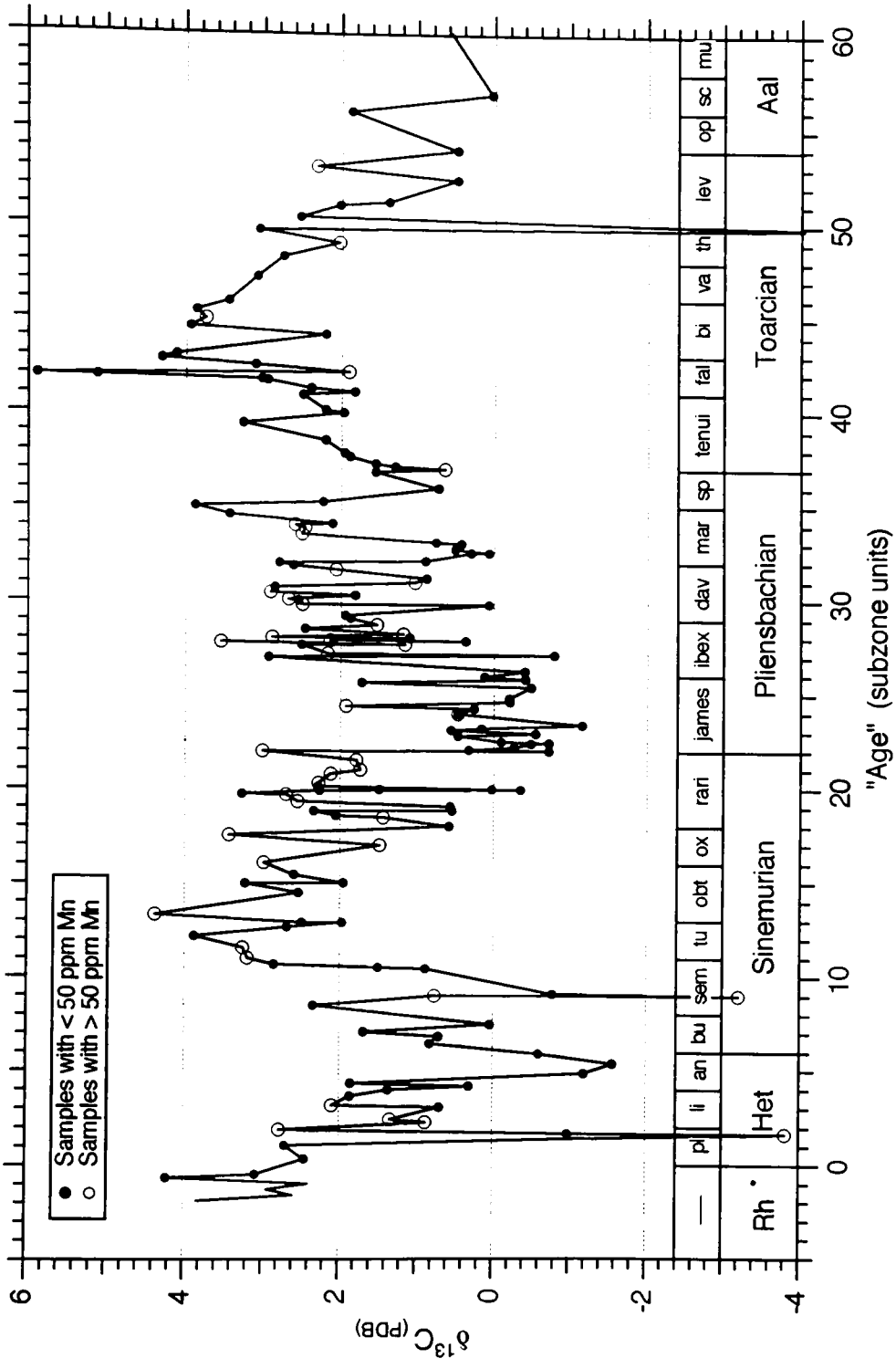

Figure 5.7: Comparison between $\partial^{13}C$ values of belemnite and oyster samples containing more and less than 50 ppm Mn. Samples with less than 50 ppm Mn tend to be well-preserved with respect to their Sr-isotopic compositions; selection of a different Mn cut-off does not significantly affect the ability of Mn to resolve between apparently altered and unaltered material.

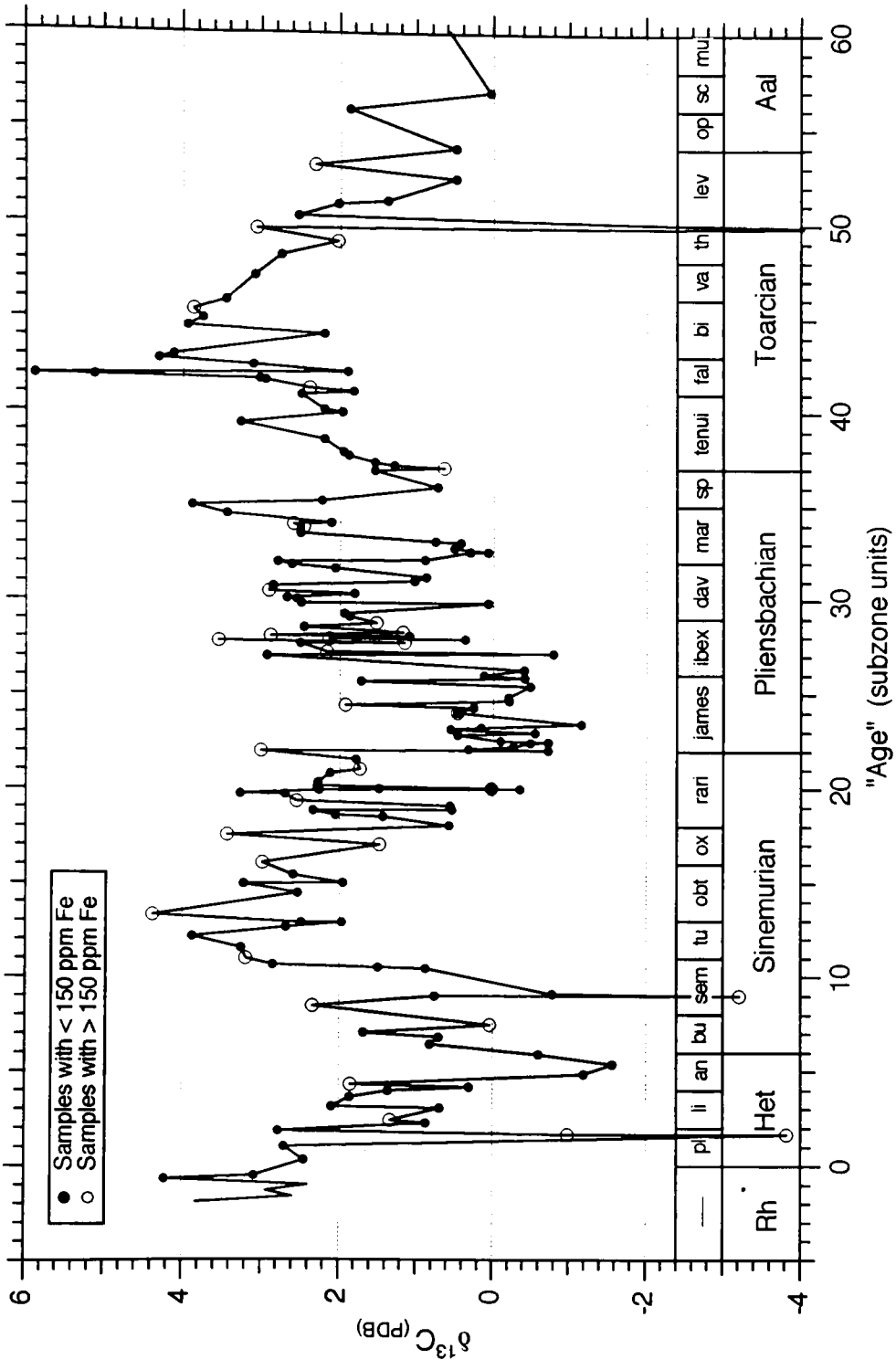

Figure 5.8: Comparison between $\partial^{13}C$ values of belemnite and oyster samples containing more and less than 150 ppm Fe. Samples with less than 150 ppm Fe tend to be well-preserved with respect to their Sr-isotopic compositions; selection of a different Fe cut-off does not significantly affect the ability of Fe to resolve between apparently altered and unaltered material.

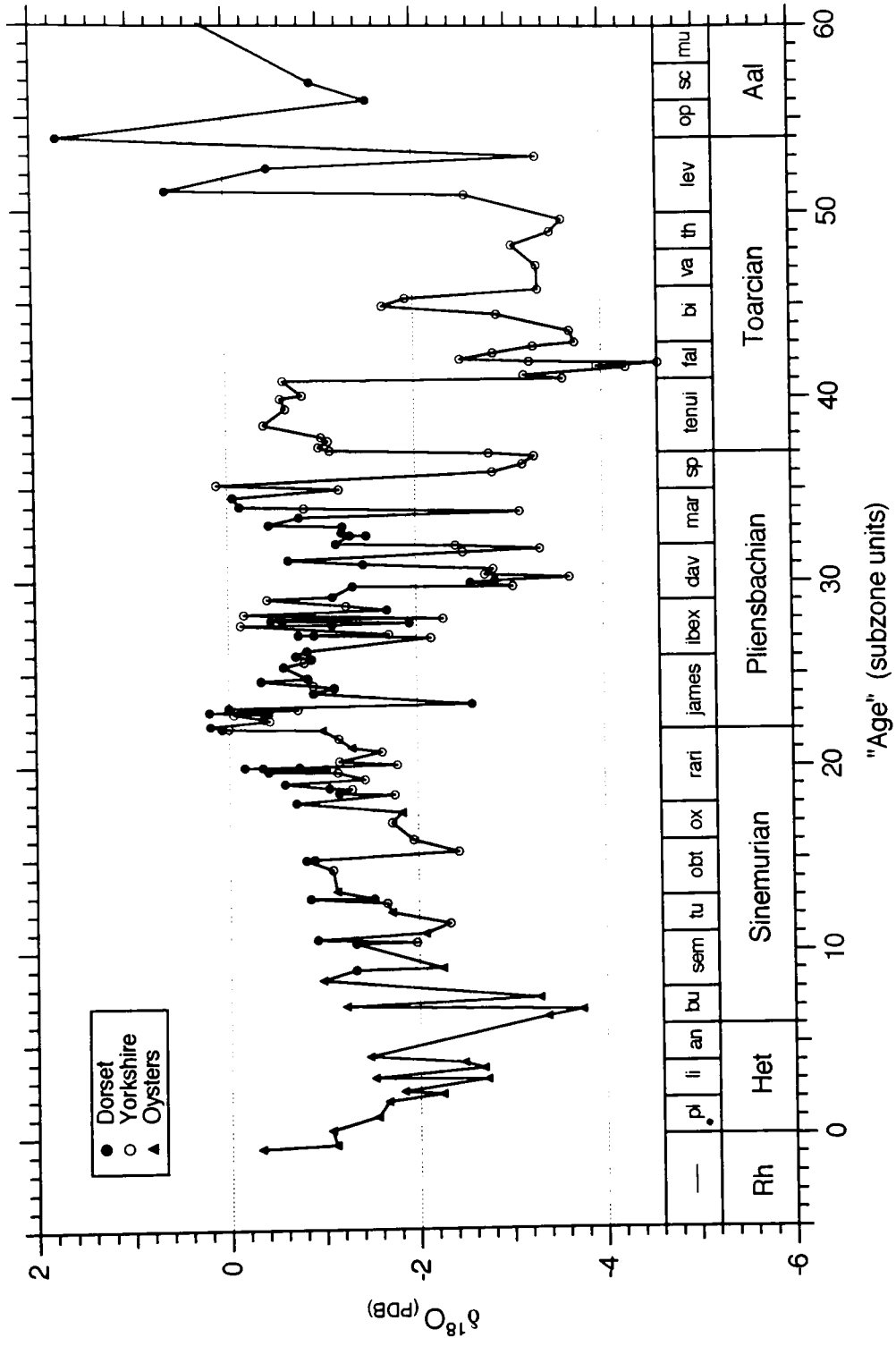

Figure 5.9: Comparison of the $\partial^{18}O$ values of samples collected in Dorset and Yorkshire. Oyster samples collected through the *bucklandi* zone of the Sinemurian come from Dorset whereas all other oysters come from Yorkshire.

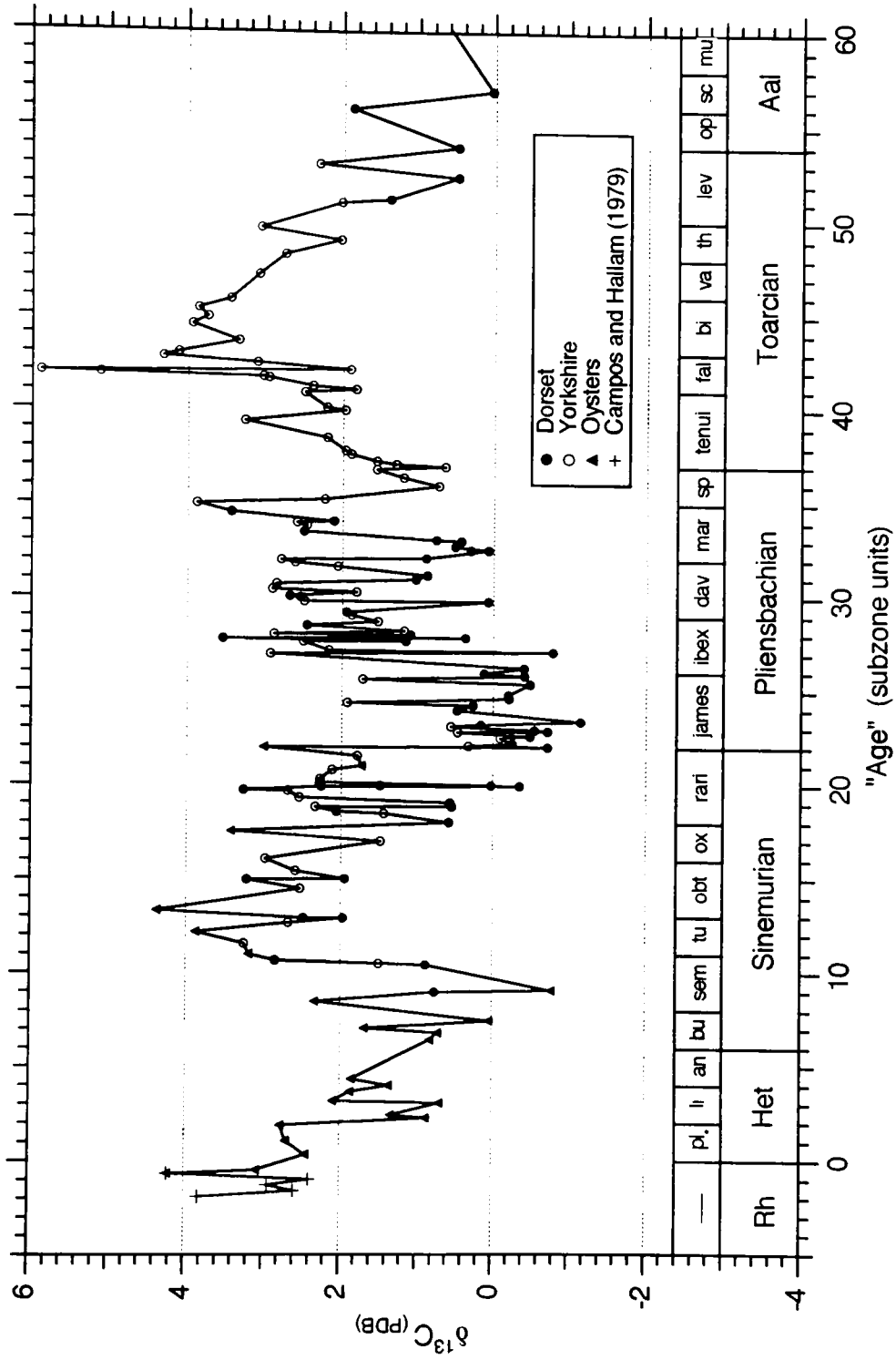

Figure 5.10: Comparison of the $\partial^{13}C$ values of samples collected in Dorset and Yorkshire. Oyster samples collected through the *bucklandi* zone of the Sinemurian come from Dorset whereas all other oysters come from Yorkshire.

5.3 Discussion of $\partial^{18}O$ Data

As indicated in the introduction, there is a large literature regarding the late Mesozoic marine $\partial^{18}O$ curve. However, much of this literature suffers from analytical procedures that may have distorted the signal as recorded in the carbonate samples and from inadequate screening for diagenetically altered material. Of this extensive literature, Hudson and Anderson (1989) have helpfully selected a number of papers covering the Triassic, Jurassic, and Early Cretaceous that they feel fulfils modern criteria for both analytical and sample selection procedures (Stahl and Jordon, 1969; Jordon and Stahl, 1970; Kaltenegger *et al.*, 1971; Spaeth *et al.*, 1971; Stevens and Clayton, 1971; Veizer and Fritz, 1976; Marshall, 1981; Wefer, 1982; Brand, 1986; Jenkyns and Clayton, 1986). Ages for the data of Veizer and Fritz (1976) are assigned using the biostratigraphic tables of Arkell (1956) and Urlichs (1977). Unfortunately, even this carefully selected data set is severely limited by the fact that it is composed of a large number of small data sets spaced widely in time and geographic coverage. The combination of poor time constraints and a mixture of different geographic settings makes delineation of any palaeoclimatic trend difficult. Figures 5.11 and 5.12 present a comparison between the compiled data (represented by boxes delimiting both age and isotopic uncertainties) and the data collected in this study.

The curves of the Hettangian, Sinemurian, and early Pliensbachian stages are virtually unconstrained by previously published data (Fig. 5.11). The data from this study seem to indicate a decline in $\partial^{18}O$ across the Triassic/Jurassic boundary hitting a minimum probably in the mid-Hettangian (a number of data points from the upper Hettangian are very negative, probably due to diagenetic alteration, and are deleted from the graph; c.f. Fig. 5.6). The Sinemurian is characterised by a well-developed rise in the $\partial^{18}O$ of samples from both coasts that culminates with a peak in the lowest Pliensbachian. The data seem to fall off somewhat through the Pliensbachian, but unfortunately beyond the mid-

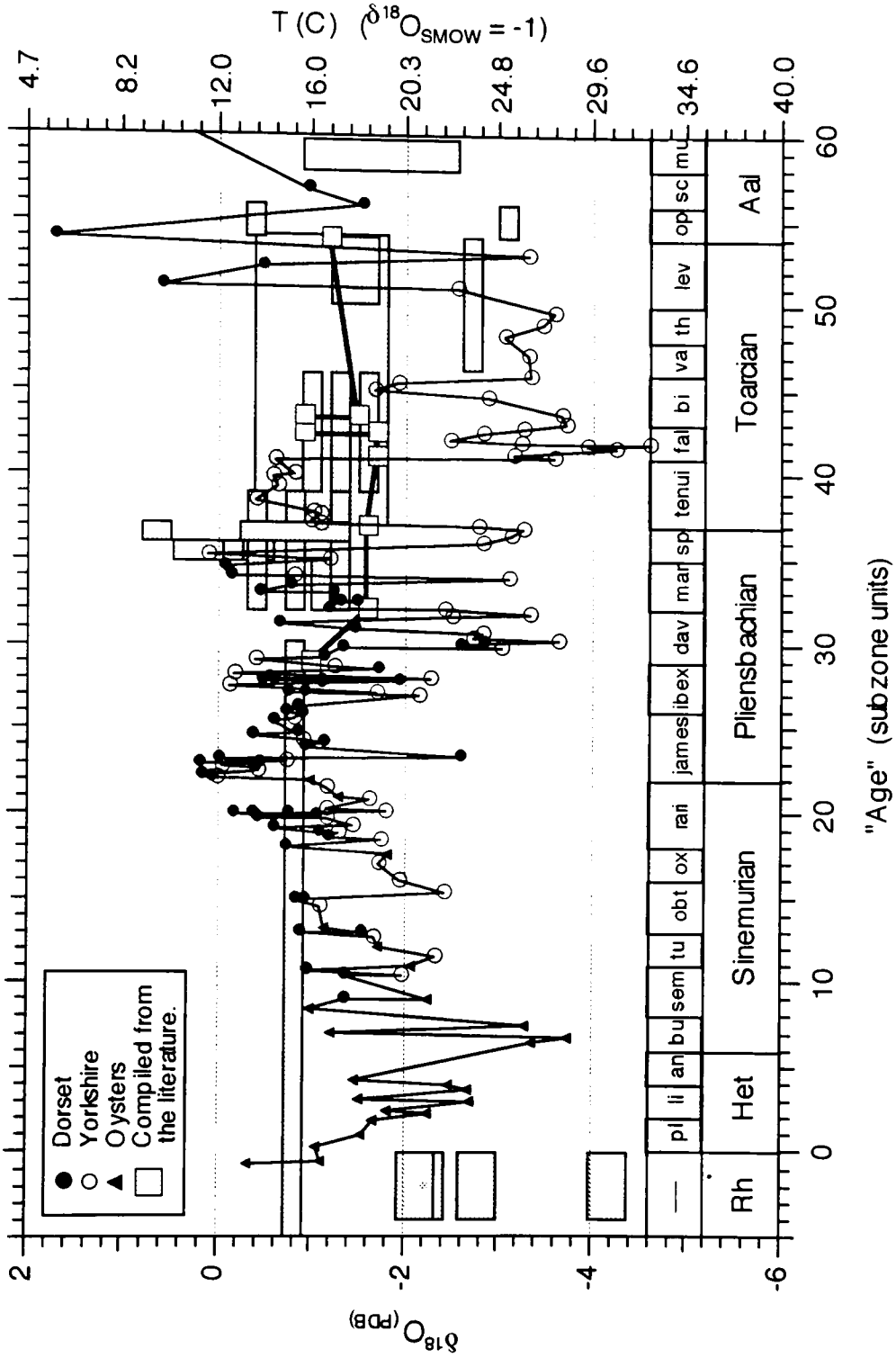

Figure 5.11: Comparison of the Early Jurassic $\partial^{18}O$ data collected in this study with previously published results collected mainly from European sections. Area of the boxes represents errors in both age assignments and $\partial^{18}O$ values compiled from the literature. Note that the temperature scale on right is non-linear (Anderson and Arthur, 1983) and that tic marks refer to the $\partial^{18}O$ scale on the left.

Pliensbachian it becomes difficult to define the trend of the curve due to many of the Yorkshire data plotting about 2‰ lower than the Dorset data. If these lower data points are ignored as diagenetic artifacts, it seems that the oxygen isotope curve reaches a minimum in the *davoei-margaritatus* zones and another maximum in the latest Pliensbachian. In the Toarcian and Aalenian there are few apparently reliable data points on which to base a best-estimate curve. The published data hint that the curve declines back to roughly -1‰ and there is an indication of another maximum in the late Toarcian and Aalenian. However, the considerable scatter over this interval, including what seem to be unreasonably positive values, makes close definition of the curve impossible.

It is impossible to assign accurate palaeotemperatures to belemnite and oyster $\partial^{18}O$ values without a knowledge of their biological fractionation effects or of the life habits of belemnites (e.g., water depths and migration patterns). However, approximate palaeotemperature estimates (Fig. 5.11; right axis) may be made by application of the palaeotemperature equation of Anderson and Arthur (1983),

$$T(C) = 16.0 - 4.14(\partial^{18}O_{\text{sample PDB}} - \partial\ ^{18}O_{\text{SMOW}}) + 0.13(\partial^{18}O_{\text{sample PDB}} - \partial^{18}O_{\text{SMOW}})^2,$$

assuming that calcite precipitated from global mean seawater has $\partial^{18}O_{\text{SMOW}}$ equal to -1.0‰ on the SMOW scale (Shackleton and Kennett, 1975). According to this conversion, Early Jurassic palaeotemperatures off the coast of Britain ranged between a maximum of 18 - 23 °C in the Hettangian to minima of 12 °C at the beginning and end of the Pliensbachian and probably in the latest Toarcian and Aalenian. The southern coast of Great Britain was at about 30 °N at the beginning of the Jurassic and moved to about 35 °N by the late Pliensbachian (Smith and Briden, 1977). Palaeotemperatures of 18 - 23 °C are perfectly compatible with modern ocean summer surface temperatures at similar latitudes (Gross, 1987), although they seem slightly cool if it is considered that Britain was in the midst of the "European archipelago" at that time and may therefore have had warmer temperatures analogous to the Mediterranean located at a similar latitude today. The palaeotemperature

minima of ~12 °C is compatible with modern winter temperatures at the same latitude, but again these temperatures seem too cool for a long-term change for an inland seaway at this palaeolatitude. The fact that the rest of the Jurassic and Early Cretaceous data also indicate palaeotemperatures as cold or colder than ~12 °C (see below) suggests several possibilities: either the local water masses were relatively depleted in ^{16}O, perhaps due to enhanced evaporation in the interior seaway; that the ice-free world calculations of Shackleton and Kennett (1975) are in error for the Jurassic and Early Cretaceous; that there were episodic developments of Mesozoic ice that led to oceans depleted in ^{16}O; or that oysters and belemnites exert systematic biological fractionation effects on $\partial^{18}O$.

The $\partial^{18}O$ data for the rest of the Jurassic and the Early Cretaceous are more sparsely distributed through time and are characterised by greater scatter (Fig. 5.12). The Aalenian, Bajocian, and Bathonian data of this and previous studies continue at the relatively heavy values of 0‰ or even somewhat greater in the early Bathonian. This corresponds to palaeotemperatures of 12 °C or cooler according to the palaeotemperature equation listed above. While the scattered Bathonian and Callovian data seem to indicate a drop in seawater $\partial^{18}O$ values, the evidence is not really strong enough to eliminate the simpler possibility that the curve continues undisturbed at ~ 0‰ through at least the earliest Oxfordian. The succeeding Oxfordian and Kimmeridgian data are difficult to interpret due to a systematic offset between the oyster and belemnite data. Although in general there is no $\partial^{18}O$ offset between the two fossil groups, over this interval the oyster data show a well-defined decline that by the Kimmeridgian reaches its lowest $\partial^{18}O$ values (highest temperatures) since the Hettangian whereas the sparse belemnite data are consistent, in conjunction with the previously published data, with a continuation of the curve at about 0‰. This offset is unlikely to be due to primary difference in water temperatures inhabited by the two groups because the oysters come from the relatively deep-water facies of the Kimmeridge Clay and thus are unlikely to have lived in warmer waters than the belemnites

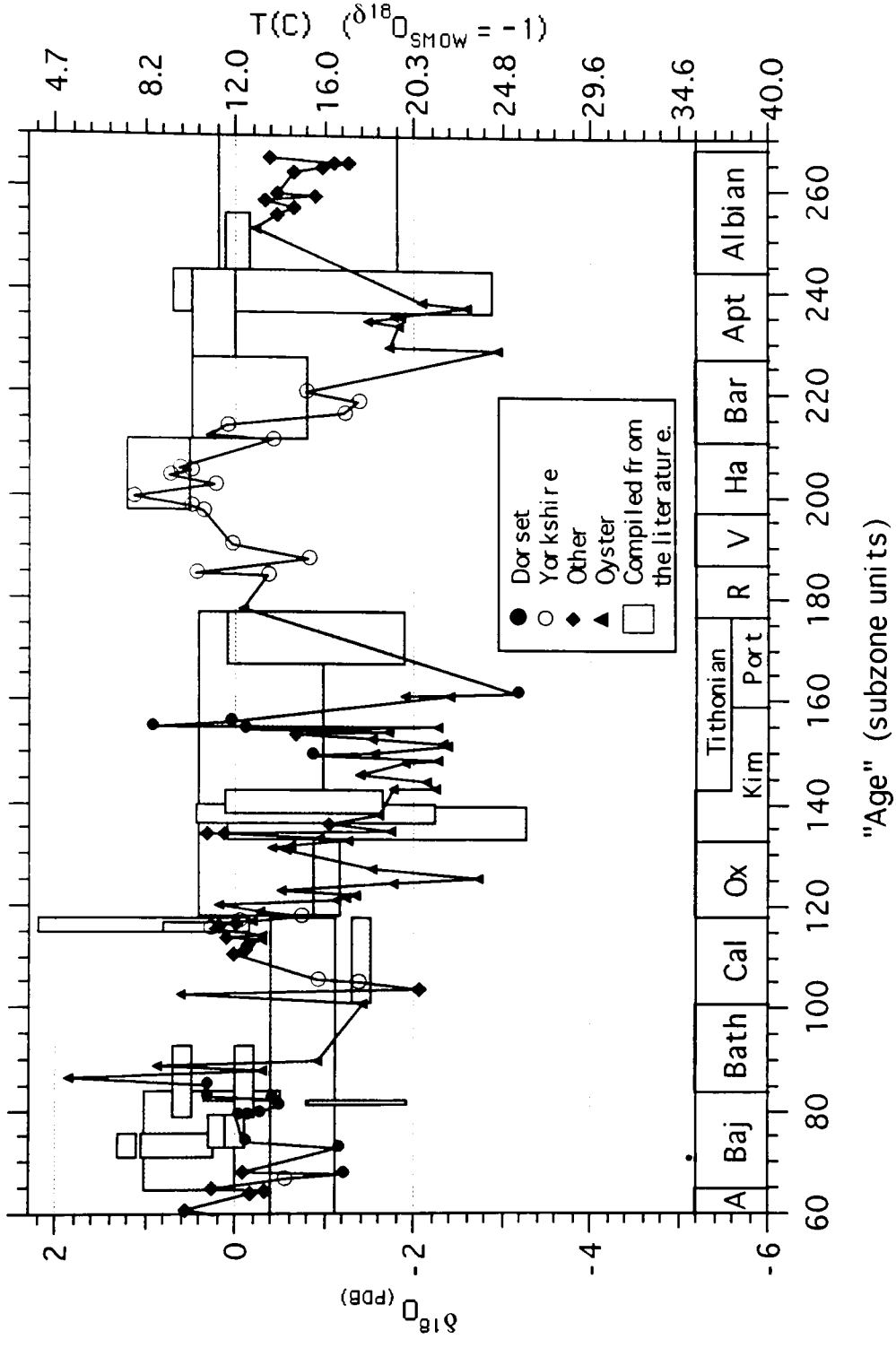

Figure 5.12: Comparison of the Jurassic and Early Cretaceous $\partial^{18}O$ data collected in this study with previously published results collected mainly from European sections. Area of the boxes represents errors in both age assignments and $\partial^{18}O$ values compiled from the literature. Note that the temperature scale on right is non-linear and that tic marks refer to the $\partial^{18}O$ scale on the left.

living at shallower water depths. Diagenetic alteration is unlikely because although the low Mn concentrations, high pyrite content, lowered $\partial^{18}O$ values, and apparently well-preserved Sr isotopes are consistent with fairly pervasive alteration during the zone of sulphate reduction, the fact that the oyster carbon isotopes are heavier than those of coeval belemnites (see Fig. 5.15) is inconsistent with substantial recrystallisation during sulphate reduction. Diagenesis during methanogenesis is a possible explanation, although the extremely low oyster Mn concentrations are inconsistent with the Mn-rich pore waters that are expected under reducing conditions in mudrocks. Perhaps the most likely explanation is that the small, thin-shelled oysters of the Kimmeridge Clay exerted a biological fractionation against ^{18}O as a result of a specialised metabolism that enabled them to live in the faunally impoverished, low-oxygen bottom-waters of the Kimmeridge Clay (Oschmann, 1988; Wignall, 1990).

The Early Cretaceous data begin at about 0‰ in the Ryazanian and reach a maximum of slightly more than +0.5‰ in the Hauterivian. Following this rise both the published data and the data of this study indicate a decline through the Barremian. The Aptian data are suspect because the oysters, although giving reasonable Sr-isotope values, show very high Fe concentrations (Chapter 3). It may be that the curve reaches a minimum in the Barremian and then, following the published data, recovers by the Aptian and declines slightly into the Albian. It is worth collecting more Early Cretaceous data because although the Aptian data are consistent with the proposed warming associated with a volcanic CO_2-induced "greenhouse" (Weissert, 1989; Weissert and Lini, 1991; Larson, 1991), the probable diagenetic alteration of this material means that the current data cannot be used to test this hypothesis.

In overview, it is interesting to note that, assuming $\partial^{18}O_{SMOW}$ has remained constant over the Mesozoic, the Early Jurassic seems to have been generally warmer than the rest of the Jurassic and Early Cretaceous. The best-estimate Early Jurassic curve

oscillates around about –1‰ (Fig. 5.11), which is near the –1.2 $\partial^{18}O_{PBD}$ that Shackleton and Kennett (1975) calculate for an ice-free world, whereas the rest of the Mesozoic data indicate that the world oceans remained at about 0‰.

5.4 Discussion of $\partial^{13}C$ Data

Changes in the $\partial^{13}C$ of the world's oceans reflect variations in the relative fluxes of isotopically distinctive carbon in and out of the ocean-atmosphere-terrestrial biosphere system (Fig. 5.13). Although both positive and negative $\partial^{13}C$ excursions have been observed in the geological record, it is the positive excursions that have received the most attention. Positive excursions are thought to represent periods of accelerated global organic carbon burial. Because organic carbon is isotopically very light ($\partial^{13}C \approx -25‰$), accelerated removal of this carbon from the ocean-atmosphere-biosphere system results in a significant depletion of ^{12}C and thus results in a positive $\partial^{13}C$ excursion.

A number of globally synchronous carbon burial events in the Jurassic and Cretaceous have received a considerable amount of attention due to their importance as potential oil source rocks and as sudden, naturally occurring major perturbations of the global carbon cycle (e.g., Schlanger *et al.*, 1987; Arthur *et al.*, 1987; Jenkyns, 1988; Arthur *et al.*, 1990; Weissert and Lini, 1991; Lini *et al.*, 1992). The best way to document firmly the timing, duration, and global importance of a given carbon-burial event is to record a positive $\partial^{13}C$ excursion in a large number of widely distributed, biostratigraphically calibrated localities. Global coverage is essential to distinguish between local and truly global events.

In the absence of carbon isotope data it is possible to highlight candidate global carbon burial events by tracing the prevalence of organic-rich shales restricted to synchronous horizons around the world. The difficulty with this approach is twofold. First, for times such as the Triassic and most of the Jurassic where the deep-sea record has long since been subducted, the identification of carbon-burial events relies on the

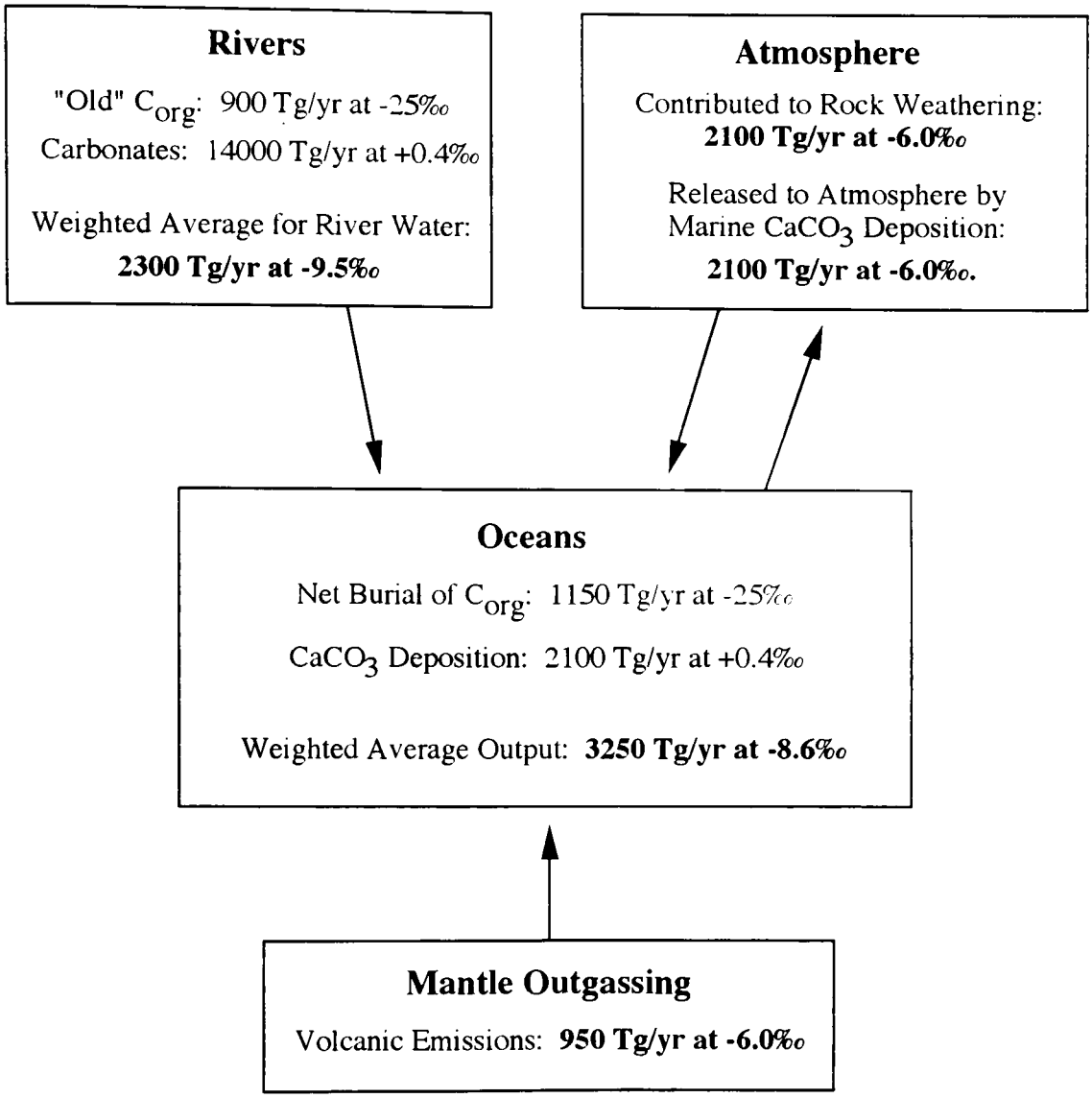

A Balanced Carbon Cycle for the Holocene (from Arthur *et al.*, 1985)

Figure 5.13: The major inputs to the marine carbon cycle are the weathering of carbonates and organic-rich sediments on land and mantle outgassing of primordial carbon. Atmospheric CO_2 participates in the weathering cycle, but makes no net contribution due to the balance between rock weathering and the marine precipitation of $CaCO_3$. The main marine sinks of ocean carbon are the sedimentary burial of organic matter and $CaCO_3$. Note that the most extreme $\partial^{13}C$ values are associated with the burial of organic matter ($\partial^{13}C \approx$ -25‰).

land-based record. For times of restricted epicontinental seas, the sedimentary record is necessarily sparse and it may be that periods of enhanced carbon burial are therefore overlooked. For times of extensive epicontinental seas the record may yield abundant stratigraphic sections, but the difficulties of precise global biostratigraphic correlation and a lack of quantitative information as to the relative changes in global organic carbon buried make any conclusions tentative.

The best documented Mesozoic carbon burial events occur during the Early Toarcian (*falciferum* zone, Jenkyns, 1988), across the Valanginian/Hauterivian boundary (Lini *et al.*, 1992), from the middle to late Aptian (Weissert and Lini, 1991), in the early and latest Albian (Arthur *et al.*, 1990), across the Cenomanian/Turonian boundary (Schlanger *et al.*, 1987), and in the latest Coniacian (Jenkyns, 1991). The existence of these events is firmly based on well-correlated $\partial^{13}C$ isotope excursions and backed up by the wide-spread occurrence of organic-rich sediments at these times. In addition to these events, Hallam (1987) has compiled a list of times that, based on the documentation of widely distributed organic-rich sediments, may also be characterised by accelerated rates of carbon burial. Although Lower Jurassic sediments are not common around the world, the Early Jurassic was a time of widely distributed ammonite genera, and this has allowed Hallam (1987) to achieve the most detailed results for this interval of the Mesozoic.

According to Hallam (1987), thin but widespread organic-rich shales of Rhaetian and early Hettangian age are found throughout northwestern Europe and in northern Canada. Unfortunately the restricted epicontinental seas of the time and make it difficult to assess the significance of these shales as representing a global carbon burial event. The Sinemurian *semicostatum* and *turneri* zones mark an apparently global transgression characterised by a transition to shaley, frequently organic-rich deposits in eastern Asia, North and South America, and throughout Europe, (Hallam, 1981). The wide distribution of documented carbon-rich strata at this time make this is a good candidate for a global

carbon burial event. The *davoei* and *margaritatus* zones of the late Pliensbachian also show biostratigraphically well-documented evidence for transgressive deposition of organic-rich shales in Europe and especially in eastern Asia and North America (Hallam, 1981, 1987). This event manifests itself as a minor positive $\partial^{13}C$ excursion restricted to the *margaritatus* zone (Jenkyns and Clayton, 1986; Jenkyns, 1988). By far the best-documented event in the Early Jurassic occurs during the early Toarcian *falciferum* zone. This event is associated with a strong positive $\partial^{13}C$ excursion (Jenkyns and Clayton, 1986) as well as with well-documented black shales found around the world (Jenkyns, 1988).

Figure 5.14 demonstrates that for each of the candidate burial events discussed above there is a corresponding shift in the belemnite and oyster carbon-isotope data. The proposed Rhaetian/earliest Hettangian event appears to be confirmed by relatively positive (~ +4‰) $\partial^{13}C$ values for oyster data collected in this study and whole-rock data collected from slightly lower in the same stratigraphic succession by Campos and Hallam (1979). The relatively well-documented, widely distributed organic-rich shales from the *turneri-obtusum* zones correspond to what appears to be the peak of a long-term increase in the $\partial^{13}C$ curve. The curve then declines slowly until reaching the earliest Pliensbachian, when it suddenly shifts downwards from +2 to 0‰. Data from both coastal sections confirm this excursion, although later on there is a divergence between the Dorset and Yorkshire data. It is not certain whether this shift represents an actual negative excursion or merely increased diagenetic alteration at the two lithologically similar sample localities. The carbon-isotope curve recovers from 0 to nearly +3‰ in the *ibex* zone. This positive shift probably does not constitute what is normally considered to be a positive carbon-isotope excursion, both because Hallam (1987) does not note the *ibex* zone as being characterised by organic-rich shales and because $\delta^{13}C$ values of +3‰ are not markedly more positive than much of the Lower Jurassic data. The curve levels off for the remainder of the Pliensbachian until the *margaritatus* zone, when there is another positive excursion

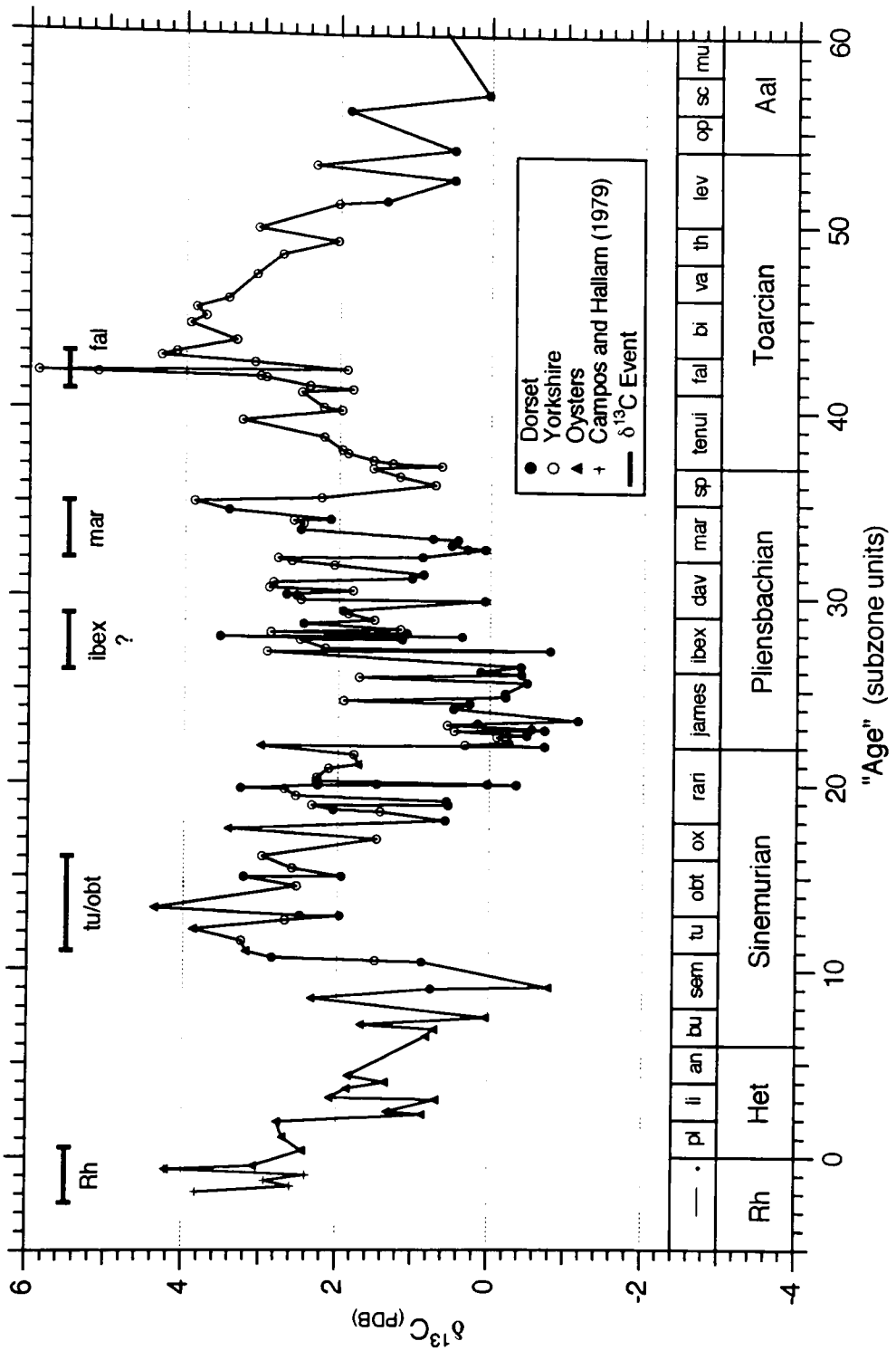

Figure 5.14: The carbon-isotope curve for the Early Jurassic. The timing of the candidate carbon-burial events of Hallam (1987) is plotted for comparison with the positive $\partial^{13}C$ excursions in the belemnite and oyster data set. The *ibex* zone event is the only one not predicted by Hallam (1987); it may represent merely a recovery from the negative $\delta^{13}C$ values of the lower Pliensbachian and not a true positive carbon-isotope excursion.

reaching nearly +4‰. Although the data of this study suggest that the peak of this event occurs in the latest *margaritatus*, the more extensive data set of Jenkyns and Clayton (1986) and Jenkyns (1988) places the peak in the mid-*margaritatus* zone. From this point through most of the rest of the Toarcian the data are from the Yorkshire coast only. The most prominent feature is the +6‰ peak centred exactly at the *exaratum-falciferum* subzone boundary in the mid-*falciferum* zone. The timing of this peak corresponds exactly to that of the Jenkyns and Clayton (1986) and Jenkyns (1988) data. The rest of the Early Jurassic sees a decline towards a level of roughly +1‰ in the Aalenian.

For the rest of the Jurassic there is no convincing evidence for globally synchronous carbon-burial events. According to Hallam's (1987) analysis of the sedimentary record, the next candidate interval for organic-rich shales occurs in the Callovian. The English Middle Callovian is certainly marked by organic-rich, bituminous shales, but similar correlative deposits are not traceable into Europe or found extensively elsewhere. Hallam finds some Callovian organic-rich shales in a Blake Ridge DSDP hole and in Saudi Arabia, but there appears to be no compelling evidence to suggest that the Middle Callovian hosts a truly global event. His review suggests that the Oxfordian through the Early Cretaceous Ryazanian/Berriasian stages seem to mark an extended interval generally characterised by organic-rich oil source rocks, but there does not seem to be any clear indication of a single, narrowly confined event analogous to that of the Toarcian.

The Jurassic and Early Cretaceous $\partial^{13}C$ data of Figure 5.15 appear to suggest a major shift from roughly 0.5 to 3‰ in the early Bathonian and major carbon-isotope excursions in the early Oxfordian and Aptian/Albian. However, the early Bathonian transition from +0.3 to +3‰ coincides exactly with a change from belemnite to oyster samples. It is not simple to gauge the significance of this change in sample materials because there is no simple systematic offset between the belemnite and oyster data. It turns

out that whereas the belemnite and oyster data from the Lower Jurassic and Callovian show little or no systematic offset, there are large offsets between the belemnite and oyster data of the Kimmeridgian, Ryazanian, Barremian, and Aptian/Albian.

It seems likely that the Aalenian, Bajocian, and Bathonian data are relatively accurate since these samples come from oolitic rocks where any diagenetic shift of the primary $\partial^{13}C$ signal was probably buffered by the carbonate of the host rocks. There also seems to be little doubt about the Callovian data because both oysters and belemnites give similar results and because the positive $\partial^{13}C$ shift corresponds to a transition to organic-rich sediments where diagenetic alteration is most likely to result in a negative shift. Thus, whereas there is good evidence for a carbon-isotope shift from ~0.5 to ~3.0‰ some time during the Bathonian, the transition from belemnites to oyster samples means that the timing of this shift cannot be constrained to have occurred suddenly in the early Bathonian. The shift may have been gradual or occurred somewhat later, perhaps across the apparently transgressive Bathonian/Callovian boundary.

The next major feature is a peak reached in the early Oxfordian *cordatum* subzone. Because this excursion is defined entirely by one fossil group (oysters), it seems likely that this peak is primary. Although there is additional stable isotopic evidence for an early Oxfordian event from sections in Italy and France (Jenkyns, pers. comm., 1991), these excursions are restricted to the *transversarium* zone (Submediterranean faunal province), which occurs roughly one zone after the Dorset *cordatum* subzone event. Hallam (1987) notes that the late Jurassic is generally characterised by relatively organic-rich sediments, but unfortunately there is no independent sedimentological evidence in support of a carbon-burial event in the early Oxfordian. Without strong supporting sedimentological and stable isotopic evidence from other stratigraphic sections, this isotope excursion must be regarded as tentative and perhaps of only local importance.

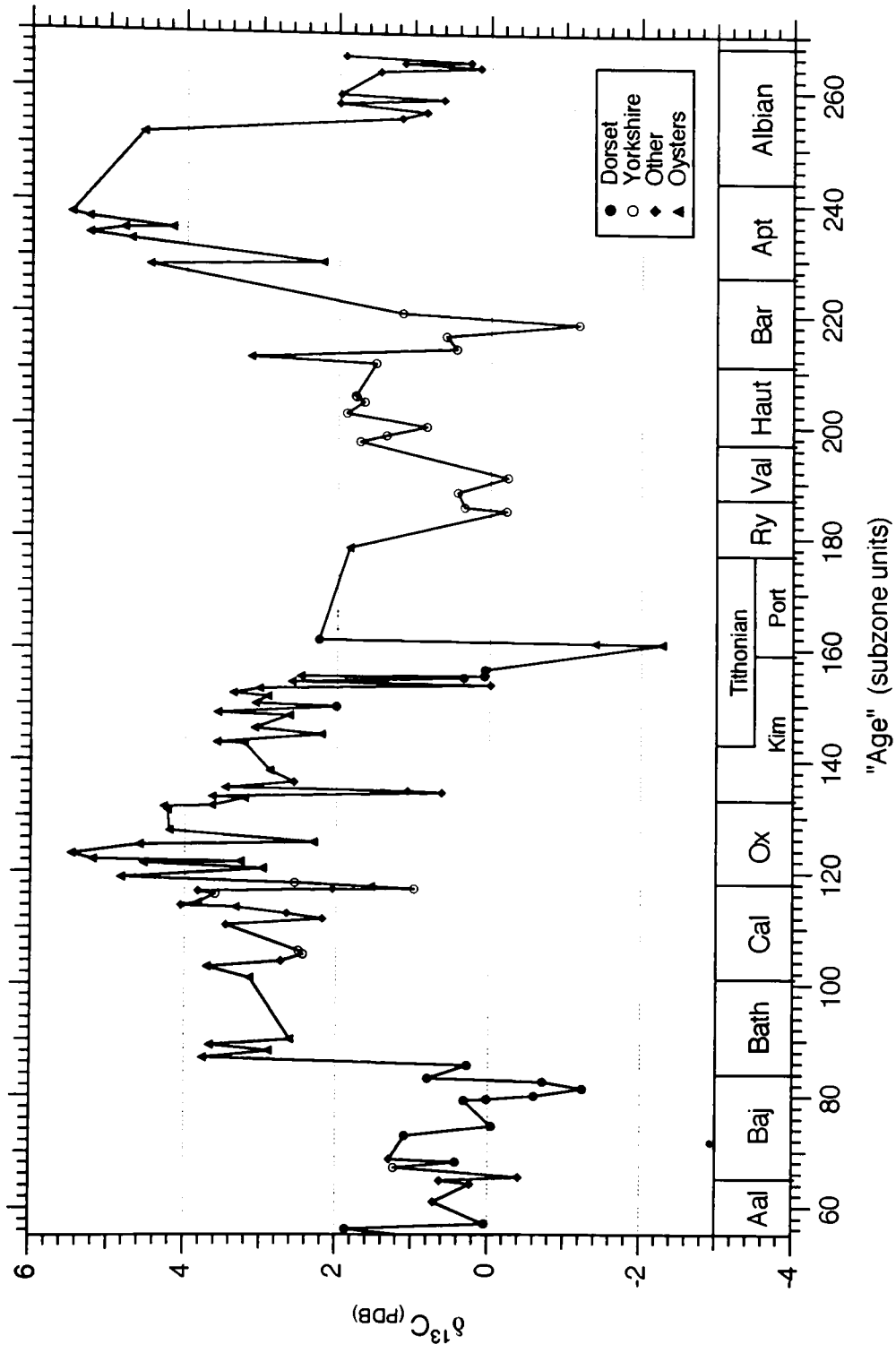

Figure 5.15: The carbon-isotope curve for the Middle and Late Jurassic and the Early Cretaceous. The interpretation of this curve is complicated by systematic offsets between the oyster and belemnite data that appear to be significant during some intervals but insignificant during others.

After the early Oxfordian the $\partial^{13}C$ data decline towards a minimum reached near the basal stage of the Cretaceous. This parallels a trend documented by Weissert and Channell (1989) for four Italian sections spanning the Kimmeridgian, Tithonian, and Berriasian stages. The large negative spike near the Kimmeridgian-Portlandian boundary is most probably a diagenetic artifact. The data then rise towards about +1.5‰ during the Valanginian, Hauterivian, and Barremian, but without any suggestion of the carbon-isotope event documented for the Valanginian/Hauterivian boundary by Lini *et al.* (1992). Although this may be a function of the sparsity of the data coverage, it should be noted that this is the only known carbon-isotope event that is not independently supported by the belemnite and oyster stable isotope data. The negative excursion in the mid-Barremian is probably a result of diagenesis, and, although there is no doubt as to the existence of major carbon-isotope excursions during the Aptian and Albian, there are no belemnite data to confirm the magnitude of the oyster-dominated positive excursion through this interval. The pattern of carbon-isotope excursions in the Aptian/Albian is complex, but it appears that there are two events that cover much of the early and middle Aptian (Weissert and Lini, 1991) while a third is concentrated in the late Aptian and earliest Albian (Weissert, 1989; Arthur *et al.*, 1990). The data of this study seem to confirm the early Aptian excursion, but unfortunately coverage is too incomplete to be used to confirm the late Aptian/earliest Albian excursion. The time interval covering a latest Albian event (Arthur *et al.*, 1990) is not represented by data collected in this study.

5.5 Conclusion

In conclusion, belemnites and oysters appear to preserve reasonable stable isotopic data that may be useful in sorting out certain palaeoceanographic problems in the Jurassic and Cretaceous. At the current level of understanding, the considerable scatter of belemnite and oyster data requires that samples must be densely collected as a function of time in order to separate "noise" from what may be the primary seawater trends. A detailed

consideration of different taxonomic groupings and of the variability within individual belemnites and oysters may yield useful insight not only into the trend of a primary seawater curve, but also into the palaeobiology of the different belemnite and oyster groups. A second area requiring much work is diagenesis. It is essential to develop tracers of diagenesis that are more sensitive to alteration as it affects the stable isotopic composition of belemnites and oysters preserved in a variety of host rocks. Finally, a more quantitative interpretation of the relationship between the $\partial^{18}O$ data and the assigned palaeotemperatures requires a calibration of belemnite and oyster calcites to calcites whose biological effects are better understood. A good step in this direction would be to compare detailed measurements of belemnites collected in well-preserved nannofossil chalks with isotopic measurements obtained from the surrounding chalk matrix.

Chapter 6: The Marine Geochemical Cycle of Strontium

6.1 Introduction

The interaction between the various components of the marine geochemical cycle of strontium determines the evolution of the seawater Sr-isotope curve through geological time. A detailed understanding of the components of this cycle is therefore a necessary prerequisite for a better understanding of the seawater Sr-isotope curve. Sr is primarily transported to the oceans by rivers and meteoric groundwaters, mid-ocean ridge (MOR) hydrothermal springs, and pore fluids escaping compacting marine sediments. Sr is removed from the oceans as a component of calcium carbonates, sulphates, and phosphates. The $^{87}Sr/^{86}Sr$ ratio of seawater Sr is controlled by the balance between river waters, with generally high $^{87}Sr/^{86}Sr$ ratios, MOR hydrothermal fluids, with low ratios, and Sr derived from the recrystallisation of ocean sediments, with intermediate ratios. Table 6.1 contains a set of quantitative estimates of these parameters used by various authors in their mass balance calculations.

Table 6.1: Published parameters of the geochemical cycle of Sr

Ref.	R_{sw}	J_{rw}	R_{rw}	J_h	R_h	J_d	R_d	J_g	R_g
1	0.70924	2.5	0.7111	0.38	0.7040	0.34	0.7084		
2	0.7092	2.5	0.7111	1.45	0.7029	0.55	0.7084	2.22	0.711
3	0.70917	3.0	0.7101	0.38	0.7036	0.24	0.7087		
4	0.70916	2.5	0.7101	0.38	0.7036	0.30	0.7087		
5	0.70924	3.1	0.7101	0.48	0.7035	0.34	0.7084	2.22	0.7101
6	0.70916	3.3	0.7119	~1.08	0.7035	0.34	0.7084		

$R = {}^{87}Sr/{}^{86}Sr$ ratio of Sr^{2+}; J = flux of dissolved Sr in 10^{10} mol/yr
Subscripts sw = seawater, rw = river water, h = MOR hydrothermal spring water, d = diagenetic pore fluids, g = subsurface ground water (runout)

1 Palmer and Elderfield (1985)
2 Chaudhuri and Clauer (1986)
3 Goldstein and Jacobsen (1987)
4 Hodell *et al.* (1989)
5 Veizer (1989)
6 Palmer and Edmond (1989a)

While the estimates are in broad agreement, the differences are large enough , particularly as regards the hydrothermal flux, to effect significantly the modelled evolution of the marine Sr-isotope curve through geological time. Figure 6.1, for example, shows the calculated effects of changing the hydrothermal flux proportionally to the amount of new oceanic crust produced each year (according to the data of Kominz, 1984; see Chapter 7 for calculations). It is evident from this diagram that the importance of the hydrothermal component varies considerably according to the mass balance adopted. Thus, while we know qualitatively that the observed Sr-isotope curve simply reflects the relative contributions of radiogenic riverine Sr and nonradiogenic MOR Sr, it proves difficult to model quantitatively even the main features of the Sr-isotope curve over past 150 Ma. It is the purpose of this chapter to determine whether or not the main fluxes of the Sr cycle may be more closely constrained such that the seawater Sr isotope curve may be more quantitatively understood.

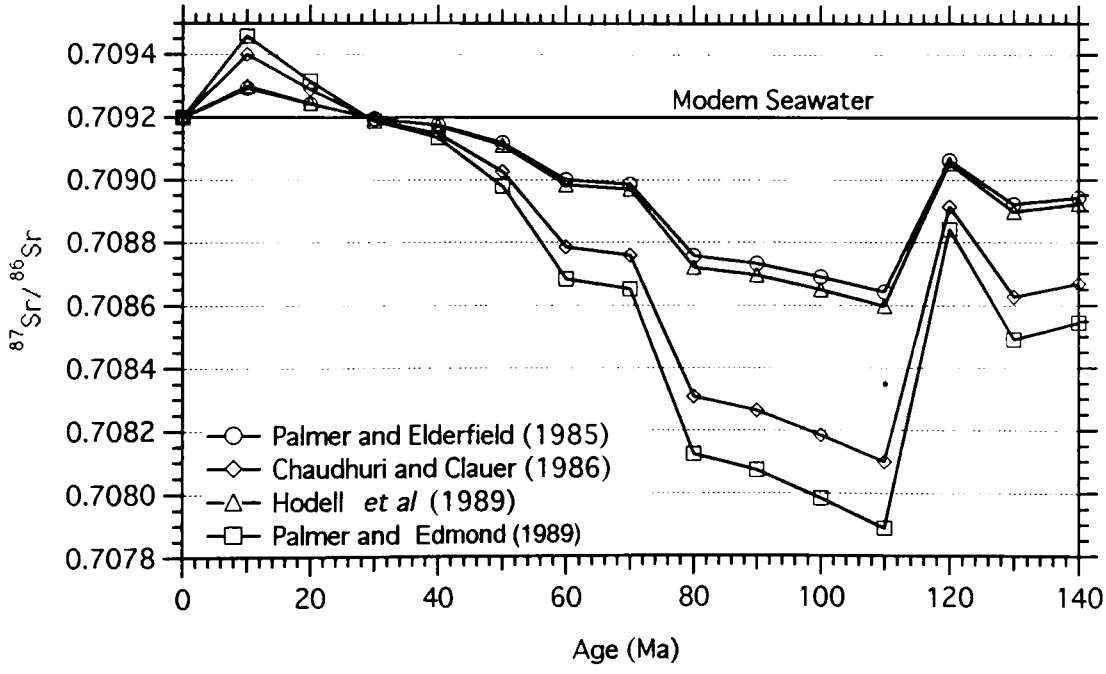

Figure 6.1: Calculated effects of varying the magnitude of the hydrothermal flux of Sr proportionally to the changes in the area of new oceanic crust produced each year (as tabulated by Kominz, 1984). Four different Sr cycles (see Table 6.1) give significantly different results.

6.2 Strontium in Modern Seawater

6.2.1 Distribution, Concentration, and Mass in World Oceans

There are relatively few high quality data on the distribution of Sr throughout the world's oceans. Early efforts were hampered by the poor precision, accuracy, and reproducibility of analytical techniques whereas more recent studies, using isotope dilution mass spectrometry (IDMS), are few in number. These later studies (Bernat *et al.*, 1972; Brass and Turekian, 1972, 1974) find that whereas Sr is quite conservative throughout most of the water column, it can be strongly affected by biological activity in the surface layers of the ocean. The detailed profiles of Bernat *et al.* (1972) and Brass and Turekian (1972, 1974) show a significant depletion of Sr in surface waters (upper 100 m), a variable enrichment between about 500 m and 1500 m, and conservative behaviour below 1500 m. A strong correlation between Sr and the nutrient elements P, N, and Si suggests a biological carrier of Sr. While the calcareous tests of pteropods, foraminifera, and coccolithophores are obvious candidate carriers for Sr, the celestite ($SrSO_4$) tests of the radiolarian genus *Acantharia* appear to be the only medium capable of producing the observed Sr tends. The strong undersaturation of seawater with respect to $SrSO_4$ means that these tests dissolve after only a few hundred meters of descent through the water column (Broecker and Peng, 1982) and thus do not remove Sr from the oceans.

Table 6.2 shows a compilation of mean Sr/salinity ratios (measured in milligrams of Sr per gram of total salts) based on the data collected below the oceanic depths affected by biological activity. Although the Atlantic data appear to be systematically lower than the Pacific data, this is probably only an artefact of the data set. The Atlantic data of Brass and Turekian (1972) and Bernat *et al.* (1972) may not be representative of the Atlantic Ocean because the former were collected using AAS while the later were collected from the Mediterranean Sea. The mean of the remaining Atlantic data, 0.2207, is nearly identical to

the mean of the Pacific IDMS data, 0.2205, and the global mean Sr/salinity ratio is thus estimated at 0.2206 ± 0.0015.

Table 6.2: Sr/salinity ratios (mg Sr/g salt) in world oceans

Reference	Atlantic		Pacific		Notes
Brass and	0.217 ± 0.003	(n=18)	0.220 ± 0.004	(n=14)	1
Turekian (1972)	No IDMS data		0.220 ± 0.006	(n=3)	
Bernat et al (1972)	0.217 ± 0.003	(n=10)	0.219 ± 0.001	(n=13)	2
Brass and	0.2201 ± 0.0003	(n=13)	0.2225 ± 0.0006	(n=7)	
Turekian (1974)	0.2214 ± 0.0003	(n=11)	0.2224 ± 0.0005	(n=17)	3

All data collected using IDMS unless otherwise noted.
1 Analysed using atomic adsorption spectrophotometry (AAS)
2 Atlantic data collected in the Mediterranean Sea
3 Pacific data collected in the Drake Passage

The average salinity of the oceans, not including the marginal seas, is 34.72‰ (Worthington, 1981). An earlier estimate of Montgomery (1958) has given 34.71‰ not including marginal seas and 34.72 ‰ including the marginal seas (e.g., the Black Sea at 22.5 ‰, Mediterranean Sea at 38.5 ‰, Arctic/Greenland-Norwegian Seas at 34.95 ‰, and the Red Sea/Persian Gulf at 40.5 ‰). The global average is best taken at 34.72 ± 0.01 ‰. Taking (0.2206 +/- 0.0015 mg Sr/g TDS) times (34.72 +/- 0.01 g TDS/kg seawater) yields a mean Sr concentration in the world's oceans of 7.66 +/- 0.05 mg/kg or 87.4 ± 0.6 μmol/kg. Using a volume of 136,891 X 10^4 km^3 for the world's oceans (Montgomery, 1958; Berner and Berner, 1987) and a density of seawater of 1.025 g/cm^3 (Berner and Berner, 1987), the total mass of Sr in the world's oceans is estimated at 1.075 +/- 0.007 * 10^{19} g or 1.227 +/- 0.008 * 10^{17} moles of Sr.

6.2.2 The Isotopic Composition of Strontium in Modern Seawater

The analyses of an impressive array of calcareous organisms and seawater samples from a variety of marine environments scattered around the world have yielded two important conclusions: the world's oceans are isotopically homogeneous with respect to Sr and biogenic calcites accurately record the $^{87}Sr/^{86}Sr$ ratio of contemporary seawater

(Burke *et al.*, 1982; Faure, 1982, 1986; Palmer and Elderfield, 1985; DePaolo and Ingram, 1985; Hess *et al.*, 1986). DePaolo and Ingram (1985), for example, report a standard deviation of 0.000009 for the mean $^{87}Sr/^{86}Sr$ ratio of 14 shell samples from around the world. This certainly suggests that the oceans are very well stirred with respect to Sr.

Despite the agreement regarding the homogeneity of seawater Sr isotopes, the reported $^{87}Sr/^{86}Sr$ ratios of seawater are not identical (Table 6.3, first column). This variability stems from differences between mass spectrometers, laboratory procedures, and the assumed or measured values for the Eimer and Amend and NBS SRM 987 standards. The Eimer and Amend (E & A) standard is generally *assumed* to have a $^{87}Sr/^{86}Sr$ ratio of 0.708000. The accepted value of the NBS 987 standard, however, has varied between 0.71014 and 0.710275. Both Faure (1982, 1986) and Burke *et al.* (1982), for example, assume that E & A equals 0.70800 and NBS 987 equals 0.71014, resulting in estimates of seawater $^{87}Sr/^{86}Sr$ of, respectively, 0.70906 and 0.70910. Both values, while representing a large number of analyses, are considerably lower than those values obtained on more modern machines and are therefore not used when calculating the mean seawater $^{87}Sr/^{86}Sr$ ratio.

Only two subsequent seawater Sr-isotope studies report both the E & A and the NBS 987 standards. Palmer and Elderfield (1985) quote E & A = 0.708066 and NBS 987 = 0.710275; normalising to E & A = 0.708000 gives an NBS 987 of 0.710209. Hess *et al.* (1986) normalised their NBS 987 values to an E & A value of 0.708000 to give NBS 987 = 0.710220. In this study a large number of E & A and NBS 987 standards were measured in the same turrets such that the two are directly related by nearly identical operating conditions. The result is a mean of 0.708028 for E & A and 0.710254 for NBS 987. Normalised to E & A = 0.708000, NBS 987 becomes 0.710226, which is nearly identical to the result obtained by Hess *et al.* (1986). In an effort to define more rigorously the isotopic composition of seawater, Table 6.3 summarises the observed seawater

Table 6.3: Measured $^{87}Sr/^{86}Sr$ of Modern Seawater

Ref.	Measured $^{87}Sr/^{86}Sr$	E & A Standard	NBS 987 Standard	Normalised to 0.708000	Normalised to 0.710220	Normalised to 0.710226
1	--	0.70800	--	0.70906	--	--
2	0.70907	0.70797	0.71014	0.70910	0.70915	0.709156
3	0.709238	0.708066	0.710275	0.709172	0.709183	0.709189
4	0.709234	--	0.71031	--	0.709144	0.709150
5	--	0.70800	--	0.709200	--	--
6	0.709187	--	0.71026	--	0.709147	0.709153
7	--	0.70800	0.710220	0.709198	0.709198	0.709204
8	0.709175	--	0.710235	--	0.709160	0.709166
9	0.709250	--	--	--	--	--
10	0.709189	0.708028	0.710254	0.709161	0.709153	0.709161
Mean (without ref's 1,2):				0.709183 ± 19	0.709164 ± 22	0.709171 ± 21

1 Faure (1982, 1986)
2 Burke *et al.* (1982)
3 Palmer and Elderfield (1985)
4 DePaolo and Ingram (1985)
5 Staudigel *et al.* (1985)
6 Elderfield and Greaves (1981), as updated in Elderfield(1986)
7 Hess *et al.* (1986)
8 Hodell *et al.* (1989)
9 Ludwig *et al.* (1988)
10 This study

$^{87}Sr/^{86}Sr$ ratios from a number of studies, the observed or assumed E & A and NBS 987 standards for each study, and the seawater $^{87}Sr/^{86}Sr$ ratios normalised to E & A = 0.708000, NBS 987 = 0.710220 (Hess *et al.*, 1986; Elderfield, 1986), and NBS 987 = 0.710226 (this study). The 3 averages are within 1 standard deviation of each other (0.709183 ± 19; 0.709164 ± 22; 0.709171 ± 21). The best estimate for the modern marine $^{87}Sr/^{86}Sr$ ratio is taken as 0.709180 ± 25 when normalised to E & A = 0.708000.

6.3 Continental Runoff and Groundwater Sr

Continentally derived Sr is carried to the oceans by rivers and subsurface groundwaters. To constrain the impact of this Sr on the marine budget it is necessary to estimate the annual flux of river and ground waters and the concentration and isotopic composition of Sr in these waters.

6.3.1 Estimates of River Runoff

For the purposes of examining the hydrological cycle, runoff (Q) is defined as the difference between the amount of precipitation (P) that falls on a given area and the amount of water that evaporates (E) or soaks into the ground (GW):

$$Q = P - E - GW.$$

Time-series data of measured river discharge and precipitation are used as the core of any estimate of global river runoff. For the significant areas of the world for which there are no data, regional extrapolations based on various models (e.g., water balance or precipitation/runoff ratios) must be used to fill in the gaps.

The most recent estimates of river runoff range between 39,700 and 44,700 km^3/yr (Baumgartner and Reichel, 1975; Korzun *et al.*, 1974). To my knowledge there is no detailed study that evaluates and compares the relative merits of the data sources and interpolation techniques of the two studies, and it is certainly beyond the scope of this study to undertake such an analysis. The work of Baumgartner and Reichel (1975) is more often favoured simply because the river runoff data (as well as the E and P data) are conveniently tabulated not only by continent and ocean but also by 5° belts of latitude (Berner and Berner, 1987; Meybeck, 1988; Tardy *et al.*, 1989). However, comparison of the Baumgartner and Reichel (1975) data with previously published runoff estimates suggests that their estimate is in fact the more accurate.

A compilation of global river runoff estimates published since 1920 (Table 6.4) shows that the pre-1970 estimates tend to cluster near 37,000 km^3/yr whereas those made after 1970 tend to cluster around 40,000 km^3/yr. This offset in the flux estimates is due to several significant improvements in the basic hydrological data set (measured Q and P values) that forms the heart of any global water budget. Baumgartner and Reichel (1975) make a detailed comparison between their work and the work of Marcinic (1964/5) and find that improved runoff estimates for the Amazon and Orinoco rivers and the Antarctic, as

well as improved precipitation estimates for a number of areas around the world, account for 2460 km^3/yr out of the total 3350 km^3/yr difference between the river runoff estimates of the two studies. If this extra 2460 km^3/yr, which represents real improvements in the data base, is added to the pre-1970 estimates, the "jump" disappears and most estimates cluster near 40,000 km^3/yr (Table 6.4). The exceptions are Livingstone (1963), which is too low, and Budyko (1963), Nace (1968), and Korzun *et al.* (1974), which are too high. Because most estimates are nearer to the 39,700 km^3/yr of Baumgartner and Reichel (1975) than to the 44,700 km^3/yr of Korzun *et al.* (1974), it is likely that the former is the more accurate.

Table 6.4: A compilation of global river runoff estimates.

Author	Year	Runoff (km^3/yr)	Corrected Runoff[4]
Wust[1]	1920	37,100	39,560
Lvovitch[1]	1945	37,000	39,460
Budyko[2]	1963	47,000	49,460
Livingstone[3]	1963	34,690	37,150
Lvovitch[1]	1964	37,320	39,780
Marcinec[2]	1964/5	36,350	38,810
Mira Atlas[2]	1964	36,000	38,460
Nace[1]	1968	42,600	45,060
Lvovitch[1]	1969	38,150	40,610
Mather[2]	1970	37,000	39,460
Baumgartner and Reichel[2]	1973	40,000	40,000
Lvovitch	1973	40,930	40,930
Korzun *et al*	1974	44,700	44,700
Baumgartner and Reichel	1975	39,700	39,700
Mean (Standard Deviation)		39,180 (3,550)	40,940 (3,270)

[1] Cited in Lvovitch (1973) [2] Cited in Baumgartner and Reichel (1975)
[3] Corrected for an additional 2300 km^3/yr from Greenland and Antarctica
[4] Corrected by 2460 km^3/yr due to improvements in the core data.

Of this total runoff, a certain amount reaches the oceans as glacial ice and thus does not transport dissolved weathered material to the seas. Korzun *et al.* (1974) consider runoff in polar regions in some detail and conclude that out of the 2965 km^3/yr of total

polar runoff, 2405 km^3/yr (80%) is in the form of ice. Taking 80% of Baumgartner and Reichel's (1975) total of 2300 km^3/yr for Greenland and Antarctica yields 1840 km^3/yr of frozen runoff. Subtracting this from the total runoff yields 37,860 km^3/yr of river runoff. Meybeck (1988), Berner and Berner (1987) and others using Meybeck's work use a non-ice runoff of 37,400 km^3/yr (not corrected for the 20% liquid runoff in Antarctica and Greenland), and this estimate will be used in this study for reasons of stability. Qualitative error estimates range from 34,000 (-10%) to the 42,300 km^3/yr of ice-free runoff calculated by Korzun *et al.* (1974).

3.3.2 River-Water Strontium

The concentration and isotopic composition of Sr in a given river is primarily controlled by the lithology of the basin. As a first approximation, three end-members may be defined: rivers draining Archaean crystalline terranes have low Sr concentrations and high $^{87}Sr/^{86}Sr$ ratios (e.g., the Grande Riviere de la Baliene in Canada: [Sr] = 0.10 μmol/kg, $^{87}Sr/^{86}Sr$ = 0.7384; Wadleigh *et al.*, 1985); rivers draining basaltic or young volcanic terranes have intermediate Sr concentrations and low $^{87}Sr/^{86}Sr$ ratios (e.g., the Pampanga River in the Philippines: 1.3 μmol/kg, 0.7054; Goldstein and Jacobsen, 1987); and rivers draining limestone terranes have high Sr concentrations and intermediate $^{87}Sr/^{86}Sr$ ratios (e.g., the St. Lawrence River, North America: 2.0 μmol/kg, 0.7095; Goldstein and Jacobsen, 1987). Most rivers drain a variable mixture of these end-members in addition to the spectrum of other possible rock-types. The final Sr composition of each river is a function of the relative proportion of each rock type exposed to weathering and the relative weathering rates of each lithology. These weathering rates are in turn a complex function of the local geology, the topographic relief of the basin, and the climate of the basin. As a result, it is exceedingly difficult to predict accurately the concentration and isotopic composition of a given river.

The weighted average of all published river Sr data yields a concentration of 0.890 μmol/kg Sr and an isotopic composition of $^{87}Sr/^{86}Sr = 0.7119$ (Palmer and Edmond, 1989a). A number of factors affect the accuracy of these estimates and make the assignment of accurate error bars difficult. First, Palmer and Edmond (1989a) feel that the average concentration may be somewhat low because many of the rivers were sampled at median to high stages when higher discharges tend to dilute the measured Sr concentrations. Second, a number of major rivers have not yet been sampled and it is difficult to assess how representative the current sample set is for the 53% of the world's river runoff that has not yet been sampled. Finally, the data set is difficult to handle statistically due to the strong river-to-river variability in the Sr concentration and isotopic composition and to the variations in the individual river discharges (which are used to weight each data point in the weighted average) that span 4 orders of magnitude.

It is useful to look at how the weighted average of the river data changes as a function of river runoff in order to evaluate any systematic changes in Sr concentration or isotopic composition and to gain an understanding of how representative the current data set may be for all world rivers. Figures 6.2a and b are constructed by beginning with the data from the smallest river at the far left and adding data from successively larger rivers to a weighted average moving to the right across the page. Thus the data point labelled "Rhine" in Figure 6.2a represents the weighted average of data from the Rhine and all smaller rivers. From this figure we can see that the Rhine is a Sr-rich river that acts to raise the weighted average of the data set and that the next few rivers act to bring the calculated average Sr concentration down to lower values. There are two main advantages to this type of diagram. First, using a weighted average suppresses the strong variability of the concentration and isotopic data that otherwise tends to obscure any trends in the riverine data. Second, this type of diagram clearly shows the relative effects of each river on the

weighted average of the data set and thus highlights those rivers that may have an anomalously large impact on the calculated global averages.

The evolution of the weighted mean river water Sr concentration (Fig. 6.2a) illustrates that although the medium-sized rivers (Yellow to Paraná) tend to raise the mean to 1.7 - 2.1 μmol/kg, the addition of the 10 largest rivers brings the weighted mean down to the final weighted average of 0.89 μmol/kg. The 3 largest rivers, in particular the Amazon, have the largest impact in moving the average from from 1.4 μmol/kg to 0.89 μmol/kg. Another characteristic of the data set is a 'saw-tooth' shape produced by a few Sr-rich rivers that tend to raise sharply the weighted average followed by a number of larger rivers that tend to bring the average back down. Thus the Yellow, Rhône, Rhine, Indus, Mackenzie, Mekong, and Yangtze each act to raise the global average while the rest of the rivers tend to lower it. To test the sensitivity of the final weighted average to these unusually Sr-rich rivers, each in turn was deleted from the data base and the mean was recalculated. The result is that no single Sr-rich river raises the final answer by more than 10% (at the extreme, the Mekong raises the average from 0.81 to 0.89 μmol/kg). This suggests that no individual river has an anomalously large impact on the calculated average Sr concentration and thus that the final calculated average is relatively robust.

A firm upper limit on the average river Sr concentration may be calculated by assuming that the remaining 53% of the world's river water averages near the 1.8 μmol/kg of the medium-sized rivers of Figure 6.2a. Taking the average 0.89 μmol/kg for the measured 18,722 km^3/yr of discharge plus an assumed average of 1.8 μmol/kg for the remaining 18,678 km^3/yr yields a global average of 1.34 μmol/kg. A firm lower limit is set by assuming that the remaining unmeasured rivers have an average equal to the 0.51 μmol/kg that characterises the 10 largest rivers; this yields a global average of 0.70 μmol/kg. The average concentration of Sr in river water is thus firmly bracketed to be 0.89 μmol/kg plus or minus a factor of 1.5.

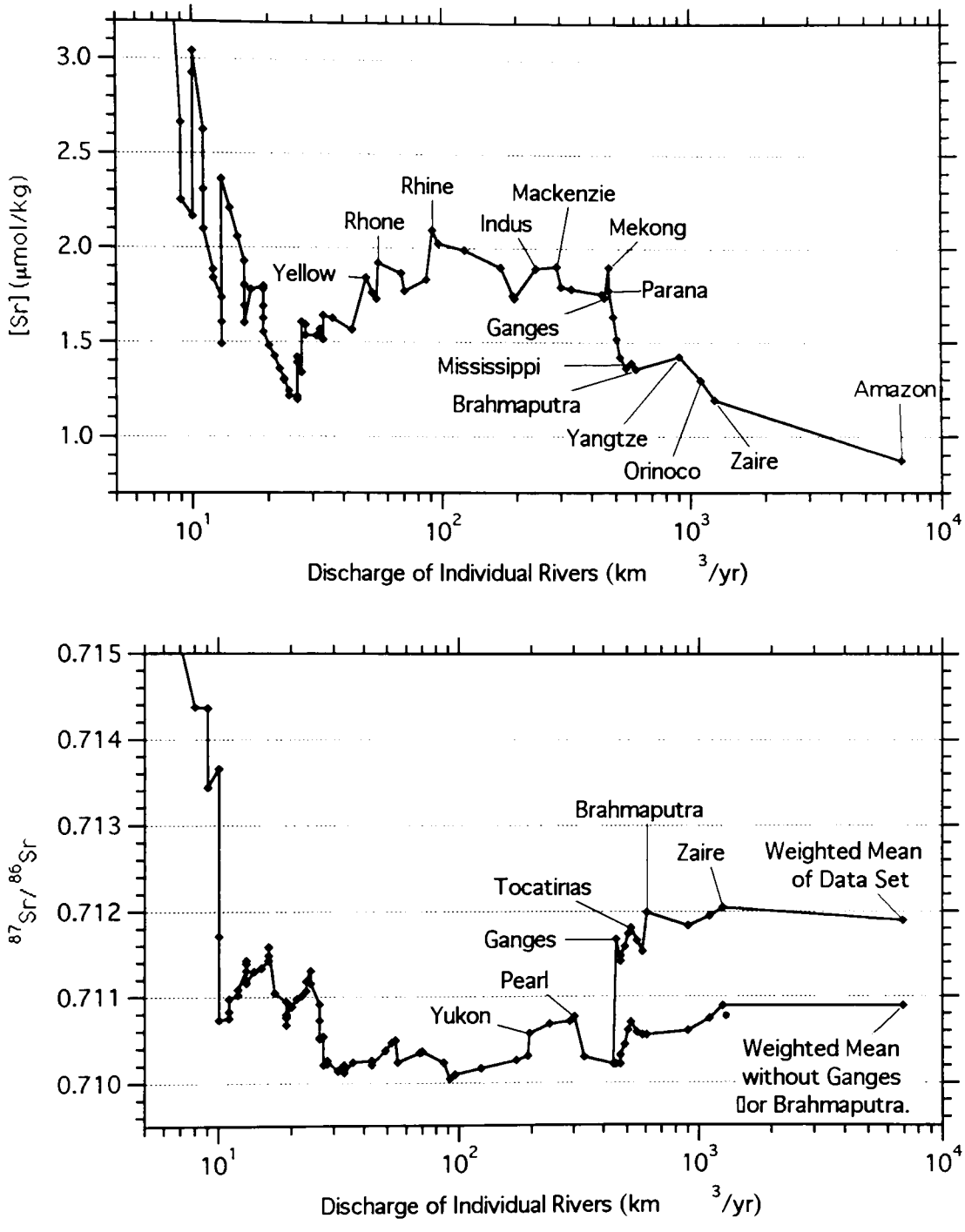

Figure 6.2 a,b: The evolution of the weighted mean concentration (a, top) and isotopic composition (b, bottom) of river water as a function of river size is calculated by starting with the smallest river (left) and adding successively larger rivers to the weighted average until the final result is obtained at the far right. See text for discussion.

Figure 6.2b shows the evolution of the weighted mean $^{87}Sr/^{86}Sr$ ratio as a function of river size. The most distinctive feature of this diagram is the jump from 0.7102 to 0.7117 that occurs with the addition of the Ganges River to the weighted average (top curve of Fig. 6,2b). As discussed by Palmer and Edmond (1989a), the Ganges and Brahmaputra are distinct from all other normal rivers in having both high Sr concentrations and high $^{87}Sr/^{86}Sr$ ratios. Normally Sr-rich waters are associated with marine sediments with intermediate Sr ratios ($^{87}Sr/^{86}Sr$ = 0.7068 - 0.7092) whereas high $^{87}Sr/^{86}Sr$ ratios are associated with Sr-poor waters draining slowly weathering silicate terranes. The Ganges and Brahmaputra are exceptional because the Himalayan mountains expose highly metamorphosed old continental basement rocks to intensive weathering that rapidly releases highly radiogenic Sr to the river systems (Edmond, 1991). A comparison of the upper and lower curves of Figure 6.2b clearly illustrates that removing the Ganges and Brahmaputra rivers from the data set results in a significantly lower global average $^{87}Sr/^{86}Sr$ ratio. The large jump to 0.7117 disappears and the evolution of the weighted average $^{87}Sr/^{86}Sr$ ratio increases only slightly from 0.7101 to 0.7109 as it moves from the medium to large rivers. This diagram dramatically illustrates the effect that a single unusual geological feature can have on the calculation of a global riverine geochemical budget.

Many of the other major rivers draining the Himalayas (Mekong, Irrawady, Indus, Salween) and other tectonically active areas in the world have been sampled or estimated (Palmer and Edmond, 1989a), but none are as exceptional as the Ganges and Brahmaputra. Because the Ganges and Brahmaputra are highly unusual, it is inappropriate to treat them as ordinary data points when calculating the global weighted average of river water. A more representative global average is obtained by excluding the Ganges and Brahmaputra from the data set, calculating the weighted average of the remaining data, and using this figure to extrapolate to the remaining 53% of unsampled runoff. Finally, the Ganges and Brahmaputra are added in to obtain the final global average. The weighted

average Sr isotopic composition excluding the Ganges and Brahmaputra (the lower curve in Figure 6.2b) is 0.7109. Adding the Ganges and Brahmaputra data (1053 km^3/yr, 1.21 μmol/kg, 0.7236) to the global extrapolation (36,347 km^3/yr, 0.801 μmol/kg, 0.7109) yields a best-estimate river water with 0.813 μmol/kg Sr and $^{87}Sr/^{86}Sr = 0.7114$. Note that this exercise only halves the influence of these two rivers on the final $^{87}Sr/^{86}Sr$ estimate (the average is raised from 0.7109 to 0.7114 instead of to 0.7119). The Ganges and Brahmaputra still have an exceptionally large impact on the global river water Sr budget. A reasonable lower limit on the $^{87}Sr/^{86}Sr$ estimate is calculated by assuming that the remaining 53% of the data set is unlikely to be below the strongly developed median of the data set at about 0.711 (Palmer and Edmond, 1989a). This defines error limits ranging from 0.7112 to the whole data set average of 0.7119.

The interpretation of the seawater Sr-isotope curve is hindered by the fact that the seawater Sr cycle is characterised by more variables than there are equations. To help overcome this problem, Figure 6.3 presents the relationship between the concentration and isotopic composition of Sr in the world's rivers. In general, one expects that rocks with high Rb/Sr ratios show radiogenic $^{87}Sr/^{86}Sr$ ratios whereas rocks with low Rb/Sr ratios show relatively non-radiogenic ratios. Rocks with high Rb/Sr ratios tend to have low Sr concentrations, while those with low Rb/Sr ratios tend to have high Sr concentrations. Thus rivers weathering rocks with high Rb/Sr ratios tend to have low concentrations of radiogenic Sr while rivers weathering rocks with low Rb/Sr ratios tend towards higher concentrations of nonradiogenic Sr. A simple mixing line between these two end-members produces a straight line on a $^{87}Sr/^{86}Sr$ - 1/[Sr] plot. For real data we would expect considerable scatter around any "mixing" line due to real rivers draining different combinations of the end-member lithologies, e.g., limestone and basalt, basalt and Archaean gneiss, gneiss and limestone, in addition to the spectrum of other rock-types.

The $^{87}Sr/^{86}Sr$ - 1/[Sr] plot of Figure 6.3 suggests a general linear relationship for the river data. The notable exceptions are the Ganges and Brahmaputra, whose combination of high Sr concentrations and radiogenic $^{87}Sr/^{86}Sr$ ratios were noted earlier, and the Avon and Murchinson rivers, which combine high Sr concentrations with radiogenic $^{87}Sr/^{86}Sr$ ratios due to the evaporative concentration of Sr in the Australian deserts. The bulk of the data from the major rivers (arbitrarily taken as having runoff > 300 km^3/yr) is indistinguishable from the data of the small and medium-sized rivers, indicating that there is no need to subdivide the data set based on river size. A regression of the data weighting each point equally yields a relationship of

$$^{87}Sr/^{86}Sr = (0.0022 \pm 0.0004)/[Sr] + (0.7085 \pm 0.0018).$$

This line is plotted in Figure 6.3. There are three estimates for the weighted global average (crosses) plotted for comparison. The estimate of Palmer and Edmond (1989a) plots well above the line, an average calculated excluding the Ganges and Brahmaputra data plots somewhat below the line and the best-estimate obtained in this study plots only slightly above the line. The three points form a trend moving towards the Ganges and Brahmaputra data. Although as a first approximation it seems reasonable to suppose that a global shift in the concentration of riverine Sr may be accompanied by a compensating shift in its isotopic composition, the poor resolution of the regression line plus the possibility that exceptional geological events may produce exceptional excursions, as illustrated by the Ganges and Brahmaputra data, make the application of the linear relationship of Figure 6.3 to the geological past somewhat hazardous.

In summary, the best-estimate of the total global river discharge is 37,400 km^3/yr, with qualitative error estimates spanning 34,000 to 42,300 km^3/yr. The best-estimate of Palmer and Edmond (1989a) is an average riverine Sr concentration of 0.890 μmol/kg and a $^{87}Sr/^{86}Sr$ ratio of 0.7119. In this study it was shown that the Ganges and Brahmaputra

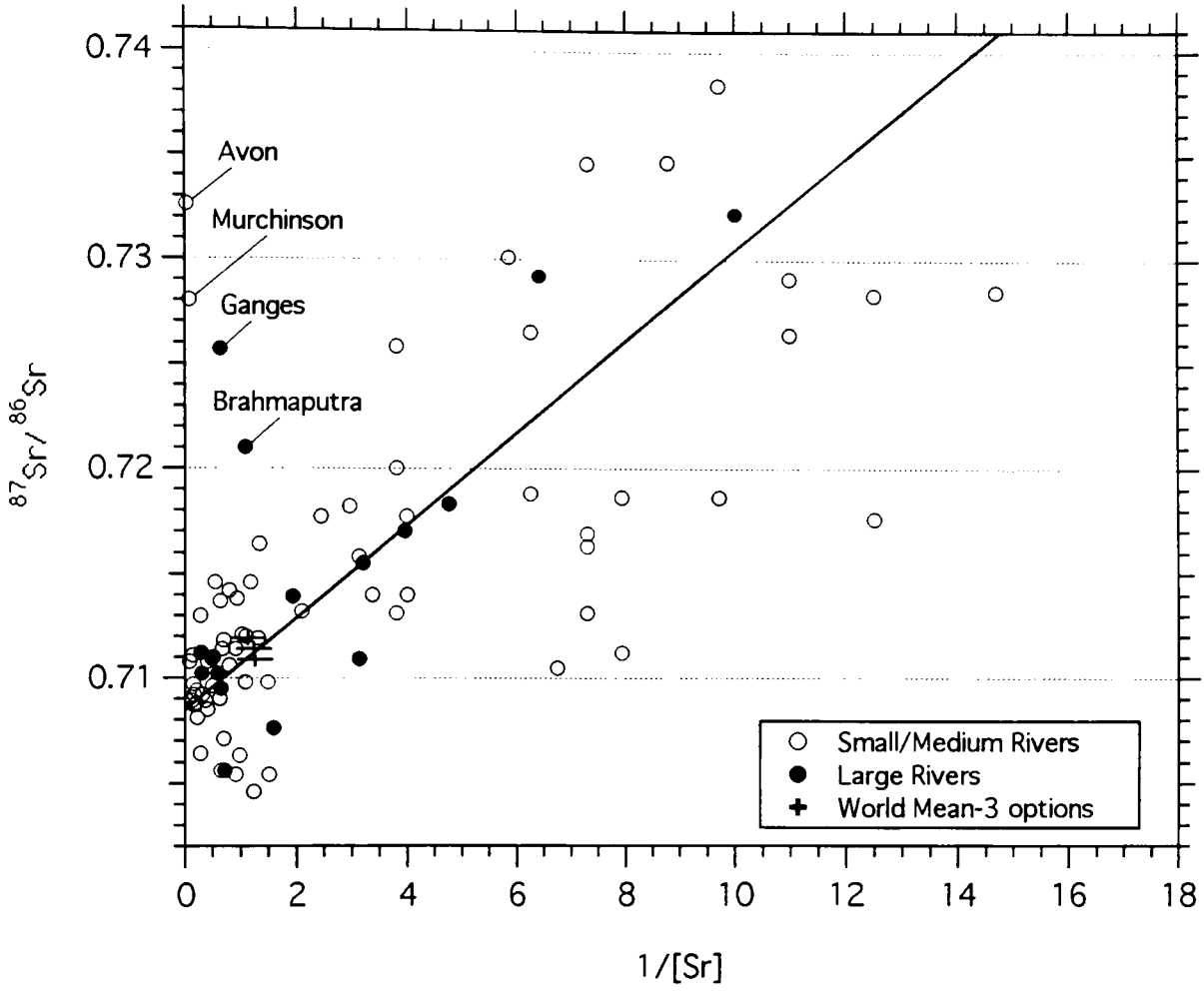

Figure 6.3: A $^{87}Sr/^{86}Sr$ - 1/[Sr] plot of the river data produces a generally linear trend, but with considerable scatter due to the variety of rock-types weathered by world rivers. The 3 'world mean' data points represent the estimate of Palmer and Edmond (1989a), the best-estimate of this study, and a weighted mean calculated without the Ganges and Brahmaputra data.

data are exceptional and exert a disproportionate effect on the weighted average of the river data. Therefore the weighted average used to extrapolate to the 53% of unsampled river runoff is calculated using all river data except the Ganges and Brahmaputra, and the Ganges and Brahmaputra are added to the global best-estimate only after this estimate is obtained for all other river water. The revised best-estimate is 0.81 μmol/kg with a $^{87}Sr/^{86}Sr$ ratio of 0.7114. The Sr concentration is firmly constrained to be between 0.70

and 1.34 μmol/kg and the $^{87}Sr/^{86}Sr$ ratio to between 0.7112 and 0.7119. The global Sr flux to the oceans, taking into account various error limits, is presented below:

$$37{,}400\ (34{,}000 - 42{,}300)\ km^3/yr * 0.81\ \mu mol/kg$$

$$= 3.0\ (2.8 - 3.4) * 10^{10}\ mol/kg$$

$$37{,}400\ km^3/yr * 0.81\ (0.70 - 1.34)\ \mu mol/kg$$

$$= 3.0\ (2.6 - 5.0) * 10^{10}\ mol/kg$$

$$37{,}400\ (34{,}000 - 42{,}300)\ km^3/yr * 0.81\ (0.70 - 1.34)\ \mu mol/kg$$

$$= 3.0\ (2.4 - 5.7) * 10^{10}\ mol/kg$$

Thus the flux of Sr to the oceans is constrained to within factors of +1.9 and -0.8, with much of the error attributable to uncertainties in the average concentration of Sr in river water. Palmer and Edmond (1989a) consider that the river data constrain the Sr flux to within about 30%. This yields narrower error limits of (2.1 - 3.9) * 10^{10} mol/kg Sr.

6.3.3 "Runout"

The magnitude of the subsurface flow of meteoric waters into the oceans ("runout") is difficult to measure. The flux of groundwaters into the oceans shows large variations both from point to point along a given coastline and as a function of depth below the earth's surface. There are few direct measurements of this flow, and only a few rough estimates of the global flux. Nace's (1969) rough calculations for the coterminous United States suggest that the subsurface flow is equal to about 5% of the total streamflow. Extrapolating this proportion to the global system, 0.05*37,400 km^3/yr yields 1870 km^3/yr. Korzun *et al.* (1974) assume a zone of runout that is 200 m deep, with a 10% active porosity, a groundwater flow velocity of 0.5 m/day, and a total coastline (not including Antarctica or regions with coastal permafrost) of 600,000 km. They calculate a groundwater flux of 2200 km^3/yr. Chaudhuri and Clauer (1986) break the system into two levels: the upper 10 m is characterised by a high fluid flow (15 m/day) while the next 3000 m has a much lower flow rate of 0.1 mm/day. With effective porosities, respectively, of

0.2 and 0.15 and a total coastline of 312,000 km (of which only 50% has sufficiently permeable rocks), an estimate is obtained of 1700 km^3/yr for the upper 10 m and 2.6 km^3/yr for the lower 3000 m. The most recent estimate, based on 33% of global rain falling on an area equal to 5% of the continental shelves infiltrating and half of this amount discharging into the oceans through submarine springs, is 100 km^3/yr ± a factor of 3 (COSOD II, 1987). The estimates of the global subsurface meteoric fluid flux thus range between 30 and 2200 km^3/yr.

6.3.4 Strontium in Meteoric Groundwaters

There are few data on the concentration and isotopic composition of Sr in groundwaters. Chaudhuri and Clauer (1986) compiled the results from 3 studies for waters draining the upper 10 m zone and estimated a global average Sr concentration of 1 ppm, and from 5 studies estimated a global average of 100 ppm for the fluids draining the lower 3000 m zone. The resultant global flux of Sr is $2.2 * 10^{10}$ mol/yr. They found no measurements of the isotopic composition of Sr, and assumed a ratio near average river water (0.711). Palmer and Edmond (1989a) briefly considered the runout term and concluded that because most groundwater flow occurs through carbonate and evaporate formations, the groundwater Sr is predominantly of marine origin ($^{87}Sr/^{86}Sr$ = 0.707 0.709) and therefore does not have a significant impact on the Sr-isotope budget of the oceans. Recently published results from ODP cores drilled in active margins tend to support this conclusion. As is the case for the diagenetic flux (see below), the majority of continental margin sites show pore fluid $^{87}Sr/^{86}Sr$ ratios that are lower than seawater contemporaneous with the deposition of the surrounding sediments (Gieskes *et al.*, 1990; Kastner *et al.*, 1990; Elderfield *et al.* 1990). The only exceptions are two sites drilled on the Peruvian slope that showed pore fluids obviously affected by continentally derived radiogenic Sr (maximum $^{87}Sr/^{86}Sr \approx 0.70995$). However, two other sites drilled on the Peruvian slope yielded Sr isotope ratios as low as 0.7083 and showed clear evidence for

interaction with nonradiogenic volcanic or basaltic materials (Elderfield *et al.*, 1990). For the purposes of this study, the estimate of Chaudhuri and Clauer (1986) will be taken as a maximum limit of the runout flux of Sr ($2.2 * 10^{10}$ mol/kg). The isotopic composition of this Sr, based on pore fluid data collected from continental margin sediments approximately 20 m depth below the sea floor, is very roughly estimated at 0.7085 - 0.7089 (Gieskes *et al.*, 1990; Kastner *et al.*, 1990; Elderfield *et al.*, 1990). It should be emphasised that all parameters of the runout flux are very poorly constrained.

6.4 Diagenetic Flux

There are 3 potential sedimentary sources of Sr in pore fluids: volcanic detritus ($^{87}Sr/^{86}Sr \approx 0.7025$ - 0.704), continental detritus (0.712 - 0.743; Dasch, 1969), and marine carbonates (0.707 0.709). Sea-floor sediments characterised by each of these three end-members were examined by Elderfield and Gieskes (1982) in an effort to estimate the flux of Sr associated with the burial diagenesis of each sediment type.

At sites without carbonate material they find pore fluids with relatively small enrichments in dissolved Sr^{2+} but relatively large decreases in the $^{87}Sr/^{86}Sr$ ratio, indicating significant exchange of Sr^{2+} with volcanic glass and ash. The few sites that show pore water $^{87}Sr/^{86}Sr$ ratios higher than seawater contemporaneous with sediment deposition are associated with impure carbonates containing significant continental detritus. While the data are consistent with continental detritus contributing Sr to the pore fluids, they are also consistent with the possibility that the very low sedimentation rates at these sites have allowed seawater Sr^{2+} to diffuse down into the pore fluids. Thus Elderfield and Gieskes (1982) conclude that there is no conclusive evidence for continental detritus as a significant contributor of Sr to the diagenetic flux. The concentration gradients at the non-carbonate sites are roughly 0.02 - 0.03 mM Sr^{2+} per 100 m below the sea floor and have an average $^{87}Sr/^{86}Sr$ ratio of approximately 0.7064.

The pore waters at carbonate sites show Sr^{2+} concentrations up to 10 times that of seawater but with $^{87}Sr/^{86}Sr$ ratios that decrease only moderately with depth. The $^{87}Sr/^{86}Sr$ ratios of the pore fluids reflect the $^{87}Sr/^{86}Sr$ ratios of the carbonate sediments undergoing recrystallisation during compaction and lithification. The carbonate sites show concentration gradients of 0.5 - 1.0 mM Sr^{2+} per 100 m with an average $^{87}Sr/^{86}Sr$ of approximately 0.7087. This isotopic composition is equivalent to that of ≈16 Ma seawater (Hess *et al.*, 1986).

Elderfield and Gieskes (1982) convert the vertical concentration gradients into global fluxes assuming no advection, an average distribution coefficient D_{Sr} of $2 * 10^{-6}$ cm^2/s, an ocean area of $361 * 10^{16}$ cm^2, and the equation $J_d = D_{Sr}(\Delta[Sr^{2+}]/\Delta depth)$. This results in a flux of 1 $2 * 10^{10}$ mol/yr for carbonate sediments and 0.05 - $0.07 * 10^{10}$ mol/yr for non-carbonate sediments. These values are then corrected for the area of sea floor currently occupied by each sediment type. Assuming that carbonates occupy 25% of the sea floor and non-carbonates occupy the remaining 75%, this results in 0.25 - $0.50 * 10^{10}$ mol/yr for carbonate sediments and 0.038 - $0.053 * 10^{10}$ mol/yr for non-carbonate sediments. In a later publication the best estimate values were fixed at $0.3 * 10^{10}$ and $0.04 * 10^{10}$ mol/yr (Palmer and Elderfield, 1985). Goldstein and Jacobsen (1987) applied a different diffusion model to the data and general assumptions of Elderfield and Gieskes (1982) and obtained a diagenetic carbonate flux of $0.24 * 10^{10}$ mol/yr. The best-estimate values selected by Palmer and Elderfield (1985) are used in this study.

6.5 Mid-Ocean Ridge Hydrothermal Springs

6.5.1 Geophysical Constraints

The circulation of seawater through oceanic crust at elevated temperatures exerts a fundamental control on the chemistry of Sr and other elements in the oceans. The inaccessibility of deep-sea hydrothermal vents forces us to constrain the magnitude of chemical exchange in hydrothermal systems using geophysical heat flow measurements, a

small number of direct observations, geochemical basalt/seawater experiments, and simple mass-balance calculations.

The largest volume of seawater circulates through the oceanic crust along the mid-ocean ridges, with smaller volumes circulating around the ocean island hot spots (Karl *et al.*, 1988), back-arc spreading centres (Fouquet *et al.*, 1991), and other sites of sea-floor volcanism. The areal extent of seawater circulation at the mid-ocean ridges is best mapped by examining the discrepancy between the predicted and observed conductive heat flow through the oceanic crust (Figure 6.4). Thermal models of the oceanic crust predict that as it moves off-axis, the cooling of the crust causes both the elevation and conductive heat flow to decrease as a simple function of the square root of age. While the observed elevation of the sea floor beautifully matches the theoretical predictions (e.g., Tréhu, 1975; Parsons and Sclater, 1977), the observed heat flow data fall well below the model predictions near the ridge axis and only match the predictions on relatively old oceanic crust (Figure 6.4; Anderson and Hobart, 1976; Anderson *et al.*, 1977; Sclater *et al.*, 1980). This 'missing heat'--the difference between the theoretical and observed conductive heat flow--is thought to be convectively removed by cold sea water circulating through the highly fractured basaltic crust (Lister, 1972, 1974; Anderson and Hobart, 1976; Sclater *et al.*, 1976).

As indicated in Figure 6.4, convective heat flow generally dominates in oceanic crust 0-50 Ma in age while conductive heat flow generally dominates in crust older than 60 Ma. In detail, however, the timing of the transition from predominantly convective heat flow to predominantly conductive heat flow varies from site to site (Figure 6.5), ranging from 4-6 Ma at the Galapagos rift, 10-15 Ma along the East Pacific Rise, 40-60 Ma in the Indian Ocean, and 50-70 Ma in the Atlantic Ocean (Anderson *et al.*, 1977). The timing of this transition depends on a number of locally controlled variables such as burial of the permeable basaltic basement by more than 300 m of relatively non-calcareous sediments,

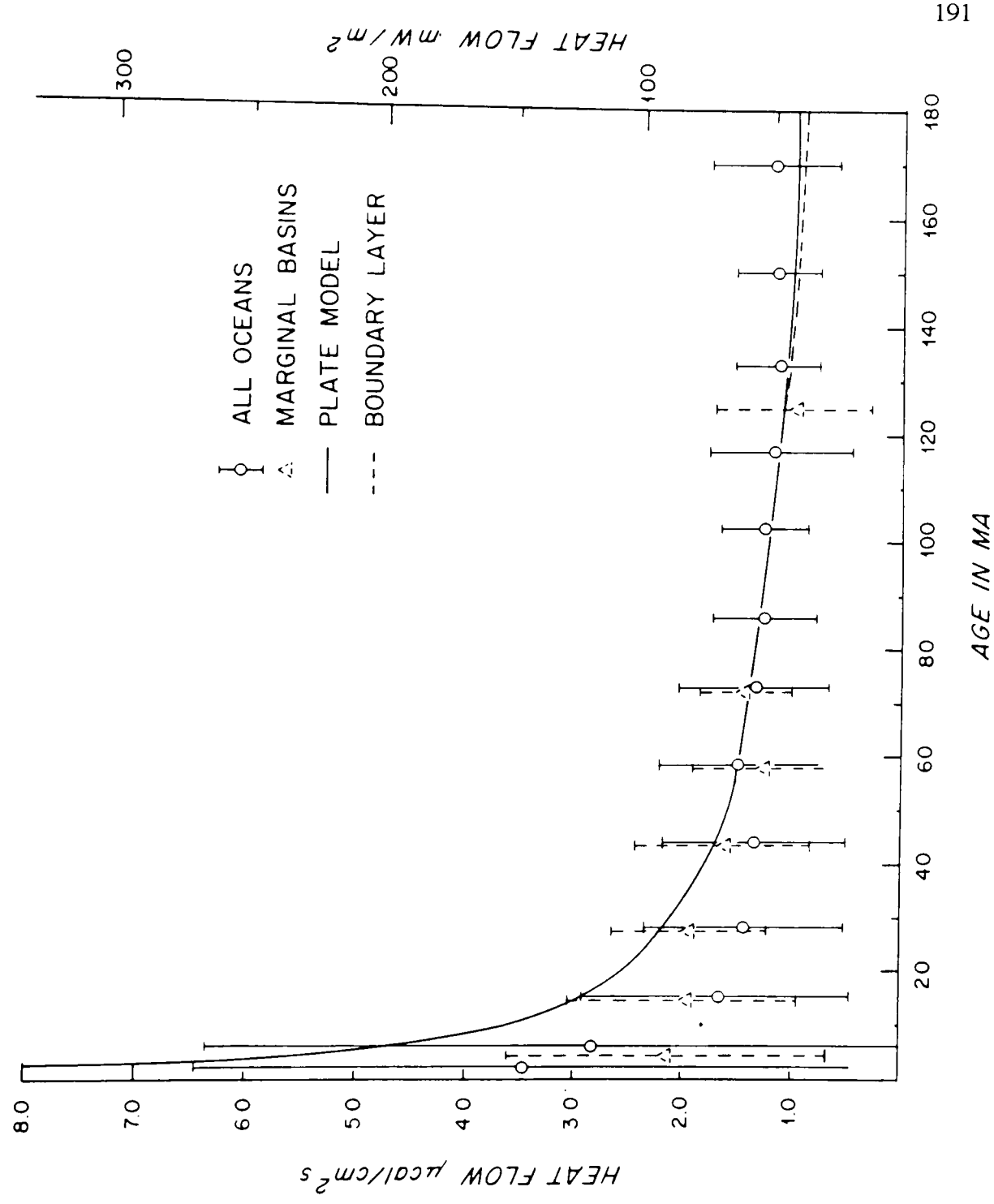

Figure 6.4: Variation in the conductive heat flow in oceanic crust as a function of age. Solid and dashed curves represent the theoretically predicted heat flow estimates as compared to the actual measurements (circles and triangles). The difference between the theoretical curve and the curve defined by the data is the 'missing heat' thought to be convectively removed by seawater circulation. Figure from Sclater *et al.* (1976).

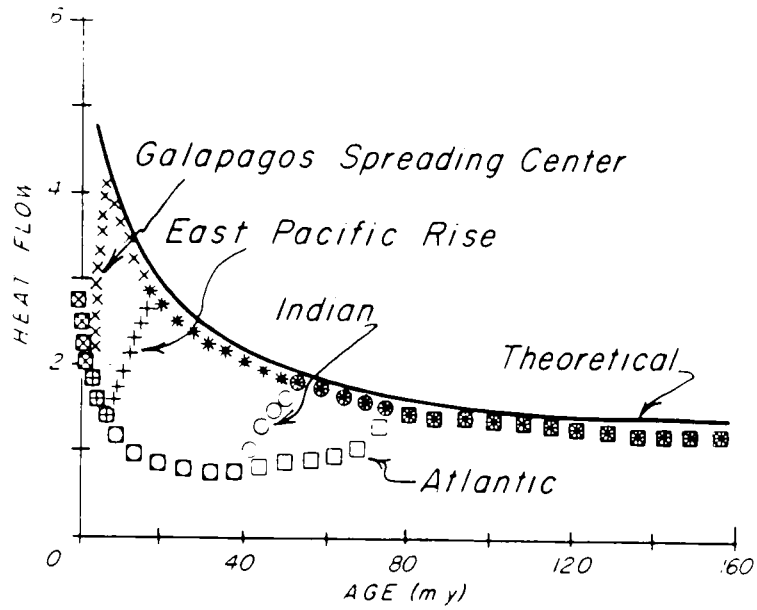

Figure 6.5: Comparison between the theoretical heat flow curve and the observed heat flow data from a number of oceans, showing the variations in the timing of the shut-down of convective flow. From Anderson *et al.* (1977).

burial of all topographic irregularities of the basement, and the precipitation of sufficient secondary material in the fluid pathways (Anderson *et al.*, 1977; Sleep and Wolery, 1978). When near-axis conductive heat flow measurements are restricted to only those areas where thick sedimentary cover has shut down convective exchange, the observations match the theoretical predictions all the way up to the ridge axis and thus confirm the basic correctness of the geophysical models (Sclater *et al.*, 1976).

In addition to giving an impression of the areal extent and geographic variability of oceanic crust open to seawater circulation, the 'missing heat' removed by seawater can be

used to estimate the amount of seawater moving through the seafloor. The total convective heat loss is calculated by subtracting the globally averaged, observed heat flow curve from the theoretical curve (e.g., Fig. 6.4). The results vary from about 20.9 * 10^{19} J/yr (50 * 10^{18} cal/yr) (Anderson *et al.*, 1977; Sleep and Wolery, 1978) to 31.8 * 10^{19} J/yr (76 * 10^{18} cal/yr) (Sclater *et al.*, 1980). Williams and von Herzen (1974) arrive at a similar estimate of 25.8 * 10^{19} J/yr (61.5 * 10^{18} cal/yr) based on the amount of heat released by newly emplaced crust at spreading centres and assuming that 50% of the heat lost in < 2 Ma crust is due to hydrothermal circulation. These convective heat flow estimates may be converted to an estimate of hydrothermal fluid flux using an entropy-balance equation (Sleep and Wolery, 1978):

$$J_h = H/(T_h C_{p\,h} - T_{in} C_{p\,in}),$$

where J_h is the hydrothermal flux of water (kg/yr), H is the heat flux (J/yr), T_{in} is the temperature (°C) of the fluid entering the system, T_h is the maximum hydrothermal temperature attained at depth (and presumably the temperature at which most interesting geochemical reactions occur), and C_p is the heat capacity (J/g°C) of the fluid when it enters and leaves the system. We have estimates for T_{in} (= 2 °C), and the heat capacity of seawater over a range of T and P (Bischoff and Rosenbauer, 1985), but we have to consider the appropriate values of H and T_h in more detail.

For geochemical reasons it is useful to divide hydrothermal fluids into those emanating from high temperature axial systems ($T_h \geq 250$ °C) and those exiting from low-temperature, off-axis (flank) systems. The amount of heat lost through axial hydrothermal flow is constrained by geophysical models of the thermal structure of the crust at mid-ocean ridges (Sleep *et al.*, 1983; Morton and Sleep, 1985; Wolery and Sleep, 1988; Sleep, 1991). In these models, heat is supplied to the mid-ocean ridges by the intrusion of hot magmas and by the latent heat of crystallisation released by the cooling magmas. If heat were only conductively removed, the top of the magma chamber would be at about 1 km depth,

whereas the chamber tops are seismically observed at 2.3 - 2.5 km depth. Sleep *et al.* (1983) and Morton and Sleep (1985) modelled the effect of hydrothermal vents on the thermal balance of a mid-ocean ridge by distributing a series of heat sinks at and near the ridge axis and then increasing the efficiency of these sinks until the depth and shape of the model magma chamber matched the seismically imaged magma chambers at three different spreading centres. Their results suggest that a time-averaged convective heat loss of 2.5 - 4.1 * 10^{19} J/yr (mean of three = 3.3 * 10^{19} J/yr) is required to explain the observed thermal structure within about 2 km of the ridge axis. This is only about 12 - 20% of the total 'missing heat' estimate of Sleep and Wolery (1978) and 8 - 13% of the estimate of Sclater *et al.* (1980). The remainder of the mid-ocean ridge convective heat loss is thus thought to occur through low-temperature, off-axis circulation.

Because the heat capacity of seawater rapidly changes at elevated temperatures and pressures (Bischoff and Rosenbauer, 1985), the calculated hydrothermal flux required to remove a given amount of heat from the ridge axis is strongly dependant on the assumed temperature and pressure of the hydrothermal fluids. Figure 6.6 clearly illustrates that it is essential to know not only the general P and T conditions for axial hydrothermal systems, but also the relative proportions of heat removed by different systems at specific P,T conditions. For example, if all heat were removed by fluids at 400 °C and P = 400 bars, roughly 11 * 10^{12} kg/yr of water would be required to do the job. If only 25% of the heat were removed by fluids at these conditions while the rest were removed by fluids at 200 °C, a total of (1.1 * 10^{12}) + (36 * 10^{12}) = 37 * 10^{12} kg/yr of water would be required. Thus it is clearly essential to consider not only the maximum temperatures attained by the hydrothermal springs, but also the range of temperatures characterising the fluids of geochemical interest.

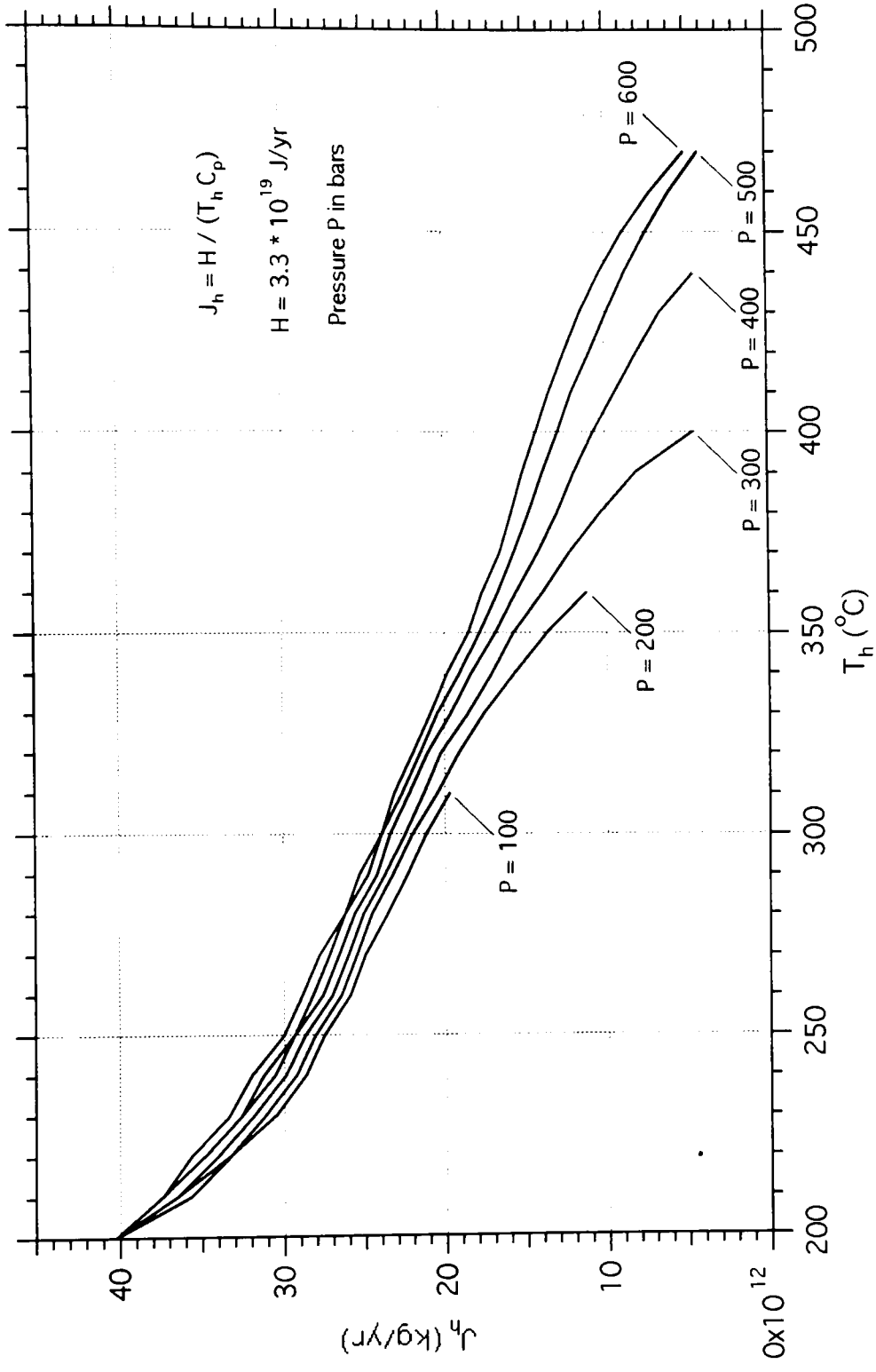

Figure 6.6: Variation in the amount of seawater required to remove 3.3 * 10^{19} J/yr heat as a function of temperature and pressure attained by the seawater. Calculated using the entropy balance equation of Sleep and Wolery (1978) and the heat capacity data of Bischoff and Rosenbauer (1985)

So far only high-temperature, vigorously circulating, black- and white-smoker vents have been well-sampled. These springs are characterised by relatively tight plumbing systems that prevent the subsurface admixture of large amounts of cold seawater and relatively small vent openings that allow relatively pure hydrothermal fluid samples to be taken. While there is evidence for diffusively flowing springs in close proximity to these smokers (Von Damm, 1990), diffuse venting makes sampling difficult and in any case it is likely that subsurface mixing with seawater has strongly altered the chemical and thermal properties of the original hydrothermal fluid. Thus, although lower temperature hydrothermal fluids are important, the bulk of the experimental and observational data concerns the high-temperature smokers.

Recent experimental data indicate a narrow temperature range for the reaction zone in which modified seawater interacts with basalt to become a typical black-smoker fluid. In a variety of basalt/modified seawater experiments at 400 bars pressure, Seyfried *et al.* (1988), Berndt *et al.* (1989), and Seewald and Seyfried (1990, and references therein) find that in order to produce the chemical characteristics of observed black smoker fluids, a temperature of at least 375 °C to about 400 °C is required. Their best-estimate range is between 385 and 400 °C. By contrast, a compilation of observed vent temperature data shows an apparent maximum exit temperature of only 350 ± 5 °C (Cambell *et al.*, 1988; Seewald and Seyfried, 1990). While some recent work (Tivey *et al.*, 1990; Fouquet *et al.*, 1991) has indicated exit temperatures up to 405 °C, 350 °C is still taken as an appropriate maximum exit temperature for the majority of vents. To bridge the gap between exit temperatures of 350 °C and reaction zone temperatures of 385 - 400 °C, Seewald and Seyfried (1990) propose the following model: All black smoker fluids react at temperatures of 385 - 400 °C at pressures of around 400 bars. The fluids undergo adiabatic decompression as they rise towards the seafloor; this lowers their temperatures by about 10 - 15 °C. The remainder of the 20 °C or more cooling takes place as the fluids pass through

the massive sulphide deposits and vent chimneys. These structures are bathed in cold seawater and, especially when plumbing systems are complex, are thought to account for the number of vents with measured exit temperatures that are an additional 20 to 50 °C cooler than 350 °C. Because this conducted heat is emplaced very locally and on the surface, it does not affect the overall conductive heat flux of the new crust and thus is not detected in regional conductive heat-flux surveys (Sleep and Wolery, 1978). There is no reason, therefore, to take special consideration of this 20 - 70 °C/kg H_2O conductive heat loss and it is appropriate to use hydrothermal fluid temperatures corrected only for adiabatic decompressive cooling (e.g., T_{exit} = 370 - 390 °C).

A more traditional approach to the problem of maximum hydrothermal reaction temperatures has been to assume that the rapid ascent of the vent fluids does not allow significant conductive cooling (*contra* Seewald and Seyfried, 1990) and thus to take 350 °C as the maximum exit temperature attained by the black smoker fluids. Vent temperatures that are significantly cooler than 350 °C are assumed, with some evidence (e.g., Bowers *et al.*, 1988; Palmer and Edmond, 1989b), to reflect cooler temperatures at depth. Following this approach, a histogram of the exit temperature data for the chemically analysed vents (N = 20, Guaymas data excluded) yields a range of vent temperatures (T_{exit}) between 320 and 360 °C.

Returning to the enthalpy-balance equation of Sleep and Wolery (1978),

$$J_h = H/(T_h C_{p\,h} - T_{in} C_{p\,in}),$$

the estimated axial heat flux H is 3.3 (2.5 - 4.1) * 10^{19} J/yr, the heat capacity data come from Bischoff and Rosenbauer (1985), the pressure range is 300 - 500 bars, the experimental exit temperatures are 370 - 390 °C, and the observed exit temperatures span 320 - 360 °C. The estimated global high-temperature hydrothermal flux using the experimental temperatures ranges between 6.2 and 17.2 * 10^{12} kg/yr, with a best estimate of 13.0 * 10^{12} kg/yr, while the same estimate using the observed exit temperatures yields

between 10.5 and 26.7 * 10^{12} kg/yr with a best-estimate of 18.3 * 10^{12} kg/yr. Incorporating both estimates yields a final best-estimate of 15 * 10^{12} kg/yr plus or minus a factor of 2. As a final comment, this estimate assumes that all axial 'missing heat' is removed by high-temperature (> 320 °C) fluids. If 50% of this heat were removed by lower temperature fluids at 200 °C, a total of 29.3 * 10^{12} kg/yr of seawater is required to do the job, with only 9.2 * 10^{12} kg/yr being due to high-temperature vents (T_{exit} = 340 °C). It is thus important in the future to place more rigorous constraints on the lower temperature limits of geochemically significant hydrothermal activity.

6.5.2 Geochemical Constraints

6.5.2.1 High-Temperature Axial Vents

The discovery of MOR (mid-ocean ridge) hydrothermal springs in the late 70's was of great interest to the geochemists who were unable to balance the geochemical cycles of a variety of seawater elements. In the case of Mg, for example, the known sources of Mg^{2+} to the oceans far outweighed the known sinks. Thus one had either to assume that modern riverine fluxes were seriously out of equilibrium with respect to the oceans, or to postulate widespread authigenic formation of Mg-bearing phyllosilicates for which there was little supporting evidence (see reviews in Holland, 1978; Berner and Berner, 1987). The proposed existence of hydrothermal springs along the mid-ocean ridges therefore led to a large number of experiments in which seawater was made to react with basalt under a variety of elevated temperature and pressure conditions. The results of these experiments indicated that seafloor hydrothermal springs could be a major sink for Mg as well as significantly impacting the geochemical cycles of a number of other seawater components.

In 1979 Edmond *et al.* published the first chemical data on a series of hydrothermal vents discovered at the Galapagos Ridge. Since then a number of other sites have been discovered and sampled, including vents at 11-13° and 21° N on the East Pacific Rise (Michard *et al.*, 1984; Grimaud *et al.*, 1985; Bowers *et al.*, 1988; Von Damm *et al.*, 1985a;

Campbell *et al.*, 1988a), in the Guaymas Basin in the Gulf of California (Von Damm *et al.*, 1985b), on the Juan de Fuca Ridge off the coast of Oregon/Washington USA (Von Damm and Bischoff, 1987; Massoth *et al.*, 1989), at 23° and 26° N on the Mid-Atlantic Ridge (Campbell *et al.*, 1988b), and in the Lau back-arc basin (Fouquet *et al.*, 1991). The data collected from these systems, in conjunction with the results of ongoing basalt/sea water experiments, have been used in a variety of thermodynamic models aimed at understanding the major controls on the chemistry of hydrothermal systems (e.g., Mottl, 1983; Bowers *et al.*, 1985; Bowers and Taylor, 1985; Seyfried, 1987; Berndt *et al.*, 1988, 1989; Seyfried *et al.*, 1988; Von Damm, 1988; Seewald and Seyfried, 1990). As a result, although several problems remain and more data will surely yield new insight, the current data set and level of understanding are probably adequate to provide realistic constraints on the geochemical cycle of Sr.

As a whole, the chemistry of the sampled high-temperature vent fluids is remarkably similar despite salinity variations from 0.6 to 2.1 times that of normal seawater and the variety of seafloor depths and spreading rates encountered from site to site. All vent fluids show a complete loss of Mg and SO_4, variable enrichments of K, Ca, Li, and H_2S, and variable enrichments/depletions of Na, Cl, and Sr when compared to ambient seawater (Von Damm, 1990). The relative constancy of the relationships between various major and trace elements suggests that the relative proportions of these elements are controlled primarily by an equilibrium between the fluid and a variety of primary and secondary mineral phases (Von Damm, 1988). Indeed, computer-modelled thermodynamic calculations indicate a general equilibrium between these fluids and a variety of greenschist-facies alteration minerals (Bowers *et al.*, 1988). The wide salinity variations are apparently due to variable mixtures between normal seawater-derived fluids and the vapour or brine component of an evolved fluid that has undergone phase separation (Von Damm, 1988, 1990; Massoth *et al.*, 1989).

Despite the overall consistency of the fluids, there are several vent sites that deserve special mention. Nearly all vents are located along the central spreading axis on what appear to be the youngest, freshest basalt flows. Thus it is likely that the fluids from these sites have reacted with a relatively uniform basaltic reservoir and then vented directly into the oceans. The most prominent exceptions are the vents from the Guaymas basin in the Gulf of California (Von Damm *et al.*, 1985b). Because the basaltic basement is buried by 500 m of sediments, the fluids are strongly modified through interaction with sedimentary carbonates, detrital and biogenic silicates, and organic matter. Also unusual are the Galapagos vent fluids, which have undergone substantial subsurface mixing with cold seawater, with the result that the trace metal concentrations are strongly altered by extensive sulphide precipitation and that extrapolation back to the pure hydrothermal end-member is subject to large errors.

Table 6.5 presents the average composition of the sampled hydrothermal vents, excluding the Guaymas data, compared to average seawater. The averages suggest that all compiled elements--except Mg--show a considerable enrichment over seawater. Thus the axial hydrothermal springs appear to be a significant source of many elements to the oceans. While this seems reasonable in the sense that high-temperature alteration of basalt at low water/rock ratios seems likely to produce fluids rich in dissolved material, there are reasons for concern. First, the sample set is undoubtedly biased towards the metal-rich solutions that are able to build the sulphide chimneys that focus the flow of the hydrothermal fluids into easily-sampled vents. Solute-poor fluids that form as a result of phase separation are unlikely to precipitate the volume of sulphides necessary to channelise their flow and thus are likely to undergo diffuse venting. Although there is visual evidence for such solute-poor springs, they have, with one exception (Massoth *et al.*, 1989), not been adequately sampled (Von Damm, 1990).

That the compiled data are biased towards solute-rich solutions is clearly indicated by the excess of nearly 60 mM/kg of Cl compared to seawater. This Cl excess is unlikely to have come from the alteration of basalts because basalt contains only trace quantities of Cl. Instead, it seems more reasonable to pursue the idea that Cl and other elements are enriched in many observed hydrothermal fluids due to the admixture of brines or the separation of vapours from fluids originally of seawater chlorinity.

Table 6.5: Mean composition of axial hydrothermal springs

Element	Unit	MOR Spring	± 1 S.D.	Seawater (35‰)
Li	μM/kg	983	375	26
Na	mM/kg	497	142	468
K	mM/kg	26	9	10
Rb	μM/kg	22	8	1.4
Mg	mM/kg	0	--	53
Ca	mM/kg	35	24	10
Sr	μM/kg	124	74	87
$^{87}Sr/^{86}Sr$		0.7033	0.0004	0.7092
Cl	mM/kg	604	198	545
SiO_2	mM/kg	19	3	0.16
Salinity	‰	36.9	--	34.7
pH		3.5	0.3	7.8

Sources cited in text; Von Damm (1990) contains a summary of most published data.

There seems to be no compelling evidence that Cl is either released or incorporated into oceanic crust during high or low temperature alteration (Palmer and Edmond, 1989a). For example, Ito *et al.* (1983) have compiled data on altered and unaltered oceanic crust in an effort to balance the flux of H_2O and Cl through the hydrosphere, crust, and mantle. A compilation of literature analyses suggests an average of 48 ppm Cl (± a factor of two) in fresh MORB and 45 ±25 ppm Cl in the upper 2-5 km of altered sea floor basalt. Although the data are sparse, there is clearly no observational evidence for large-scale movements of Cl into or out of oceanic crust. A variety of seawater-basalt experiments (Mottl and Holland,1978; Seyfried and Bischoff, 1981; Rosenbauer and Bischoff, 1983; Seewald and Seyfried, 1990) also indicate that Cl behaves conservatively, with minor changes in

concentration attributable to rock hydration. In a study specifically aimed at mechanisms of altering Cl concentrations in hydrothermal fluids, Seyfried *et al.* (1986) find evidence for a Cl-bearing phase that is stable at temperatures greater than 350° C (P = 400 bar) but which shows strong retrograde solubility at lower temperatures. There is no experimental evidence for a volumetrically significant, stable, Cl-bearing greenschist-facies mineral that could store Cl in oceanic crust.

There is, however, some evidence for the incorporation of seawater Cl into amphibolite-grade alteration products, fluid inclusions, and basaltic magmas. Wicks and Plant (1979), Rehtijarvi (1984), Vanko (1986), and Nehliq (1991) find relatively elevated Cl levels in amphiboles (up to 4 wt%) and serpentinites (up to a few tenths wt%). Michael and Schilling (1989) favour seawater-derived Cl as a source of elevated Cl concentrations in evolved MORB rocks (up to 1500 ppm Cl in FeTi basalts and up to 8000 ppm Cl in rhyodacites) because fractional crystallisation cannot alone account for the high Cl concentrations. Assimilation of bulk altered oceanic crust is not seen as a Cl source due to its low average Cl content; instead Michael and Schilling (1989) look towards melting or subsolidus breakdown of Cl-rich amphiboles or the incorporation of Cl-rich brines trapped in fluid inclusions as the most likely sources of Cl. Despite this evidence for some Cl incorporation into oceanic crust, Nehliq (1991) concludes, based on fluid inclusion and mineral studies from the Semail and Trinity ophiolites, the East Pacific Rise (13 °N), and ODP Hole 504B, that the Cl content in all hydrated minerals and most amphiboles is too low and the fluid inclusions and Cl-rich amphiboles are too volumetrically insignificant to have any effect on the chlorinity of hydrothermal vent fluids. It appears, therefore, that the conservative behaviour of Cl allows it to be used as an index of the enhancement or depletion of other elements in hydrothermal vent fluids relative to seawater.

The elimination of the formation and breakdown of Cl-bearing minerals leaves rock hydration and phase separation as possible mechanisms to account for the wide variations

in vent fluid chlorine levels (e.g., Von Damm, 1988, 1990). Rock hydration and dehydration could produce small changes, but is unlikely to account for the 188 - 1050 mmol/kg range of Cl found in hydrothermal fluids (compared to seawater with 545 mmol/kg Cl). Although the mechanism of phase separation has its problems (e.g., Campbell and Edmond, 1989b), it is currently favoured as the best way to produce the wide range of observed fluid chlorinities (Von Damm, 1988, 1990; Berndt and Seyfried, 1990).

The phase diagram of seawater in P-T space is divided into 3 fields by a two-phase boundary and a critical point at about 405 °C and 300 bars (Bischoff and Rosenbauer, 1985). When seawater (or evolved seawater in a hydrothermal system) is progressively heated at a pressure less than 300 bars, it eventually crosses the two-phase boundary and a small amount of dilute vapour separates from the bulk liquid. Above the critical point pressure of 300 bars, intersection with the two-phase curve results in the separation of a small amount of dense brine. According to measured exit temperatures and experimental efforts concerning controls on major element chemistry, most hydrothermal systems at depth cover a temperature range of 320 to at least 400 °C at pressures of 250 to 500 bars. These systems are very near the two-phase boundary for seawater, and it is thus entirely possible that some fraction of mid-ocean ridge hydrothermal fluids reacts at conditions above the two-phase boundary.

At present there is only one vent field with clear evidence for phase-separated fluids (Massoth *et al.*, 1989; Butterfield *et al.*, 1990). To account for both the large chlorinity variations and the lack of clear corroborating evidence from gas contents (vapour-rich fluids should be gas-rich, and brine-rich fluids gas-poor), Von Damm and Bischoff (1987) and Von Damm (1988, 1990) propose variable mixtures between a low-solute vapour phase, a fluid of roughly seawater chlorinity that has not undergone phase-separation, and a solute-rich brine. Geophysical calculations indicate that the different density and

viscosity characteristics of the vapour and brine result in fluid migration along different pathways (although Goldfarb and Delaney (1988) and Fox (1990) indicate contradictory fluid pathways for the two fluids), and this provides a mechanism for their initial separation and later remixing during migration through the crust.

During simple phase separation the fluid metal/chlorine ratios should remain unchanged in the vapour and brine components. Mixing of either component with the original solution also preserves the original metal/chlorine ratios, but produces a linear array of data points that follows mixing lines between the vapour, original solution, and brine. As outlined by Palmer and Edmond (1989a), most hydrothermal spring data yield Sr and Cl concentrations that are similar to seawater, but with a linear spread towards more dilute (vapour-rich) and concentrated (brine-rich) values. However, Von Damm (1988) has demonstrated, using a wider array of elements, that while Cl-poor fluids are consistent with simple mixing between a Cl-normal (≈ seawater chlorinity) fluid and a dilute vapour, the Cl-rich fluids indicate mixing between the Cl-normal fluid and a brine with a distinctly different chemical composition. Data on gas concentrations from the Plume vent of the Juan de Fuca Ridge (Von Damm and Bischoff, 1987) has allowed Von Damm (1988) to calculate the composition of a geochemically distinctive brine that has mixed with Cl-normal fluids to produce the observed Plume chemistry. Although based on only one vent, the calculated composition of this brine produces a mixing model that is compatible with observed vent chemical constraints. This consistency lends weight to the use of this brine composition as a fairly good approximation to the brine component found in any mid-ocean ridge hydrothermal spring.

The 3-component mixing model is presented in Figure 6.7 as a plot of the Ca and Cl data placed in the context of mixing lines connecting a pure vapour (~distilled water) end-member, seawater acting as reference for a fluid of seawater chlorinity, and the pure brine end-member of Von Damm (1988; 441 mmol/kg Ca, 3270 mmol/kg Cl). The results of

numerous basalt/seawater experiments indicate that the hydrothermal alteration of basalt releases Ca into solution. The excess of Ca relative to Cl for samples with chlorine concentrations near and slightly below that of seawater confirms the results of these experiments. Although it is possible that each of these samples reflects a complex combination of the three end-members, the data are also consistent with a simpler mixing scenario. In this paper it is assumed that all samples with Cl concentrations less than seawater are the result of simple mixing between a pure vapour and a Cl-normal fluid. All samples with elevated Cl concentrations are the product of mixing between the Cl-normal fluid and a dense brine similar to that calculated by Von Damm (1988). Given this arrangement, one can use a simple 2-component mixing model to calculate the average composition of the pure Cl-normal fluid end-member:

(Vapour or Brine)*X + (Cl-normal fluid)*(1-X) = Sampled Fluid.

The compositions of the vapour (pure water), brine and sample are known. Since Cl appears to behave conservatively during seawater/basalt interaction, the concentration of Cl in a sample can be used to calculate how much (X) of either vapour or brine was added to the fluid to move the Cl concentration away from the seawater concentration of 545 mmol/kg. The calculation may be visualised on Figure 6.7 as a series of mixing lines that project from either the vapour or brine end-members, pass through a given data point, and intersect a vertical line drawn at the seawater chlorine concentration of 545 mmol/kg. These points of intersection, which yield the calculated Ca concentrations in the pure Cl-normal fluids, are shown in Figure 6.7 as short horizontal lines. Nearly all points project above the seawater concentration of 10.2 mmol/kg Ca and yield an average Ca concentration of 21.7 mmol/kg (standard deviation = 11.0 mmol/kg). This result may be slightly high because the inclusion of a brine component in the vapour/Cl-normal mixtures or a vapour component in the Cl-normal/brine mixtures act to raise the calculated concentration of a given metal in the Cl-normal end-member.

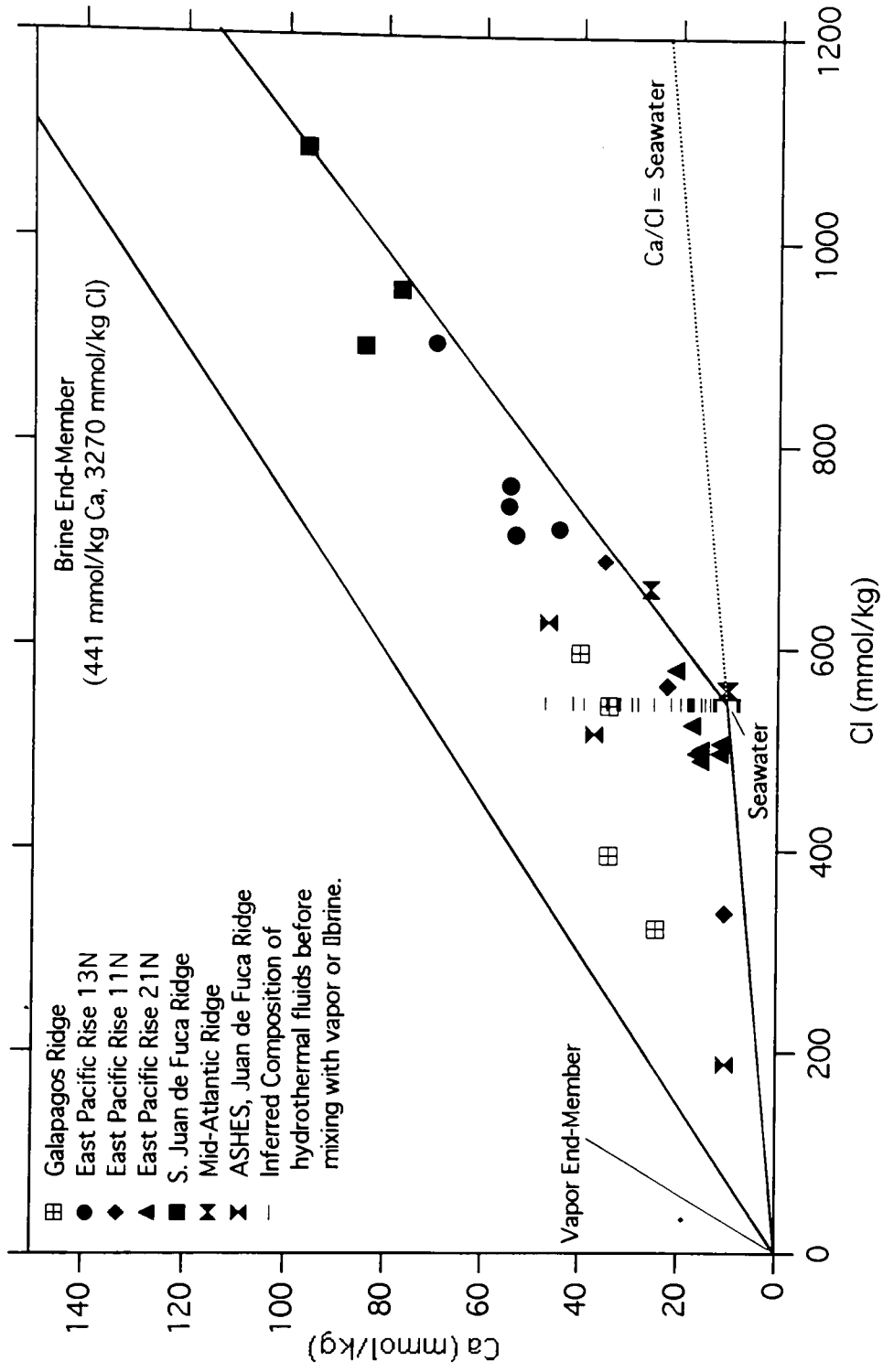

Figure 6.7: A plot of Ca versus Cl for the vent fluids shows a distribution best modeled as two line segments representing mixing between a vapour and Cl-normal fluid and a brine and the Cl-normal fluid. The heavy lines represent mixing lines between vapour/brine, vapour/seawater, and seawater/brine. Although mixing between vapour and brine cannot be ruled out, the distance of the data points from the vapour/brine mixing line suggests that any such mixing is minor. The seawater Ca/Cl ratio reference line (dotted) indicates that virtually all samples have an excess of Ca relative to Cl.

A similar diagram has been constructed for Sr (Fig. 6.8). Sr differs from Ca in that instead of showing a clear enrichment relative to seawater, the vent fluids with near-seawater Cl concentrations tend to have Sr concentrations that are lower than seawater. The Galapagos data are unusual in that the 4 vent fluids show identical Sr concentrations despite showing wide variations in Cl. While two of the samples are indistinguishable from the data set as a whole, the other two have higher Sr concentrations than what might be expected for fluids diluted with a vapour. The accuracy of these measurements is not beyond doubt because, as noted previously, the Galapagos fluids have undergone extensive subsurface mixing with cold seawater and this makes it difficult to calculate accurately the relative proportions of vent fluid and seawater. The average Sr concentration of the hydrothermal fluids that have not undergone phase separation, calculated as for Ca above, is 83.4 μmol/kg with a standard deviation of 23.2 μmol/kg. If the Galapagos data are excluded as being subject to excessive uncertainties, the average falls to 79.8 μmol/kg with a smaller standard deviation of 18.6 μmol/kg. These later figures are taken as the best estimate Sr concentration for the Cl-normal hydrothermal fluids. For comparison, seawater contains 87 μmol/kg Sr.

The existence of a chemically distinct hydrothermal brine end-member is of considerable importance to the marine Sr cycle. If the brine of Von Damm (1988; 1210 μmol/kg Sr, 3270 mmol/kg Cl) is reunited with its vapour to produce a fluid of seawater chlorinity, a Sr concentration of 202 μmol/kg results. Thus, the brine end-member shows a considerable enrichment in Sr relative to the seawater concentration of 87 μmol/kg. This brine is in marked contrast to the results of the basalt/seawater experiments, the majority of vent data, and the calculations performed above, which indicate that Cl-normal fluids show only minor differences from a seawater Sr concentration (Mottl, 1983; Berndt *et al.*, 1988; Von Damm, 1990), Although there is as yet only one estimate of the brine end-member based on the vent fluids from one site, the coherence between the calculated mixing lines

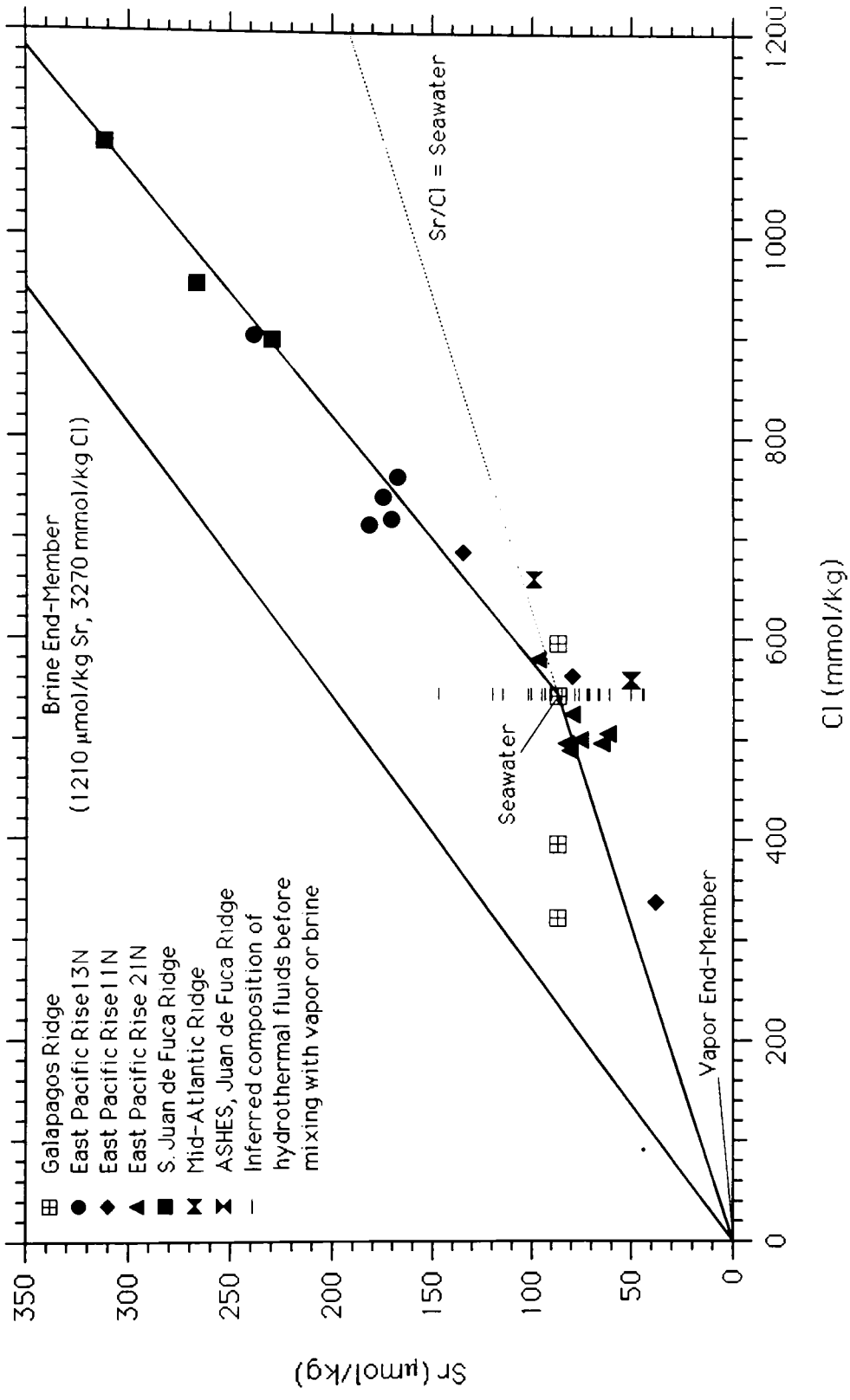

Figure 6.8: A Sr versus Cl plot for vent fluids shows a similar double mixing trend between the vapour and Cl-normal fluids and the brine and Cl-normal fluids as was seen for Ca. However, in contrast to Ca, Sr is slightly depleted relatively to seawater.

and the vent data for Na, K, Sr, Ca, and other trace elements (Figs. 6.7, 6.8, 6.9 and Von Damm, 1988) suggest that the composition calculated by Von Damm (1988) is a reasonable estimate. These calculations also indicate that the brine component is chemically distinct with respect to a number of other major and trace elements, showing considerable enrichments in Li, K, Rb, and Ca and a depletion in Na as compared to the bulk of hydrothermal fluids with Cl concentrations near that of seawater. It thus seems clear that the composition of hydrothermal brines is controlled by a somewhat different set of chemical reactions and equilibria as compared to those fluids that have not undergone phase separation. It is of considerable importance to outline the geological processes that favour the production of such fluids and to understand whether these differences relate to different P-T conditions or to the greatly increased salinity of the brine fluids. For the present consideration of the Sr cycle, it is important to constrain the relative mass fluxes of Sr from the brines and Cl-normal fluids.

One way to determine the relative importance of the flux of these brines into the oceans is to look at the geochemical controls of the molar seawater Na/Cl ratio. This ratio is largely determined by rivers adding relatively Na-rich waters to the oceans and mid-ocean ridge hydrothermal springs providing relatively Na-poor fluids. If the flux of river water is known, the flux of hydrothermal fluids required to make a solution with a seawater Na/Cl ratio may be calculated. The advantage of considering the relative fluxes of Na and Cl to and from seawater, rather than simply performing a mass balance for Na, is that a number of poorly documented fluxes equally affecting Na and Cl can be ignored. For example, the burial of pore waters and any net landward transfer of NaCl in sea salts (Berner and Berner, 1987) can be disregarded as they are unlikely to exert a significant fractionation of one element over the other. In addition, there is some debate as to how much Na and Cl in river water is due to cyclic sea salts, how much due to the weathering of halite, and how much is due to the weathering of primary silicate minerals (e.g., Holland,

1978; Meybeck, 1983; Berner and Berner, 1987). When the Na/Cl ratio is considered, the excess riverine NaCl due to cyclic salts and the dissolution of halite essentially drops out of the equation such that it does not matter which set of "corrected" river water data is chosen. The major limitation to this approach is that the residence times of Na and Cl are so long (~50 - 90 Ma; Holland, 1978; Berner and Berner, 1987) that it is very unlikely that the seawater concentrations of Na and Cl are at equilibrium with respect to modern sources and sinks. It is unfortunately difficult to estimate accurately the errors associated with the assumption that the modern seawater Na/Cl ratio is at steady state with respect to the modern flux terms.

A flux of 37,400 km^3/yr of river water containing 0.159 mmol/kg Na and 0.086 mmol/kg Cl yields a flux of some 595 * 10^{10} mol/yr Na and 322 * 10^{10} mol/yr Cl to the oceans. Once in the oceans the geochemistry of Cl is uneventful. The only major output for Cl is the formation of evaporite deposits, but since evaporites are expected to remove Na and Cl in roughly equal proportions, evaporites need not be considered further. Na has a more eventful cycle. Cerling *et al.* (1989) have recently estimated that a maximum of 200 * 10^{12} mol/yr of Na is removed from the oceans by cation exchange of Na for Ca on river-borne clays deposited in the oceans. This estimate assumes that 100% of the modern suspended load of rivers (Milliman and Meade, 1983) consists of recycled smectite clays bearing plenty of exchangeable Ca. Berner and Berner (1987) have also considered cation exchange and the transport of clays to the oceans and conclude that, due to a combination of agricultural practices and recent glacial activity, the modern suspended load is roughly twice what the recent long-term average would be. This already cuts the maximum rate of cation exchange removal in half, and if the proportion of exchangeable clays to total clays were known accurately, this would undoubtedly cut the importance of this sink still further. 100 * 10^{12} mol/yr is therefore taken as a maximum Na removal rate and 50 * 10^{12} mol/yr as a best-estimate.

A second potentially significant sedimentary sink is the diffusional flux of Na into sediments (Sayles, 1979). While Sayles (1979) estimates a removal rate of 500 * 10^{10} mol/yr, Drever *et al.* (1988) reconsider the diffusional flux of Na and other major seawater elements in the light of a mass balance model and conclude that 210 * 10^{10} mol/yr is the maximum allowable value. Going still further, Berner and Berner (1987) state that while the concentration gradients observed by Sayles (1979, 1981) may be significant evidence for authigenic clay mineral formation in sediments, they may also be explained by diagenetic reactions that do not imply a sink for many elements. Berner and Berner (1987) therefore do not include the diffusional flux estimates in their mass-balance budgets. It is difficult to pick a best-estimate for this flux and therefore the Na/Cl budget will be balanced both with and without this diffusional term.

Another sink for Na, the magnitude of which is also poorly documented, is the low temperature alteration of basalt (Mottl *et al.*, 1985; Mottl *et al.*, 1988; Mottl, 1989; Mottl and Gieskes, 1990). In the absence of more information, it is assumed that the magnitude of this flux is included within the uncertainty of the diffusional flux.

The final sink of Na involves the high-temperature alteration of basalt at the axial mid-ocean ridges. Figure 6.9 presents a Na versus Cl diagram constructed as for Ca and Sr (Figs. 6.7 and 6.8). Mixing lines between a pure vapour, seawater, and the brine fluid calculated by Von Damm (1988) appear to yield a reasonable model explaining the variations in Na and Cl levels in the vent fluids. Although there are a number of points that are more Na-rich than would be expected from simple 3-component mixing, the majority of data form a good array along the mixing lines. Extrapolation of each data point back to a primary fluid of seawater chlorinity (following the procedure outlined above for Ca and Sr) produces an average Na concentration of 472 mmol/kg (standard deviation = 27 mmol/kg) for Cl-normal fluids. This is virtually identical to the seawater concentration of 468 mmol/kg and thus suggests that the hydrothermal fluids that have not undergone phase

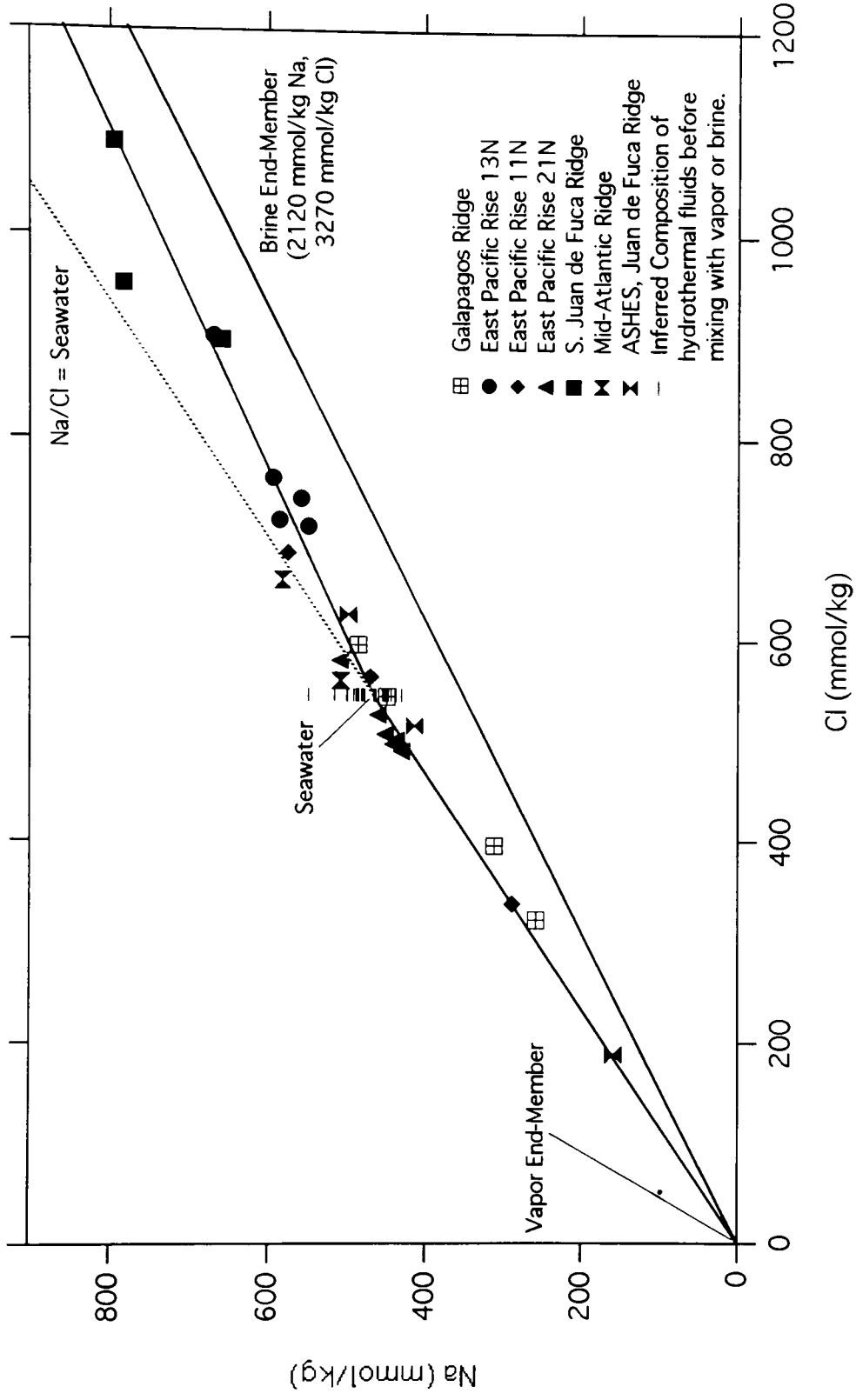

Figure 6.9: The Na and Cl vent data plot closely to mixing lines defined by vapour/seawater, vapour/brine, and seawater/brine, lending further support to the mixing model of Von Damm (1988). The Na content of the Cl-normalised fluids is very near that of seawater while the more Cl-rich fluids show a depletion of Na relative to Cl.

separation do not alter the Na/Cl ratio of seawater. The brine end-member, however, contains 2120 mmol/kg Na and 3270 mmol/kg Cl, which, if normalised to seawater chlorinity, produces a fluid containing only 353 mmol/kg Na. It is thus clear that the hydrothermal processes that produce brine fluids cause a significant loss of Na relative to Cl and therefore represent a significant sink of Na in the world's oceans.

The mass balance is constructed by setting the seawater Na/Cl ratio equal to the sum of Na added to or removed from the oceans divided by the total Cl added to the oceans (neglecting those fluxes that do not affect the Na/Cl ratio). Thus,

$$(Na/Cl)_{sw} = \Sigma J_{Na}/\Sigma J_{Cl} = (J_{r\text{-}Na} - J_{cx\text{-}Na} - J_{dif\text{-}Na} + J_{h\text{-}Na}) / (J_{r\text{-}Cl} + J_{h\text{-}Cl}),$$

where $(Na/Cl)_{sw}$ is the molar seawater Na/Cl ratio, $J_{r\text{-}Na}$ is the river flux of Na into the oceans, $J_{cx\text{-}Na}$ is the amount of Na lost through cation exchange, $J_{dif\text{-}Na}$ is the amount of Na lost through diffusion into the sediments, $J_{h\text{-}Na}$ is the hydrothermal Na flux (brine component), $J_{r\text{-}Cl}$ is the river Cl flux, and $J_{h\text{-}Cl}$ is the flux of the hydrothermal brine Cl. Because Cl is assumed to be conservative in oceanic hydrothermal systems, the mass balance could equally have been written with a term for the hydrothermal depletion of Na in the numerator ($-J_{h\text{-}Na}$) and no $J_{h\text{-}Cl}$ term. Rearranging to isolate the hydrothermal flux terms,

$$(Na/Cl)_{sw}*J_{h\text{-}Cl} - J_{h\text{-}Na} = J_{r\text{-}Na} - J_{cx\text{-}Na} - J_{dif\text{-}Na} \quad (Na/Cl)_{sw}*J_{r\text{-}Cl}.$$

The hydrothermal flux of Na and Cl can be rewritten in terms of the flux of hydrothermal fluid times the concentration of Na and Cl in that fluid, e.g.,

$$J_{h\text{-}Na} = J_{H2O}*[Na]_{fluid}; \; J_{h\text{-}Cl} = J_{H2O}*[Cl]_{fluid}.$$

Na and Cl concentrations of either the brine of Von Damm (1988; 2120 mmol/kg Na, 3270 mmol/kg Cl) or of the brine reunited with its vapour to produce a fluid of seawater chlorinity (353 mmol/kg Na, 545 mmol/kg Cl) can be used, depending on whether a fluid flux of brine or Cl-normal composition is desired. Substituting the above relationship into

the mass balance equation and solving for the hydrothermal fluid flux yields

$$J_{H2O} = (J_{r\text{-}Na} - J_{cx\text{-}Na} - J_{dif\text{-}Na} - (Na/Cl)_{sw} * J_{r\text{-}Cl}) / ((Na/Cl)_{sw} * [Cl]_{fluid} \quad [Na]_{fluid}).$$

Uncertainty in the magnitude of the cation exchange (0 - 100 * 10^{10} mol Na/yr) and diffusional sink (0 - 210 * 10^{10} mol Na/yr) terms results in a calculated brine flux spanning (0.13 - 4.7) * 10^{12} kg/yr. Assuming 0 mol Na/yr for both sink terms yields the maximum flux estimates. Although many authors ignore the diffusional sink term, it is important to include some Na loss, say 50 * 10^{10} mol/yr, due to the uptake of Na during low temperature basaltic alteration (Davis, Mottl, *et al.*, 1992). Thus a combination of 50 * 10^{10} mol/yr lost to sediments and low temperature basaltic alteration plus 50 * 10^{10} mol/yr lost through the Na-for-Ca cation exchange produces a best-estimate brine flux of 3.2 (0.13 - 4.7) * 10^{12} kg/yr. Additional uncertainty in this estimate is derived from the fact that, given the very long residence time of Na and Cl in seawater (50 - 70 Ma), it is unlikely that the Na/Cl ratio of modern seawater is in equilibrium with its present-day sources and sinks.

The flux of brines calculated by the Na/Cl balance implies a much larger flux of dilute fluids forming when the brines separated from the fluids of seawater chlorinity. The formation of a pure water vapour and Von Damm's (1988) brine from a fluid of seawater chlorinity (19.32‰) produces the smallest possible total fluid flux, roughly 19 (0.78 - 28) * 10^{12} kg/yr (seawater = 1 part brine plus 5 parts pure water). If the dilute fluids have a chlorinity of 10‰, a total fluid flux of (1 - 41) * 10^{12} kg/yr is implied; if the chlorinity is 16‰ a total flux of (3 - 110) * 10^{12} kg/yr is implied. Clearly, any one of these possibilities more than uses up the total geophysically allowed axial fluid flux of 15 (6.2 - 27) * 10^{12} kg/yr and thus leaves no room for the non-phase-separated fluids that are observed to make up the bulk of hydrothermal fluids.

The geophysical constraints on the amount of heat that can be removed by high-temperature (T > 320 °C) axial springs appear to be severe. However, it is possible to accommodate the brine and total fluid fluxes to these constraints. The simplest way to do

this is to assume that a large proportion of the phase-separated vapours are quite dilute and therefore able to make their way to the surface through widespread porous flow. This mechanism relies on the metal- and silica-poor chemistry of the fluids to prevent the precipitation of secondary mineral deposits that would otherwise rapidly clog small fluid conduits and channelise fluid flow into more readily observable vents (Sleep and Wolery, 1978; Fox, 1990). Von Damm (1990) reports visual evidence for relatively diffuse outpourings of clear (and hence metal- and sulphur-poor) fluids, but there are no reliable analyses of these fluids due to the difficulty of obtaining good samples. If these fluids make their way to the surface by widespread porous flow, the slower rates of ascent combined with much more extensive interaction with the host rocks will allow conductive transfer of a significant proportion of their heat to the oceanic crust. Because the geophysical measurements detect conductive heat flow, the heat carried and transferred by these fluids would not contribute to the 'missing heat' anomaly and thus these dilute fluids would not be subject to the geophysical constraints.

In the simplest case all 3.2 (0.13 - 4.7) * 10^{12} kg/yr of brines would form by the separation of pure water vapours that would not come under the constraints of the geophysical calculations. This would leave 12 (6.1 22) * 10^{12} kg/yr for non-phase-separated fluids. At another extreme it is possible that all fluids have undergone some phase separation. In one example phase separation could produce 3.2 (0.13 - 4.7) * 10^{12} kg/yr of brines, 12 (6.1 22) * 10^{12} kg/yr of fluids with a 16‰ chlorinity, and diffusive venting of 29 (5.8 - 46) * 10^{12} kg/yr pure water vapour. These fluxes are not excessive and suggest that from a geophysical point of view the calculated brine flux is possible.

Another difficulty with the brine fluxes is the relative proportions of brine and non-phase separated fluids. The observed chlorinities of the hydrothermal vent fluids suggest that each fluid generally can contain at most only a few percent of the brine of Von Damm (1988). By contrast, the best-estimate figures above suggest typical hydrothermal fluids

containing on the order of 20% brine. One way around this problem is to relax the geophysical constraints on axial fluid flow, as is done in Palmer and Edmond (1989a), which allows about a factor of 5 higher total axial fluid flux. However, given that the geophysical constraints seem stronger than the mass balance constraints, it might be more prudent to simply select brine and non-phase separated fluid fluxes that are in a proportion of roughly 1:50. This implies that of a total geophysically allowed fluid flux of 15 (6.2 - 27) * 10^{12} kg/yr, 0.30 (0.12 - 0.54) * 10^{12} kg/yr is brines and the rest is non-phase-separated fluids. This brine flux is at the lower range of the 3.2 (0.13 - 4.7) * 10^{12} kg/yr estimated by Na/Cl balance. The Sr flux resulting from this brine may be calculated assuming a brine Sr concentration of 1210 μmol/kg (Von Damm, 1988) and results in an estimated Sr flux of 0.04 (0.01 - 0.07) * 10^{10} mol/yr. This compares to the range of 0.39 (0.02 - 0.56) * 10^{10} mol/yr calculated by Na/Cl mass balance. The isotopic composition of the brine Sr is assumed equal to that of hydrothermal fluids that have not undergone phase separation (0.7033).

6.5.2.2 Low-Temperature Off-Axis Hydrothermal Fluxes

As noted earlier, only some 8 to 20% of the total 'missing heat' is removed through the high-temperature axial systems. Assuming that the remaining 80% of the total 20.9 * 10^{19} J/yr is removed at a temperature only 10 °C warmer than ambient seawater, the entropy-balance equation of Sleep and Wolery (1978),

$$J_h = H/(T_h C_{p\,h} - T_{in} C_{p\,in}),$$

yields about 5000 * 10^{12} kg/yr of seawater. By comparison, the best-estimate high-temperature fluid flux (see above) is only 15 * 10^{12} kg/yr. With such a large potential flux of warm seawater through the crust, only slight modifications of primary seawater chemistry are required to affect the mass balance of the oceans.

Although it has been demonstrated that there is extensive Sr isotopic exchange between seawater and basalt in off-axis oceanic crust (Hart and Mottl, 1983; Mottl *et al.*,

1985; Mottl and Gieskes, 1990), there is not a large amount of work specifically addressing the mass flux of basaltic Sr in off-axis settings. In one such study, Hess *et al.* (1991) selected 3 sites on the basis of high heat flow measurements (high heat flow = convective discharge of warmed fluids, low heat flow = recharge area) in an effort to document the effects of low-temperature basaltic alteration on the Sr budget. Unfortunately, although all three sites contained evidence for upwelling of fluids, only the Galapagos site showed strong evidence (Mg and F depletion, Ca enrichment) for interaction with basalts. Thus, within relatively large analytical errors, most samples had $^{87}Sr/^{86}Sr$ ratios indistinguishable from seawater and only the deepest Galapagos samples had significantly lower $^{87}Sr/^{86}Sr$ ratios. Based on these Galapagos samples, the estimated average Sr concentration in low-temperature fluids is taken as 92 μmol/kg with a $^{87}Sr/^{86}Sr$ ratio of 0.709143. To calculate the mass flux, an exit temperature of 30 °C and a 'missing heat' flux of $20.9 * 10^{19}$ J/yr was used in the the entropy balance equation to calculate a fluid flux of $1670 * 10^{12}$ kg/yr and a Sr mass flux (including seawater and basaltic Sr) of $15.4 * 10^{10}$ mol/yr. Taking the seawater $^{87}Sr/^{86}Sr$ ratio as 0.70918 and the basaltic component as 0.7035, the flux of Sr due to the low-temperature alteration of basalt is calculated at $0.11 * 10^{10}$ mol/yr.

A second way of addressing the flux of low-temperature basaltic Sr is to look at the marine geochemical cycle of Mg. It is generally agreed that the only significant source of Mg to the oceans is river water. Taking an average 0.13 mmol/kg for unpolluted river water (Meybeck, 1979; 1983) and a best-estimate 37,400 km^3/yr for the flux of river water yields a total of $486 * 10^{10}$ mol/yr Mg. There are two views as to the relative importance of various Mg sinks in the world oceans. At one extreme, Palmer and Edmond (1989a) assume that the *only* important sink for Mg in the oceans is mid-ocean ridge hydrothermal activity. At the other extreme, Drever *et al.* (1988) find that a large fraction of the riverine input can be removed by authigenic mineral formation in the sediments. All agree that other

oceanic sinks for Mg are minor (Holland, 1984; Drever *et al.*, 1988): a total of $67 * 10^{10}$ mol/yr Mg is lost through cation exchange of Ca for Mg on river-borne clays ($32 * 10^{10}$ mol/yr), burial of pore waters in sediments ($9 * 10^{10}$ mol/yr), and the incorporation of Mg in carbonates and siliceous microorganisms ($26 * 10^{10}$ mol/yr).

The predominance of the authigenic sink in the estimate of Drever *et al.* (1988) is based on the pore water data of Sayles (1979), which indicate that some $460 * 10^{10}$ mol/yr of Mg is removed into the oceanic sedimentary record. However, there are several problems with this estimate, including the use of diffusion coefficients that are probably inappropriate (Felmy and Weare, 1991), the fact that Mg is involved in exchange reactions that remove or add Mg to pore waters according to the breakdown of organic matter (von Breymann *et al.*, 1990), and the fact that the calculated flux of Mg and other elements in or out of sediments (Sayles, 1979) produces serious imbalances in the cycles of several elements (Drever *et al.*, 1988). Drever (1974) and Drever *et al.* (1988) use independent methods to arrive at a *maximum* removal rate of $135 * 10^{10}$ mol/yr for <u>all</u> sedimentary sinks of Mg. Subtracting the minor sedimentary sinks ($67 * 10^{10}$ mol/yr) and the authigenic sink ($0 - 68 * 10^{10}$ mol/yr) from the total Mg flux of $486 * 10^{10}$ mol/yr leaves $(351 - 419) * 10^{10}$ mol/yr of riverine Mg to be removed by basalt/seawater interaction.

All researchers agree that the major oceanic sink for Mg is the hydrothermal alteration of basalts. This consensus is based on the results of seawater/basalt experiments, which are unanimous in indicating that Mg is rapidly removed from solution during the hydrothermal alteration of basalt. At water/rock ratios less than 10, Mg is rapidly removed from seawater from at least 70 to 500 °C, and at temperatures greater than 150 °C Mg is quantitatively removed from seawater at all water/rock ratios less than 50 (Mottl, 1983). At lower temperatures and/or higher water/rock ratios, Mg is removed more slowly and/or less completely, but the process is still significant. Mg depletion is commonly observed during, and is in fact a useful indicator of, low-temperature alteration of volcanic material present in

deep sea sediments or of the basaltic basement (e.g., Gieskes and Lawrence, 1981; Langseth *et al.*, 1988; Egeberg *et al.*, 1990; Hess *et al.*, 1991).

A second characteristic of basalt/seawater interaction is that the depletion of Mg is directly related to an enrichment of Ca. Estimates of the stoicheiometry of the exchange vary between about 2/3 mole of Ca released for every mole Mg consumed (Drever *et al.*, 1988) to a mole-for-mole exchange (Mottl, 1983; Mottl *et al.*, 1983; Langseth *et al.*, 1988), to an excess of Ca over Mg (Mottl *et al.*, 1985; Mottl and Gieskes, 1990). Recent experimental work designed to simulate high-temperature hydrothermal alteration is based on the premise that 'evolved' seawater solutions are depleted in Mg and that this Mg has been replaced on a mole-for-mole basis by basalt-derived Ca so as to maintain charge-balance and seawater salinity (e.g., Seyfried *et al.*, 1988). However, not all of the Ca (and Sr) released during this step reaches the heart of the hydrothermal system. Seawater enters the basaltic crust with 10 mmol/kg Ca, 28 mmol/kg SO_4, and 52 mmol/kg Mg. As the water descends into the crust it is heated and Mg begins to precipitate and is replaced in solution on a roughly mole-for-mole basis by Ca. This Ca is in turn removed by anhydrite precipitation until all seawater SO_4 is exhausted. Thus,

$$(10 + 52)\ \text{mmol/kg Ca} - (28)\ \text{mmol/kg } CaSO_4 = 34\ \text{mmol/kg Ca}.$$

Accordingly, basalt/seawater experiments currently use Ca concentrations in the range of 29 to 38 mmol/kg (e.g., Berndt *et al.*, 1988; Seewald and Seyfried, 1990). Of the 34 mmol/kg Ca that enters the high-temperature system, roughly one third must be consumed by alteration minerals to produce the observed Cl-normalised average of 22 mmol/kg.

The dissolution of the Ca-bearing phases in basalt (largely plagioclase) also releases Sr into solution (Berndt *et al.*, 1988). The amount of Sr released into solution may be calculated using the Ca mass flux and the average molar Sr/Ca ratio in basalts. The importance of this Sr with regards to the off-axis flux depends on how much Sr is carried in solution through the high-temperature alteration zone and vented as part of the axial flux

term, and on how much Sr is permanently sequestered, along with Ca, in subsurface anhydrite deposits. Experimental work that avoids the problem of re-dissolution of anhydrite during quenching gives hydrothermal Sr concentrations of only 20 μmol/kg (compared to quenched results yielding near-seawater concentrations of 80 - 90 μmol/kg), indicating that the precipitation of anhydrite efficiently removes Sr from solution (Berndt *et al.*, 1988). Thus, of a total Sr concentration of 80 μmol/kg determined for Cl-normalised axial solutions, roughly 20 μmol/kg may have derived from the downwelling Mg-for-Ca alteration of the oceanic crust. The flank Sr flux calculated below will be adjusted accordingly.

Although the co-precipitation of Sr in anhydrite removes most Sr from solution before the fluids enter the high-temperature portion of the hydrothermal system, this Sr (and Ca) is not thought to be permanently stored in the oceanic crust. Sleep (1991) considers the problem in some detail and cites the lack of seismic or physical evidence for major anhydrite deposits to suggest that most anhydrite dissolves as the system cools and moves off-axis. Thus, a large proportion of the Sr and Ca in hydrothermal anhydrite is returned to the sea.

The calculation of the low temperature Sr flux is now straight-forward. Assuming that the Mg-for-Ca exchange occurs on a mole-for-mole basis, the 351 - 419 * 10^{10} mol/yr of riverine Mg that is consumed through the alteration of basalt indicates the release of 351 419 * 10^{10} mol/yr of basaltic Ca. This Ca flux, assuming an average molar Sr/Ca ratio of 0.0007 for seafloor basalts (Berndt *et al.*, 1988), implies an annual flux of 0.25 - 0.30 * 10^{10} mol/yr of basaltic Sr. If a maximum of one quarter of this flux is already included in the axial term, the estimated flux changes to 0.19 - 0.30 * 10^{10} mol/yr. This estimate is similar to the 0.11 * 10^{10} mol/yr that was obtained by Hess *et al.* (1991) based on the Sr flux measured largely from one site.

The dissolution of the surface anhydrite deposits also serves to release seawater Sr back into the system. The magnitude of this flux may be calculated by determining the percentage of seawater Sr in the axial vent fluids, using this figure to calculate how much of the Sr that makes it through the anhydrite precipitation zone must be seawater Sr (assuming no near-surface mixing between the hydrothermal fluids and seawater), and using this figure to calculate what percentage of the Sr in the anhydrite deposits is of seawater origin. Assuming $^{87}Sr/^{86}Sr$ ratios of 0.7025 - 0.7030 for primary basaltic Sr, 0.70918 for seawater, and 0.7033 for vent fluids, roughly 5 - 15% of the Sr in the final vent fluid is of seawater origin. Of a Sr concentration of 80 μmol/kg for Cl-normalised vent fluids, roughly 4 - 12 μmol/kg of the Sr must be of seawater origin. The results of the seawater/basalt experiments of Berndt *et al.* (1988) suggest that 20 μmol/kg total Sr leaves the zone of anhydrite formation. At least 4 - 12 μmol/kg of this 20 μmol/kg Sr must be of seawater origin, suggesting that at least 20 - 60% of the total Sr in the anhydrite deposits is of seawater origin. Thus the flank basaltic flux of 0.19 - 0.30 * 10^{10} mol/yr is accompanied by 0.05 - 0.45 * 10^{10} mol/yr of seawater Sr. The impact of this Sr on the geochemical cycle of Sr depends on how long the seawater Sr remains stored in the anhydrite deposits. The longer the storage, the larger the difference between the $^{87}Sr/^{86}Sr$ ratio of the stored Sr as compared to seawater Sr, and the larger the impact of this flux on the marine budget. Although anhydrite dissolution is likely to occur within a few million years of its deposition, for the purpose of this study the effect of this flux will be slightly exaggerated by assuming an isotopic composition equivalent to the diagenetic flux term ($^{87}Sr/^{86}Sr$ = 0.7084 = 16 Ma seawater).

6.5.3 Mass Balance Calculations

The purpose of this section is to reconcile the geophysical and geochemical constraints on the volume of hydrothermal fluid flow along the mid-ocean ridges. The geophysical and geochemical calculations offer independent, complementary constraints as

to the importance of hydrothermal fluid flow, but each approach has its advantages and limitations. The geophysical calculations are useful in that they are relatively straightforward and robust. It seems difficult to see a way in which the parameters or calculations may be adjusted such that an axial fluid flux larger than 15 (6.7 - 27) * 10^{12} kg/yr can be accommodated without violating firm geological constraints. However, the geophysical calculations are limited mainly in that they are not directly related to the temperature-dependent geochemistry of the fluids. On the one hand the calculations are useful in that they indicate the volume of fluids circulating through the axial systems assuming a given temperature for all axial fluids. On the other hand, because axial fluids are likely to span a range of temperatures and because the geochemical cycling of different elements is likely to be affected by different hydrothermal temperature ranges, it is difficult to relate a geophysically estimated fluid flux directly to the flux actually taking place within a given distance of a mid-ocean ridge axis or to the flux of hydrothermal fluids relevant to the cycle of a given element.

By contrast, the geochemical approach based on mass-balance calculations for various seawater elements is a more direct measure of the volume of fluids passing through given geochemical regimes. However, these calculations are limited by the uncertainties of the estimates used to quantify the various sources and sinks in the world's oceans and by the assumption that the oceans are in chemical equilibrium with respect to their inputs and sinks, i.e. that the modern-day concentration of a given element in seawater is currently determined by the relative inputs and outputs of this element. It is difficult to assess this validity of this assumption beyond fairly broad limits (Holland, 1984).

An upper-limit on the fluid flux through the mid-ocean ridges is provided by the Mg cycle. As discussed above, Mg is removed through reaction with basalt at temperatures from at least 70 °C up to the maximum temperatures expected in hydrothermal systems. Of the total 486 * 10^{10} mol/yr Mg provided by the rivers, between 67 and 135 * 10^{10} mol/yr

are removed into sediments. Elimination of the remaining 351 - 419 * 10^{10} mol/yr through the alteration of basalt requires the quantitative removal of Mg from the equivalent of 66 - 79 * 10^{12} kg/yr seawater having a Mg concentration of 52.8 mmol/kg. This flux of fluids reaching temperatures of at least 70 °C is nearly a factor of 5 higher than the geophysically derived estimate of 15 (6.7 - 27) * 10^{12} kg/yr for fluids limited to temperatures between 320 and 390 °C. If Mg is partially removed from solution at temperatures less than 70 °C the calculated flux of seawater through the oceanic crust would be still larger. It should be noted that Palmer and Edmond (1989a) use the Mg mass balance to calculate the fluid flux through only the high-temperature (T = 350 °C) vents. Because they do not correct for any sedimentary sinks of Mg and because Mg is rapidly removed over a wide range of temperatures, their estimate for the axial high-temperature hydrothermal flux (70 - 130 * 10^{12} kg/yr) *must* be too large. That their Sr mass balance yields a similar range of values (90 - 150 * 10^{12} kg/yr) therefore indicates one of a number of possibilities: the geochemical exchange of Sr occurs over a similar temperature range as for Mg; their riverine Sr flux is too large or too radiogenic; there may be additional fluxes of relatively nonradiogenic Sr into seawater; or the modern oceans are out of equilibrium with respect to present sinks and sources.

A potentially more accurate means of calculating the high-temperature axial hydrothermal fluid flux is through a mass balance of seawater Sr isotopes. This balance is calculated by summing up the mass flux and isotopic composition of each input into the ocean and removing an equal mass of Sr with an isotopic composition of present-day seawater:

$$J_rR_r + J_gR_g + J_dR_d + J_hR_h + J_bR_b + J_{lt}R_{lt} + J_aR_a - (J_r + J_g + J_d + J_h + J_b + J_{lt} + J_a)R_{sw} = 0,$$

where J and R represent the mass flux and isotopic composition of Sr from river water (r), groundwater (g), the diagenetic recrystallisation of marine sediments (d), Cl-normalised axial hydrothermal fluids (h), hydrothermal brines (b), low-temperature off-axis alteration

of basalt (lt), dissolution of anhydrite (a), and seawater (sw). All variables are estimated except for the high-temperature axial Sr flux associated with fluids that have not undergone phase separation. The flux of riverine Sr (J_r) is estimated at 3.0 (2.1 - 5.7) * 10^{10} mol/kg with an isotopic composition (R_r) of 0.7114 (0.7112 - 0.7119); the flux of groundwater Sr (J_g) is taken to be 1.1 (0 - 2.2) * 10^{10} mol/kg with an isotopic composition (R_g) of 0.7087± 0.0002; and the flux of diagenetic Sr from the recrystallisation of carbonate and non-carbonate sediments (J_d) is estimated to be 0.34 * 10^{10} mol/yr with a weighted average isotopic composition (R_d) of 0.7084. The average concentration of Sr in hydrothermal vent fluids is 124 μmol/kg. Analysis of the vent data suggests that the high-temperature fluids may be broken into two components: a fluid of seawater chlorinity containing 80 μmol/kg Sr and a brine containing 1210 μmol/kg Sr (202 μmol/kg when normalised to seawater chlorinity). While the fluid flux of the former (h) remains to be calculated, a Na/Cl ratio mass balance combined with a consideration of the vent data suggest that the phase-separated brines (b) vent some 0.04 (0.01 - 0.07) * 10^{10} mol/yr. Consideration of the Mg cycle indicates an off-axis, low temperature (lt) basaltic Sr flux of 0.25 (0.19 - 0.30) * 10^{10} mol/yr. The isotopic composition of the Cl-normalised fluid, brine, and off-axis fluxes are all considered equal to the mean of the observed vent fluid $^{87}Sr/^{86}Sr = 0.7033 \pm 0.0004$. The flux and isotopic composition of the seawater component released during anhydrite dissolution are poorly constrained; estimates of 0.25 (0.05 - 0.45) * 10^{10} mol/yr and 0.7084 ± 0.0006 may be appropriate The isotopic composition of modern seawater (R_{sw}) is 0.70918.

Solving the isotopic mass balance equation for the Cl-normalised fluid flux J_h yields

$$J_h = [R_{sw}(J_r + J_g + J_d + J_b + J_{lt} + J_a) - J_rR_r - J_gR_g - J_dR_d - J_bR_b - J_{lt}R_{lt} - J_aR_a] / [R_h - R_{sw}].$$

The main opposing fluxes in this mass balance are the riverine and combined basaltic terms. The river term by itself requires 1.1 (0.82 - 2.6) * 10^{10} mol/yr of basaltic Sr (0.7033) to produce a mixture of seawater isotopic composition. The geophysical estimate

of an axial fluid flux of 15 (6.7 - 27) * 10^{12} kg/yr indicates a Sr flux of only 0.19 (0.08 - 0.33) * 10^{10} mol/yr (assuming an average vent fluid Sr concentration of 124 μmol/kg). The addition of each additional flux term in the Sr cycle helps reduce the amount of axial basaltic Sr required to balance the budget, but none really brings the estimate within the geophysical range (Fig. 6.10). The addition of the diagenetic flux has a minor impact, reducing the required basaltic flux from 1.13 * 10^{10} to 1.09 * 10^{10} mol/yr. The groundwater flux has a relatively important impact, reducing the required combined riverine and diagenetic mass balance flux from 1.09 * 10^{10} mol/yr to 0.998 * 10^{10} mol/yr. Unfortunately both the mass flux and isotopic composition of the groundwater term are poorly known. The addition of the flux of old seawater Sr associated with the dissolution of hydrothermal anhydrite deposits has a very minor effect, reducing the required flux only from 1.09 to 1.05 * 10^{10} mol/yr. All together the non-basaltic Sr flux terms have a relatively minor impact on the amount of basaltic Sr required to balance the budget, reducing the necessary basaltic flux of Sr from 1.13 * 10^{10} to 0.97 * 10^{10} mol/yr.

The inclusion of the brine and low-temperature off-axis fluxes acts to reduce the amount of material required from axial fluids that have not undergone phase separation. The brine term could be quite significant if the Na/Cl mass balance results are accurate (bringing a reduction from 1.09 to 0.70 * 10^{10} mol/yr), but the most likely flux based on limited admixture of Von Damm's brine (0.04 (0.01 - 0.07) * 10^{10} mol/yr) results in a minor decrease from 1.09 to 1.05 * 10^{10} mol/yr. The low-temperature flank flux (0.25 (0.19 - 0.30) * 10^{10} mol/yr) has the biggest single effect on the Sr budget, reducing the required basaltic flux from 1.09 to 0.84 * 10^{10} mol/yr. Combined, the brine and off-axis fluxes reduce the required flux from 1.09 to 0.79 (0.41 - 2.4) * 10^{10} mol/yr. The minimum error limits do not overlap the maximum limits placed by the geophysically estimated 0.19 (0.08 - 0.33) * 10^{10} mol/yr. If the Na/Cl brine flux is used, the reduction is much more dramatic, from 1.09 to 0.45 (-0.08 - 2.4) * 10^{10} mol/yr, and the error estimates

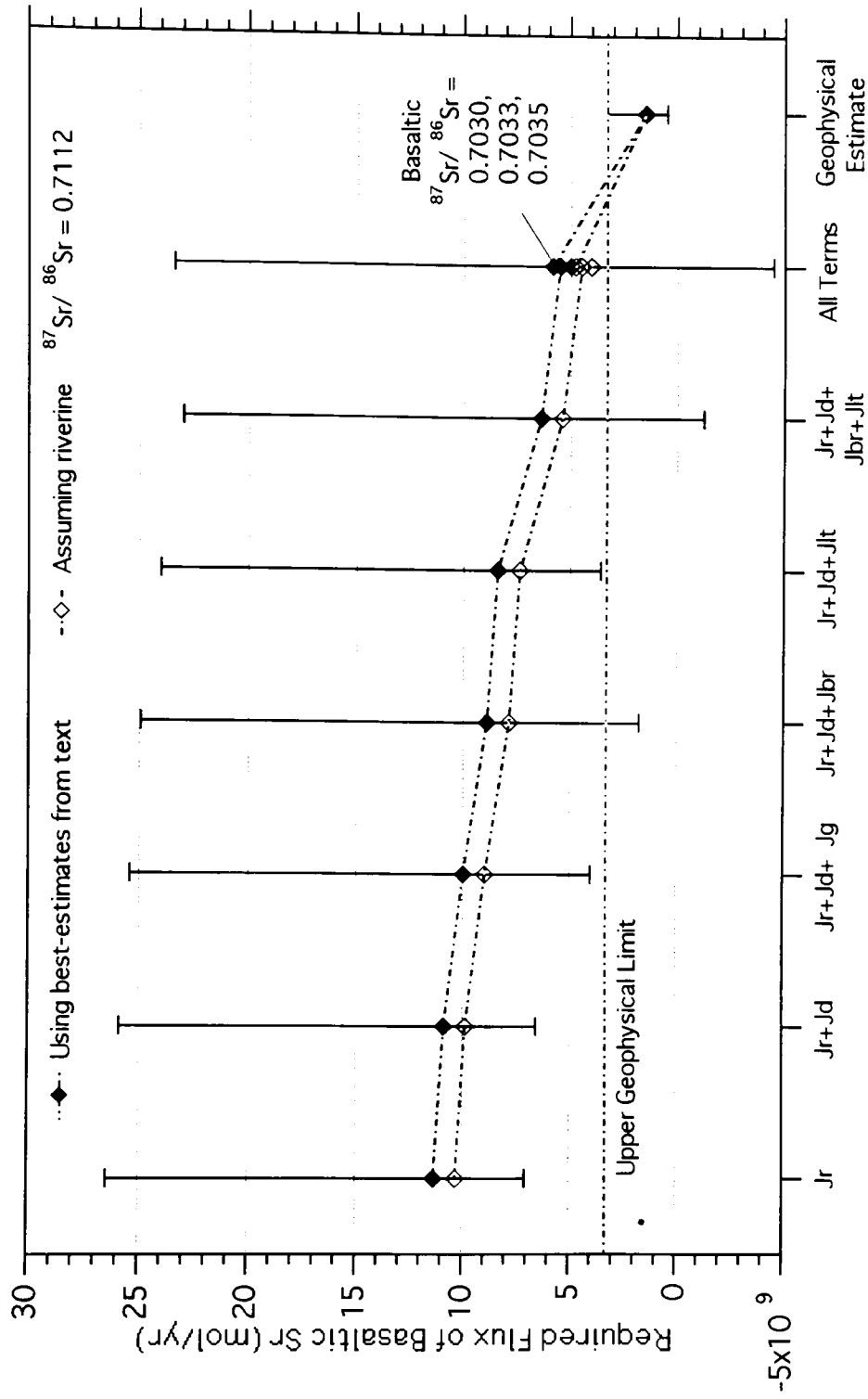

Figure 6.10: Calculation of the mass flux of basaltic Sr required to balance the marine geochemical cycle of Sr. The estimates moving from left to right successively include additional terms (x-axis labels) to the Sr cycle such that the relative importance of each may be seen. A comparison between a riverine $^{87}Sr/^{86}Sr$ ratio of 0.7114 and 0.7112 and basaltic isotopic ratios of 0.7030 to 0.7035 shows that differences in the calculated mass flux are relatively minor.

easily include the geophysical limits (0.19 (0.08 - 0.33) * 10^{10} mol/yr). The potential of the brine flux to affect the Sr budget significantly highlights the importance of further evaluating its relative magnitude.

Taking all flux terms together (Fig. 6.10), the required flux of axial Sr is reduced from 1.13 to 0.676 * 10^{10} mol/yr with error estimates (0.09 - 2.3 * 10^{10} mol/yr) covering the range defined by the geophysical limits (0.19 (0.08 - 0.33) * 10^{10} mol/yr). Substitution of a riverine $^{87}Sr/^{86}Sr$ = 0.7112 or basaltic hydrothermal $^{87}Sr/^{86}Sr$ = 0.7030, 07033, or 0.7035 does not significantly affect these results. Although the propagated error estimates associated with each flux term result in a final estimate that includes the geophysical limits, the best-estimate flux of Sr associated with axial vent fluids that have not undergone phase separation remains a factor of 2 higher than the highest geophysical limit. This is despite scrapping together every possible Sr term that may significantly affect the Sr budget. The difficulty of bringing the geophysical and geochemical estimates together implies either that the geophysical limits are too low, the measured riverine Sr concentration or isotopic composition data are biased towards unrepresentatively high values, the individual basaltic Sr fluxes are under-estimated, or that the modern riverine fluxes or isotopic composition are significantly higher today than in the past and thus are out of equilibrium with the balancing basaltic mass fluxes.

It seems most likely that the fault lies with the isotopic composition of riverine Sr. It seems unlikely that an over-estimated riverine Sr flux is the culprit because such a large reduction of the riverine flux is required to bring the geochemical cycle of Sr into balance with the geophysical constraints (from 3.0 to 1.7 * 10^{10} mol/yr). Such a large reduction seems unlikely from the point of view of either bias in the data set or increased global weathering rates over the late Cenozoic. A large bias in the riverine data set is not suggested by Figure 6.2a, which demonstrates that no single river or set of rivers strongly skews the weighted average Sr concentration toward higher values. An increase in

weathering rates over the late Cenozoic has been postulated by several authors (Hess *et al.*, 1986; Raymo *et al.*, 1988; Hodell *et al.*, 1989, 1990), but an increase of nearly 100% over the last few millions of years seems unlikely to the present author.

By contrast, the isotopic composition of river water need only be changed from 0.7114 to 0.7104 to bring the Sr cycle into balance with the geophysical constraints. Figure 6.2b and Section 6.3.2 have already demonstrated that two rivers, the Ganges and Brahmaputra, have an exceptionally large influence on the weighted average of the data set, raising it from 0.7109 to 0.7119. It is thus clear that a bias in the data set towards the more tectonically active regions of the world, especially focusing on the rivers draining the Himalayas, may have resulted in an estimated riverine $^{87}Sr/^{86}Sr$ ratio that is too high compared to the actual world average.

Alternatively, it may be that increased glacial activity during the late Cenozoic in old continental shield areas and along mountain belts has resulted in enhanced weathering of older silicate rocks and that this has resulted in average riverine $^{87}Sr/^{86}Sr$ ratios that are too high relative to an equilibrium between modern seawater $^{87}Sr/^{86}Sr$ ratios and the main riverine and basaltic Sr inputs. Recent work by Dia *et al.* (1992) has demonstrated that the $^{87}Sr/^{86}Sr$ ratio of seawater appears to change on the time scale of 100 ka and that the most likely cause of these variations is changing riverine $^{87}Sr/^{86}Sr$ ratios. Although there was a marked increase beginning at roughly 25 ka, which would support the concept of riverine $^{87}Sr/^{86}Sr$ ratios being too high relative to equilibrium with the basaltic flux, the resolution of the data is not sufficient to determine a rising or lowering trend since 25 ka. However, if the pattern established by the previous 100 ka cycle is currently being repeated, the seawater $^{87}Sr/^{86}Sr$ ratio should be decreasing at present. This would suggest that the riverine terms are not presently too large relative to the basaltic flux and therefore that the lack of mass balance in the Sr cycle is due to bias in the riverine data set.

In conclusion, the current understanding of the geochemical cycle of Sr does not yet provide strong constraints as to the volume of seawater that flows through the mid-ocean ridges each year. The uncertainties associated with the various terms of the cycle result in large error bars that overlap the mass fluxes constrained by geophysical estimates, but the best-estimate mass flux of Sr calculated by mass balance is still roughly a factor of 2 higher than the geophysical estimate. This suggests either, as suggested by Hodell *et al.* (1990), that the modern seawater $^{87}Sr/^{86}Sr$ is not at equilibrium with respect to its various Sr sources and sinks due to an excessive flux of radiogenic riverine Sr or, as seems more likely, that the riverine data base is biased towards relatively radiogenic rivers draining such tectonically active regions as the Himalayas.

6.5.4 Alternative Geochemical Cycles

For the purposes of geochemical modelling it is useful, in the absence of a single, well-constrained model, to present several different mass balance calculations. This allows one to judge the generality of model calculations given a number of plausible scenarios. The first cycle (Table 6.6) uses the best-estimate parameters for each of the non-basaltic fluxes and assumes that the the combined basaltic fluxes are large enough to exactly balance the cycle and produce a modern seawater $^{87}Sr/^{86}Sr$ ratio of 0.70918. The second and third Sr cycles are designed to present maximum and minimum likely hydrothermal Sr fluxes. The second cycle is essentially that of Palmer and Edmond (1989). This cycle, as noted earlier, implies an axial high-temperature fluid flux comparable to that of the Mg mass balance, which is appropriate for hydrothermal fluids circulating at temperatures down to 70 °C or lower. The third cycle is that of Palmer and Edmond (1989) except for the removal of the Ganges and Brahmaputra rivers from the riverine data set. The result is a lowered riverine isotopic composition (0.7109 versus 0.7119) and an implied hydrothermal flux cut by 45%. This cycle is intended to provide a lowered total basaltic Sr flux consistent with the riverine data as they currently stand. Lowering the riverine isotopic

composition still further to 0.7102 and taking into consideration the basaltic flank and brine fluxes results in an axial Sr flux of 0.19 * 10^{10} mol/yr, which matches exactly the best-estimate geophysical Sr flux.

Table 6.6: Balanced Marine Geochemical Cycles of Sr. Terms identified as 'calculated' are estimated by Sr-isotope mass balance.

Cycle 1: Best-Estimate

Sr Source	Mass Flux (10^{10} mol/yr)	$^{87}Sr/^{86}Sr$
River Water:	3.00	0.7114
Groundwater:	1.10	0.7087
Diagenetic Flux:	0.34	0.7084
Anhydrite Flux:	0.25	0.7084
Flank Basaltic Flux:	0.25	0.7033
Brine Basaltic Flux:	0.04	0.7033
Cl-Normalised Flux:	0.67 (calculated)	0.7033
Total of 3 Hydrothermal Fluxes:	0.96 (calculated)	
Weighted Average (Seawater):		0.70918

Cycle 2: Palmer and Edmond (1989)

Sr Source	Mass Flux (10^{10} mol/yr)	$^{87}Sr/^{86}Sr$
River Water:	3.34	0.7119
Diagenetic Flux:	0.34	0.7084
Hydrothermal Flux:	1.50 (calculated)	0.7033
Weighted Average (Seawater):		0.70918

Cycle 3: Palmer and Edmond (1989) without Ganges and Brahmaputra Rivers

Sr Source	Mass Flux (10^{10} mol/yr)	$^{87}Sr/^{86}Sr$
River Water:	3.00	0.7109
Diagenetic Flux:	0.34	0.7084
Hydrothermal Flux:	0.832 (calculated)	0.7033
Weighted Average (Seawater):		0.70918

Chapter 7: Seawater Sr-Isotopes, Carbon-Burial Events, and Hydrothermalism

7.1 Introduction

Seawater $\delta^{13}C$, $\delta^{18}O$, $\delta^{34}S$, and $^{87}Sr/^{86}Sr$ curves are of fundamental importance for deciphering the history of oxygen and carbon dioxide on the earth's surface. In turn, the evolution of oxygen and carbon dioxide in the atmosphere and oceans has critical implications for the evolution of global climate and the history of life. A variety of approaches have been used to infer the history of atmospheric oxygen and carbon dioxide and to link the observed isotopic records to related events in the geological record, such as inferred climate shifts, carbon-burial events, and periods of accelerated evolution or extinction. For example, a number of authors (e.g., Lasaga *et al.*, 1985 ; Walker, 1986; Berner, 1987; Kump, 1989; Lasaga, 1989) have used the combined record of seawater $\delta^{13}C$ and $\delta^{34}S$ to model the history of oxygen and carbon dioxide in the atmosphere. A less model-based approach examines the occurrences of positive and negative $\delta^{13}C$ excursions in the stratigraphic record in an effort to understand the significance and causes of variation in marine organic productivity and organic matter burial and to explore the consequences of these events on climate and the history of life in the oceans (e.g., Arthur *et al.*, 1987, 1988; Bralower, 1988; Jenkyns, 1988; Zachos *et al.*, 1989; Kennett and Stott, 1991; Woodruff and Savin, 1991; Weissert and Lini, 1991; Wignall, 1991; Lini *et al.*, 1992). Still another line of research, just recently yielding its first crop of papers, uses the seawater Sr-isotope curve as an index of continental weathering to model the effects of variable continental weathering on the global CO_2 budget (Berner and Rye, 1992; François and Walker, 1992; François *et al.*, 1992).

In this thesis I would like to follow a more empirical approach and present evidence for a correlation between periods of rapid increase or decrease in the seawater Sr-isotope curve, the occurrence of positive $\delta^{13}C$ excursions, and the eruption of major flood basalts.

Following this presentation a number of simple model calculations will be used to demonstrate the plausibility of a predominantly hydrothermal control on the Sr-isotope curve during at least the late Cretaceous and early Cenozoic. Finally, I will discuss some possible links between flood basalts, hydrothermal events, the evolution of the Sr-isotope curve, and carbon-burial events.

7.2 The $\delta^{13}C$, $^{87}Sr/^{86}Sr$, and Flood Basalt Record

The seawater Sr-isotope curve forms the basic template against which $\delta^{13}C$ excursions and major flood basalt eruptions are plotted. For the Jurassic the correlation between the Sr-isotope curve and the $\delta^{13}C$ events is extremely precise because both sets of data come from the same stratigraphic sections. The constraints on the timing of the flood basalt events over this interval are poor due to the difficulties of radiometrically dating basaltic rocks. Moreover, the absolute ages of the stage boundaries of the Jurassic time scale are subject to errors of at least ± 10 Ma (Harland *et al.*, 1990). In the Cretaceous, correlation between the Sr-isotope curve and $\delta^{13}C$ events is complicated by the use of several different biostratigraphic schemes (different faunal provinces, different taxonomic groups) that are not always precisely intercalibrated. Thus I have applied generous error bars to the possible duration of the carbon-isotope excursions; the reader will see that the correlations nevertheless remain quite precise. Flood basalts are significantly better dated during the Cretaceous, but for some events significant errors still exist. The absolute ages of the Early Cretaceous stage boundaries are subject to fairly large error estimates of ±5 - 10 Ma, but by the Aptian/Albian boundary (112 Ma) the estimated errors are reduced to significantly less than ±5 Ma. In the Cenozoic, correlation between the Sr-isotope curve and $\delta^{13}C$ events is greatly facilitated by standard foraminiferal, nannofossil, and palaeomagnetic zones and by the fact that nearly all data are reported relative to the time scale of Berggren *et al.* (1985). For convenience the Harland *et al.* (1990) time scale is used for the Jurassic and Cretaceous whereas the Berggren *et al.* (1985) time scale is

retained for the Cenozoic. With the exception of the Columbia River Flood Basalts, the dating of the Cenozoic flood basalts is poorer than in some of the Cretaceous examples.

The numerous ^{40}K-^{40}Ar and ^{40}Ar-^{39}Ar dates constraining the age of each flood basalt province have been recently compiled in two papers. Rampino and Stothers (1988) combed through the literature and compiled histograms of dates (using 5-Ma bins) for each of the major flood basalt events. In some cases palaeomagnetic information is available to further constrain the duration of an event. The histograms typically show a few scattered older ages, then show a sharp increase in the occurrence of samples spanning a certain age range, and then tail away somewhat irregularly for the younger ages (Fig. 7.1). In addition to possible longer-lived volcanism, the scatter in the K-Ar dates (which are far more common than Ar-Ar dates) is caused by both loss of radiogenic ^{40}Ar during weathering or metamorphism and by the gain of ^{40}Ar released from older rocks (e.g., xenoliths) encountered by the rising basaltic magmas. Because the best-studied flood basalts seem to have erupted over less than a few million years (e.g., the Columbia River and Deccan Traps flood basalts), Rampino and Stothers have taken the start-up age of each province as the point at which the frequency distribution shows the fastest rate of increase towards the maximum. It is clearly difficult to be certain that one is actually dating a single main phase of a short-duration volcanic episode using this approach, but it is a consistent way of handling a large number of relatively scattered data points. The other recent compilation of flood basalt dates is by Baksi (1990). Baksi presents a much more critical appraisal of the data for selected events, but with the loss of systematic coverage.

7.2.1 Early Jurassic

The Early Jurassic interval is one of the best for comparing the distribution in time of black shales, positive $\delta^{13}C$ excursions, and the features of the Sr-isotope curve. The abundance, wide distribution, and rapid evolution of ammonites during the Early Jurassic has allowed Hallam (1987) to recognise a number of ammonite zones that seem to be

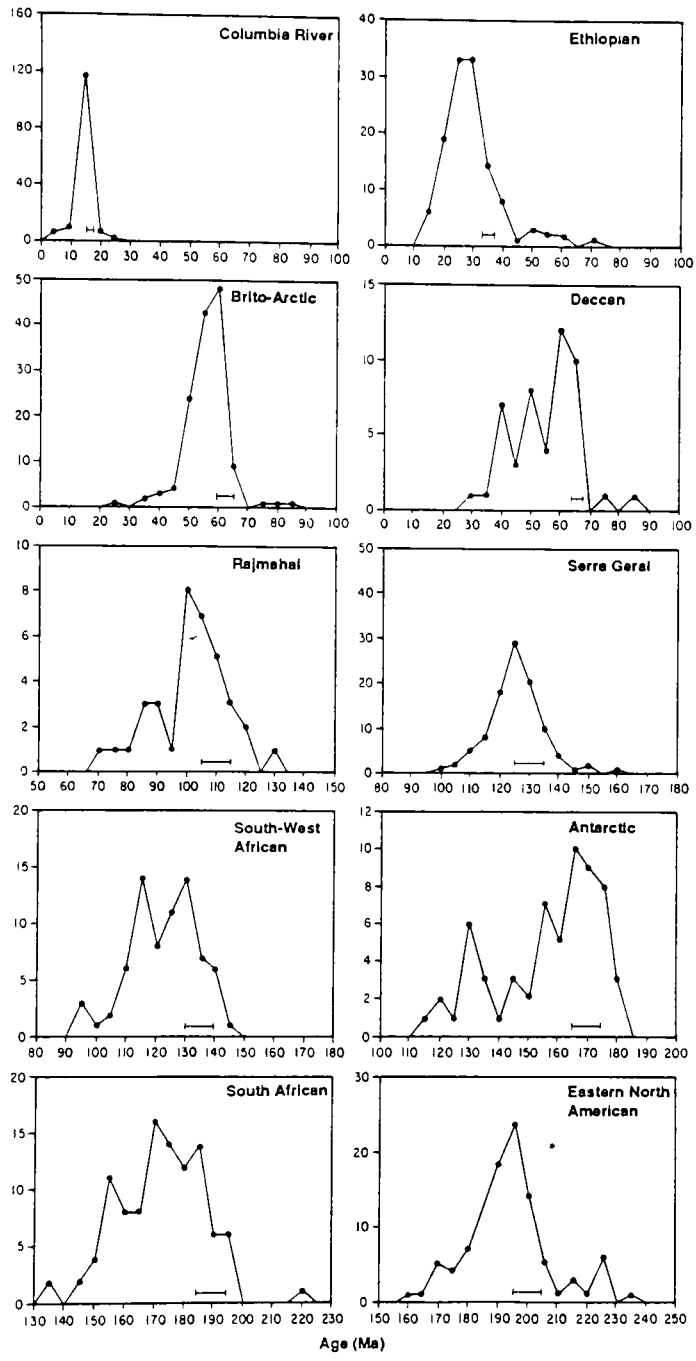

Figure 7.1 Histograms showing the distribution of ^{40}K-^{40}Ar and ^{40}Ar-^{39}Ar dates for each of the major flood basalt provinces over the last 210 Ma. The initiation of each event is determined as the interval over which the histogram most rapidly rises towards the first maximum. Figure from Rampino and Stothers (1988).

generally characterised by organic-rich shales at localities around the world. Although neither the stratigraphic observations of Hallam nor the $\partial^{13}C$ data of this study are entirely convincing on their own, together they allow the definition of those stratigraphic intervals that are most likely to host globally extensive carbon burial events.

According to Hallam (1987), the earliest candidate event is suggested by the thin but widespread organic-rich shales of Rhaetian (latest Triassic) to earliest Hettangian age found in northern Canada and throughout northwestern Europe. The data of Figure 7.2 indicate $\delta^{13}C$ values as high as +4.2‰ during the latest Triassic and confirm that a carbon-burial event may have occurred at this time. The $\delta^{13}C$ data come from the White Lias (Campos and Hallam, 1979) and *Ostrea* Beds of the Dorset Blue Lias. The dating of these strata is somewhat uncertain due to the lack of ammonites and, in addition, the presence of the organic-rich Cotham Member immediately below the White Lias suggesting that an earlier timing may also be possible. For the purposes of the present study the White Lias and *Ostrea* Beds are taken as each representing one ammonite subzone unit of time (their stratigraphic thicknesses are comparable to those of the subzones of the lowest Jurassic). The best-estimate duration of the event therefore runs from approximately 2.5 subzone units before the Triassic/Jurassic boundary to roughly 0.5 subzone units after the boundary. Although the highest $\delta^{13}C$ values are located approximately 0.5 subzone units below the boundary, the nature of the oyster $\partial^{13}C$ data does not allow the precise determination of the timing of a $\partial^{13}C$ "spike".

The next candidate carbon-burial event occurs during the Sinemurian *turneri* and *obtusum* zones. Hallam (1981) records these zones as marking an apparently global transgression characterised by a transition to shaley, frequently organic-rich deposits in eastern Asia, North and South America, and throughout Europe. The carbon-isotope data collected in this study suggest that the maximum possible duration of this event is from the *brooki* and *birchi* subzones of the *turneri* zone through to the end of the *obtusum*

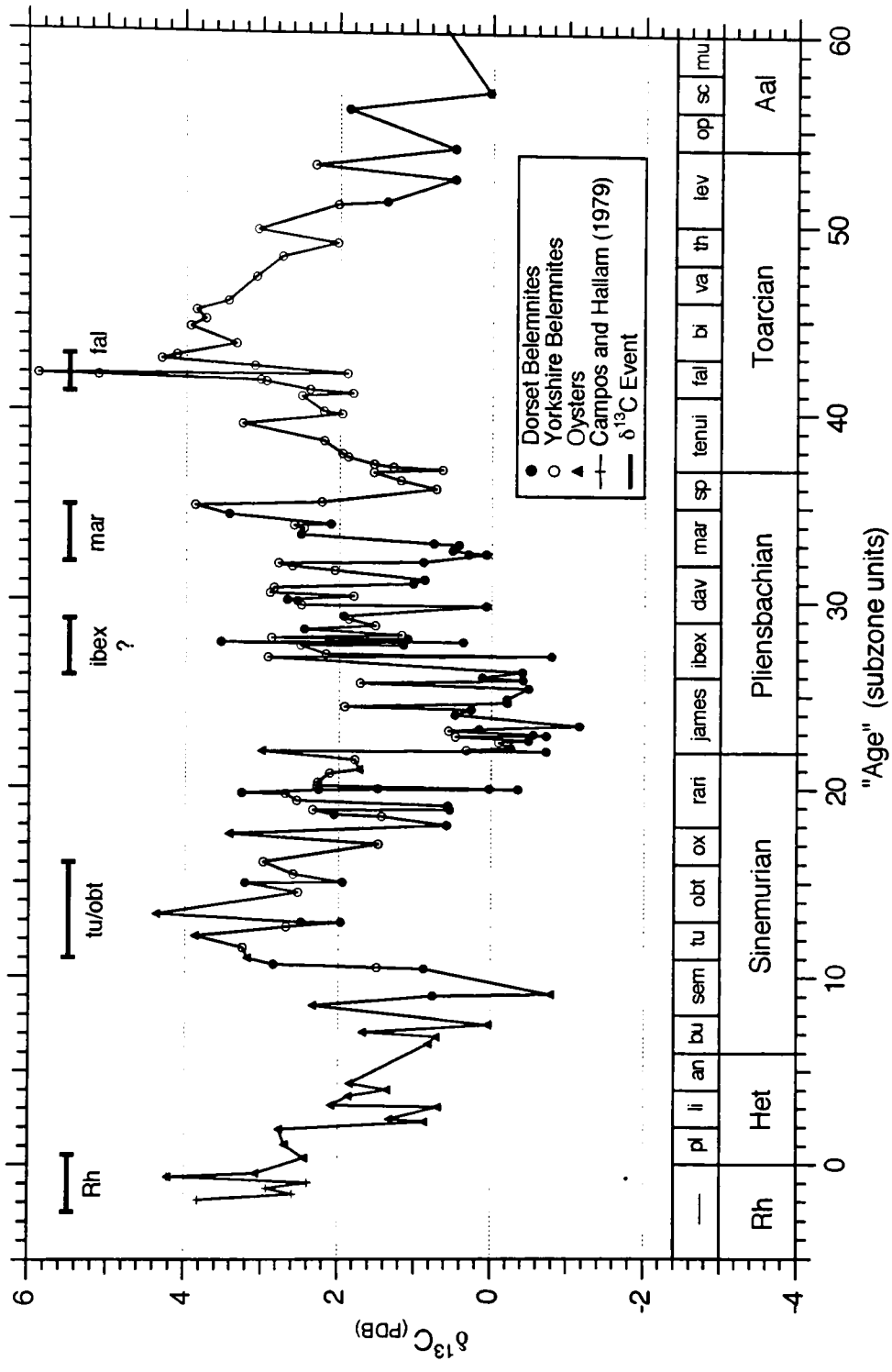

Figure 7.2: $\partial^{13}C$ data from belemnites and oysters collected from the Lower Jurassic of Great Britain. Abbreviations above stage names refer to the ammonite zones of Cope *et al.*, (1980a) and time is measured in equal-duration ammonite subzones counting above the base of the Jurassic.

subzone of the *obtusum* zone. Although the $\partial^{13}C$ maximum appears to be centred in the *obtusum* subzone, the nature of the belemnite data actually preclude a precise determination of the timing of this peak (Fig. 7.2).

The next major feature is a negative shift apparently taking place in the basal Pliensbachian. Whether this shift is real or an artefact of diagenesis or belemnite biological fractionation remains to be determined by further work. The succeeding sudden shift towards more positive $\partial^{13}C$ values in the *ibex* zone (Fig. 7.2) probably does not represent a true carbon-burial event, both because no extreme $\partial^{13}C$ values were measured and because Hallam (1987) did not note this zone as being generally characterised by organic-rich shales. This positive shift is probably best interpreted as either a recovery from the negative excursion of the *jamesoni* zone or a return to belemnite samples largely unaffected by diagenesis.

The best-documented Jurassic carbon-burial events occur during the *margaritatus* zone of the latest Pliensbachian and the *falciferum* zone of the early Toarcian. The *margaritatus* event is suggested by the transgressive organic-rich shales of *davoei* and *margaritatus* age found in Europe and especially throughout eastern Asia and North America (Hallam, 1981, 1987). The magnitude of this $\delta^{13}C$ excursion is relatively minor compared to the *falciferum* zone event to follow, but it is documented in a number of sections throughout Europe (Jenkyns and Clayton, 1986) and is confirmed by the data of this study (Fig. 7.2). The maximum duration of the event is constrained by the $\delta^{13}C$ data to be within the *margaritatus* zone and, although the data of this study suggest a $\delta^{13}C$ maxima near the end of the *margaritatus* zone, the much more extensive data set of Jenkyns and Clayton (1986) suggest that the acme occurs near the middle of the zone.

The *falciferum* zone event is exhaustively documented by the global distribution of black shales of this age (Hallam, 1987; Jenkyns, 1988). A major positive $\partial^{13}C$ excursion during the *falciferum* zone is suggested by a wealth of stable isotope data from a variety of

European sections (Jenkyns and Clayton, 1986; Jenkyns, 1988) and confirmed by data collected in the present study yielding $\delta^{13}C$ values of up to +5.9‰. The maximum duration of this event is taken to be the entire *falciferum* zone with the acme occurring at the middle of the zone (*exaratum/falciferum* subzonal boundary). It is worth emphasising that the combination of the broad geographic distribution of ammonites throughout the Early Jurassic and the high-resolution $\delta^{13}C$ and $^{87}Sr/^{86}Sr$ data allows exceptionally precise correlation between carbon events recorded at different sections and between the $\delta^{13}C$ and $^{87}Sr/^{86}Sr$ curves.

There are two known episodes of flood basalt volcanism during the Early Jurassic, and the constraints on the timing of the initiation these events are poor. The earlier event is represented by the Eastern North American basalt province associated with the rifting between North America and Africa. Rampino and Stothers (1988) have collected 104 dates from basalt flows, sills, and dykes scattered between Nova Scotia and North Carolina and estimate an initiation date of 200 ± 5 Ma. Figure 7.1 indicates that the start-up date could be any time between 210 and 195 Ma. The initiation of the Karoo Province flood basalt episode, which is associated with rifting along the east coast of South Africa, is dated at 190 ± 5 Ma by Rampino and Stothers (1988) and at 193 ± 5 by Fitch and Miller (1984). An estimate of 193 ± 7 Ma would cover the full range of probable start-up dates implied by the histogram of Figure 7.1. In addition to the uncertainty associated with the timing of the start-up dates, the geological time scale of Harland *et al.* (1990) has errors associated with the Early Jurassic stage boundaries that are not easily quantified, but which are on the order of ± 10 Ma. These errors dramatically reduce the confidence with which radiometrically dated events can be correlated to the biostratigraphically calibrated time scale.

The compilation of Sr-isotope data, carbon-isotope events, and flood basalt eruptions is presented in Figure 7.3. The late Rhaetian, *margaritatus*, and *falciferum* carbon-isotope excursions are each clearly associated with times of rapid change in the

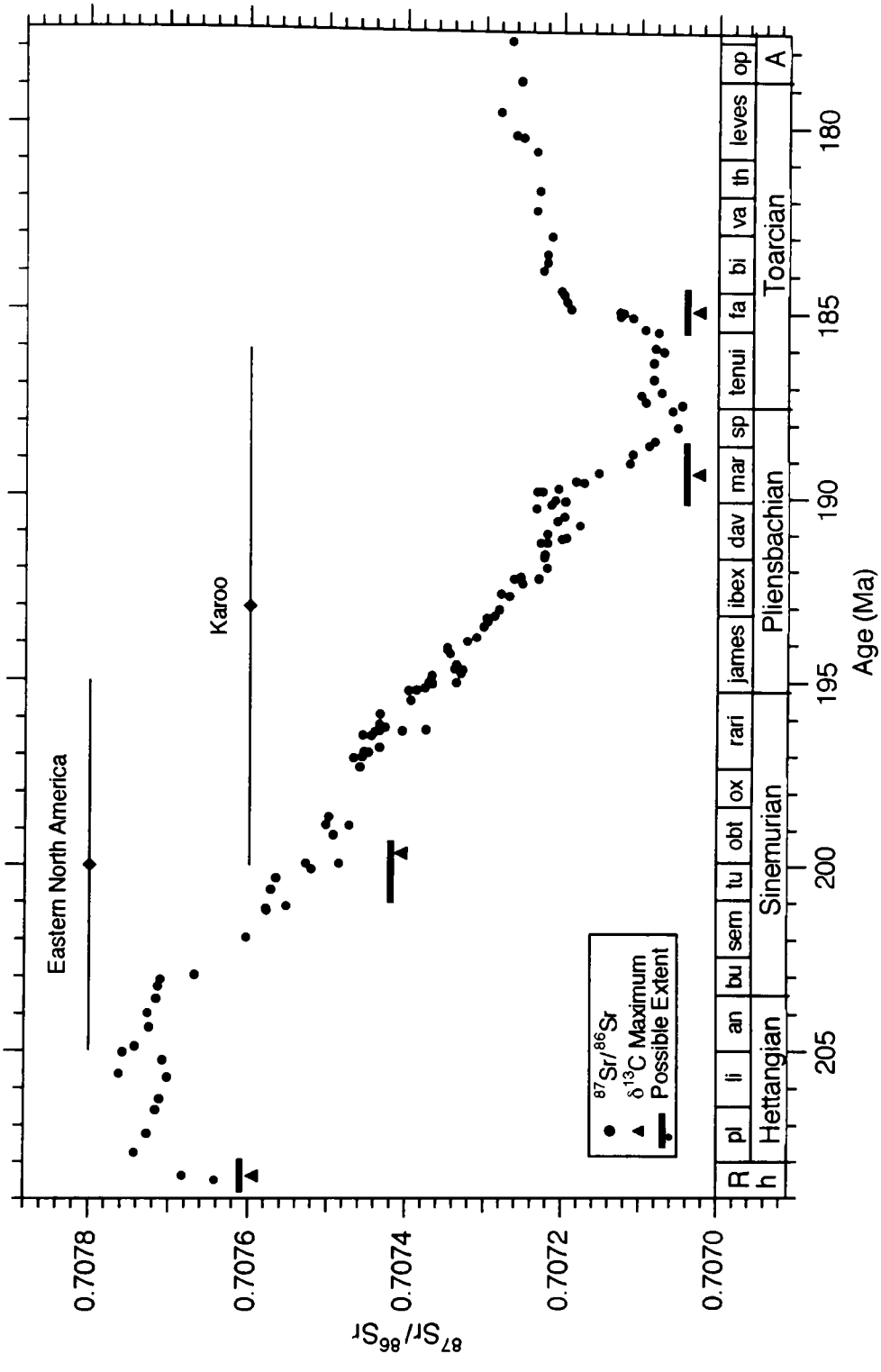

Figure 7.3 Correlation between the seawater Sr-isotope curve, positive $\delta^{13}C$ excursions, and flood basalt events. Abbreviations above Early Jurassic stages refers to the ammonite zones of Cope *et al.* (1980a).

seawater Sr-isotope curve. There is no clear shift in the Sr-isotope curve during the *turneri/obtusum* carbon event, although a rapid downwards shift in the early *obtusum* zone is possible. In addition, the constraints as to the timing of the $\delta^{13}C$ maximum are not firm, and it is possible that the actual maximum occurred at the same time as a rapid shift in the Sr-isotope curve. Age-constraints on the flood basalts are extremely poor relative to the precision of the Sr and C data. It is thus entirely possible, but not yet proven, that the Eastern North American and Karoo basaltic provinces are associated, respectively, with the downwards shifts in the *turneri/obtusum* and *margaritatus* zones. Note that the late Pliensbachian and early Toarcian $\delta^{13}C$ events seem to be linked together by the Sr-isotope curve: one carbon event occurs during a downwards shift in the Sr-isotope curve whereas the next occurs during the succeeding upwards shift.

7.2.2 Middle and Upper Jurassic

There is no evidence suggesting that the Aalenian, Bajocian, or Bathonian stages (Middle Jurassic) host any unusual accumulations of carbon. Moreover, the stable isotopic record, although quite incomplete over this interval (Chapter 5), does not suggest any positive $\delta^{13}C$ excursions. The Callovian, Oxfordian, Kimmeridgian, and Tithonian stages, by contrast, are generally characterised by relatively organic-rich strata (Hallam, 1987). However, there is no firm stratigraphic evidence supporting a narrowly defined, globally synchronous interval characterised by carbon-rich sediments and there are no well-documented carbon-isotope excursions. There are some $\partial^{13}C$ data from oysters collected in this study and from Oxfordian pelagic carbonate sections in Italy and France (Jenkyns, 1991, pers. comm.) that indicate a possible excursion in the early Oxfordian, but the timing of the event is not quite clear. The English data suggest a *cordatum* zone age (Northwest European faunal province) whereas the Italian and French data suggest a *transversarium* age (Submediterranean province) that implies a separation of roughly one ammonite zone. Thus, while it is possible that the positive carbon-isotope excursions during the early

Oxfordian are of global significance, the current data do not afford a clear resolution of this matter. Isotopic evidence presented for the Kimmeridgian and Tithonian (Weissert and Channell, 1989; Weissert and Lini, 1991; this study) do not suggest any positive $\partial^{13}C$ excursions during these times. Thus, despite the generally organic-rich strata in the Callovian through Tithonian and with the possible exception of the early Oxfordian, there are no proven carbon-burial events during the Middle and Late Jurassic.

The Middle and Late Jurassic also host no known, clearly identified flood basalt events. Rampino and Stothers (1988) note that although the Ferrar Group dolerites and basalts of Antarctica and similar dolerites in Tasmania are regionally extensive, they may not in fact represent a true episode of flood basalt volcanism. The best-estimate eruption date for these Antarctic and Tasmanian rocks is 170 ± 5 Ma. Errors on the ages of the stage boundaries during the Middle and Late Jurassic are roughly ± 10 Ma (Harland *et al.*, 1990) and thus significantly reduce the confidence with which radiometrically dated events can be correlated to a biostratigraphically calibrated time scale.

Figure 7.4 compares the Sr-isotope curve with the timing of the Callovian-Kimmeridgian organic-rich strata, possible early Oxfordian $\delta^{13}C$ excursion, and the Antarctic-Tasmanian flood basalts. The organic-rich sediments are found during the broad minimum in the seawater Sr-isotope curve. However, without more information as to the importance of these and adjacent intervals as regards carbon burial, it is difficult to make anything of this correlation. The Antarctic-Tasmanian flood basalts occur during a time of general decline in the Sr-isotope curve. Although there is no known carbon event associated with these basalts, this interval of time lacks the data to prove that the Bajocian does not host a carbon-isotope excursion. Also, there is additional uncertainty as to whether the Antarctic-Tasmanian basalts and dolerites do in fact represent true flood basalts. Thus, the Middle and Late Jurassic do not support or detract from the proposed correlation between Sr-isotope shifts, carbon events, and flood basalts.

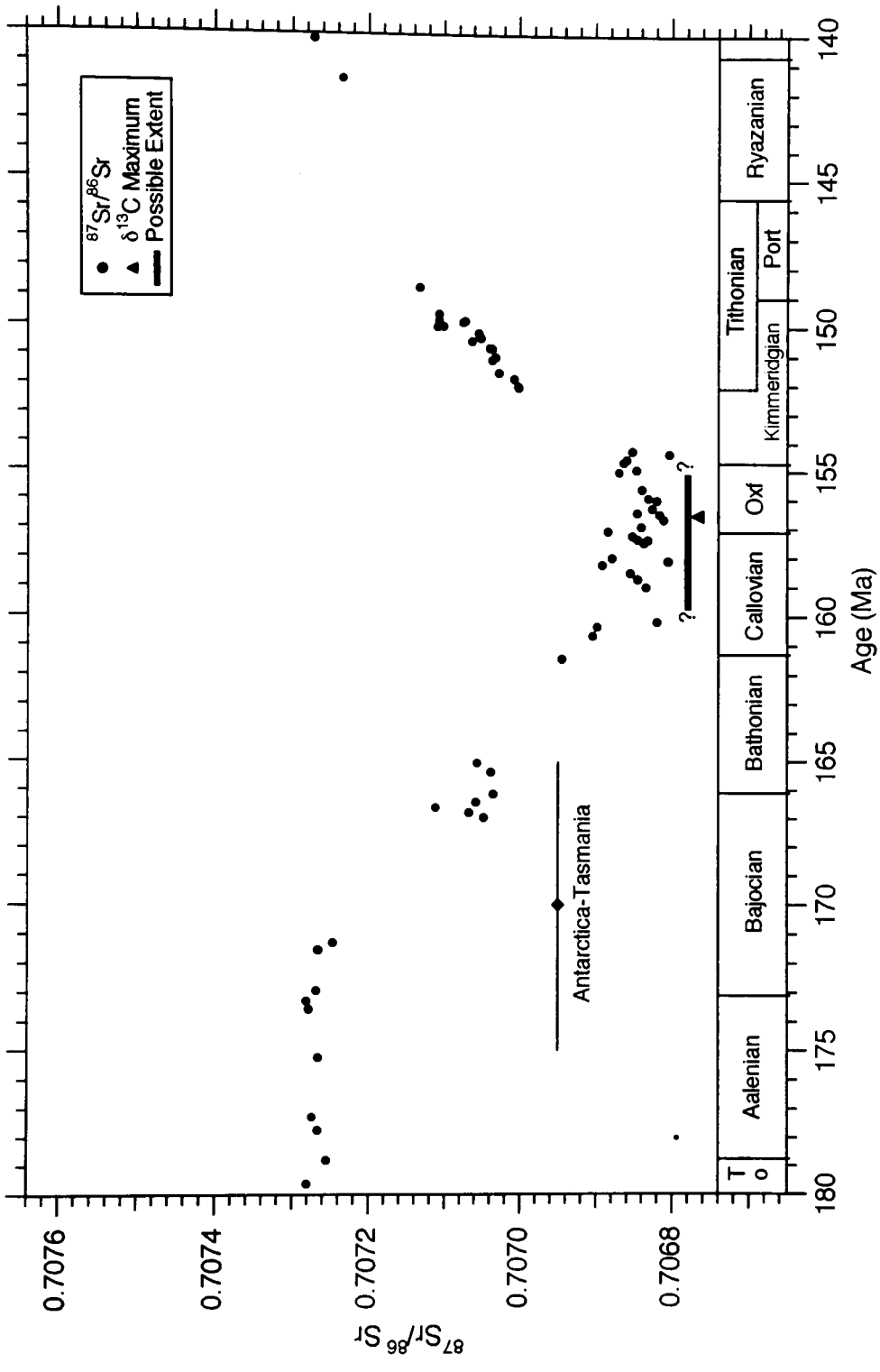

Figure 7.4 Middle and Late Jurassic correlation between the seawater Sr-isotope curve, positive $\delta^{13}C$ excursions, and flood basalt events. No events are well-enough proved to support or detract from the proposed correlations.

7.2.3 Cretaceous

The carbon-burial events of the Cretaceous are in general much better documented due to the availability of extensive outcrop and DSDP/ODP drill cores. The earliest documented Cretaceous $\partial^{13}C$ excursion occurs near the Valanginian/Hauterivian boundary (Weissert and Lini, 1991; Lini *et al.*, 1992). A positive $\partial^{13}C$ excursion restricted to the *Calcicalathina oblongata* nannofossil zone has been documented at five sites from the southern Alps of Italy and at one site each in the Gulf of Mexico, the western North Atlantic, and the central Pacific. In addition, a transition to organic-rich sediments has been observed at this time at a variety of other sites around the world. Thus, this excursion of approximately +1‰ appears to reflect a globally synchronous carbon-burial event (Lini *et al.*, 1992). This event is roughly dated as occurring in the upper half of the Valanginian stage, which according to the time scale of Harland *et al.* (1990) indicates an age of between 138 and 135 Ma with a $\partial^{13}C$ peak at roughly 136 Ma.

The timing, number, and duration of events during the Aptian and Albian are not yet clear. Arthur *et al.* (1990) argue for three separate events. The oldest occurs during the *forbesi/deshayesi* ammonite zones, which are in part equivalent to the *G. blowi* foraminifera zone of the lower Aptian. Black shales of this age are known from around Europe and in the Pacific Ocean (Sliter, 1989) and Weissert and Lini (1991) present $\partial^{13}C$ evidence from northwest Tethys, the Southern Alps of Italy, and the North Atlantic that confirms the beginning of the event in the mid-*G. blowi* zone. However, their data also suggest a rather complicated history of carbon burial at this time. In contrast to other carbon-burial events, which tend to be of very short duration (< 1 Ma; Schlanger *et al.*, 1987; Jenkyns, 1988), the *G. blowi* event seems to have continued through the *S. cabri* zone, peaked finally in the *G. ferreolensis* zone, and finally ended abruptly in the succeeding mid-*algerianus* zone. Their data also indicate that a second event began immediately again in the *G. algerianus* zone, peaked at the *algerianus/trocoidea* boundary,

and ended in the succeeding *T. bejaouaensis* zone. These two events thus seem to have persisted over a considerable period of time. Correlated to the time scale of Harland *et al.* (1990), the zones of the first event indicate a duration from roughly 122 to 117.5 Ma, with a peak at 118.5 Ma, and the second event goes from roughly 117.5 to 113.5 Ma with a peak at 116.5 Ma.

Following Arthur *et al.* (1990), the next event is thought to have occurred during the lower Albian *tardefurcata* ammonite zone, which corresponds to the upper portion of the long *T. bejaouaensis* foraminiferal zone (Harland *et al.*, 1990). This event thus begins in the same zone that saw the end of the previously described event. A *tardefurcata* date gives a time-scale age of roughly 112.0 - 110.0 Ma. The final event of Aptian/Albian times is placed in the *dispar* ammonite zone and the *R. appennica* foraminiferal zone of the late Albian. This event, well-separated from adjacent events above and below, receives radiometric dates based on the ammonite zone of 97.7 - 97.0 Ma. The existence of these separate, discrete carbon-burial events during the Aptian/Albian is not universally accepted (Arthur *et al.*,1990), but it does seem clear that particularly the Aptian and early Albian were times characterised by high carbon burial rates.

The Cenomanian-Turonian Boundary Event is the best-documented interval of accelerated carbon burial in the Cretaceous. A large amount of work on this boundary (summarised by Schlanger *et al.*, 1987; Bralower, 1988; Arthur *et al.*, 1990) finds that organic-rich sediments characterise strata of this age from around the world and that the timing of the associated positive $\partial^{13}C$ excursion is constrained to within a few hundred thousand years of the Cenomanian/Turonian boundary (within the *W. archeocretacea* foraminifera zone). Following Harland *et al.* (1990), this event is therefore precisely dated at 90.4 ± 0.5 Ma.

The next Cretaceous carbon-burial event, although not yet well-documented, is thought to have occurred during the Coniacian stage (Arthur *et al.*, 1990). There is no

published summary of the sedimentary or isotopic record covering this interval, but Jenkyns (1991), on the basis of unpublished data, places this event in about the upper 0.5 Ma of the Coniacian. This implies a date of 86.85 ± 0.25 Ma. The final carbon-isotope excursion of the Cretaceous occurs some 0.2 Ma before the Cretaceous/Tertiary boundary and before the more famous negative excursion associated with the K/T boundary (Stott and Kennett, 1989; Zachos *et al.*, 1989; Kennett and Barker, 1990). These workers report results from three sites (one each in the Atlantic, Pacific, and Antarctic oceans) that indicate the global nature of this event and that suggest a date of 64.9 ± 0.2 Ma for the duration of this event.

The Cretaceous hosted a number of flood basalt eruptions both on land and under the sea. The Etendeka Province in southwestern Africa and the Paraná Flood Basalts in southern Brazil are both dated at around 135 Ma, although there is some debate as to whether they are in fact contemporaneous. Rampino and Stothers (1988) estimate the initiation of the Etendeka eruptions at 135 ± 5 Ma as compared to 130 ± 5 Ma for the Paraná. Baksi (1990) estimates an age of at least 131 Ma for the Etendeka based on the oldest offshore seafloor magnetic chron M4 and an age of 130 Ma for the Paraná, although the histogram that he plots would argue for an age of 135 ± 5 Ma if the logic of Rampino and Stothers (1988) were followed. It seems reasonable to conclude that these events are nearly contemporaneous, erupting at approximately 132 ± 8 Ma.

The Rajmahal Traps of eastern India are relatively poorly dated. Rampino and Stothers (1988) estimate a starting date of 110 ± 5 Ma, but their frequency distribution (Fig. 7.1) is such that any time between 100 and 120 Ma seems plausible. The more recent work of Baksi (1988) demonstrates that the Rajmahal Traps formed rapidly at 117 ± 1 Ma; this date will be taken as marking the initiation of the event.

In addition to the continental flood basalt provinces, there is evidence for extensive basaltic eruptions on the sea floor. Larson (1991; personal communication) has recently

tabulated the estimated ages and eruptive volumes for each of the major oceanic plateaus and finds that there is a major pulse of Aptian activity between 125 and 115 Ma, a second smaller pulse between 95 and 90 Ma just before the Cenomanian/Turonian boundary (90.4 Ma), and a third pulse at 60 - 55 Ma spanning the Palaeocene/Eocene boundary (Fig. 7.5). The dating of these pulses is hampered by the long Cretaceous interval of normal polarity (C34 runs from 124 to 83 Ma) and the fact that dates are inferred from the oldest age of sediments on the plateau, dredged rocks that have been radiometrically dated, or from tectonic associations with features of known age.

The final episode of Cretaceous flood basalt volcanism is represented by the Deccan Traps. These are dated at 66 ± 2 Ma by Rampino and Stothers (1988) and at 65 Ma by Baksi (1990). In both papers it is concluded that the eruptions took place within 1 Ma of the Cretaceous/Tertiary boundary.

Figure 7.6 presents the temporal relationships between fluctuations of the Sr-isotope curve, carbon-isotope excursions, and flood basalt eruptions. The late Valanginian carbon-isotope excursion is not associated with an obvious sudden shift in the Sr-isotope curve, although the gap in Sr-isotope data does not entirely eliminate this possibility. Although the best-estimate age of eruption of the Etendeka/Paraná provinces is somewhat younger than the Valanginian $\delta^{13}C$ event, it is entirely within the constraints of both the basalt data and the estimated stage boundary ages that the basalts are the same age as the $\delta^{13}C$ excursion. Although the Aptian and early Albian Sr-isotope data are relatively poor, it is clear that the Aptian $\delta^{13}C$ excursions occur at the same time the Sr-isotope curve is rapidly declining. Moreover, Larson's (1991, personal communication) largest outpouring of seafloor basalts occurs at this time, as do the Rajmahal Traps flood basalts. By contrast, the early and latest Albian carbon excursions occur when the Sr-isotope curve is moving back towards more radiogenic values; they are not associated with flood basalt events. The latest Albian event coincides with what appears to be a rapid jump in the Sr-isotope curve,

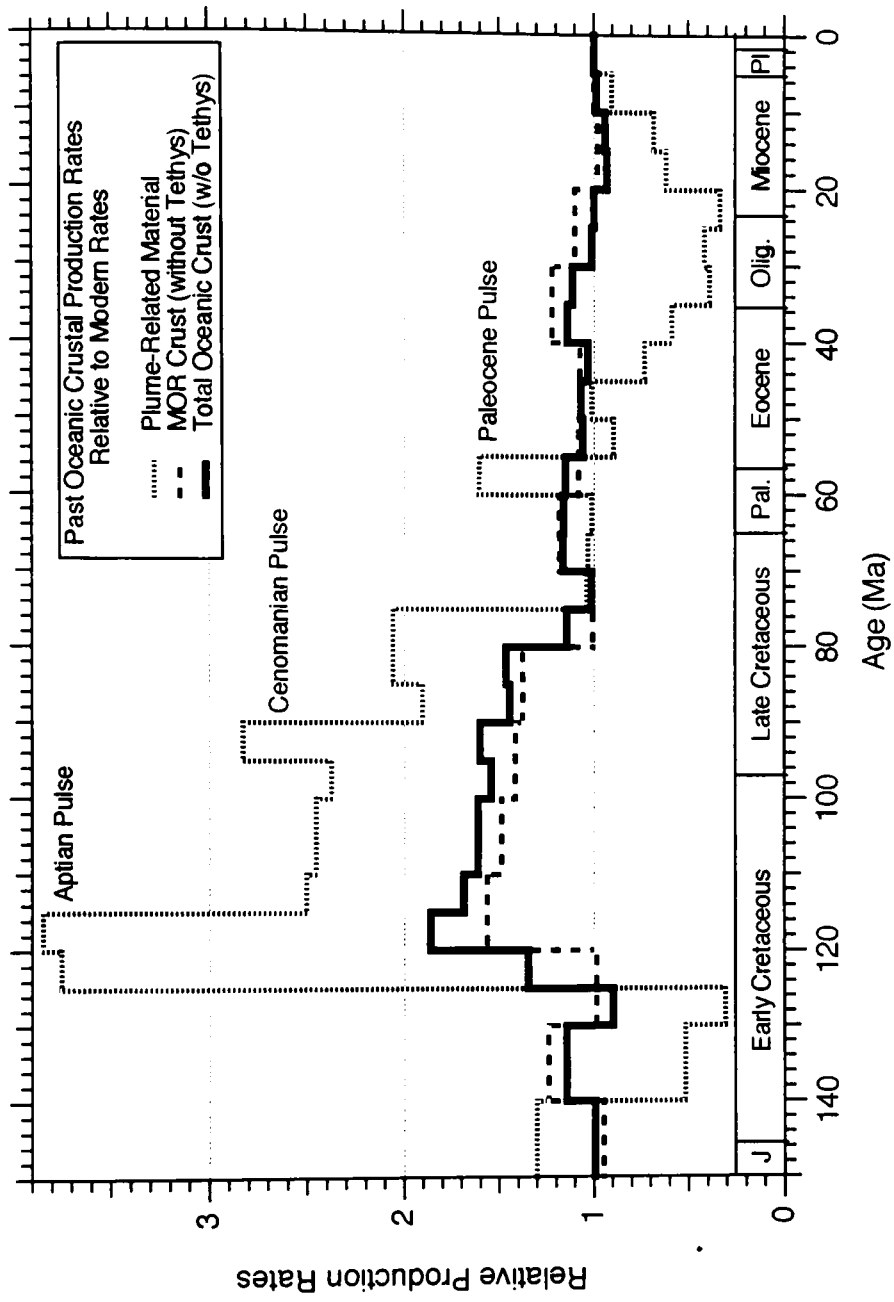

Figure 7.5 The relative generation rates of oceanic crust (by area) over the past 150 Ma. All rates are normalised to the present day. The finely-dashed line traces the relative generation rates of sea floor materials related to mantle plume activity. The resultant oceanic plateaus are analogous to the continental flood basalts. The three main pulses occur during the Aptian, Cenomanian, and Palaeocene. The heavy dashed line represents the relative generation rates for all mid-ocean ridge materials with the exception of the presently subducted Tethyan ridge systems. The solid line represents both the plume-related and mid-ocean ridge crustal generation rates and demonstrates the predominance of the mid-ocean ridge system in the total amount of oceanic crust generated.

although it should be noted that this shift also marks the boundary between two different data sets. The next downwards shift in the Sr-isotope curve is also associated with a carbon-isotope excursion--the well-known Cenomanian-Turonian Boundary Event--and also with an accelerated outpouring of seafloor basalts. There is no known continental flood basalt dating to this time. The Sr-isotope curve recovers rapidly through the Coniacian and early Santonian, and another carbon-isotope event occurs during this rapid rise in the latest Coniacian. Finally, at the end of the Cretaceous, the latest Maastrichtian carbon-isotope excursion and Deccan Traps flood basalts occur within 1 Ma of each other. In contrast to most previously described events, there is no pronounced downwards shift in the Sr-isotope curve accompanying this episode of flood basalts. In this regard the latest Cretaceous events seem to mark a transition to the Cenozoic when the Sr-isotope curve no longer shows a pronounced negative excursion in conjunction with flood basalt eruptions.

It should be emphasised that, as in the case of the late Pliensbachian, the Aptian and Cenomanian portions of the Sr-isotope curve show strong downward shifts that correlate in time with major flood basalt eruptions. Moreover, each carbon excursion associated with a downwards Sr-isotope shift is paired with a second $\delta^{13}C$ excursion associated with an upwards Sr-isotope shift. For those flood basalt events not associated with large shifts in the Sr-isotope curve, there is only one $\delta^{13}C$ excursion occurring at the same time as the flood basalt eruption.

7.2.4 Cenozoic

The first and strongest positive carbon-isotope excursion of the Cenozoic occurs during the Late Palaeocene, spanning roughly 56.5 to 60.5 Ma with a peak at about 59 Ma (Shackleton, 1986; Rea *et al.*, 1990; Kennett and Barker, 1990). The second event of the Cenozoic is a minor $\delta^{13}C$ excursion near the end of palaeomagnetic chron C13R in the Early Oligocene dated at 35.2 ± 0.2 Ma (Zachos *et al.*, 1992). The third and final positive carbon excursion of the Cenozoic is the famous Middle Miocene Monterey Excursion

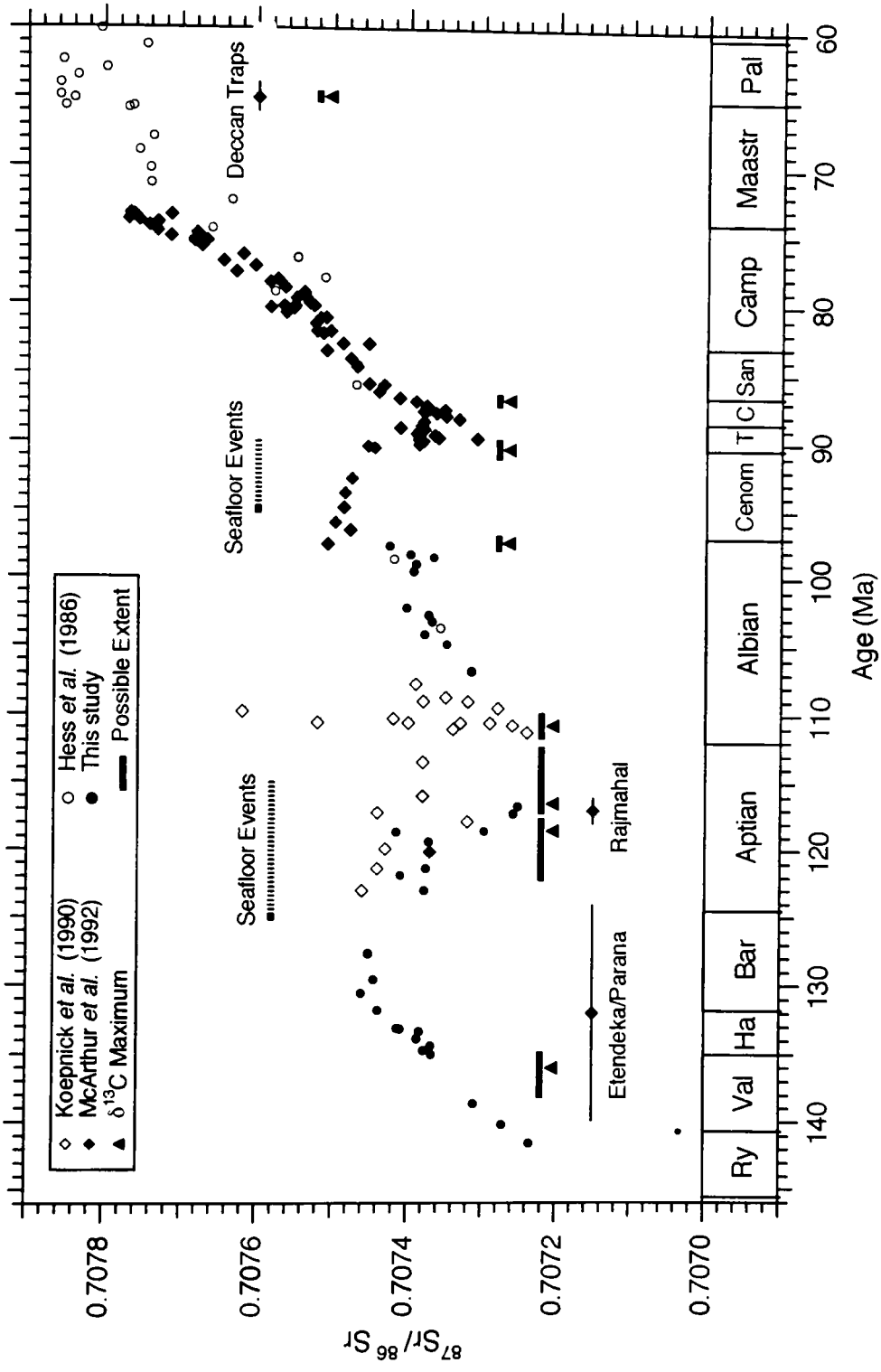

Figure 7.6 Correlation of the seawater Sr-isotope curve, positive $\delta^{13}C$ excursions, and flood basalt events in the Cretaceous. Periods of increased oceanic plateau-building ("Seafloor Events") are taken from Larson (1991; personal communication).

associated with oil-producing rocks around the Pacific rim. This excursion is more protracted and complex than the "spikes" typically encountered in the Mesozoic and spans much of the Middle Miocene (~17 - 14 Ma; Berger and Vincent, 1986; Woodruff and Savin, 1991). The extensive data compilation of Woodruff and Savin (1991) allows this complex event to be more precisely dated and broken down into its components. The first $\delta^{13}C$ occurs near the foraminiferal N7/N8 boundary and within the nannofossil zone NN4. This dates the initiation of the event as near 16.4 Ma. Following this initial excursion there are further pulses at about 15.8, 15.5, 15.1, 14.6, and 14.1 Ma.

The first flood basalts of the Cenozoic are those of the North Atlantic Tertiary Province. The 138 dates compiled by Rampino and Stothers (1988) form a well-defined frequency maximum indicating a starting date of 62 ± 3 Ma. Baksi (1990) summarises data that suggest a somewhat younger date of roughly 60 ± 1 Ma. For this study a start-up of 62 ± 3 Ma is assumed. The Ethiopian flood basalts are poorly dated relative to their young age. The compilation of 122 ages by Rampino and Stothers (1988) shows a large number of dates between roughly 20 and 40 Ma. Baksi (1990) considers a small number of dates clustering around 24 - 28 Ma, but the much more extensive data set of Rampino and Stothers (1988) suggests a start-up date of 35 ± 3 Ma. The most recent flood basalts are those of the Columbia River Basalt Group. The detailed work reviewed by Baksi (1990) indicates that nearly all of the basalts erupted between 17 and 15 Ma, with the main phase starting at approximately 16.4 Ma. Rampino and Stothers (1988) estimate a less precise starting date of 17 ± 1 Ma.

The Cenozoic differs from the Mesozoic in that the Sr-isotope curve shows no sudden, strong shifts towards either higher or lower $^{87}Sr/^{86}Sr$ ratios (Fig. 7.7). Instead the curve remains flat or slowly declining during the early Cenozoic and then begins a steady increase, with several changes in slope, moving towards the present. However, the good correlation between $\delta^{13}C$ events and flood basalt eruptions remains. The dating of the

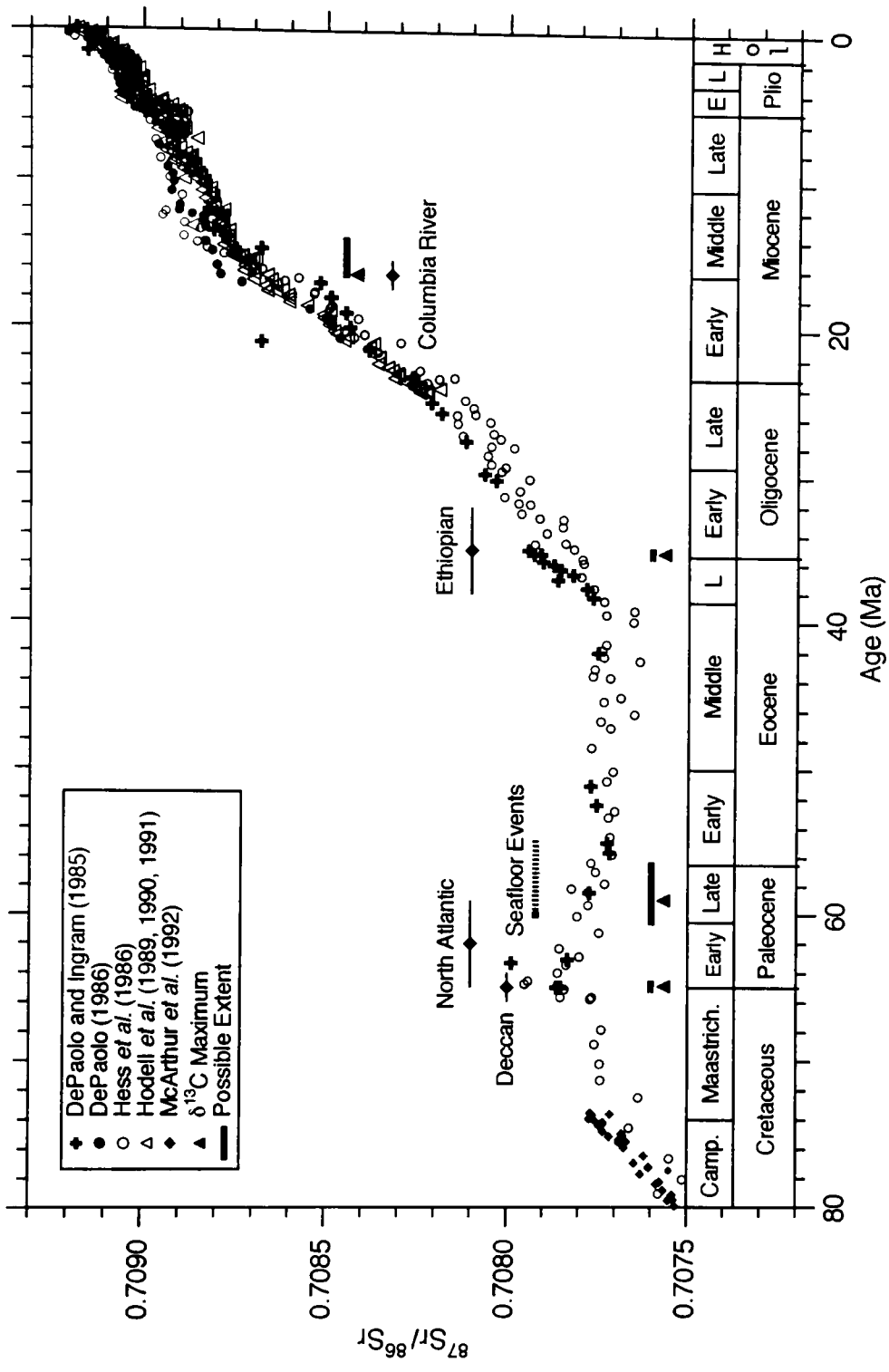

Figure 7.7 Correlation of the seawater Sr-isotope curve, positive $\delta^{13}C$ excursions, and flood basalt events in the Cenozoic. Periods of increased oceanic plateau-building are taken from Larson (1991; personal communication).

North Atlantic Tertiary Province and a pulse of sea-floor basaltic generation (Fig. 7.5) both overlap the Late Palaeocene positive carbon excursion. Although it is possible that these events are responsible for the decline the in the Sr-isotope curve from the Cretaceous/Tertiary boundary, it is also possible that this decline simply represents a recovery from an unusual event centred around the Cretaceous/Tertiary boundary (e.g., Macdougall, 1988; Javoy and Courtillot, 1989; Martin and Macdougall, 1991). There is also a good correspondence between the timing of the Ethiopian flood basalts and the minor Early Oligocene $\delta^{13}C$ excursion. However, the poor age constraints on the flood basalts weakens the strength of this correlation. If the Sr-isotope data of DePaolo and Ingram (1985) are more accurate than those of Hess *et al.* (1986) over this interval, it is possible that the flood basalts are associated with the temporary dampening of a rapid seawater $^{87}Sr/^{86}Sr$ increase that began in the late Eocene. Finally, the time of initiation of the Columbia River Flood Basalts, which are unusual in that they are not associated with a successful continental rifting event, corresponds exactly with the first of the Monterey carbon-isotope excursions. Moreover, the timing of these events, although not clear from Figure 7.7, corresponds exactly to a distinctive reduction in the rate of increase of the seawater Sr-isotope curve (Hodell *et al.*, 1991).

In summary, there appears to be a close link between events in the seawater Sr-isotope and $\delta^{13}C$ curves. Every rapid shift in the Sr-isotope curve, with the exception of the rapid rise between 6 and 4 Ma (Fig. 7.7), has a corresponding carbon-isotope event. This includes the events of the late Rhaetian, *margaritatus, falciferum*, Aptian, Albian, Cenomanian/Turonian, and Coniacian. Moreover, other positive carbon-isotope excursions may be associated with minor rapid shifts in the Sr-isotope curve (e.g., the *turneri/obtusum* event). In the Mesozoic the carbon-isotope events tend to be paired, with the first occurring at the same time as both a downwards shift in the Sr-isotope curve and the eruption of a flood basalt and the second corresponding to a rapid recovery to more

radiogenic Sr-isotope values. In the latest Cretaceous and Cenozoic this pattern breaks down such that there are no negative shifts in the Sr-isotope curve and every carbon-isotope event is associated with a flood basalt. Over the last 70 Ma, the largest changes in the Sr-isotope curve possibly associated with flood basalts are an interruption of the late Cretaceous increase and the prolonged decline of the Palaeocene, a possible levelling off of a rapid increase at the time of the Ethiopian basalts, and a reduction in the rate of increase at exactly the time of the initiation of the Columbia River Basalts.

These observations suggest that positive carbon-isotope excursions are somehow linked to flood basalts and to the processes associated with the rapid negative and positive shifts in the Sr-isotope curve. Because the downward shifts in the Sr-isotope curve are associated in time with the eruption of flood basalts and because the likely effect of increased mantle interaction with the earth's surface is the introduction of nonradiogenic Sr to the oceans, it seems likely that the downward shifts in the Sr-isotope curve are the result of increased mid-ocean ridge hydrothermal activity and that this hydrothermal activity is in turn associated with the tectonic events that brought about the eruption of the flood basalts. One common link between the carbon and strontium isotope curves and the eruption of flood basalts could be hydrothermalism. Because there is a strong tendency in the literature to attribute the majority of changes in the seawater Sr-isotope curve to changes in the riverine inputs, it is necessary in the next section to demonstrate that a hydrothermal control on the evolution of the Sr-isotope curve cannot be ignored.

7.3 Major Controls on the Seawater $^{87}Sr/^{86}Sr$ ratio

There seems to be universal agreement that although the hydrothermal flux of Sr is important in controlling the absolute value of the seawater $^{87}Sr/^{86}Sr$ ratio, it is variations in either the flux or the isotopic composition of river water Sr that must account for the main fluctuations in the observed seawater curve (Palmer and Elderfield, 1985; DePaolo, 1986; Hess *et al.*, 1986; Raymo *et al.*, 1988; Hodell *et al.*, 1989, 1990; Capo and DePaolo, 1990;

François and Walker, 1992; Berner and Rye, 1992; Richter *et al.*, 1992; Krishnaswami *et al.*, 1992; François *et al.*, 1992). This conclusion is reached through a process of elimination. Because the Sr flux from the recrystallisation of sea-floor sediments is small and the $^{87}Sr/^{86}Sr$ ratio is not very different from seawater (Elderfield and Gieskes, 1982), it is also difficult to conceive of a mechanism that would cause changes of sufficient magnitude to affect the marine $^{87}Sr/^{86}Sr$ ratio. Because sea-floor basalts are relatively isotopically homogeneous with respect to Sr, it is difficult to conceive of a mechanism that would change this component of the hydrothermal flux. The fact that global sea-floor spreading rates have experienced only limited variation over the past 150 Ma plus the assumption that the hydrothermal Sr flux changes in direct proportion to sea-floor crustal generation rates suggests that the hydrothermal flux term has undergone only limited changes over the Cenozoic. Moreover, the possibility of short-term pulses of hydrothermal activity are eliminated under the assumption that the palaeomagnetic record of sea-floor magnetic lineations adequately rules out any short-term pulses in spreading rates (Hodell *et al.*, 1988; 1990; Capo and DePaolo, 1990). In the end, the elimination of these two major terms in the Sr cycle leaves either the mass flux or the isotopic composition of riverine Sr to vary. Although changes in the average riverine Sr-isotopic composition seem likely (Palmer and Elderfield, 1985; Berner and Rye, 1992), the majority of authors focus on changing chemical weathering fluxes, perhaps in part because it is easier to find geochemical and sedimentological evidence that may be interpreted in terms of past chemical weathering rates.

The basaltic Sr flux is easily characterised due to the relatively homogeneous nature of the sea-floor basement basalts. Although it is difficult to characterise accurately the precise concentration and isotopic composition of hydrothermal fluid Sr and to partition the basaltic Sr flux into its various components (off-axis, axial brine, and axial Cl-normal; see Chapter 6), the problem is greatly simplified by the fact that the $^{87}Sr/^{86}Sr$ ratio is unlikely to

vary significantly over time. Although different authors favour $^{87}Sr/^{86}Sr$ ratios between 0.7029 and 0.7035 for the basaltic Sr flux, within a single model one constant ratio is assumed. Thus, an increase in hydrothermal venting always tends to bring the seawater $^{87}Sr/^{86}Sr$ down while a decrease in hydrothermal activity always tends to allow the ratio to move back up.

The hydrothermal flux of seawater through mid-ocean ridges is most simply modelled by assuming that the volume of seawater circulating through the global mid-ocean ridge system is directly proportional to the area of new crust extruded along the ridge system (e.g., Berner *et al.*, 1983). The production of more oceanic crust per unit time brings a proportionally larger quantity of heat to the ridge axis which, because the circulation of seawater through the sea floor is thermally driven, brings a higher flux of water to dissipate the heat. The area of new oceanic crust produced over the past 150 Ma can be calculated from the spreading rate and ridge length data compiled by Kominz (1984) for the world's spreading centres. Larson (1991) has recalculated the data of Kominz (1984) using the time scale of Harland *et al.* (1990) and has added to the data set the area of flood basalts and oceanic crust added by mantle plumes. According to the marine Sr budget presented in Chapter 6, the basaltic Sr flux is divided into the low-temperature off-axis flux and the high-temperature axial fluxes of phase-separated (brine) and nonphase-separated (Cl-normal) fluids. Changing the area of new crust produced each year should have an immediate effect on the axial Sr flux terms. It is assumed for the present that the relative proportions of the brine and Cl-normal components of the axial flux remain constant over the long-term. It is difficult to predict the variation of the off-axis flux because it is not known how this term varies as a function of distance from the ridge axis. If there is some sort of an exponential decline in Sr exchange as a function of increasing crustal age and decreasing crustal temperatures, then an increase in spreading rates should, after a relatively short time-lag, result in a larger area of hot, young crust able to support a

higher off-axis Sr exchange. Hence the off-axis flux should also increase with increasing crustal generation rates, but with some time-lag behind the changes in the axial component. In the models to follow two end-member situations will be considered. In one end-member both the axial and flank terms are varied proportionally to crustal generation rates while in the other only the axial term is varied.

The model curves presented in Figure 7.8 show the evolution of the equilibrium seawater $^{87}Sr/^{86}Sr$ ratio as a function of time assuming that the hydrothermal Sr flux varies proportionally to changes in the area of new seafloor produced each year. The axial model (thin line) includes only the brine and Cl-normal fluids whereas the the solid line includes the off-axis term with the axial terms. In nature the response should lie in between these two curves, depending on how the off-axis flux varies with crustal generation rates. Comparison between the model curves and the isotope data indicate that over the Cenozoic, where spreading rate and ridge length data are most accurate, there is little correspondence between the model curve and the seawater Sr-isotope curve. The slight increases in the model curve brought about by slight decreases in the production rates of oceanic crust are no match for the rapid increase in the Sr-isotope curve from the Oligocene to present. For example, at about 20 Ma there is decrease in crustal generation rates that should accelerate the rate of increase of the Sr-isotope curve; instead, the curve abruptly slows its increase. It is the overall lack of correspondence between the model and observed curves that has forced the widely held conclusion that variations in the riverine term must be most important in controlling the variations in the seawater Sr-isotope curve.

Close examination of the curves of Figure 7.8 suggests that there is a certain degree of parallelism between the model and observed curves between 40 and 125 Ma. This raises the possibility that the Sr-isotope curve was controlled by hydrothermal variations from at least 125 Ma to 40 Ma, and that since 40 Ma the trend of the Sr-isotope curve has been

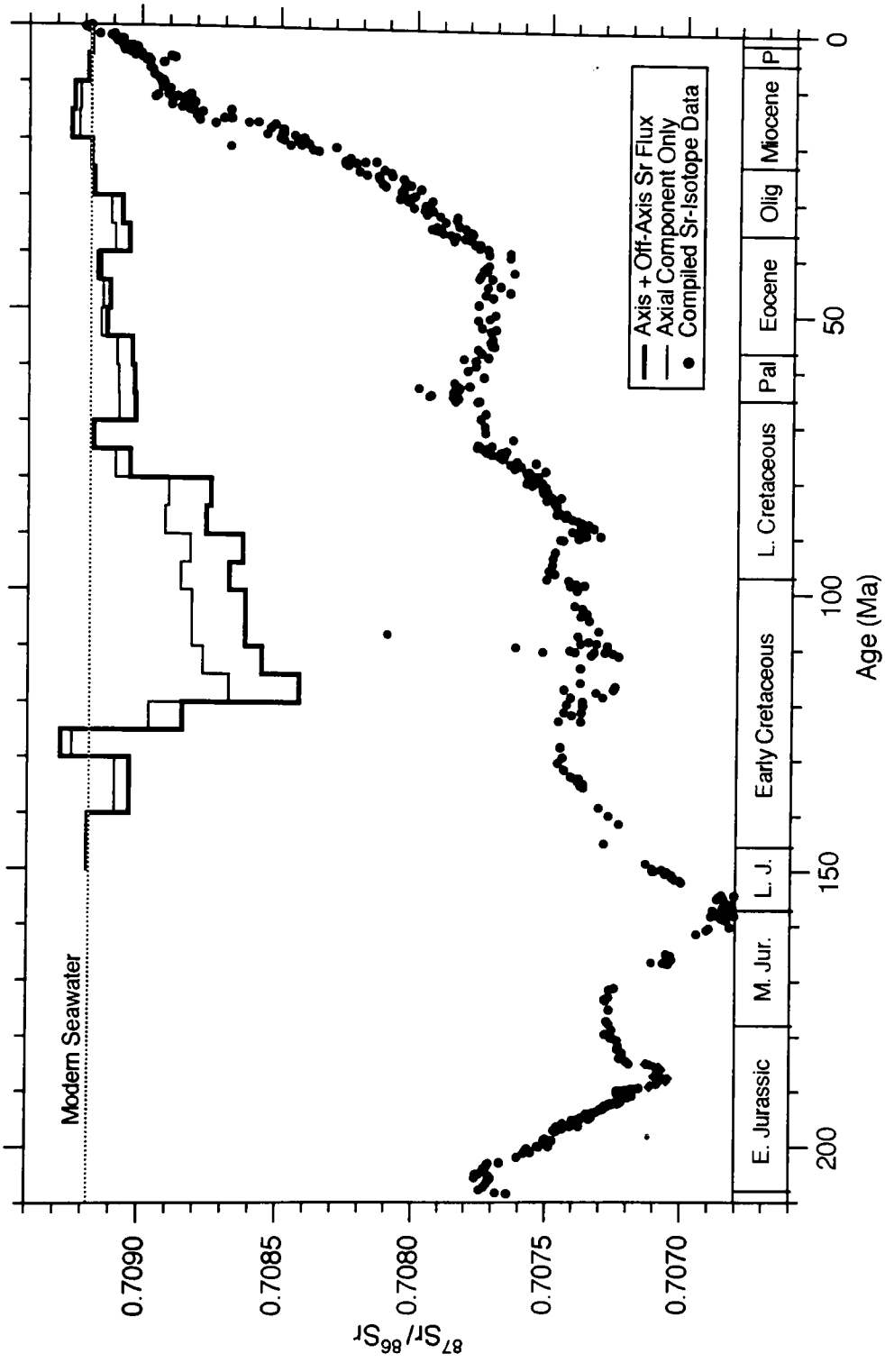

Figure 7.8: Calculated effects of changing the hydrothermal Sr flux proportionally to the observed changes in ocean crustal generation rates. The rapid increase of the past 40 Ma is not duplicated by the model curve, suggesting that variations in hydrothermal activity are unimportant in determining the evolution of the seawater Sr-isotope curve.

dominated by the riverine component. A test of the plausibility of this hypothesis requires that the riverine and hydrothermal components of the Sr-cycle be adjusted to what they were at 40 Ma. While the hydrothermal Sr flux may be adjusted by reference to the relative rates of sea floor crustal generation, it is presently not possible to determine whether it is the mass flux or the isotopic composition of riverine Sr that was significantly lower before 40 Ma. Thus, the model calculations were performed for both cases, one in which the riverine isotopic composition was lowered until the model curve matched the observed curve at 40 Ma and a second in which the riverine mass flux was reduced until a match was obtained. To evaluate the sensitivity of these results to the parameters chosen for the Sr cycle, four different cycles were used (Table 7.1): the best-estimate obtained in Chapter 6, where both the axial and flank are lumped together and the flank term is held constant; the cycle of Palmer and Edmond (1989) representing the maximum estimated hydrothermal flux; and a cycle in which the Ganges and Brahmaputra rivers are deleted so as to obtain a minimum estimated hydrothermal flux. In the model calculations the diagenetic flux is assumed be constant over the past 40 Ma but with an isotopic composition equal to seawater 20 Ma before the interval of interest. Before 40 Ma it is difficult to determine the nature of the diagenetic flux due to the decreasing importance of pelagic carbonates and the increasing importance of shelf carbonates prior to this time (e.g., Wilkinson and Walker, 1989). Therefore, in order to focus on the ability of the changing hydrothermal flux to determine the shape of the Sr-isotope curve, the isotopic composition of the diagenetic flux is simply held constant prior to 40 Ma. For lack of better information, the isotopic composition of the groundwater flux term used in the best-estimate cycle is set equal to the diagenetic term.

Figure 7.9 presents the model results for the case in which the isotopic composition of the river water is adjusted to obtain a match at 40 Ma. The key features of this model that support the hypothesis of hydrothermal control on the 125-40 Ma portion of the Sr-

Table 7.1 Sr Cycles used in model calculations. Modern on left, Eocene on right.

Each Eocene cycle has the mass flux and isotopic composition of the riverine term independently calculated.

	Modern Seawater = 0.70918		Eocene (40 Ma) Seawater = 0.70773	
	Flux*	$^{87}Sr/^{86}Sr$	Flux*	$^{87}Sr/^{86}Sr$
Best-Estimate, Axial + Flank lumped together				
Hydrothermal	0.942	0.7033	0.971	0.7033
Diagenetic	0.34	0.7084	0.34	0.70783
Groundwater	1.1	0.7084	1.1	0.70783
Riverine	3.0	0.7114	1.133 (calc.)†	0.7114
			3.0	0.709166 (calc.)
Best-Estimate, Axial Only (Flank Sr flux assumed constant)				
Axial	0.692	0.7033	0.7135	0.7033
Flank	0.25	0.7033	0.25	0.7033
Diagenetic	0.34	0.7084	0.34	0.70783
Groundwater	1.1	0.7084	1.1	0.70783
Riverine	3.0	0.7114	1.124 (calc.)	0.7114
			3.0	0.709105 (calc.)
Palmer and Edmond (1989): Maximum Hydrothermal Sr Flux				
Hydrothermal	1.50	0.7033	1.55	0.7033
Diagenetic	0.34	0.7084	0.34	0.70783
Riverine	3.34	0.7119	1.638 (calc.)	0.7119
			3.34	0.709776 (calc.)
Ganges and Brahmaputra Rivers Excluded: Minimum Hydrothermal Sr Flux				
Hydrothermal	0.832	0.7033	0.858	0.7033
Diagenetic	0.34	0.7084	0.34	0.7084
Riverine	3.0	0.7109	1.188 (calc.)	0.7109
			3.0	0.708986 (calc.)

* 10^{10} mol/yr

† Calc = calculated values for riverine terms

isotope curve are the timing and relative magnitude of the calculated shifts. Hence at 125 Ma the sudden increase in oceanic crustal generation (see Fig. 7.5) produces a model curve that duplicates the decrease in the Aptian Sr-isotope curve. Following this both the model and observed Sr-isotope curves gradually increase through to about 85 Ma, when both

curves show an increase through to the Maastrichtian. There is a slight deviation near the Cretaceous/Tertiary boundary and through the Palaeocene, but the more radiogenic Sr-isotope curve may be a result of unusual events associated with that boundary (e.g., Martin and MacDougall, 1991). The curves again match through the Eocene until about 40 Ma when the Sr-isotope curve begins its rapid rise towards the present day. It is difficult to ascertain whether or not the deviation in the model and observed curves before 125 Ma is significant; it is entirely possible that the limited area of extant oceanic crust older than 125 Ma is an unrepresentative sample of the total oceanic crust extruded at that time.

Comparison of the four curves in Figure 7.9 indicates the importance of certain terms in the Sr cycle. The largest difference is between the two best-estimate curves and the two maximum/minimum hydrothermal flux curves. The reason for this deviation rests on the inclusion of the large groundwater flux in the best-estimate cycles. The effect of this term is to buffer the model curve against large changes with the result that the best-estimate curves happen to follow the observed curve quite closely. A second observation is that the larger the hydrothermal term, the more responsive the model curve to changes in the crustal generation rates. Thus the Palmer and Edmond (1989) cycle produces significantly larger negative shifts than the minimum hydrothermal flux cycle. While it is gratifying that the best-estimate axial only and axial plus flank curves generally bracket the observed Sr-isotope curve, not too much weight can be attached to this given the uncertainty in the parameters of the Sr cycles.

For comparison, Figure 7.10 presents the model calculations assuming that the flux of riverine Sr was significantly lower at 40 Ma as compared to today. The most immediate observation is that a lowered riverine mass flux allows significantly larger model variations to occur. Although obviously the timing of the model curve shifts remains the same, the magnitude of each shift is significantly larger than what is observed in the geological record. Taken together, the results in Figures 7.9 and 7.10 suggest that the problem is not

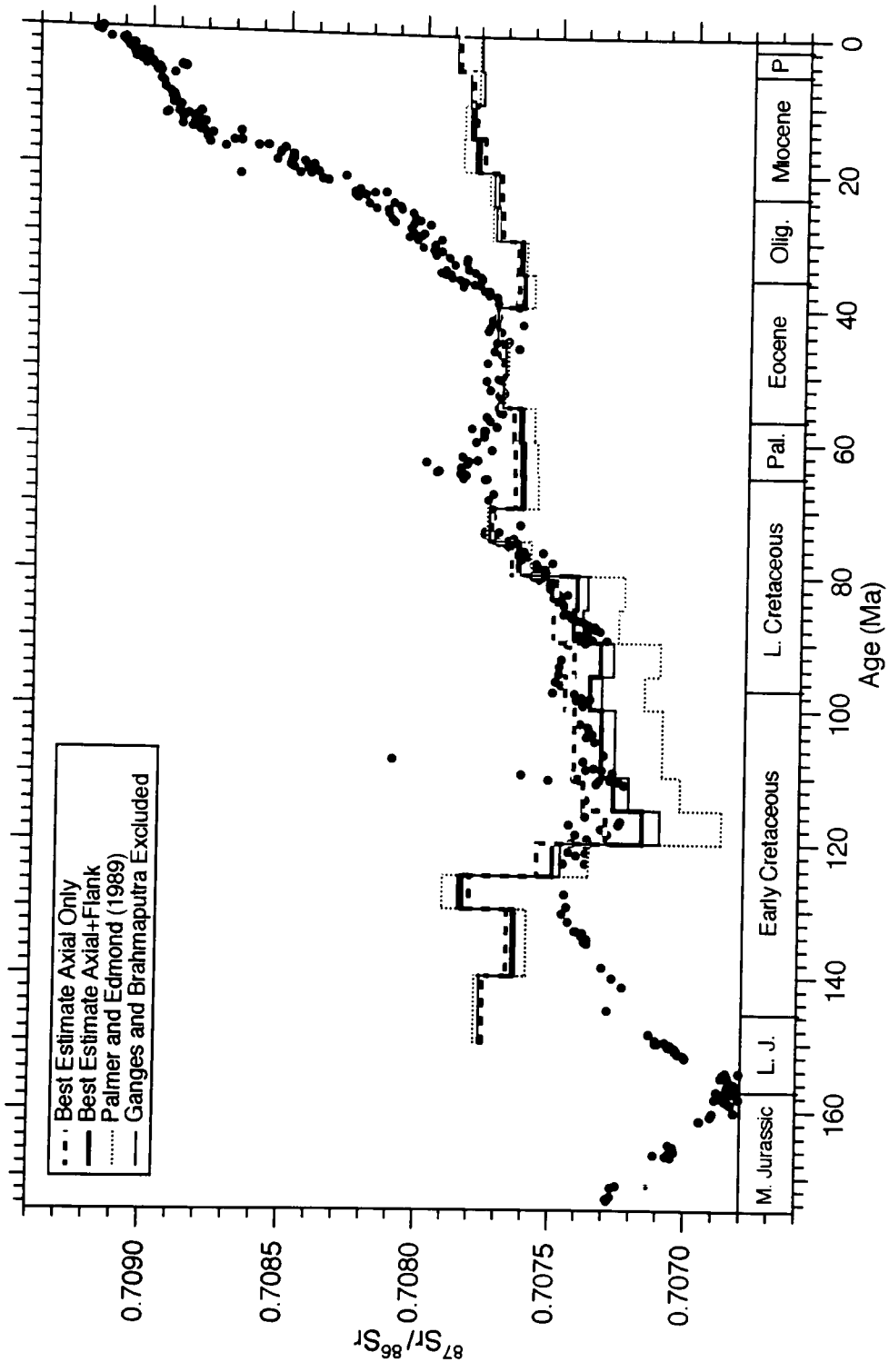

Figure 7.9: Comparison between the model and observed Sr-isotope curves over the past 150 Ma. The model curves are produced for each of 4 alternative Sr cycles (Table 7.1) by adjusting the riverine $^{87}Sr/^{86}Sr$ ratio such that the model and observed curves match at 40 Ma. Then the hydrothermal flux is varied according to the observed sea floor crustal generation rates.

how to stretch the calculations to make the hydrothermal flux strong enough to duplicate the observed data, but instead how to construct a Sr cycle that produces hydrothermally induced changes that are small enough to match the observed curve. Thus it seems a firm conclusion that the hydrothermal flux is perfectly capable of explaining the Sr-isotope curve from at least 125 Ma to 40 Ma. Without an adequate record of sea floor spreading rates prior to 125 Ma it is impossible to know whether the interval from at least 210 Ma to 125 Ma is similarly dominated by variations in the hydrothermal flux. It is at least plausible to interpret the dramatic negative excursion that occurred in the late Pliensbachian as being due to a burst of hydrothermal activity.

If the Sr-isotope curve was controlled by variations in hydrothermal activity over much of the Cretaceous and early Cenozoic, what caused one or both of the riverine terms to come to dominance over the past 40 Ma? Although it is difficult to say for certain, there are several factors that could have contributed to this transition. First, over the past 40 Ma the oceanic crustal generation rates indicate that the hydrothermal flux underwent only small variations and thus was unlikely to leave a strong mark on the Sr-isotope curve. Second, Palmer and Elderfield (1985) note that there is a general shift from the Cretaceous dominated by rifting and volcanism to the Cenozoic becoming increasingly dominated by continental collision and orogeny. More specifically, Rona and Richardson (1978) document the late Palaeocene through Eocene as a time characterised by a reorganisation of tectonic stresses from predominantly N-S spreading to predominantly E-W spreading. During the course of this reorganisation the total length of divergent plate boundaries remained the same (at 50,000 km), the length of subduction zone boundaries increased by 6000 km (to 55,500 km), and, most importantly, the length of convergent boundaries involving continent-continent or island arc-continent collisions increased from 2,500 km to 19,000 km (total convergent boundaries after reorganisation = 74,500 km). These results indicate that the pre-Eocene world may have been relatively flat, with a large proportion of

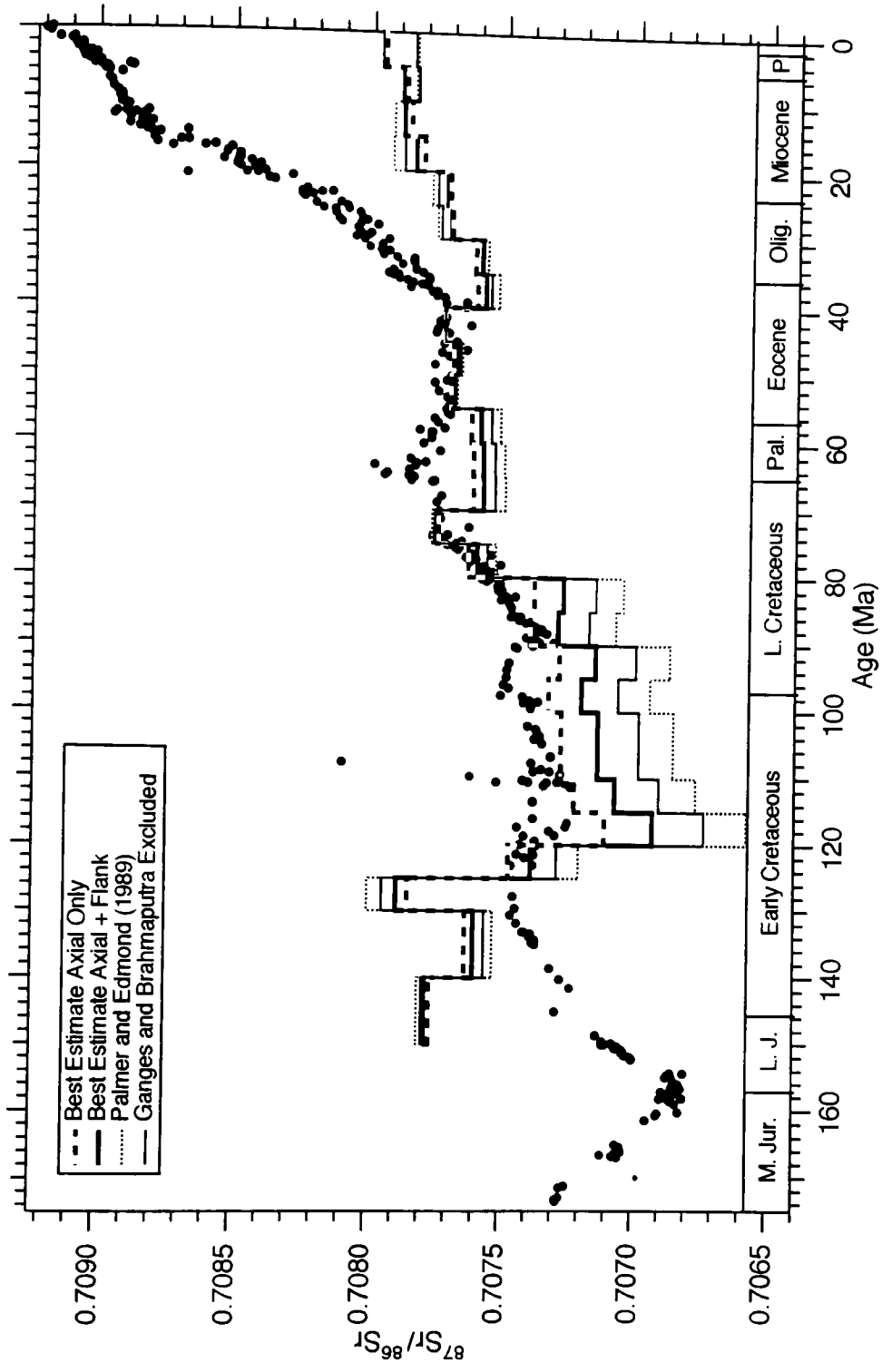

Figure 7.10: Comparison between the model and observed Sr-isotope curves over the past 150 Ma. The model curves are produced for each of 4 alternative Sr cycles (Table 7.1) by adjusting the riverine Sr flux such that the model and observed curves match at 40 Ma. Then the hydrothermal flux is varied according to the observed crustal generation rates.

the land area covered by sediments laid down during the Late Cretaceous sea-level highstand. With the onset of continent-continent or island arc-continent collisions, the post-Eocene world would have seen a large increase in orogenic activity. The resultant mountain belts would have allowed the exposure and rapid erosion of older granitic rocks that in turn would yield their radiogenic Sr to the world's rivers. Because this major tectonic reorganisation set the tectonic style of the rest of the Cenozoic (Rona and Richardson, 1978), it may have been responsible for the progressive exposure and increased erosion of older crustal rocks over the course of the Cenozoic and thus for the dramatic rise in the seawater Sr-isotope curve over the last 40 Ma. Seen in this light, the Sr-isotope curve highlights 40 Ma as an important moment marking a transition from one style of continental weathering and erosion to another.

7.4 Linking Sr-Isotopes, Flood Basalts, and Positive $\delta^{13}C$ Excursions

The first section of this chapter demonstrates that flood basalts show a strong correlation in time with positive carbon-isotope excursions when the Sr-isotope curve either shows a rapid downward shift or no change from its long-term trend. Carbon-isotope excursions that are not associated with flood basalts show a strong correlation with sudden upwards shifts in the Sr-isotope curve. The second section of this chapter demonstrates that between at least 125 Ma and 40 Ma the Sr-isotope curve may be adequately explained simply in terms of a changing hydrothermal Sr flux driven by changing global rates of sea floor crustal production. Thus, for example, it is reasonable to interpret the negative excursions in the Sr-isotope curve that occurred during the Pliensbachian/Toarcian, Aptian/Albian, and Cenomanian-Coniacian as being due to pulses in hydrothermal activity. It is also possible that the broad minimum in the Sr-isotope curve spanning the Callovian through Kimmeridgian represents the largest globally integrated hydrothermal flux of the past 250 Ma. In this, the third and final section, it remains to outline possible ways in which flood basalts and hydrothermal events are related and the ways in which

hydrothermal events may influence the carbon cycle so as to produce a short-term, global carbon-burial events.

7.4.1 Flood Basalts and Hydrothermalism

By making a correlation between flood basalts and carbon-isotope excursions I do not wish to imply that the eruption of a flood basalt initiates a series of processes that leads to a carbon-isotope excursion. Instead, it seems more likely that flood basalts are an important symptom of wider tectonic processes that are accompanied by significantly increased levels of oceanic hydrothermal activity. One frequent objection to the importance of hydrothermal events in the evolution of the Sr-isotope curve is the assumption that the volume of the hydrothermal fluid flux changes only slowly because crustal generation rates change only slowly through geological time (e.g., DePaolo and Ingram, 1985; Hodell *et al.*, 1989, 1990; Capo and DePaolo, 1990). Thus it would be difficult to generate the rapid downward shifts seen in the Pliensbachian/Toarcian and Cenomanian-Coniacian. However, a number of studies have recently demonstrated that large and rapid changes in the chemistry or volume of hydrothermal vents appear to accompany such tectonic disturbances as earthquakes, volcanic eruptions, ridge jumping, or changes in relative plate motions. At a small scale, Baker *et al.* (1987), Nojiri *et al.* (1989), and Baker and Lupton (1990) document transient "superplumes" that buoyantly rise more than 1 km above the sea floor (normal steady-state plumes generally rise only 200 - 400 m) and display greatly elevated ^{3}He/heat ratios in addition to the more usual indicators of hydrothermal activity (e.g., hydrothermal particulates and elevated Mn and CH_4 concentrations). These superplumes are thought to be the result of cataclysmic venting associated with a rapid access of seawater to fresh, hot rocks, caused either by tectonic stretching that allows a deeper penetration of seawater or by the eruption and/or shallow emplacement of new magma bodies.

At a more regional scale, Lyle *et al.* (1987) have documented a good correlation in time between the rates of hydrothermal Mn accumulation at various sites near the East Pacific Rise (DSDP Sites 597, 598) and major regional tectonic events. Instead of showing gradual changes of mass accumulation through time, the rate of hydrothermal Mn accumulation shows sudden, short accumulation spikes registering 5 to 24 times the background levels at certain horizons. The largest spike at 18 Ma correlates exactly with the jumping of the Mendoza Ridge to its current spreading site at the East Pacific Rise and a spike at 25 Ma correlates exactly with the initiation of the Cocos-Nazca Rift. Based on these and other correlations, Lyle *et al.* conclude that anomalously high rates of hydrothermal activity (ejection of hydrothermal particulates into the water column) correlate with large-scale tectonic reorganisation events on the sea floor. More generally, Olivarez and Owen (1989) have examined the tectonic history and timing of a number of well-dated hydrothermal ore deposits from a variety of tectonic settings. They find that in each case the vast bulk of each deposit was created during a major reorganisation of tectonic stresses caused, for example, by large-scale changes in relative plate motions or by the initiation of new island arc-continent or continent-continent collisions. In no case is there evidence for major ore formation during times of such normal "background" tectonic processes as subduction, arc volcanism, and ocean ridge spreading.

Both Lyle *et al.* (1987) and Olivarez and Owen (1989) conclude, in concurrence with Baker *et al.* (1987), Nojiri *et al.* (1989), and Baker and Lupton (1990), that the extreme increases in hydrothermal venting and chemical exchange may be the result of a changing stress field profoundly affecting the spacing and depth of fractures in the crust and providing opportunities for the accelerated emplacement of magma bodies. These conditions give fluids much freer access to fresh, hot rocks and this results in a marked increase in chemical exchange and hydrothermal fluid flow. Of particular relevance to this study is the fact that such sudden access to hot rocks may result in the formation of the

chemically distinctive brine component of the axial hydrothermal fluid flux (Von Damm, 1990). A sudden increase in the flux of the Sr-rich axial brine fluids would result in large increase in the flux of basaltic Sr to the oceans, and this could help explain the sudden downward shifts observed in the Pliensbachian/Toarcian, Aptian/Albian, and Cenomanian-Coniacian portions of the Sr-isotope curve.

The correlations and calculations presented so far suggest that the downward shifts in the Sr-isotope curve are the result of hydrothermal activity associated with the emplacement of flood basalts. Coffin and Eldholm (1991) and Coffin (1992) suggest that the "emplacement of large igneous provinces may be linked to 'instantaneous' plate tectonic events such as changes in rate and direction of plate motion". A relationship between flood basalts and large-scale changes in tectonic stresses provides a link between flood basalts and major pulses of hydrothermal activity because the results of the studies quoted above suggest that a major regional or global realignment of tectonic stresses will produce a rapid increase in the flux of mid-ocean ridge hydrothermal materials into the oceans and moreover that this pulse of activity will continue until the new stress fields are established. If this link between changing regional tectonic stresses, emplacement of flood basalts, and major hydrothermal events is valid, the Sr-isotope curve appears to indicate that the magnitude of hydrothermal pulses, and therefore of tectonic reorganisations, has decreased since the Aptian. The Aptian Sr-isotope curve shows a strong downward shift lasting for several million years and is accompanied by several major positive carbon-isotope excursions. There is a short but pronounced downward shift across the Cenomanian/Turonian boundary, accompanied by a single major black shale event. Since that time the Sr-isotope curve appears to show little or no response to the hydrothermal events inferred on the basis of flood basalt eruptions and carbon-isotope excursions.

7.4.2 Previous Models for Carbon-Burial Events

The models attempting to explain the occurrence of carbon-burial events fall into two broad groups (Arthur *et al.*, 1990). In the first, marine biological productivity remains roughly constant, but lowered O_2 concentrations in seawater lead to more organic carbon settling through the water column and getting incorporated into sediments. In the second, marine biological productivity greatly increases, requiring an influx of nutrients into the surface waters, and the enhanced rain of biological particles expands and intensifies the O_2-minimum zone and thus allows for enhanced burial and preservation of organic carbon. During the Cretaceous and probably the Jurassic the development of an expanded O_2-minimum zone would have been easier than in the modern day due to the fact that the warmer seawater of the Mesozoic would have held less dissolved oxygen than the colder oceans of today. The degree of oxygen depletion relative to today depends on the average temperature of the Mesozoic oceans, which in addition to depending on average surface temperatures, depends on the processes responsible for deep-water formation. If, instead of high-latitude deep-water formation, the Mesozoic deep ocean waters formed through intense evaporation in the hot tropical shelves and epicontinental seaways (Brass *et al.*, 1982), the oxygen content of deep waters could have been a mere 36 μmol/kg, as compared to approximately 160 μmol/kg in the modern oceans (Arthur *et al.*, 1990).

It is worth elaborating on several proposed carbon-burial models to provide a context for subsequent discussion. In the stagnant ocean model, the reduced temperature gradients in the notoriously warm and equable Cretaceous result in sluggish deep-water circulation. The longer a given packet of seawater remains out of contact with the atmosphere, the more the oxidation of the constant rain of organic particles acts to strip the water of its oxygen. If deep-ocean circulation was dominated by high-latitude cool water sources, the introduction of a burst of CO_2, perhaps through volcanic activity, could initiate a global warming that would warm the polar regions enough to significantly reduce or even

stop the rate of deep-water production. (Alternatively, gradually increasing CO_2 levels could simply pass a threshold beyond which polar temperatures become too warm to stimulate deep-water production.) As a result of this sluggish circulation the deeper waters would tend towards anoxia and a much larger proportion of the settling organic particles would become incorporated into the sedimentary record and in this way produce the observed positive $\delta^{13}C$ excursion. This event would be self-limiting due to the removal of critical nutrient elements into the sedimentary record, the reduced upwelling resulting from sluggish deep-water formation, and the fact that the enhanced removal of organic carbon into the sedimentary record would remove excess CO_2 from the atmosphere and thus bring the planet out of its greenhouse state. The cooling of the polar regions would then allow normal deep water formation to resume.

An interesting observation regarding carbon-burial events is that they generally seem to be associated with a rapid rise in sea level (e.g., Arthur *et al.*, 1987; Hallam, 1987; Jenkyns, 1988; Weissert and Lini, 1991; Wignall, 1991). Accordingly, the model of Arthur *et al.* (1987) depends on the rapid transgression/regression inferred for the Cenomanian/Turonian boundary to explain the genesis of the Cenomanian/Turonian carbon-burial event. This model contrasts with the previous model in that it is based on the generation of deep-ocean water masses in tropical shelf and epicontinental seas (the Warm, Saline Bottom Waters (WSBW) of Brass *et al.*, 1982). In this second model the normal conditions prevailing in the late Cretaceous are punctuated by a rapid sea level rise at the Cenomanian/Turonian boundary. This transgression greatly increases the area of tropical shelf seas and results in a greatly increased flux of WSBW into the deep oceans. This increased flux spurs more rapid rates of upwelling and nutrient cycling and hence results in a burst of biological productivity. The corresponding increase in the rain of organic particles to the sea floor results in a greatly expanded and intensified mid-water O_2-minimum, and this allows for the accelerated burial of organic carbon. The sea-level

highstand also allows the deposition of black shales in the shelf and epicontinental seas. By the mid-Turonian a rapid regression has reduced the area of highly evaporative tropical shallow seas, the rate of WSBW formation has returned to normal with a consequent reduction in the upwelling nutrient flux and biological productivity, and the system has returned to normal. The cause of the sea level changes is not specified, but it is possible that it is related to tectonic events in the ocean basins.

A third model is proposed by Weissert and Lini (1991). They propose that the trigger of the Aptian carbon-burial events was widespread Aptian volcanism and accelerated oceanic crustal production. This volcanic activity released enough CO_2 to trigger a shift to a new warmer greenhouse climatic state. The increased CO_2 content of the atmosphere combined with warmer global temperatures increased the rate of chemical weathering, which consumes CO_2, and the volume of global runoff. The resultant increased flux of nutrient elements to the oceans stimulated and sustained biological productivity. The burial and preservation of this rain of organic carbon was facilitated by relatively sluggish deep water circulation, low concentrations of dissolved oxygen in the warm Aptian waters, and increased sedimentation rates associated with the increased weathering of the continents. The increased burial rates of organic carbon removed the excess volcanic CO_2 from the atmosphere and thus brought the planet back to its pre-greenhouse state. The sea-level highstands associated with the accelerated carbon-burial events aided carbon-burial by providing a larger area for deposition, but are not genetically related to the initiation of the event.

In the first and third models, increased volcanic activity is important in that it increases the flux of CO_2 to the atmosphere, warms the planet, and thus initiates a series of events that produces a carbon-isotope excursion. In the second model sea-level change is seen as the driving variable in that it increases the rate of WSBW formation by increasing the area of shallow tropical seas. The rate of WSBW formation could also be increased

given a constant sea level if volcanic CO_2 warmed the planet sufficiently to increase the rates of seawater evaporation in the tropics. Thus, for all three models there is a possible link between volcanism, which could be expressed as increased hydrothermal activity along the mid-ocean ridges, and positive carbon-isotope excursions. The question is, are the observations regarding the relationships between the seawater Sr-isotope curve, positive $\delta^{13}C$ excursions, and flood basalt eruptions consistent with one or more of these carbon-burial models?

7.4.3 Constraints Imposed by This Study

The nature of the constraints imposed by the correlations outlined in section 7.2 depends on how these correlations are viewed. On the one hand, the strong correlation between positive $\delta^{13}C$ excursions and flood basalts suggests that bursts of CO_2 from continental volcanic and marine hydrothermal sources could have formed the driving force leading to accelerated organic carbon burial rates, as outlined in the 3 models described above. The carbon excursions of the early Toarcian, late Albian, and Coniacian are not associated with known flood basalt episodes but may nevertheless have been the result of global volcanic events that were expressed on land but not under the sea. Such a view stresses the importance of volcanic CO_2 emissions in the development of earth history. On the other hand, a different picture emerges when the Sr data are fully incorporated into the picture. Because there is a strong suggestion that the variations in the Jurassic and Cretaceous portions of the Sr-isotope curve may be determined largely by variations in the hydrothermal input, the downward excursions in the Pliensbachian/Toarcian (Fig. 7.3), Aptian/Albian, and Cenomanian-Coniacian (Fig. 7.6) portions of the Sr-isotope curve may be interpreted as recording the initiation, duration, and termination of major hydrothermal pulses. For these major hydrothermal events, a carbon-isotope excursion occurs at the outset of hydrothermal activity, normal carbon-burial rates occur throughout the rest of the hydrothermal event, and a second carbon-burial event occurs at the end of the inferred

hydrothermal pulse.

It is the presence of the second carbon event that presents difficulties for standard carbon-burial models. For example, although the initial pulse of volcanic CO_2 emissions could produce the first event, what would cause a CO_2 pulse at the termination of the hydrothermal event? Although it is possible that a major tectonic event on the sea floor could cause a sudden rise in sea level that may in turn produce a carbon-burial event, it is difficult to see how such a mechanism would produce a sea-level change that would rapidly rise and fall across the Cenomanian/Turonian boundary (Arthur *et al.*, 1987). Moreover, what would produce the sea-level change required to produce the second carbon-isotope excursion at the end of a hydrothermal event? Because both the volcanic CO_2 and sea-level mechanisms appear to be inconsistent with carbon-isotope excursions occurring at the beginning and end of major hydrothermal events, it is necessary to search for an alternative explanation for the genesis of carbon-burial events.

The most obvious impact of the hydrothermal springs is to add excess K, Ca, and Li to seawater while at the same time removing Mg and SO_4^{2-} (e.g., Von Damm, 1990). Of these elements, Ca is probably the most significant for this study because the precipitation or dissolution of $CaCO_3$ minerals can have a major impact on the global CO_2 budget. According to the reaction

$$Ca^{2+} + 2HCO_3^- \leftrightarrow CaCO_3 + CO_2 + H_2O,$$

the injection of volcanic CO_2 into the ocean-atmosphere system results in the dissolution of $CaCO_3$ minerals. The huge reservoir of carbonate minerals available for dissolution relative to the total mass in the atmosphere means that this carbonate buffer has considerable ability to absorb excess volcanic CO_2 as it it produced. However, the injection of hydrothermal Ca into the oceans should have the opposite effect, causing the precipitation of $CaCO_3$ and releasing more CO_2 into the ocean-atmosphere system (e.g., Owen and Rea, 1985). Thus the net flux of CO_2 into the ocean-atmosphere system depends on the magnitude of the

volcanic CO_2 and hydrothermal Ca fluxes and the ability of the latter to prevent the oceanic carbonate buffer from absorbing the excess volcanic CO_2. In this way the sustained Ca flux throughout a hydrothermal event may help maintain elevated atmospheric CO_2 concentrations for the duration of the event.

A less widely recognised aspect of mid-ocean ridge hydrothermal systems concerns the effects of the hydrothermal particulates on seawater chemistry. Hydrothermal vents inject large quantities of reduced elements, largely H_2S, Mn^{2+}, and Fe^{2+}, into the water column. While much of the H_2S precipitates as metal sulphides immediately after leaving the vent system, significant quantities of Mn^{2+} and Fe^{2+} reach some 200 - 400 m above the seafloor during normal venting and some 1000 m during major hydrothermal events. The oxidation of these elements consumes seawater oxygen and produces detectible oxygen depletions in the hydrothermal plume (Charlou *et al.*, 1991). The precipitated Fe and Mn oxyhydroxides exert an additional influence on seawater chemistry through their ability to scavenge a wide variety of elements. Although this scavenging mechanism removes a large percentage of many trace metals exiting the vent orifices (German *et al.*, 1991), one of the more significant scavenging reactions for this study involves the removal of phosphorous. Feeley *et al.* (1990) document both a direct correlation of particulate P/Fe ratios and a corresponding depletion of dissolved P in the seawater surrounding hydrothermal vents and calculate that up to 12% of the riverine P input is removed on Fe oxides. During the major hydrothermal events postulated in this study, the greatly increased hydrothermal output of fluids could have injected dissolved Mn^{2+} and Fe^{2+} 1000 m or more into the water column, maximising the consumption of dissolved oxygen and the scavenging of dissolved P. As a result the combined effects of major hydrothermal events may be the depletion deep waters in both oxygen and the critical nutrient element P.

It is difficult to quantify accurately the possible magnitude of these depletions due to uncertainties in how much Fe^{2+}, Mn^{2+} and H_2S are introduced into the oceans via

hydrothermal springs, what proportion of these fluxes are permanently precipitated as sulphides and thus not oxidised, and what oxygen concentrations existed at various depths in the Jurassic and Cretaceous palaeo-oceans. Assuming that roughly $0.1 * 10^{10}$ moles of Fe^{2+}, Mn^{2+} and H_2S are oxidised each year, that Cretaceous deep waters had dissolved O_2 concentrations averaging between 160 μmol/kg (modern deep water) and 36 μmol/kg (WSBW formed at tropics; Arthur *et al.*, 1987) and that the oceans contain roughly $1.4 * 10^{21}$ kg water, then in the normal course of 500,000 years (an approximate duration of a carbon burial event) roughly $0.5 * 10^{15}$ mol O_2 is consumed out of a total of between $0.5 * 10^{17}$ and $2.2 * 10^{17}$ moles O_2. Thus, if major hydrothermal events result in the ejection and oxidation of between one and two orders of magnitude more Fe^{2+}, Mn^{2+} and H_2S, significant depletions of dissolved oxygen may occur at certain levels in the oceans, particularly if circulation patterns are such that deeper water masses remain out of contact with the atmosphere for significant periods of time.

The current flux of Fe oxyhydroxides in hydrothermal plumes consumes up to 12% of the riverine flux each year (Feely *et al.*, 1990). An increase of one to two orders of magnitude in the output of hydrothermal Fe oxyhydroxides is unlikely to produce a similarly large increase in the removal of P because the rate of P removal by Fe-oxide scavenging decreases in direct proportion to the concentration of dissolved P in the water column (Feely *et al.*, 1991). Thus, while it is possible that increased hydrothermal activity may result in relatively P-poor deep waters, it is unclear how efficient this process would be until more data are available regarding Fe-oxide scavenging of P in waters with lower P concentrations.

There are thus three possible effects of increased hydrothermal activity of relevance to the carbon cycle: increased atmospheric CO_2 concentrations, O_2-depleted deep waters, and P-depleted deep waters. Each of these effects is expected to persist for the duration of the hydrothermal event. Although there are several possible ways that a sudden injection of

CO_2 into the atmosphere could trigger a carbon-burial event (see the three carbon-burial models above), it is more difficult to envision how ending the CO_2 flux at the end of a hydrothermal event will produce the second carbon-burial event of the pair. It seems likely that when the enhanced CO_2 flux ends, the ocean-atmosphere system will gradually restore itself to the equilibrium CO_2 concentrations that existed before the hydrothermal event. One way to produce a more rapid change is to assume that once the hydrothermal flux of Ca drops back to normal levels, the carbonate buffering equation will be tipped towards carbonate dissolution and CO_2 consumption, thus leading to a relatively rapid drawdown of atmospheric CO_2.

Such a mechanism could operate under the "stagnant ocean" model. Under this model, the hydrothermal event causes a CO_2-induced global warming that heats the poles to the point where polar deep-water production and deep-water circulation slow down. The initial carbon-burial event occurs when these slowly circulating waters become oxygen depleted. The burial of the organic carbon also removes a significant proportion of the nutrient elements from the ocean, leading to a new equilibrium between riverine input of nutrient elements and organic productivity such that carbon-burial rates return to normal. This accounts for the lack of carbon-rich sediments throughout the hydrothermal event. At the end of the hydrothermal event adsorption of CO_2 by the oceanic carbonate buffer cools the planet and speeds up polar deep-water production. Although O_2-depleted, the deep waters are likely to be nutrient-rich and thus the renewal of strong deep-water circulation and upwelling is able to stimulate enhanced biological productivity and thus produce the second carbon-burial event. This second event further draws down CO_2 levels in the ocean-atmosphere system, aiding the recovery to normal climate, rates of deep-water circulation, upwelling, biological productivity, and carbon burial.

A second model relies on the other possible effects of a major hydrothermal event: a reduction of oxygen and P concentrations in deep ocean waters. At the initiation of a

hydrothermal event the increased flux of reduced material into the water column would begin to remove oxygen and phosphorous from the deep water masses. If the reduction in oxygen content of the bottom waters occurs more quickly than the reduction in P, biological productivity could carry on as normal, perhaps stimulated by higher atmospheric CO_2 levels and raised sea-level, while the low-oxygen deep waters would facilitate the expansion and intensification of the O_2-minimum zone. This expanded O_2-minimum would in turn allow the enhanced preservation and burial of organic carbon as required for the production of the positive $\delta^{13}C$ spike. The accelerated burial of organic carbon is self-limiting, both because P continues to be removed by hydrothermal particulates but mainly because the accelerated burial of organic matter also buries essential nutrient elements. Thus, even though organic matter is more likely to be preserved in the low-oxygen deep waters, less organic matter is settling through the water column and the relative rates of production and oxidation in the water column can once again balance to result in carbon burial rates that are similar to before the hydrothermal event. This would account for the fact that the whole period of hydrothermal activity (e.g. during the Pliensbachian/Toarcian, Aptian/Albian, and Cenomanian-Coniacian) is not characterised by unusually organic-rich sediments. If at the end of a hydrothermal event nutrient levels recover faster than dissolved O_2 concentrations, due to continued riverine input and biological cycling to deeper waters, the renewed biological productivity could result in a second episode of accelerated carbon burial in the still low-oxygen waters. This would produce the carbon spike observed at the end of each negative Sr-isotope excursion. The weaker, single-pulse hydrothermal events that seem to be indicated by the correlation of flood basalts and carbon events and the lack of significant Sr-isotope excursions may have caused carbon-burial events simply by temporarily lowering deep-water oxygen levels.

7.5 Summary and Conclusions

This chapter demonstrates that there is often an intriguing and well-constrained relationship between sudden shifts in the Sr-isotope curve, the occurrence of positive $\delta^{13}C$ excursions representing accelerated carbon-burial events, and the eruption of flood basalts. Each major downward shift in the Sr-isotope curve during the Jurassic and Cretaceous is accompanied by a positive $\delta^{13}C$ excursion and the eruption of a flood basalt. During the Cenozoic the Sr-isotope curve shows no strong downward excursions, but nevertheless the relationship between $\delta^{13}C$ excursions and the eruption of flood basalts still stands. Finally, there is a correlation between sudden upwards shifts in the Sr-isotope curve and positive $\delta^{13}C$ excursions, but not with flood basalts. Although the Sr-isotope curve is frequently interpreted exclusively in terms of the rate of continental weathering (changing the flux of riverine Sr), in this study it is proposed that variations in the hydrothermal flux provide a satisfactory explanation of the evolution of the Sr-isotope curve between 125 and 40 Ma. This, in combination with the occurrence of major flood basalts at the initiation of downward shifts in the Sr-isotope curve, suggests that the negative shifts in the Sr-isotope curve are the result of major hydrothermal events.

These correlations are of considerable importance to models attempting to explain the genesis of carbon-burial events. Of particular importance is the suggestion that the carbon-isotope excursions at the beginning and end of major downward shifts in the Sr-isotope curve are paired (i.e., the Pliensbachian/Toarcian, Aptian/Albian, and Cenomanian-Coniacian events) and genetically related to the initiation and termination of major pulses of hydrothermal activity. If each carbon-burial event was triggered independently then the correlations presented in this chapter could support a genetic connection between mantle CO_2 outgassing and carbon-burial events. If, however, these carbon-burial events bracketing downward shifts in the Sr-isotope curve are genetically related to the beginning and end of major pulses in hydrothermal activity, then current models appear to be inadequate in explaining the genesis of these events and new models will have to be developed that focus on the transitions

between normal and hydrothermal states. The two preliminary, qualitative models presented in this study are intended to illustrate the need for new thinking in the light of paired carbon-isotope excursions.

The possible pairing of carbon-burial events also has implications for future field work. It is possible that sediments hosting a $\delta^{13}C$ excursion at the initiation of a hydrothermal event may be geochemically distinctive compared to the sediments deposited at the end of such an event. For example, Brumsack and Thurow (1986) find that the trace metal chemistry of black shales from the Cenomanian/Turonian boundary (initiation of hydrothermal event) are most compatible with slow sediment accumulation rates. By contrast, the trace metal chemistry of lower Toarcian black shales (termination of hydrothermal event) are compatible with a elevated levels of biological productivity. The $\partial^{13}C$ signal of organic matter found at the Cenomanian/Turonian boundary also contrasts with that of the lower Toarcian. Arthur *et al.* (1988) find that the Cenomanian/Turonian $\partial^{13}C_{org}$ positive excursion is of greater magnitude that the corresponding $\partial^{13}C$ preserved in carbonate. This is interpreted to be a result of a significantly increased drawdown of CO_2 during the carbon-burial event. The $\partial^{13}C$ of Toarcian organic matter, by contrast, shows a pronounced negative excursion during the carbon burial event. It would be helpful for future work to concentrate on the sedimentary geochemistry of a signal pair of excursions, tracing the evolution of a given parameter from before the first event all of the way through the second event. For example, if the contrast between $\partial^{13}C_{org}$ and $\partial^{13}C_{calcite}$ is related to the partial pressure of CO_2 in seawater (e.g., Arthur *et al.*, 1988), it may be possible to see if a low partial pressure is indicated before and after a hydrothermal event relative to a higher partial pressure indicated during the hydrothermal event. Comparisons as these may, in the context of the Sr-isotope data, yield significant insight as to the processes responsible for organic carbon burial and yield key constraints leading to a significantly improved understanding of the geochemical interactions between the lithosphere and biosphere.

References

Aharon, P., Socki, R.A. and Chan, L., 1987, Dolomitization of atolls by seawater convection flow: test of a hypothesis at Nine, South Pacific, **Journal of Geology**, 95: 187-203.

Al-Aasm, I.S. and Veizer, J., 1982, Chemical stabilization of low-Mg calcite: an example of brachiopods, **Journal of Sedimentary Petrology**, 54: 1101-1109.

Anderson, R.N. and Hobart, M.A., 1976, The relation between heat flow, sediment thickness, and age in the eastern Pacific, **Journal of Geophysical Research**, 81: 2968-2989.

Anderson, R.N., Langseth, M.G. and Sclater, J.G., 1977, The mechanisms of heat transfer through the floor of the Indian Ocean, **Journal of Geophysical Research**, 82: 3391-3409.

Anderson, T.F. and Arthur, M.A., 1983, Stable isotopes of oxygen and carbon and their application to sedimentologic and paleoenvironmental problems, *in* Arthur, M.A. (organizer), **Stable Isotopes in Sedimentary Geology**, SEPM Short Course No. 10, 1-1 -- 1-151.

Andrews, J.E., Hamilton, P.J. and Fallick, A.E., 1987, The geochemistry of early diagenetic dolostones from a low-salinity Jurassic Lagoon, **Journal of the Geological Society, London**, 144: 687: 698.

Arkell, W.J., 1933, **The Jurassic System in Great Britain**, Clarendon Press, Oxford, 681pp.

Arkell, W.J., 1939, The ammonite succession at the Woodham Brick Company's pit, Akeman Street Station, Buckinghamshire, and its bearing on the classification of the Oxford Clay, **Quarterly Journal of the Geological Society of London**, 95: 135-222.

Arkell, W.J., 1956, **Jurassic Geology of the World**, Oliver and Boyd, Ltd., Edinburgh, 806p.

Arthur, M.A., Dean, W.E. and Schlanger, S.O., 1985, Variations in the global carbon cycle during the Cretaceous related to climate, volcanism, and changes in atmospheric CO_2, *in* Sundquist, E.T. and Broecker, W.S. (eds.), **The Carbon Cycle and Atmospheric CO_2: Natural Variations Archean to Present**, American Geophysical Union Geophysical Monograph 32: Washington, D.C., 504-530.

Arthur, M.A., Schlanger, S.O., and Jenkyns, H.C., 1987, The Cenomanian-Turonian Oceanic Anoxic Event, II. Palaeoceanographic controls on organic-matter production and preservation, *in* Brooks, J. and Fleet, A.J. (eds.), **Marine Petroleum Source Rocks**, Geological Society of London Special Publication 26: 401-420.

Arthur, M.A., Dean, W.E. and Pratt, L.M., 1988, Geochemical and climatic effects of increased marine organic carbon burial at the Cenomanian/Turonian boundary, **Nature**, 335: 714-717.

Arthur, M.A., Jenkyns, H.C., Brumsack, H.J., and Schlanger, S.O., 1990, Stratigraphy, geochemistry, and paleoceanography of organic carbon-rich Cretaceous sequences, *in* Ginsburg, R.N. and Beaudoin, B. (eds.), **Cretaceous Resources, Events and Rhythms**, 75-119.

Astin, T.R. and Scotchman, I.C., 1988, The diagenetic history of some septarian concretions from the Kimmeridge Clay, **Sedimentology**, 35: 349-368.

Baker, E.T., Massoth, G.J. and Feely, R.A., 1987, Cataclysmic venting on the Juan de Fuca Ridge, **Nature**, 329: 149-151.

Baker, E.T. and Lupton, J.E., 1990, Changes in submarine hydrothermal ^{3}He/heat ratios as an indicator of magmatic/tectonic activity, **Nature**, 346: 556-558.

Baksi, A.K., 1988, Estimation of lava extrusion and magma production rates for two flood basalt provinces, **Journal of Geophysical Research**, 93: 11809-11818.

Baksi, A.K., 1990, Timing and duration of Mesozoic-Tertiary flood-basalt volcanism, **EOS**, 71: 1836-1840.

Banner, J.L., Hanson, G.N. and Meyers, W.J., 1988, Determination of initial Sr isotopic composition of dolostones from the Burlington-Keokuk Formations (Mississippian): constraints from cathodoluminescence, glauconite paragenesis, and analytical methods, **Journal of Sedimentary Petrology**, 58: 673-687.

Bate, R.H., 1959, The Yons Nab Beds of the Middle Jurassic of the Yorkshire coast, **Proceedings of the Yorkshire Geological Society**, 32: 153-164.

Baumgartner, A. and Reichel, E., 1975, **The World Water Balance**, Munich and Vienna: R. Olenburg, 179p.

Berger, W.H. and Vincent, E., 1986, Deep-sea carbonates: Reading the carbon-isotope signal, **Geologische Rundschau**, 75: 249-269.

Berggren, W.A., Kent, D.V., Flynn, J.J. and Van Couvering, J.A., 1985, Cenozoic geochronology, **Geological Society of America Bulletin**, 96: 1407-1418.

Bernat, M., Church, T. and Allègre, C.J., 1972, Barium and strontium concentrations in Pacific and Mediterranean seawater profiles by direct isotope dilution mass spectrometry, **Earth and Planetary Science Letters**, 16: 75-80.

Berndt, M.E., Seyfried, W.E., Jr. and Beck, J.W., 1988, Hydrothermal alteration processes at mid-ocean ridges: experimental and theoretical constraints from Ca and Sr exchange reactions and Sr isotopic ratios, **Journal of Geophysical Research**, 93: 4573-4583.

Berndt, M.E., Seyfried, W.E., Jr. and Janecky, D.R., 1989, Plagioclase and epidote buffering of cation ratios in mid-ocean ridge hydrothermal fluids: experimental results in and near the supercritical region, **Geochimica et Cosmochimica Acta**, 53: 2283-2300.

Berndt, M.E. and Seyfried, W.E., Jr., 1990, Boron, bromine, and other trace elements as clues to the fate of chlorine in mid-ocean ridge vent fluids, **Geochimica et Cosmochimica Acta**, 54: 2235-2245.

Berner, E.K. and Berner, R.A., 1987, **The Global Water Cycle**, Prentice-Hall, Inc., Englewood Cliffs, New Jersey, 397p.

Berner, R.A., 1981a, Authigenic mineral formation resulting from organic matter decomposition in modern sediments, **Fortschritte der Mineralogie**, 59: 117-135.

Berner, R.A., 1981b, A new geochemical classification of sedimentary environments, **Journal of Sedimentary Petrology**, 51: 359-365.

Berner, R.A., 1984, Sedimentary pyrite formation: an update, **Geochimica et Cosmochimica Acta**, 48: 605-615.

Berner, R.A., 1987, Models for carbon and sulfur cycles and atmospheric oxygen: application to Paleozoic geology, **American Journal of Science**, 287: 177-196.

Berner, R.A., Lasaga, A.C. and Garrels, R.M., 1983, The carbonate-silicate geochemical cycle and its effect on atmospheric carbon dioxide over the past 100 million years, **American Journal of Science**, 283: 641-683.

Berner, R.A. and Rye, D.M., 1992, Calculations of the Phanerozoic strontium isotope record of the oceans from a carbon cycle model, **American Journal of Science**, 292: 136-148.

Birkelund, T., Hancock, J.M., Hart, M.B., Rawson, P.F., Remane, J., Robaszynski, F., Schmid, F. and Surlyk, F., 1984, Cretaceous stage boundaries--proposals, **Bulletin of the Geological Society of Denmark, Copenhagen**, 33: 3-20.

Bischoff, J.L. and Rosenbauer, R.J., 1985, An empirical equation of state for hydrothermal seawater (3.2 percent NaCl), **American Journal of Science**, 285: 725-763.

Blake, J.F., 1875, On the Kimmeridge clay of England, **Quarterly Journal of the Geological Society of London**, 31: 196-237.

Bottrell, S. and Raiswell, R., 1989, Primary versus diagenetic origin of Blue Lias rhythms (Dorset, UK): evidence from sulphur geochemistry, **Terra Nova**, 1: 451-456.

Bowers, T.S., Campbell, A.C., Measures, C.I., Spivack, A.J., Khadem, M. and Edmund, J.M., 1988, Chemical controls on the composition of vent fields at 13° N - 11° N and 21° N, East Pacific Rise, **Journal of Geophysical Research**, 93: 4576-4522.

Bowers, T.S. and Taylor, H.P., 1985, An integrated chemical and stable isotope model of the origin of mid-ocean ridge hot spring systems, **Journal of Geophysical Research**, 90: 12583-12606.

Bowers, T.S., Von Damm, K.L. and Edmond, J.M., 1985, Chemical evolution of mid-ocean ridge hot springs, **Geochimica et Cosmochimica Acta**, 49: 2239-2252.

Bralower, T.J., 1988, Calcareous nannofossil biostratigraphy and assemblages of the Cenomanian/Turonian boundary interval: Implications for the origin and timing of oceanic anoxia, **Paleoceanography**, 3: 275-316.

Brand, U., 1986, Paleoenvironmental analysis of Middle Jurassic (Callovian) ammonoids from Poland: trace elements and stable isotopes, **Journal of Paleontology**, 60: 293-301.

Brand, U., 1987, Depositional analysis of the Breathitt Formation's marine horizons, Kentucky, U.S.A.: Trace elements and stable isotopes, **Chemical Geology (Isotope Geosciences Section)**, 65: 117-136.

Brand, U., 1989, Aragonite-calcite transformation based on Pennsylvanian molluscs, **Geological Society of America Bulletin**, 101: 377-390.

Brand, U., 1991, Strontium isotope diagenesis of biogenic aragonite and low-Mg calcite, **Geochimica et Cosmochimica Acta**, 55: 505-513.

Brass, G.W. and Turekian, K.K., 1972, Strontium distributions in seawater profiles from the Geosecs I (Pacific) and Geosecs II (Atlantic) test stations, **Earth and Planetary Science Letters**, 16: 117-121.

Brass, G.W. and Turekian, K.K., 1974, Strontium distribution in Geosecs oceanic profiles, **Earth and Planetary Science Letters**, 23: 141-148.

Brass, G.W., Saltzman, E., Sloan, J.L, Southam, J.R., Hay, W.W., Holser, W.T. and Peterson, W.H., 1982, Ocean circulation, plate tectonics, and climate, *in*, Berger, W.H. and Crowell, J.C. (panel co-chairmen), **Climate in Earth History**, Studies in Geophysics Series, National Acadamy Press, Washington, D.C., 83-89.

Broecker, W.S., 1963, Radioisotopes and large-scale oceanic mixing, *in* Hill, M.N. (ed.), **The Sea**, Vol. 2, Chapt. 4, Interscience, New York.

Broecker, W.S. and Peng, T.-H., 1982, **Tracers in the Sea**, Palisades, New York, Eldigio Press, 690 p.

Brookfield, M.E., 1978, The lithostratigraphy of the Upper Oxfordian and Lower Kimmeridgian beds of south Dorset, **Proceedings of the Geologists' Association**, 89: 1-32.

Brookins, D.G., Chaudhuri, S. and Dowling, P.L., 1969, The isotopic composition of strontium in Permian limestones, eastern Kansas, **Chemical Geology**, 4: 439-444.

Brookins, D.G., 1988, Seawater $^{87}Sr/^{86}Sr$ for the Late Permian Delaware Basin Evaporites (New Mexico, U.S.A.), **Chemical Geology**, 69: 209-214.

Buckman, S.S., 1893, The Bajocian of the Sherborne district: its relation to subjacent and superjacent strata, **Quarterly Journal of the Geological Society of London**, 49: 479-522.

Buckman, S.S. and Wilson, E., 1896, Dundry Hill: its upper portion, or the beds marked as Inferior Oolite (g^5) in the maps of the Geological Survey, **Quarterly Journal of the Geological Society of London**, 52: 669-720.

Burke, W.H., Denison, R.E., Hetherington, E.A., Koepnick, R.B., Nelson, H.F., Otto, J.B., 1982, Variation of seawater $^{87}Sr/^{86}Sr$ throughout Phanerozoic time, **Geology**, 10: 516-519.

Burtner, R.L., 1987, Origin and evolution of Weber and Tensleep formation waters in the Greater Green River and Uinta-Piceance basins, northern Rocky Mountain area, U.S.A., **Chemical Geology (Isotope Geosciences Section)**, 65: 255-282.

Butterfield, D.A., Massoth, G.J., McDuff, R.E., Lupton, J.E. and Lilley, M.D., 1990, Geochemistry of hydrothermal fluids from Axial Seamount Hydrothermal Emissions Study vent field, Juan de Fuca Ridge: Subseafloor boiling and subsequent fluid-rock interaction, **Journal of Geophysical Research**, 95: 12895-12921.

Callomon, J.H., 1955, The ammonite succession in the Oxford Clay and Kellaways Beds at Kidlington, Oxfordshire, and the zones of the Callovian Stage, **Philosophical Transactions of the Royal Society of London**, B239: 215-264.

Callomon, J.H., 1968, The Kellaways Beds and the Oxford Clays, *in* Sylvester-Bradley, P.C. and Ford, T.D. (eds.), **The Geology of the East Midlands**, University Press, Leicester, 264-290.

Callomon, J.H., 1985, Biostratigraphy, chronostratigraphy and all that--again!, *in* Michelson, O. and Zeiss, A. (eds.), International Symposium on Jurassic Stratigraphy, Erlangen, 1984, **Geological Survey of Denmark, Copenhagen**, 3: 611-624.

Callomon, J.H. and Chandler, R.B., 1990, A review of the ammonite horizons of the Aalenian-Lower Bajocian Stages in the Middle Jurassic of southern England, **Memorie Descrittive della Carta Geologica D'Italia**, 15: 85-112.

Callomon, J.H., Dietl, G., and Page, K.N., 1988, On the ammonite faunal horizons and standard zonations of the Lower Callovian Stage in Europe, **Second International Symposium on Jurassic Stratigraphy, Lisbon, 1987**, 359-376.

Campbell, A.C., Bowers, T.S., Measures, C.I., Falkner, K.K., Khadem, M. and Edmond, J.M., 1988a, A time series of vent fluid compositions from 21°N, East Pacific Rise (1979, 1981, 1985), and the Guaymas Basin, Gulf of California (1982, 1985), **Journal of Geophysical Research**, 93: 4537-4549.

Campbell, A.C., Palmer, M.R., Klinkhammer, G.P., Bowers, T.S., Edmond, J.M., Lawrence, J.R., Casey, J.F., Thompson, G., Humphris, S., Rona, P. and Karson, J.A., 1988b, Chemistry of hot springs on the Mid-Atlantic Ridge, **Nature**, 335: 514-519.

Campbell, A.C. and Edmond, J.M., 1989, Halide systematics of submarine hydrothermal vents, **Nature**, 342: 168-170.

Campos, H.S. and Hallam, A., 1979, Diagenesis of English Lower Jurassic limestones as inferred from oxygen and carbon isotope analysis, **Earth and Planetary Science Letters**, 45: 23-31.

Carroll, D., 1958, Role of clay minerals in the transportation of iron, **Geochimica et Cosmochimica Acta**, 14: 1-27.

Capo, R.C. and DePaolo, D.J., 1990, Seawater strontium isotopic variations from 2.5 million years ago to the present, **Science**, 249: 51-55.

Casey, R., 1961, The stratigraphical palaeontology of the Lower Greensand, **Palaeontology**, 3: 487-621.

Cerling, T.E., Pederson, B.L. and Von Damm, K.L., 1989, Sodium-calcium ion exchange in the weathering of shales: Implications for global weathering budgets, **Geology**, 17: 552-554.

Channon, P.J., 1950, New and enlarged Jurassic sections in the Cotswolds, **Proceedings of the Geologists' Association**, 61: 242-260.

Charlou, J.L., Bougault, H., Appriou, P., Jean-Baptiste, P., Etoubleau, J. and Birolleau, A., 1991, Water column anomalies associated with hydrothermal activity between 11°40' and 13°N on the East Pacific Rise: Discrepancies between tracers, **Deep-Sea Research**, 38: 569-596.

Chaudhuri, S. and Clauer, N., 1986, Fluctuations of isotopic composition of strontium in seawater during the Phanerozoic Eon, **Chemical Geology (Isotope Geoscience Section)**, 59: 293-303.

Claypool, G.E. and Threlkeld, C.N., 1983, Anoxic diagenesis and methane generation in sediments of the Blake Outer Ridge, Deep Sea Drilling Project Site 533, Leg 76, *in* Sheridan, R.E., Gradstein, F.N., *et al.*, **Initial Reports of the Deep Sea Drilling Program**, U.S. Government Printing Office, 76: 391-402.

Coe, A.L., 199 2, **Unconformities within the Upper Jurassic of the Wessex Basin, Southern England**, unpublished D.Phil. dissertation, Department of Earth Sciences, University of Oxford.

Coffin, M.F., 1992, Large igneous provinces studied, **EOS**, 73: 66-67.

Coffin, M.F. and Eldholm, O. (eds.), 1991, **Large Igneous Provinces**, JOI/USSAC Workshop Report, Technical Report 114: 79p.

Coleman, M.L. and Raiswell, R., 1981, Carbon, oxygen and sulphur isotope variations in concretions from the Upper Lias of N.E. England, **Geochimica et Cosmochimica Acta**, 45: 329-340.

Condie, K.C., 1989, Origin of the Earth's crust, **Palaeogeography, Palaeoclimatology, Palaeoecology (Global and Planetary Change Section)**, 75: 57-81.

Cope, J.C.W., 1967, The palaeontology and stratigraphy of the lower part of the Upper Kimmeridge Clay of Dorset, **Bulletin of the British Museum (Natural History)**, Geology Series 15: 1-79.

Cope J.C.W., 1978, The ammonite faunas and stratigraphy of the upper part of the Upper Kimmeridge Clay of Dorset, **Palaeontology**, 21: 469-533.

Cope, J.C.W., Getty, T.A., Howarth, M.K., Morton, N. and Torrens, H.S., 1980a, **A Correlation of Jurassic Rocks in the British Isles, Part One: Introduction and Lower Jurassic**, Geological Society of London Special Report 14: 73p.

Cope, J.C.W., Duff, K.L., Parsons, C.F., Torrens, H.S., Wimbledon, W.A. and Wright, J.K., 1980b, **A Correlation of Jurassic Rocks in the British Isles, Part Two: Middle and Upper Jurassic**, Geological Society of London Special Report 15, 109p.

Cope, J.C.W., 1991a, Discussion on the correlation of the Triassic-Jurassic boundary in England and Austria, **Journal of the Geological Society of London**, 148: 420-422.

Cope, J.C.W., 1991b, Further discussion on the correlation of the Triassic-Jurassic boundary in England and Austria, **Journal of the Geological Society of London**, 148: 943-944.

COSOD II, 1987, **Report from the Second Conference on Scientific Ocean Drilling**, COSOD II, JOI/ESF, 142p.

Cox, B.M. and Gallois, R.W., 1981, The stratigraphy of the Kimmeridge Clay of the Dorset type area and its correlation with some other Kimmeridgian sequences, **Reports of the Institute of Geological Sciences**, 80/4: 44p.

Cox, B.M., Hopson, P.M. and Sumbler, M.G., 1991, A new record of the Upper Cornbrash near Buckingham, **Proceedings of the Geologists' Association**, 102: 63-65.

Cox, B.M., Horton, A., Sumbler, M.G., 1990, The upper Kimmeridge Clay of the M40 motorway, east of Oxford, **Proceedings of the Cotteswold Naturalists Field Club**, 39: 261-269.

Curtis, C.D., 1977, Sedimentary geochemistry: environments and processes dominated by the involvement of aqueous phases, **Philosophical Transactions of the Royal Society of London**, A286: 353-372.

Curtis, C.D. and Coleman, M.L., 1986, Controls on the precipitation of early diagenetic calcite, dolomite and siderite concretions in complex depositional sequences, *in* Gautier, D.L. (ed.), **Roles of Organic Matter in Sediment Diagenesis**, SEPM Special Publication 38: 23-33.

Dasch, E.J., 1969, Strontium isotopes in weathering profiles, deep-sea sediments, and sedimentary rocks, **Geochimica et Cosmochimica Acta**, 33: 1521-1552.

Dean, W.T., 1954, Notes on part of the Upper Lias succession at Blea Wyke, Yorkshire, **Proceedings of the Geologists' Association**, 29: 161-179.

Dean, W.T., Donovan, D.T. and Howarth, M.K., 1961, The Liassic ammonite zones and subzones of the North-West European Province, **Bulletin of the British Museum of Natural History (Geology Series)**, 4: 435-505.

DePaolo, D., 1986, Detailed record of the Neogene Sr isotopic evolution of seawater from DSDP Site 590B, **Geology**, 14: 103-106.

DePaolo, D.J. and Ingram, B.L., 1985, High-resolution stratigraphy with strontium isotopes, **Science**, 227: 938-941.

Derry, L.A. and Jacoben, S.B., 1988, The Nd and Sr isotopic evolution of Proterozoic seawater, **Geophysical Research Letters**, 15: 397-400.

Derry, L.A., Keto, L.S., Jacobsen, S.B., Knoll, A.H. and Swett, K., 1989, Sr isotopic variations in Upper Proterozoic carbonates from Svalbard and East Greenland, **Geochimica et Cosmochimica Acta**, 53: 2331-2339.

Doe, B.R., Hedge, C.E. and White, D.E., 1966, Preliminary investigation of the source of lead and strontium in deep geothermal brines underlying the Salton Sea geothermal area, **Economic Geology**, 61: 462-483.

Doyle, J.C., 1989, The stratigraphy of a late Lower Hauterivian horizon in the Speeton Clay formation (Lower Cretaceous) of East Yorkshire, **Proceedings of the Geologists' Association**, 100: 175-182.

Drever, J.I., 1974, The magnesium problem, *in* Goldberg, E.D. (ed.), **The Sea**, Wiley-Interscience, New York, 5: 337-357.

Drever, J.I., Li, Y.-H. and Maynard, J.B., 1988, Geochemical cycles: the continental crust and the oceans, *in* Gregor, C.B., Garrels, R.M., Mackenzie, F.T. and Maynard, J.B. (eds.), **Chemical Cycles in the Evolution of the Earth**, Wiley-Interscience, New York, 17-54.

Dromgoole, E.L. and Walter, L.M., 1990, Iron and manganese incorporation into calcite: effects of growth kinetics, temperature and solution chemistry, **Chemical Geology**, 81: 311-336.

Edmond, J.M., 1991, The marine strontium isotope record as an index of Himalayan tectonics, **EOS**, 72: 257.

Edmond, J.M., Measures, C., McDuff, R.E., Chan, L.H., Collier, R., Grant, B., Gordon, L.I. and Corliss, J.B., 1979, Ridge crest hydrothermal activity and the balances of the major and minor elements in the oceans: the Galapagos data, **Earth and Planetary Science Letters**, 46: 1-18.

Egeberg, P.K. and the Leg 126 Shipboard Scientific Party, 1990, Unusual composition of pore waters found in the Izu-Bonin fore-arc sedimentary basin, **Nature**, 344: 215-218.

Elderfield, H., 1986, Strontium isotope stratigraphy, **Palaeogeography, Palaeoclimatology, Palaeoecology**, 57: 71-90.

Elderfield, H. and Greaves, M.J., 1981, Sr isotope geochemistry of Icelandic geothermal systems and implications for seawater chemistry, **Geochimica et Cosmochimica Acta**, 45: 2201-2212.

Elderfield, H. and Gieskes, J.M., 1982, Sr isotopes in interstitial waters of marine sediments from Deep Sea Drilling Project cores, **Nature**, 300: 493-497.

Elderfield, H., Kastner, M. and Martin, J.B., 1990, Compositions and sources of fluids in sediments of the Peru subduction zone, **Journal of Geophysical Research**, 95: 8819-8827.

Emery, D., Dickson, J.A.D. and Smalley, P.C., 1987, The strontium isotope composition and origin of burial cements in the Lincolnshire Limestone (Bajocian) of central Lincolnshire, England, **Sedimentology**, 34: 795-806.

Ensom, P.C., 1986, An annotated section of the Purbeck Limestone Formation at Worbarrow Tort, Dorset, **Proceedings of the Dorset Natural History and Archaeological Society**, 108: 87-91.

Eriksson, E., 1985, **Principles and Applications of Hydrochemistry**, Chapman and Hall, London, 187p.

Faure, G., 1982, The marine-strontium geochronometer, *in* Odin, G.S. (ed.), **Numerical Dating in Stratigraphy**, John Wiley & Sons: New York, 73-79.

Faure, G., 1986, **Principles of Isotope Geology**, 2nd ed., John Wiley & Sons: New York, 589p.

Feely, R.A., Massoth, G.J., Baker, E.T., Cowen, J.B., Lamb, M.F. and Krogslund, K.A., 1990, The effect of hydrothermal processes on mid-water phosphorous distributions in the northeast Pacific, **Earth and Planetary Science Letters**, 96: 305-318.

Feely, R.A., Trefry, J.H., Massoth, G.J. and Metz, S., 1991, A comparison of the scavenging of phosphorous and arsenic from seawater by hydrothermal iron oxyhydroxides in the Atlantic and Pacific oceans, **Deep-Sea Research**, 38: 617-623.

Felmy, A.R. and Weare, J.H., 1991, Calculation of multicomponent ionic diffusion from zero to high concentration: I. The system Na-K-Ca-Mg-Cl-SO_4-H_2O at 25°C, **Geochimica et Cosmochimica Acta**, 55: 113-131.

Fischer, H. and Gygi, R., 1989, Numerical and biochronological time scales correlated at the ammonite subzone level; K-Ar, Rb-Sr ages, and Sr, Nd, and Pb sea-water isotopes in an Oxfordian (Late Jurassic) succession of northern Switzerland, **Geological Society of America Bulletin**, 101: 1584-1597.

Fisher, I.St.J., 1986, Pyrite formation in bioturbated clays from the Jurassic of Britain, **Geochimica et Cosmochimica Acta**, 50: 517-523.

Fitch, F.J. and Miller, J.A., 1984, Dating Karoo igneous rocks by the conventional K-Ar and ^{40}Ar-^{39}Ar spectrum methods, **Special Publications of the Geological Society of South Africa**, 13: 247-265.

Fitton, W.H., 1847, A stratigraphical account of the section from Atherfield to Rocken End, on the south-west coast of the Isle of Wight, **Quarterly Journal of the Geological Society of London**, 3: 289-327.

Fletcher, B.N., 1969, A lithological subdivision of the Speeton Clay C Beds (Hauterivian), East Yorkshire, **Proceedings of the Yorkshire Geological Society**, 37: 323-327.

Fouguet, Y., Von Stackelberg, U., Charlou, J.L., Donval, J.P., Erzinger, J., Foucher, J.P., Herzig, P., Mühe, R., Soakai, S., Wiedicke, M. and Whitechurch, H., 1991, Hydrothermal activity and metallogenesis in the Lau back-arc basin, **Nature**, 349: 778-781.

Fox, C.G., 1990, Consequences of phase separation on the distribution of hydrothermal fluids at ASHES vent field, Axial Volcano, Juan de Fuca Ridge, **Journal of Geophysical Research**, 95: 12923-12926.

François, L.M. and Walker, J.C.G., 1992, Modelling the Phanerozoic carbon cycle and climate: Contraints from the $^{87}Sr/^{86}Sr$ isotopic ratio of seawater, **American Journal of Science**, 292: 81-135.

François, L.M., Walker, J.C.G. and Opdyke, B.N., 1992, The history of global weathering and the chemical evolution of the ocean-atmosphere system, **Journal of Geophysical Research**, in press.

Froelich, P.N., Klinkhammer, G.P., Bender, M.L., Luedtke, N.A., Heath, G.R., Cullen, D., Dauphin, P., Hammond, O., Hartman, B. and Maynard, V., 1979, Early oxidation of organic matter in pelagic sediments of the eastern equatorial Atlantic: suboxic diagenesis, **Geochimica et Cosmochimica Acta**, 43: 1075-1090.

Gast, P.W., 1955, Abundance of ^{87}Sr during geologic time, **Bulletin of the Geological Society of America**, 66: 1449-1454.

Gerling, E.K. and Shukolyukov, Y.A., 1957, Determination of the absolute age from the ratio of isotopes $^{87}Sr/^{86}Sr$ in sedimentary rocks, **Geochemistry**, 3: 226-230.

German, C.R., Campbell, A.C. and Edmond, J.M., 1991, Hydrothermal scavenging at the Mid-Atlantic Ridge: Modification of trace element dissolved fluxes, **Earth and Planetary Science Letters**, 107: 101-114.

Getty, T.A., 1972, **Revision of the Jurassic ammonite family *Echioceratidae***, Unpublished Ph.D. thesis (University of London).

Gieskes, J.M. and Lawrence, J.R., 1981, Alteration of volcanic matter in deep sea sediments: evidence from the chemical composition of interstitial waters from deep sea drilling cores, **Geochimica et Cosmochimica Acta**, 45: 1687-1703.

Gieskes, J.M., Elderfield, H. and Palmer, M.R., 1986, Strontium and its isotopic compostion in interstitial waters of marine carbonate sediments, **Earth and Planetary Science Letters**, 77: 229-235.

Gieskes, J.M., Blanc, G., Vrolijk, P., Elderfield, H. and Barnes, R., 1990, Interstitial water chemistry--major constituents, *in* Moore, J.C., *et al.* (eds.), **Proceedings of the Ocean Drilling Program, Scientific Results**, 110: 155-178

Goldfarb, M.S. and Delaney, J.R., 1988, Response of two-phase fluids to fracture configurations within submarine hydrothermal systems, **Journal of Geophysical Research**, 93: 4585-4594.

Goldstein, S.J. and Jacobsen, S.B., 1987, The Nd and Sr isotopic systematics of river water dissolved material: implications for the sources of Nd and Sr in seawater, **Chemical Geology (Isotope Geosciences Section)**, 66: 245-272.

Gowland, S., 1989, Marine sediments of the Middle Jurassic of Yorkshire as developed in the Scarborough Formation, BSRG Field Excursion Guide, 28th Annual Meeting of the British Sedimentological Research Group, 2-1 - 2-23.

Grimaud, D., Michard, A. and Michard, G., 1984, Composition chimique et composition isotopique du strontium dans les eaux hydrothermales sous-marines de la dorsale Est Pacifique à 13° Nord, **Comptes Rendus de L'Académie des Sciences**, 299: 865-870.

Gross, M.G., 1987, **Oceanography: A View of the Earth**, Prentice-Hall, 406p.

Hallam, A., 1962, A band of extraordinary calcareous concretions in the Upper Lias of Yorkshire, England, **Journal of Sedimentary Petrology**, 32: 840-847.

Hallam, A., 1969, A pyritized limestone hardground in the Lower Jurassic of Dorset (England), **Sedimentology**, 12: 231-240.

Hallam, A., 1981, A revised sea-level curve for the early Jurassic, **Journal of the Geological Society of London**, 138: 735-743.

Hallam, A., 1987, Mesozoic marine organic-rich shales, *in* Brooks, J. and Fleet, A.J. (eds.), **Marine Petroleum Source Rocks**, Geological Society of London Special Publication 26: 251-261.

Hancock, J.M., 1988, An ammonite-scale for the Cretaceous System, *in* Beandoin, B. and Ginsburg, R. (eds.), **Cretaceous Resources, Events, and Rhythms**, Draft Position Papers for a NATO Advanced Workshop held in Digne, France, Sept. 16-23, 1988, pp. 122-182.

Harland, W.B., Armstrong, R.L., Cox, A.V., Craig, L.E., Smith, A.G. and Smith, D.G., 1990, **A Geologic Time Scale 1989**, Cambridge University Press, 263p.

Hart, S.R. and Mottl, M.J., 1983, Alkali and Sr isotope geochemistry of waters collected from basaltic basement, Deep Sea Drilling Project Hole 504B, Costa Rica Rift, *in* Langseth, J.R., Honnorez, M.G., Von Herzen, R.P., White, S.M., *et al.*, **Initial Reports of the Deep Sea Drilling Project**, 69: 487-494.

Hedge, C.E. and Walthall, F.G., 1963, Radiogenic strontium-87 as an index of geologic processes, **Science**, 140: 1214-1217.

Hemingway, J.E. and Riddler, G.P., 1982, Basin inversion in North Yorkshire, **Transactions of the Institute of Mining and Metallurgy** (Section B: Applied Earth Sciences), 91: 175-186.

Hendy, C.H., 1971, The isotopic geochemistry of speleothems I: The calculation of the effect of different modes of formation on the isotopic composition of speleothems and their applicability as palaeoclimatic indicators, **Geochimica et Cosmochimica Acta**, 35: 801-824.

Hess, J., Bender, M.L. and Schilling, J., 1986, Evolution of the ratio of strontium 87 to strontium 86 in seawater from Cretaceous to Present, **Science**, 231: 979-984.

Hess, J., Stott, L.D., Bender, M.L., Kennett, J.P. and Schilling, J., 1989, The Oligocene marine microfossil record: age assessments using Sr isotopes, **Paleoceanography**, 4: 655-679.

Hess, J., Bender, M.L. and Schilling, J.G., 1991, Assessing seawater/basalt exchange of strontium isotopes in hydrothermal processes on the flanks of mid-ocean ridges, **Earth and Planetary Science Letters**, 103: 133-142.

Hesselbo, S.P., Coe, A.L., Batten, D.J. and Wach, G.D., 1990, Stratigraphic relations of the Lower Greensand (Lower Cretaceous) of the Calne area, Wiltshire, **Proceedings of the Geologists' Association**, 101: 265-278.

Hodell, D.A., Mueller, P.A., McKenzie, J.A. and Mead, G.A., 1989, Strontium isotope stratigraphy and geochemistry of the late Neogene ocean, **Earth and Planetary Science Letters**, 92: 165-178.

Hodell, D.A., Mead, G.A. and Mueller, P.A., 1990, Variation in the strontium isotopic composition of seawater (8 Ma to present): Implications for chemical weathering rates and dissolved fluxes to the oceans, **Chemical Geology (Isotope Geosciences Section)**, 80: 291-307.

Hodell, D.A., Mueller, P.A. and Garrido, J.R., 1991, Variation in the strontium isotopic composition of seawater during the Neogene, **Geology**, 19: 24-27.

Holland, H.D., 1978, **The Chemistry of the Atmosphere and Oceans**, John Wiley and Sons, New York, 351p.

Holland, H.D., 1984, **The Chemical Evolution of the Atmosphere and Oceans**, Princeton University Press, 582p.

Howard, A.S., 1985, Lithostratigraphy of the Staithes Sandstone and Cleveland Ironstone formations (Lower Jurassic) of north-east Yorkshire, **Proceedings of the Yorkshire Geological Society**, 45: 261-275.

Howarth, M.K., 1955, Domerian of the Yorkshire coast, **Proceedings of the Yorkshire Geological Society**, 30: 147-175.

Howarth, M.K., 1957, The Middle Lias of the Dorset coast, **Quarterly Journal of the Geological Society of London**, 113: 185-204.

Howarth, M.K., 1962, The Jet Rock Series and the Alum Shale Series of the Yorkshire coast, **Proceedings of the Yorkshire Geological Association**, 33: 381-422.

Howarth, M.K., 1973, The stratigraphy and ammonite fauna of the Upper Liassic Grey Shales of the Yorkshire coast, **Bulletin of the British Museum (Natural History)**, Geology Series, 24: 235-277.

Hudson, J.D. and Anderson, T.F., 1989, Ocean temperatures and isotopic compositions through time, **Transactions of the Royal Society of Edinburgh: Earth Sciences**, 80: 183-192.

Hurley, P.M., Fairbairn, H.W. and Pinson, W.H., Jr., 1965, Evidence from western Ontario of the isotopic composition of strontium in Archeon seas (abstract), **Geolological Society of America Special Papers**, 87: 84.

Hurst, R.W., 1986, Strontium isotopic chronostratigraphy and correlation of the Miocene Monterey Formation in the Ventura and Santa Maria basins of California, **Geology**, 14: 459-462.

Irwin, H., 1980, Early diagenetic carbonate precipitation and pore fluid migration in the Kimmeridge Clay of Dorset, England, **Sedimentology**, 27: 577-591.

Irwin, H., Coleman, M. and Curtis, C., 1977, Isotopic evidence for the source of diagenetic carbonate during burial of organic-rich sediments, **Nature**, 269: 209-213.

Ito, E., Harris, D.M. and Anderson, A.T., Jr., 1983, Alteration of oceanic crust and geologic cycling of chlorine and water, **Geochimica et Cosmochimica Acta**, 47: 1613-1624.

Ivimey-Cook, H.C. and Donovan, D.T., 1983, The fauna of the Lower Jurassic, *in* Whittaker, A. and Green, G.W., **Geology of the Country around Weston-super-Mare**, Geological Survey of Great Britain Sheet Memoir 279: 126-130.

Javoy, M. and Courtillot, V., 1989, Intense acidic volcanism at the Cretaceous-Tertiary boundary, **Earth and Planetary Science Letters**, 94: 409-416.

Jenkyns, H.C., 1988, The Early Toarcian (Jurassic) anoxic event: stratigraphic, sedimentary, and geochemical evidence, **American Journal of Science**, 288: 101-151.

Jenkyns, H.C., 1991, Impact of Cretaceous sea level rise and anoxic events on the Mesozoic carbonate platform of Yugoslavia, **American Association of Petroleum Geologists Bulletin**, 75: 1007-1017.

Jenkyns, H.C. and Clayton, C., 1986, Black shales and carbon isotopes in pelagic sediments from the Tethyan Lower Jurassic, **Sedimentology**, 33: 87-106.

Jenkyns, H.C., Géczy, B. and Marshall, J.D., 1991, Jurassic manganese carbonates of Central Europe and the Early Toarcian anoxic event, **Journal of Geology**, 99: 137-149.

Jordon, R. and Stahl, W., 1970, Isotopische paläotemperaturbestimmungen an jurassischen Ammoniten und grundsätzliche Voraussetzungen für diese Methode, **Geolgie Jahrbuch**, 89: 33-62.

Karl, D.M., McMurtry, G.M., Malahoff, A. and Garcia, M.O., 1988, Loihi Seamount, Hawaii: a mid-plate volcano with a distinctive hydrothermal system, **Nature**, 335: 532-535.

Kaltenegger, W., Preisinger, A. and Rogl, F., 1971, Paläotemperaturbestimmungen an aragonit-schaligen Mullusken aus dem Alpinen Mesozoicum, **Palaeogeography, Palaeoclimatology, Palaeoecology**, 10: 273-285.

Kastner, M., Elderfield, H., Martin, J.B., Suess, E., Kuenvolden, K.A. and Garrison, R.E., 1990, Diagenesis and interstitial water chemistry at the Peruvian continental margin--major constituents and strontium isotopes, *in* Suess, E., *et al.*, **Proceedings of the Ocean Drilling Program, Scientific Results**, 112: 413-439.

Kastner, M., Elderfield, H. and Martin, J.B., 1991, Fluids in convergent margins: What do we know about their composition, origin, role in diagenesis, and importance for oceanic chemical fluxes?, **Philosophical Transactions of the Royal Society of London**, Series A, 335: 243-259.

Kemper, E., Rawson, P.F. and Thieuloy, J.-P., 1981, Ammonites of Tethyan ancestry in the Early Lower Cretaceous of north-west Europe, **Palaeontology**, 24: 251-311.

Kennett, J.P. and Barker, P.F., 1990, 53. Latest Cretaceous to Cenozoic climate and oceanographic developments in the Weddell Sea, Antarctica: an ocean-drilling perspective, Barker, P.F., Kennett, J.P., *et al.* **Proceedings of the Ocean Drilling Program, Scientific Results**, 113: 937-960.

Kennett, J.P. and Stott, L.D., 1991, Abrupt deep-sea warming, palaeoceanographic changes and benthic extinctions at the end of the Palaeocene, **Nature**, 353: 225-229.

Kent, D.V. and Gradstein, F.M., 1985, A Cretaceous and Jurassic geochronology, **Geological Society of America Bulletin**, 96: 1419-1427.

Keto, L.S. and Jacobsen, S.B., 1987, Nd and Sr isotopic variations of Early Paleozoic oceans, **Earth and Planetary Science Letters**, 84: 27-41.

Koepnick, R.B., Burke, W.H., Denison, R.E., Hetherington, E.A., Nelson, H.F, Otto, J.B. and Waite, L.E., 1985, Construction of the seawater $^{87}Sr/^{86}Sr$ curve for the Cenozoic and Cretaceous: supporting data, **Chemical Geology (Isotope Geoscience Section)**, 58: 55-81.

Koepnick, R.B., Denison, R.E., Burke, W.H., Hetherington, E.A. and Dahl, D.A., 1990, Construction of the Triassic and Jurassic portion of the Phanerozoic curve of seawater $^{87}Sr/^{86}Sr$, **Chemical Geology (Isotope Geoscience Section)**, 80: 327-349.

Kominz, M.A., 1984, Oceanic ridge volumes and sea-level change--An error analysis, *in* Schlee, J.S. (ed.), **Interregional Unconformities and Hydrocarbon Accumulation, American Association of Petroleum Geologists Memoir**, 36: 109-127.

Korzun, V.I., Sokolov, A.A., Budyko, M.I., Voskresensky, K.P., Kalinin, G.P., Konoplyantsev, A.A., Korotkevich, E.S., Kuzin, P.S. and Lvovitch, M.I., 1974, **The World Water Balance and Water Resourses of the Earth**, U.S.S.R. National Committee for the Hydrological Decade, Leningrad, Republished in English in 1978, **Studies and Reports in Hydrology**, 25, Unesco Press, 663p.

Knittel, U. and Daniels, U., 1987, Sr-isotope composition of marbles from the Puerto Galera area (Mindoro, Philippines): Additional evidence for a Paleozoic age of a metamorphic complex in the Philippine island arc, **Geology**, 15: 136-138.

Knox, R.W.O'B., 1984, Lithostratigraphy and depositional history of the late Toarcian sequence at Ravenscar, Yorkshire, **Proceedings of the Yorkshire Geological Society**, 45: 99-108.

Krishnaswami, S., Trivedi, J.R., Sarin, M.M., Ramesh, R. and Sharma, K.K., 1992, Strontium isotopes and rubidium in the Ganga-Brahmaputra river system: Weathering in the Himalaya, fluxes to the Bay of Bengal and contributions to the evolution of oceanic $^{87}Sr/^{86}Sr$, **Earth and Planetary Science Letters**, 109: 243-253.

Kump, L.R., 1989, Alternative modeling approaches to the geochemical cycles of carbon, sulfur, and strontium isotopes, **American Journal of Science**, 289: 390-410.

Lamplugh, G.W., 1889, On the subdivisions of the Speeton Clay, **Quarterly Journal of the Geological Society of London**, 45: 575-618.

Lang, W.D., 1924, The Blue Lias of the Devon and Dorset coasts, **Proceedings of the Geologists' Association of London**, 35: 169-185.

Lang, W.D., 1936, The Green Ammonite Beds of the Dorset Lias, **Quarterly Journal of the Geological Society of London**, 92: 423-437.

Lang, W.D., 1945, The Coinstone of the Charmouth Lias, **Proceedings of the Dorset Natural History and Archaeological Society**, 67: 145-149.

Lang, W.D., Spath, L.F. and Richardson, W.A., 1923, Shales-with-'Beef', a sequence in the Lower Lias of the Dorset Coast, **Quarterly Journal of the Geological Society of London**, 79: 47-99.

Lang, W.D. and Spath, L.F., 1926, The Black Marl of Black Ven and Stonebarrow, in the Lias of the Dorset coast, with notes on the Lamellibranchia by L.R. Cox; on the Brachiopoda by H.M. Muir Wood; on certain Echioceratidae by A.E. Trueman and D.M. Williams, **Quarterly Journal of the Geological Society of London**, 82: 144-187.

Lang, W.D., Spath, L.F., Cox, L.R. and Muir-Wood, H.M., 1928, The Belemnite Marls of Charmouth, a series in the Lias of the Dorset coast, **Quarterly Journal of the Geological Society of London**, 84: 179-257.

Langseth, M.G., Mottl, M.J., Hobart, M.A. and Fisher, A., 1988, 2. The distribution of geothermal and geochemical gradients near Site 501/504: Implications for hydrothermal circulation in the oceanic crust, *in* Becker, K., Sakai, H., *et al.*, **Proceedings of the Ocean Drilling Program Initial Reports (Part A)**, 111: 23-32.

Larson, R.L., 1991, Latest pulse of the Earth: Evidence for a mid-Cretaceous super plume, **Geology**, 19: 547-550.

Lasaga, A.C., 1989, A new approach to isotopic modeling of the variation of atmospheric oxygen through the Phanerozoic, **American Journal of Science**, 289: 411-435.

Lasaga, A.C., Berner, R.A. and Garrels, R.M., 1985, An improved geochemical model of atmospheric CO_2 fluctuations over the past 100 million years, *in* Sundquist, E. and Broecker, W.S. (eds.), **The Carbon Cycle and Atmospheric CO_2: Natural Variations Archean to Present**, Geophysical Monograph 32: 397-411.

Leslie, B.W., Hammond, D.E., Berelson, W.M. and Lund, S.P., 1990, Diagenesis in anoxic sediments from the California Continental Borderland and its influence on iron, sulfur, and magnetite behavior, **Journal of Geophysical Research**, 95: 4453-4470.

Lini, A., Weissert, H. and Erba, E., 1992, The Valanginian carbon isotope event: A first episode of greenhouse climate conditions during the Cretaceous, **Terra Nova**, in press.

Lister, C.R.B., 1972, On the thermal balance of a mid-ocean ridge, **Geophysical Journal of the Royal Astronomy Society**, 26: 515-535.

Lister, C.R.B., 1974, On the penetration of water into hot rock, **Geophysical Journal of the Royal Astronomy Society**, 39: 465-509.

Livingstone, D.A., 1963, Chemical composition of rivers and lakes, *in* Fleischer, M. (ed.), **Data of Geochemistry**, 6th edition, USGS Professional Paper 440-G.

Lohmann, K.C., 1988, Geochemical patterns of meteoric diagenetic systems and their application to studies of paleokarst, *in* James, N.P. and Choquette, P.W. (eds.), **Paleokarst**, 55-80.

Lowenstam, H.A. and Epstein, S., 1954, Paleotemperatures of the post-Aptian Cretaceous as determined by the oxygen isotope method, **Journal of Geology**, 62: 207-248.

Ludwig, K.R., Halley, R.B., Simmons, K.R. and Peterman, Z.E., 1988, Strontium isotope stratigraphy of Enewetak Atoll, **Geology**, 16: 173-177.

Ludwig, K.R., 1990, **Isoplot** Version 2.11, A Plotting and Regression Program for Radiogenic-Isotope Data, for IBM-PC Compatible Computers, **United States Geological Survey Open-File Report,** 88-557, 33p.

L'vovitvch, M.I., 1973, The global water balance, **EOS**, 54: 28-42.

Lyle, M., Leinen, M., Owen, R.M. and Rea, D.K., 1987, Late Tertiary history of hydrothermal deposition at the East Pacific Rise, 13°S: correlation to volcano-tectonic events, **Geophysical Research Letters**, 14: 595-598.

MacDougall, J.D., 1988, Seawater strontium isotopes, acid rain, and the Cretaceous-Tertiary boundary, **Science**, 239: 485-487.

Martin, E.E. and MacDougall, J.D., 1991, Seawater Sr isotopes at the Cretaceous/Tertiary boundary, **Earth and Planetary Science Letters**, 104: 166-180.

Marshall, J.D., 1981, Stable isotope evidence for the environment of lithification of some Tethyan limestones, **Neues Jahrbuch für Geologie und Paläontologie Abhandlungen**, 1981: 211-224.

Massoth, G.J., Butterfield, D.A., Lupton, J.E., McDuff, R.E., Lilley, M.D. and Jonasson, I.R., 1989, Submarine venting of phase-separated hydrothermal fluids at Axial Volcano, Juan de Fuca Ridge, **Nature**, 340: 702-705.

Matsumoto, R., 1983, Mineralogy and geochemistry of carbonate diagenesis of the Pliocene and Pleistocene hemipelagic mud on the Blake Outer Ridge, Site 533, Leg 76, *in* Sheridan, R.E. and Gradstein, F.M., *et al.*, **Initial Reports of the Deep Sea Drilling Program**, U.S. Government Printing Office, 76: 411-427.

McArthur, J.M., Thirlwall, M.F., Gale, A.S., Kennedy, W.J., Burnett, J.A., Lord, A.R. and Mattey, D., 1992, Strontium isotope stratigraphy for the Late Cretaceous: A refinement based on the English Chalk, *in* Hailwood, E. and Kidd, R. (eds.) **High Resolution Stratigraphy**, Geological Society of London Special Publication, in the press.

McKenzie, J.A., Hodell, D.A., Mueller, P.A. and Müller, D.W., 1988, Application of strontium isotopes to late Miocene-early Pliocene stratigraphy, **Geology**, 16: 1025-1027.

Medford, G.A., Maxwell, R.J. and Armstrong, R.L., 1983, $^{87}Sr/^{86}Sr$ ratio measurements on sulfides, carbonates, and fluid inclusions from Pine Point, Northwest Territories, Canada: an $^{87}Sr/^{86}Sr$ increase accompanying the mineralizing process, **Economic Geology**, 78: 1375-1378.

Meybeck, M., 1979, Concentrations des eaux fluviales en éléments majeurs et apports en solution aux océans, **Revue de Géologie Dynamique et de Géographie Physique**, 21: 215-246.

Meybeck, M., 1983, Atmospheric inputs and river transport of dissolved substances, *in* Dissolved loads of rivers and surface water quantity/quality relationships, Proceedings of the IASH Symposium, Hamburg, August, 1983, **International Association of Hydrologists Scientific Publication**, 141: 173-192.

Meybeck, M., 1988, How to establish and use world budgets of riverine materials, *in* Lerman, A. and Meybeck, M. (eds.), **Physical and Chemical Weathering in Geochemical Cycles**, Kluwer Academic Publishers, 247-272.

Michael, P.J. and Schilling, J-G., 1989, Chlorine in mid-ocean ridge magmas: Evidence for assimilation of seawater-influenced components, **Geochimica et Cosmochimica Acta**, 53: 3131-3143.

Michard, G., Albarede, F., Michard, A., Minster, J.-F., Charlou, J.-L. and Tan, N., 1984, Chemistry of solutions from the 13°N East Pacific Rise hydrothermal site, **Earth and Planetary Science Letters**, 67: 297-307.

Miller, K.G., Feigenson, M.D., Kent, D.V. and Olsson, R.K., 1988, Upper Eocene to Oligocene isotope ($^{87}Sr/^{86}Sr$, $\delta^{18}O$, $\delta^{13}C$) standard section, Deep Sea Drilling Project Site 522, **Paleocenography**, 3: 223-233.

Miller, K.G., Feigenson, M.D., Wright, J.D. and Clement, B.M., 1991, Miocene isotope reference section, Deep Sea Drilling Project Site 608: An evaluation of isotope and biostratigraphic resolution, **Paleoceanography**, 6: 33-52.

Milliman, J.D. and Meade, R.H., 1983, World-wide delivery of river sediments to the oceans, **Geology of Geology**, 91: 1-21.

Montgomery, R.B., 1958, Water characteristics of the world oceans, **Deep Sea Research**, 5: 134-148.

Moore, C.H., 1989, **Carbonate Diagenesis and Porosity**, Developments in Sedimentology 46, Elsevier, Amsterdam, 338p.

Morris, K.A., 1980, Comparison of major sequences of organic-rich mud deposition in the British Jurassic, **Journal of the Geological Society of London**, 137: 157-170.

Morrison, J.O. and Brand, U., 1988, An evaluation of diagenesis and chemostratigraphy of Upper Cretaceous molluscs from the Canadian Interior Seaway, *in* Chivas, A.R., (ed.) Isotopes in Palaeoenvironments, **Chemical Geology (Isotope Geosciences Section)**, 72: 235-248.

Morrison, J.O. and Veizer, J., 1990, Belemnite geochemistry: an indicator of secular and environmental variation of Cretaceous seawater, **Geological Society of America Abstracts with Programs**, 1990 Annual Meeting, 22: A116.

Morton, J.L. and Sleep, N.H., 1985, A mid-ocean ridge thermal model: constraints on the volume of axial hydrothermal heat flux, **Journal of Geophysical Reasearch**, 90: 11345-11353.

Mottl, M.J., 1983, Metabasalts, axial hotsprings, and the structure of hydrothermal systems at mid-ocean ridges, **Geological Society of America Bulletin**, 94: 161-180.

Mottl, M.J., 1989, Hydrothermal convection, reaction, and diffusion in sediments on the Costa Rica Rift flank: Pore-water evidence from ODP Sites 677 and 678, *in* Becker, K., Sakai, H., *et al.*, **Proceedings of the Ocean Drilling Program, Scientific Results**, 111: 195-213.

Mottl, M.J. and Holland, H.D., 1978, Chemical exchange during hydrothermal alteration of basalt by seawater--I. Experimental results for major and minor components of seawater, **Geochimica et Cosmochimica Acta**, 42: 1103-1115.

Mottl, M.J., Anderson, R.N., Jenkins, W.J. and Lawrence, J.R., 1983, 22. Chemistry of waters sampled from basaltic basement in Deep Sea Drilling Project Holes 501, 504B, and 505B, *in* Cann, J.R., Langseth, M.G., Honnorez, J., Von Herzen, R.P., White, S.M., *et al.*, **Initial Reports of the Deep Sea Drilling Project**, 69: 475-483.

Mottl, M.J., Druffel, E.R.M., Hart, S.R., Lawrence, J.R. and Saltzman, E.S., 1985, 15. Chemistry of hot waters sampled from basaltic basement in Hole 504B, Deep Sea Drilling Project Leg 83, Costa Rica Rift, *in* Anderson, R.N., Honnorez, J., Becker, K., *et al.*, **Initial Reports of the Deep Sea Drilling Program**, 83: 315-328.

Mottl, M.J., Sakai, H., Masuda, H. and Kawahata, H., 1988, Chemistry of waters from basement in Hole 504B, *in* Becker, K., Sakai, H., *et al.*, **Proceedings of the Ocean Drilling Program, Initial Reports (Part A)**, 111: 68-86.

Mottl, M.J. and Gieskes, J.M., 1990, Chemistry of waters sampled from oceanic basement boreholes, 1979-1988, **Journal of Geophysical Research**, 95: 9327-9342.

Nace, R.L., 1969, World water inventory and control, *in* Chorley, R.J. (ed.), **Water, Earth, and Man**, Methuen, London, 31-43.

Naydin, D.P., Teys, R.V. and Zadorozhnyy, I.K., 1966, Isotopic palaeotemperatures of the Upper Cretaceous in the Russian Platform and other parts of the U.S.S.R., **Geochemistry International**, 3: 1038-1051.

Neale, J.W., 1960, The subdivisions of the Upper D Beds of the Speeton Clay of Speeton, East Yorkshire, **Geological Magazine**, 97: 353-362.

Neale, J.W., 1962, Ammonoidea from the Lower D Beds (Berriasian) of the Speeton Clay, **Palaeontology**, 5: 272-296.

Neale, J.W., 1974, Cretaceous, *in* Rayner, D.H. and Hemingway, J.E. (eds), **The Geology and Mineral Resources of Yorkshire**, Yorkshire Geological Society, Leeds, 225-243.

Nehliq, P., 1991, Salinity of oceanic hydrothermal fluids: a fluid inclusion study, **Earth and Planetary Science Letters**, 102: 310-325.

Nelson, B.K., MacLeod, G.K. and Ward, P.D., 1991, Rapid change in strontium isotopic composition of sea water before the Cretaceous/Tertiary boundary, **Nature**, 351: 644-647.

Nojiri, Y., Ishibashi, J., Kawai, T., Otsuki, A. and Sakai, H., 1989, Hydrothermal plumes along the North Fiji Basin spreading axis, **Nature**, 342: 667-670.

Olivarez, A.M. and Owen, R.M., 1989, Plate tectonic reorganizations: Implications regarding the formation of hydrothermal ore deposits, **Marine Mining**, 8: 123-138.

Oschmann, W., 1988, Upper Kimmeridgian and Portlandian marine macrobenthic associations from southern England and northern France, **Facies**, 18: 49-82.

Owen, H.G., 1972, The Gault and its junction with the Woburn Sands in the Leighton Buzzard area, Bedfordshire and Buckinghamshire, **Proceedings of the Geologists' Association**, 83: 287-312.

Owen, H.G., 1975, The stratigraphy of the Gault and Upper Greensand of the Weald, **Proceedings of the Geologists' Association**, 86: 475-498.

Owen, H.G., 1984, Albian stage and substage boundaries, **Bulletin of the Geological Society of Denmark**, 33:183-189.

Owen, H.G., 1985, The Albian stage: European province chronology and ammonite zonation, **Cretaceous Research**, 5: 329-344.

Owen, H.G., 1988, The ammonite zonal sequence and ammonite taxonomy in the *Douvilleiceras mammillatum* Superzone (Lower Albian) in Europe, **Bulletin of the British Museum (Natural History)**, Geology Series 44: 177-231.

Owen, R.M. and Rea, D.K., 1985, Sea-floor hydrothermal activity links climate to tectonics: the Eocene carbon dioxide greenhouse, **Science**, 227: 166-169.

Page, K.N., 1989, A stratigraphical revision for the English Lower Callovian, **Proceedings of the Geologists' Association**, 100: 363-382.

Palmer, M.R. and Edmond, J.M., 1989a, The strontium isotope budget of the modern ocean, **Earth and Planetary Science Letters**, 92: 11-26.

Palmer, M.R. and Edmond, J.M., 1989b, Cs/Rb ratio of submarine hydrothermal fluids: Implications for nature of hydrothermal circulation, **Proceedings of the 28th International Geological Congress**, 2: 567.

Palmer, M.R. and Elderfield, H., 1985, Sr isotope composition of sea water over the past 75 Myr, **Nature**, 314: 526-528.

Parsons, B. and Sclater, J.G., 1977, An analysis of the variation of ocean floor bathymetry and heat flow with age, **Journal of Geophysical Research**, 82: 803-827.

Parsons, C.F., 1977, A stratigraphic revision of the Scarborough Formation, **Proceedings of the Yorkshire Geological Society**, 41: 203-222.

Parsons, C.F., 1979, A stratigraphic revision of the Inferior Oolite of Dundry Hill, Bristol, **Proceedings of the Geologists' Association**, 90: 133-151.

Peterman, Z.E., Hedge, C.E. and Tourtelot, H.A., 1970, Isotopic composition of strontium in sea water throughout Phanerozoic time, **Geochimica et Cosmochimica Acta**, 34: 105-120.

Phelps, M.C., 1985, A refined ammonite biostratigraphy for the middle and upper Carixian (Ibex and Davoei zones, Lower Jurassic) in north-west Europe and stratigraphic details of the Carixian-Domerian boundary, **Geobios**, 18: 321-362.

Pienkowski, G., 1991, Eustatically-controlled sedimentation in the Hettangian-Sinemurian (Early Jurassic) of Poland and Sweden, **Sedimentology**, 38: 503-518.

Popp, B.N., Podosek, F.A., Brannon, J.C., Anderson, T.F., Pier, J., 1986, $^{87}Sr/^{86}Sr$ ratios in Permo-Carboniferous sea water from the analyses of well-preserved brachiopod shells, **Geochimica et Cosmochimica Acta**, 50: 1321-1328.

Porrenga, D.H., 1967, Glauconite and chamosite as depth indicators in the marine environment, **Marine Geology**, 5: 495-501.

Powell, J.H. 1984, Lithostratigraphical nomenclature of the Lias Group in the Yorkshire Basin, **Proceedings of the Yorkshire Geological Society**, 45: 51-58.

Raiswell, R., 1976, The microbiological formation of carbonate concretions in the Upper Lias of NE England, **Chemical Geology**, 18: 227-244.

Raiswell, R., 1988, Chemical model for the origin of minor limestone-shale cycles by anaerobic methane oxidation, **Geology**, 16: 641-644.

Rampino, M.R. and Stothers, R.B., 1988, Flood basalt volcanism during the past 250 million years, **Science**, 241: 663-668.

Rawson, P.F., 1971, The Hauterivian (Lower Cretaceous) biostratigraphy of the Speeton Clay of Yorkshire, England, **Newsletter of Stratigraphy**, 1: 61-75.

Rawson, P.F., 1983, The Valanginian to Aptian stages--current definitions and outstanding problems, **Zitteliana**, 10: 493-500.

Rawson, P.F., Curry, D., Dilley, F.C., Hancock, J.M., Kennedy, W.J., Neale, J.W., Wood, C.J., Worssam, B.C., 1978, **A Correlation of Cretaceous Rocks in the British Isles**, Geological Society of London Special Report 9: 70p.

Rawson, P.F. and Mutterlose, J., 1983, Stratigraphy of the Lower B and basal Cement Beds (Barremian) of the Speeton Clay, Yorkshire, England, **Proceedings of the Geologists' Association**, 94: 133-146.

Raymo, M.E., Ruddiman, W.F. and Froelich, P.N., 1988, Influence of late Cenozoic mountain building on ocean geochemical cycles, **Geology**, 16: 649-653.

Rea, D.K., Zachos, J.C., Owen, R.N. and Gingerich, P.D., 1990, Global at the Paleocene-Eocene boundary: climatic and evolutionary consequences of tectonic events, **Palaeogeography, Palaeoclimatolgy, Palaeoecology**, 79: 117-128.

Rehtijärvi, P., 1984, Enrichment of bromine and chlorine in Proterozoic serpentinites from the Outokumpu Cu-Co ore district, Finland, **Economic Geology**, 79: 549-552.

Reynolds, S., 1991, A study of the carbon and oxygen isotope ratios in concretions from Jurassic mudrocks of Dorset and Yorkshire: an investigation of the origin of diagenetic calcium carbonate, Unpublished Honor's Thesis, Department of Earth Sciences, Oxford University, 96p.

Richards, P.C., 1991, Evolution of Lower Jurassic coastal plain and fan delta sediments in the Beryl Embayment, North Sea, **Journal of the Geological Society, London**, 148: 1037-1047.

Richardson, L., 1928, The Inferior Oolite and contiguous deposits of the Burton Bradstock-Broadwindsor district, Dorset, **Proceedings of the Cotteswold Naturalists Field Club**, 23: 35-68.

Richardson, L., 1932, The Inferior Oolite and contiguous deposits of the Sherborne district, Dorset, **Proceedings of the Cotteswold Naturalists Field Club**, 24: 35-85.

Richter, F.M. and DePaolo, D.J., 1987, Numerical models for diagenesis and the Neogene Sr isotopic evolution of seawater from DSDP Site 590B, **Geology**, 14: 103-106.

Richter, F.M. and DePaolo, D.J., 1988, Diagenesis and Sr isotopic evolution of seawater using data from DSDP 590B and 575, **Earth and Planetary Science Letters**, 90: 382-394.

Richter, F.M., Rowley, D.B. and DePaolo, D.J., 1992, Sr isotope evolution of seawater: the role of tectonics, **Earth and Planetary Science Letters**, 109: 11-23.

Rona, P.A. and Richardson, E.S., 1978, Early Cenozoic global plate reorganization, **Earth and Planetary Science Letters**, 40: 1-11.

Rosenbauer, R.J. and Bischoff, J.L., 1983, Uptake and transport of heavy metals by heated seawater: a summary of the experimental results, *in*, Rona, P.A., Bostrom, K., Laubier, L. and Smith, K.L., Jr. (eds.), **Hydrothermal Processes at Seafloor Spreading Centers**, NATO Conference Series IV: Marine Sciences, Plenum, New York, 12: 177-197.

Rundberg, Y. and Smalley, P.C., 1989, High-resolution dating of Cenozoic sediments from the northern North Sea using $^{87}Sr/^{86}Sr$ stratigraphy, **American Association of Petroleum Geologists Bulletin**, 73: 298-308.

Sælen, 1989, Diagenesis and construction of the belemnite rostrum, **Palaeontology**, 32: 765-798.

Sælen, G. and Karstang, T.V., 1989, Chemical signature of belemnites, **Neues Jahrbuch für Geologie und Paläontologie Abhandlungen**, 177: 333-346.

Saller, A.H., 1984, Petrologic and geochemical constraints on the origin of subsurface dolomite, Enewetak Atoll: an example of dolomitization by normal seawater, **Geology**, 12: 217-220.

Sass, E., Bein, A. and Almodi-Labin, A., 1991, Oxygen-isotope composition of diagenetic calcite in organic-rich rocks: evidence for ^{18}O depletion in marine anaerobic pore water, **Geology**, 19: 839-842.

Sayles, F.L., 1979, The composition and diagenesis of interstitial solutions; I. Fluxes across the seawater-sediment interface in the Atlantic Ocean, **Geochimica et Cosmochimica Acta**, 43: 527-546.

Sayles, F.L., 1981, The composition and diagenesis of interstitial solutions; II. Fluxes and diagenesis at the water-sediment interface in the high latitude North and South Atlantic, **Geochimica et Cosmochimica Acta**, 45: 1061-1086.

Schlanger, S.O., Arthur, M.A., Jenkyns, H.C. and Scholle, P.A., 1987, The Cenomanian-Turonian Oceanic Anoxic Event, I. Stratigraphy and distribution of organic carbon-rich beds and the marine $\delta^{13}C$ excursion, *in* Brooks, J. and Fleet, A.J. (eds.), **Marine Petroleum Source Rocks**, Geological Society of London Special Publication 26: 371-399.

Sclater, J.G., Crowe, J. and Anderson, R.N., 1976, On the reliability of oceanic heat flow averages, **Journal of Geophysical Research**, 81: 2997-3005.

Sclater, J.G., Jaupart, C. and Galson, D., 1980, The heat flow through oceanic and continental crust and the heat loss of the earth, **Reviews in Geophysics and Space Physics**, 18: 269-311.

Scotchman, I.C., 1991, The geochemistry of concretions from the Kimmeridge Clay Formation of southern and eastern England, **Sedimentology**, 38: 79-106.

Seewald, J.S. and Seyfried, W.E., Jr., 1990, The effect of temperature on metal mobility in subsurface hydrothermal systems: constraints from basalt alteration experiments, **Earth and Planetary Science Letters**, 101: 388-403.

Sellwood, B.W., Shepherd, T.J., Evans, M.R. and James, B., 1989, Origin of late cements in oolitic reservoir facies: a fluid inclusion and isotopic study (Mid-Jurassic, southern England), **Sedimentary Geology**, 61: 223-237.

Seyfried, W.E. Jr., 1987, Experimental and theoretical constraints on hydrothermal alteration processes at mid-ocean ridges, **Annual Reviews in Earth and Planetary Sciences**, 15: 317-335.

Seyfried, W.E. Jr. and Bischoff, J.L., 1981, Experimental seawater-basalt interaction at 300°C and 500 bars: Chemical exchange, secondary mineral formation and implications for the transport of heavy metals, **Geochimica et Cosmochimica Acta**, 45: 135-147.

Seyfried, W.E. Jr., Berndt, M.E. and Janecky, D.R., 1986, Chloride depletions and enrichments in seafloor hydrothermal fluids: Constraints from experimental basalt alteration studies, **Geochimica et Cosmochimica Acta**, 50: 469-475.

Seyfried, W.E. Jr., Berndt, M.E. and Seewald, J.S., 1988, Hydrothermal alteration processes at mid-ocean ridges: constraints from diabase alteration experiements, hot-spring fluids and composition of the oceanic crust, **Canadian Mineralogist**, 26: 787-804.

Shackleton, N.J., 1986, Paleogene stable events, **Palaeoceanography, Palaeoclimatology, Palaeoecology**, 57: 91-102.

Shackleton, N.J. and Kennett, J.P., 1975, Paleotemperature history of the Cenozoic and the initiation of Antarctic glaciation: oxygen and carbon isotope analyses in DSDP sites 277, 279, and 281, **Initial Reports of the Deep Sea Drilling Project**, 29: 743-755.

Shaw, H.F. and Wasserburg, G.J., 1985, Sm-Nd in marine carbonates and phosphates: Implications for Nd isotopes in seawater and crustal ages, **Geochimica et Cosmochimica Acta**, 49: 503-518.

Simpson, M.I., 1985, The stratigraphy of the Atherfield Clay Formation (Lower Aptian, Lower Cretaceous) at the type and other localities in southern England, **Proceedings of the Geologists' Association**, 96: 23-45.

Sleep, N.H., 1991, Hydrothermal circulation, anhydrite precipitation, and thermal structure at ridge axes, **Journal of Geophysical Research**, 96: 2375-2387.

Sleep, N.H., Morton, J.L., Burns, L.E. and Wolery, T.J., 1983, Geophysical constraints on the volume of hydrothermal flow at ridge axes, *in*, Rona, P.A., Bostrom, K., Laubier, L. and Smith, K.L., Jr. (eds.), **Hydrothermal Processes at Seafloor Spreading Centers**, NATO Conference Series IV: Marine Sciences, Plenum, New York, 12: 53-68.

Sleep, N.H. and Wolery, T.J., 1978, Egress of hot water from mid-ocean ridge hydrothermal systems: some thermal constraints, **Journal of Geophysical Research**, 83: 5913-5922.

Sliter, W.V., Aptian anoxia in the Pacific Basin, **Geology**, 17: 909-912.

Smalley, P.C., Nordaa, A. and Råheim, A., 1986, Geochronology and paleothermometry of Neogene sediments from the Vøring Plateau using Sr, C, and O isotopes, **Earth and Planetary Science Letters**, 78: 368-378.

Smalley, P.C., Qvale, G. and Qvale, H., 1989, Some ages from Leg 104 Site 642 obtained by Rb-Sr glauconite dating and Sr isotope stratigraphy, *in* Eldholm, O., Thiede, J. and Taylor, E., *et al.* **Proceedings of the Ocean Drilling Program, Scientific Results**, 104: 249-253.

Smalley, P.C., Råheim, A., Rundberg, Y. and Johansen, H., 1990, Strontium- isotope stratigraphy: applications in basin modelling and reservoir correlation, *in* Collinson, J. (ed.), **Correlation in Hydrocarbon Exploration**, Graham and Trotman, London, 23-31.

Smith, A.G. and Briden, J.C., 1977, **Mesozoic and Cenozoic Paleocontinental Maps**, Cambridge University Press, 63p.

Smith, D.G., 1989, Stratigraphic correlation of presumed Milankovitch cycles in the Blue Lias (Hettangian to earliest Sinemurian), England, **Terra Nova**, 1: 457-460.

Spaeth, C., Hoefs, J. and Vetter, U., 1971, Some aspects of isotopic composition of belemnites and related paleotemperatures, **Geological Society of America**, 82: 3139-3150.

Spath, L.F., 1956, The Liassic ammonite faunas of the Stowell Park Borehole, **Bulletin of the Geological Survey of Great Britain**, 11: 140-164.

Sørensen, J. and Jørgensen, B.B., 1987, Early diagenesis in sediments from Danish coastal waters: microbial activity and Mn-Fe-S geochemistry, **Geochimica et Cosmochimica Acta**, 51: 1583-1590.

Stahl, W. and Jordon, R., 1969, General considerations on isotopic paleotemperature determinations and analyses on Jurassic ammonites, **Earth and Planetary Science Letters**, 6: 173-178.

Staudigel, H., Hart, S.R. and Richardson, S.H., 1981, Alteration of the oceanic crust: processes and timing, Earth and Planetary Science Letters, v. 52, pp. 311-327.

Staudigel, H., Doyle, P. and Zindler, A., 1985, Sr and Nd isotope systematics in fish teeth, **Earth and Planetary Science Letters**, 76: 45-56.

Stevens, G.R. and Clayton, R.N., 1971, Oxygen isotope studies on Jurassic and Cretaceous belemnites from New Zealand and their biogeographic significance, **New Zealand Journal of Geology and Geophysics**, 14: 829-897.

Stott, L.D. and Kennett, J.P., 1989, New constraints on early Tertiary palaeoproductivity from carbon isotopes in foraminifera, **Nature**, 342: 526-529.

Swart, P.K., Ruiz, J. and Holmes, C.W., 1987, Use of strontium isotopes to constrain timing and mode of dolomitization of upper Cenozoic sediments in a core from San Salvador, Bahamas, **Geology**, 15: 262-265.

Sykes, R.M., 1975, **Facies and Faunal Analysis of the Callovian and Oxfordian Stages (Middle - Upper Jurassic) in Northern Scotland and East Greenland**, Unpublished D.Phil. thesis, Department of Earth Sciences, Oxford University.

Tardy, Y., N'Kounkou, R. and Probst, J.L., 1989, The global water cycle and continental erosion during Phanerozoic time (570 my), **American Journal of Science**, 289: 455-483.

Tivey, M.K., Olson, L.O., Miller, V.W. and Light, R.D., 1990, Temperature measurements during initiation and growth of a black smoker chimney, **Nature**, 346: 51-54.

Torrens, H.S., 1968, The Great Oolite Series, *in* Sylvester-Bradley, P.C. and Ford, T.D. (eds.), **The Geology of the East Midlands**, University Press, Leicester, 227-263.

Torrens, H.S., 1969a, **International Field Symposium on the British Jurassic**, William Smith and Guides to Field Excurisons from London, University of Keele, 35p.

Torrens, H.S., 1969b, **Internation Field Symposium on the British Jurassic**, Guide for Dorset and south Somerset, University of Keele, 71p.

Tréhu, A.M., 1975, Depth versus $(age)^{1/2}$: a perspective on mid-ocean ridges, **Earth and Planetary Science Letters**, 27: 287-304.

Urey, H.C., Lowenstam, H.A., Epstein, S. and McKinney, C.R., 1951, Measurement of paleotemperatures and temperatures of the Upper Cretaceous of England, Denmark, and the southern United States, **Bulletin of the Geological Society of America**, 62: 399-416.

Urlichs, M., 1977, The Lower Jurassic in southwestern Germany, **Stuttgarter Beitrge zur Zaturkunde (Series B)**, 24: 1-41.

Vahrenkamp, V.C, Swart, P.K. and Ruiz, J., 1988, Constraints and interpretation of $^{87}Sr/^{86}Sr$ ratios in Cenozoic dolomites, **Geophysical Research Letters**, 15: 385-388.

Van Buchem, F.S.P. and McCave, I.N., 1989, Cyclic sedimentation patterns in Lower Lias mudstones of Yorkshire (GB), **Terra Nova**, 1: 461-467.

Vanko, D., 1986, High-chlorine amphiboles from oceanic rocks: products of highly saline hydrothermal fluids?, **American Mineralogist**, 71: 51-59.

Veizer, J., 1974, Chemical diagenesis of belemnite shells and possible consequences for paleotemperature determinations, **Neues Jahrbuch fr Geologie und Palontologie Abhandlungen**, 147: 91-111.

Veizer, J., 1983, Chemical diagenesis of carbonates: theory and application of trace element techniques, *in* Arthur, M.A. (organizer), **Stable Isotopes in Sedimentary Geology**, Society of Economic Paleontologists and Mineralogists Short Course No. 10, pp. 3-1--3-100.

Veizer, J., 1989, Strontium isotopes in seawater through time, **Annual Reviews in Earth and Planetary Sciences**, 17: 141-167.

Veizer, J. and Compston, W., 1974, $^{87}Sr/^{86}Sr$ composition of seawater during the Phanerozoic, **Geochimica et Cosmochimica Acta**, 38: 1461-1484.

Veizer, J. and Compston, W., 1976, $^{87}Sr/^{86}Sr$ in Precambrian carbonates as an index of crustal evolution, **Geochimica et Cosmochimica Acta**, 40: 905-914.

Veizer, J., Compston, W., Clauer, N. and Schidlowski, M., 1983, $^{87}Sr/^{86}Sr$ in Late Proterozoic carbonates: Evidence for a mantle event at 900 Ma ago, **Geochimica et Cosmochimica Acta**, 47: 295-302.

Veizer, J. and Fritz, P., 1976, Possible control of post-depositional alteration in oxygen paleotemperature determinations, **Earth and Planetary Science Letters**, 33: 255-260.

von Breymann, M.T., Collier, R. and Suess, E., 1990, Magnesium adsorption and ion exchange in marine sediments: A multi-component model, **Geochimica et Cosmochimica**, 54: 3295-3313.

Von Damm, K.L., 1988, Systematics of and postulated controls on submarine hydrothermal solution chemistry, **Journal of Geophysical Research**, 93: 4551-4561.

Von Damm, K.L., 1990, Seafloor hydrothermal activity: black smoker chemistry and chimneys, **Annual Review of Earth and Planetary Sciences**, 18: 173-204.

Von Damm, K.L. and Biscoff, J.L., 1987, Chemistry of hydrothermal solutions from the southern Juan de Fuca Ridge, **Journal of Geophysical Research**, 92: 11334-11346.

Von Damm, K.L., Edmund, J.M., Grant, B., Measures, C.I., Walden, B. and Weiss, R.F., 1985a, Chemistry of submarine hydrothermal solutions at 21° N, East Pacific Rise, **Geochimica et Cosmochimica Acta**, 49: 2197-2220.

Von Damm, K.L., Edmund, J.M., Measures, C.I. and Grant, B., 1985, Chemistry of submarine hydrothermal solutions at Guaymas Basin, Gulf of California, **Geochimica et Cosmochimica Acta**, 49: 2221-2237.

Wadleigh, M.A., Veizer, J. and Brooks, C., 1985, Strontium and its isotopes in Canadian Rivers: Fluxes and global implications, **Geochimica et Cosmochimica Acta**, 49: 1727-1736.

Weedon, G.P., 1985, Hemipelagic shelf sedimentation and climatic cycles: the basal Jurassic (Blue Lias) of South Britain, **Earth and Planetary Science Letters**, 76: 321-335.

Weedon, G.P. and Jenkyns, H.C., 1990, Regular and irregular climatic cycles and the Belemnite Marls (Pliensbachian, Lower Jurassic, Wessex Basin), **Journal of the Geological Society of London**, 147: 915-918.

Wefer, G., 1982, Palotemperaturbestimmungen mit Hilfevon Sauerstoffisotopen an Ammoniten und Foraminiferen des Apt und Alb, **Geologie Jarhbuch**, A65: 273-281.

Weissert, H., 1989, C-isotope stratigraphy, a monitor of paleoenvironmental change: A case study from the Early Cretaceous, **Surveys in Geophysics**, 10: 1-61.

Weissert, H.J. and Channell, J.E.T., 1989, Tethyan carbonate carbon isotope stratigraphy across the Jurassic-Cretaceous boundary: an indicator of decelerated global carbon cycling?, **Paleoceanography**, 4: 483-494.

Weissert, H.J. and Lini, A., 1991, Ice age interludes during the time of Cretaceous greenhouse climate?, *in* Mller, D.W., McKenzie, J.A. and Weissert, H. (eds.), **Controversies in Modern Geology**, Academic Press, London, 173-191.

Whittaker, A. and Green, G.W., 1983, **Geology of the Country around Weston-super-Mare**, Geological Survey of Great Britain Sheet Memoir 279, 147p.

Wickman, F.E., 1948, Isotope ratios: A clue to the agé of certain marine sediments, **Journal of Geology**, 56: 61-66.

Wicks, F.J. and Plant, A.G., 1979, Electron microprobe and x-ray microbeam studies of serpentine textures, **Canadian Mineralogist**, 17: 785-830.

Wignall, P.B., 1990, Benthic palaeoecology of the late Jurassic Kimmeridge Clay of England, **Special Papers in Palaeontology**, 43: 74pp.

Wilkinson, B.H. and Walker, J.C.G., 1989, Phanerozoic cycling of sedimentary carbonate, **American Journal of Science**, 289: 525-548.

Williams, D.L. and Von Herzen, R.P., 1974, Heat loss from the earth: a new estimate, **Geology**, 2: 327-328.

Wimbledon, W.A., 1986, Rhythmic sedimentation in the Late Jurassic-Early Cretaceous, **Proceedings of the Dorset Natural History and Archaeological Society**, 108: 127-133.

Woodruff, F. and Savin, S.M., 1991, Mid-Miocene isotope stratigraphy in the deep sea: High-resolution correlations, paleoclimatic cycles, and sediment preservation, **Paleoceanography**, 6: 755-806.

Wolery, T.J. and Sleep, N.H., 1988, Interactions of geochemical cycles with the mantle, *in* Gregor, C.B., Garrels, R.M., Mackenzie, F.T. and Maynard, J.B. (eds.), **Chemical Cycles in the Evolution of the Earth**, Wiley-Interscience, New York, 77-103.

Worthington, L.V., 1981, The water masses of the world ocean: some results of a fine-scale census, *in* Warren, B.A. and Wunsch, C. (eds.), **Evolution of Physical Oceanography**, MIT Press, Cambridge, Massachusetts, 42-69.

Wright, J.K., 1968, The stratigraphy of the Callovian rocks between Newtondale and the Scarborough coast, Yorkshire, **Proceedings of the Geological Association of London**, 79: 363-399.

Wright, J.K., 1977, The Cornbrash Formation (Callovian) in North Yorkshire and Cleveland, **Proceedings of the Yorkshire Geological Society**, 41: 325-346.

Wright, J.K., 1986a, The Upper Oxford Clay at Furzy Cliff, Dorset: stratigraphy, palaeoenvironment and ammonite fauna, **Proceedings of the Geologists' Association**, 97: 221-228.

Wright, J.K., 1986b, A new look at the stratigraphy, sedimentology and ammonite fauna of the Corallian Group (Oxfordian) of south Dorset, **Proceedings of the Geologists' Association**, 97: 1-21.

Wright, J.K., 1989, The early Kimmeridgian ammonite succession at Staffin, Isle of Skye, **Scottish Journal of Geology**, 25: 263-272.

Zachos, J.C., Arthur, M.A. and Dean, W.E., 1989, Geochemical evidence for suppression of pelagic marine productivity at the Cretaceous/Tertiary boundary, **Nature**, 337: 61-64.

Zachos, J.C., Breza, J.R. and Wise, S.W., 1992, Early Oligocene ice-sheet expansion on Antarctica: Stable isotope and sedimentological evidence from Kerguelen Plateau, southern Indian Ocean, **Geology**, 20: 569-573.

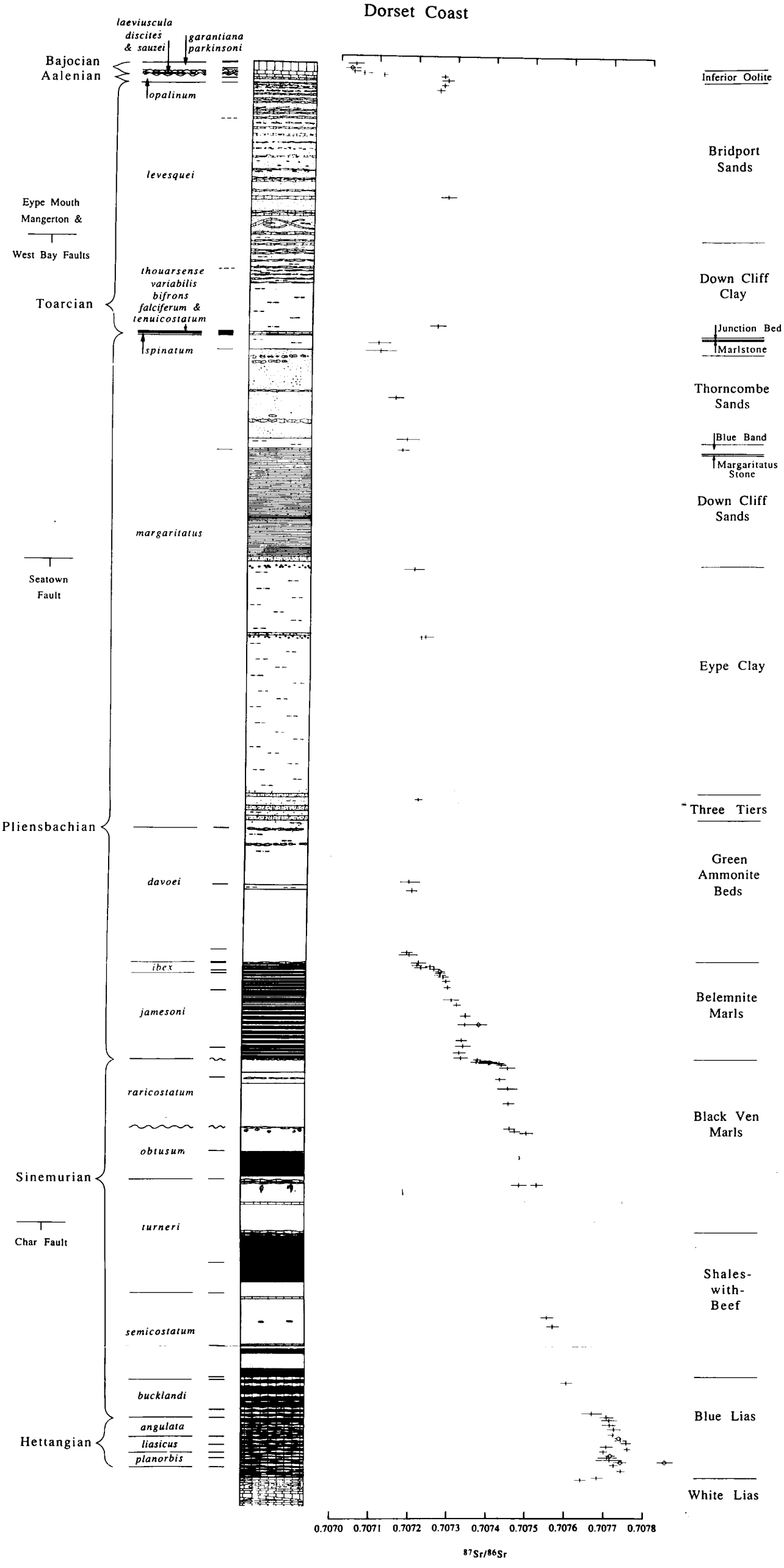
Dorset Coast
laeviuscula
discites
& sauzei
garantiana
parkinsoni
Bajocian
Aalenian
opalinum
levesquei
Eype Mouth
Mangerton &
West Bay Faults
thouarsense
variabilis
bifrons
falciferum &
tenuicostatum
Toarcian
spinatum
margaritatus
Seatown
Fault
Pliensbachian
davoei
ibex
jamesoni
raricostatum
obtusum
Sinemurian
turneri
Char Fault
semicostatum
bucklandi
angulata
liasicus
planorbis
Hettangian
Inferior Oolite
Bridport
Sands
Down Cliff
Clay
Junction Bed
Marlstone
Thorncombe
Sands
Blue Band
Margaritatus
Stone
Down Cliff
Sands
Eype Clay
Three Tiers
Green
Ammonite
Beds
Belemnite
Marls
Black Ven
Marls
Shales-
with-
Beef
Blue Lias
White Lias
0.7070
0.7071
0.7072
0.7073
0.7074
0.7075
0.7076
0.7077
0.7078
87Sr/86Sr

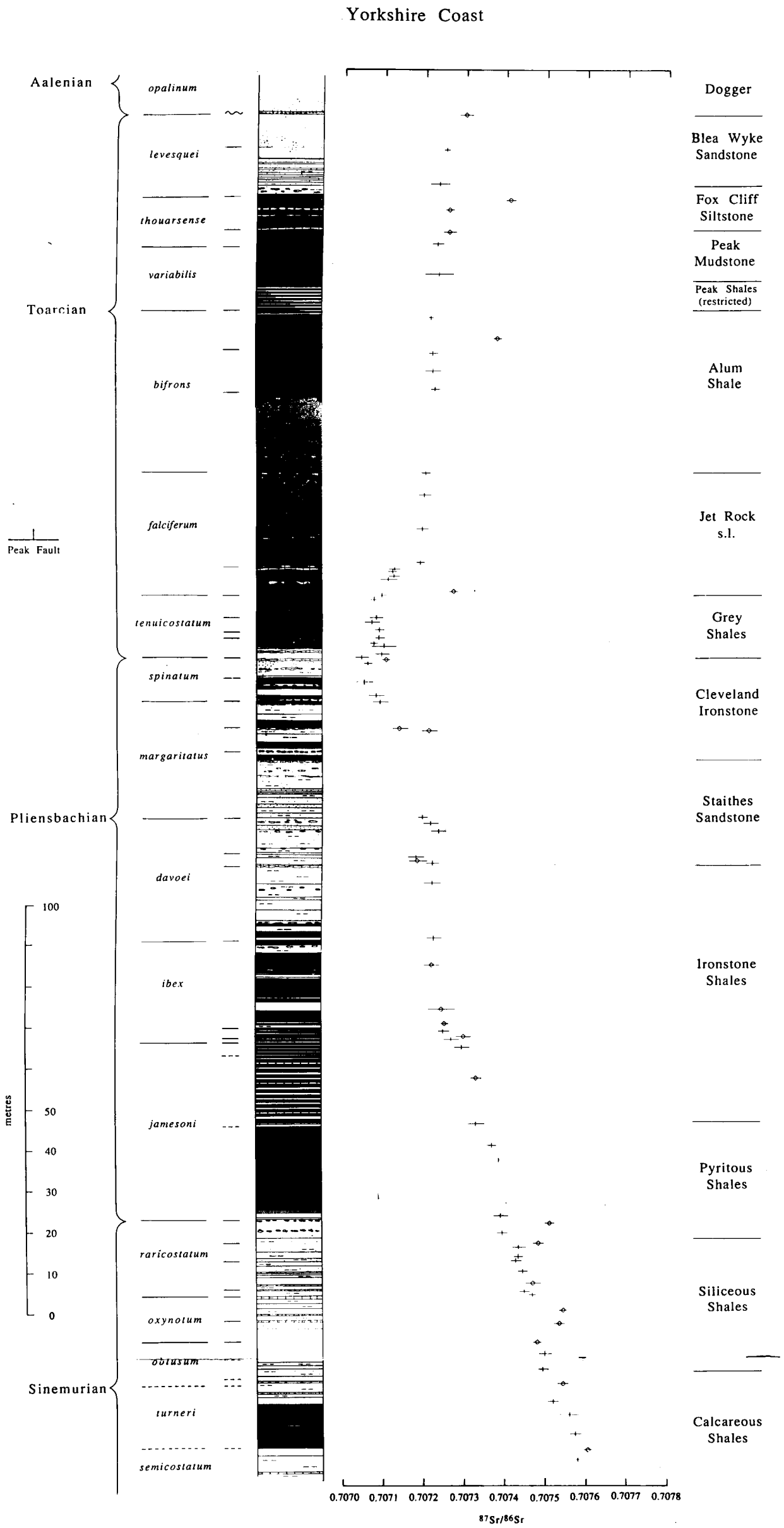
Yorkshire Coast
Aalenian
Toarcian
Pliensbachian
Sinemurian
opalinum
levesquei
thouarsense
variabilis
bifrons
falciferum
tenuicostatum
spinatum
margaritatus
davoei
ibex
jamesoni
raricostatum
oxynotum
obtusum
turneri
semicostatum
Peak Fault
metres
100
50
40
30
20
10
0
Dogger
Blea Wyke Sandstone
Fox Cliff Siltstone
Peak Mudstone
Peak Shales (restricted)
Alum Shale
Jet Rock s.l.
Grey Shales
Cleveland Ironstone
Staithes Sandstone
Ironstone Shales
Pyritous Shales
Siliceous Shales
Calcareous Shales
0.7070
0.7071
0.7072
0.7073
0.7074
0.7075
0.7076
0.7077
0.7078
87Sr/86Sr